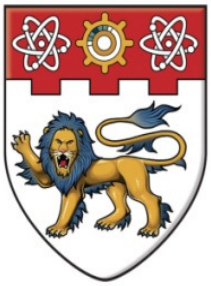

NANYANG TECHNOLOGICAL UNIVERSITY

ACTIVATION OF PEROXYMONOSULFATE BY HETEROGENEOUS CATALYSTS FOR THE REMOVAL OF ORGANIC POLLUTANTS IN WATER

OH WEN DA
Interdisciplinary Graduate School
Nanyang Environment and Water Research Institute

2016

ACTIVATION OF PEROXYMONOSULFATE BY HETEROGENEOUS CATALYSTS FOR THE REMOVAL OF ORGANIC POLLUTANTS IN WATER

OH WEN DA

Interdisciplinary Graduate School
Nanyang Environment and Water Research Institute

A thesis submitted to the Nanyang Technological University in partial fulfilment of the requirement for the degree of Doctor of Philosophy

2016

ABSTRACT

In recent decades, advanced oxidation process employing sulfate radical has emerged as a very promising method to remove recalcitrant organic pollutant in water. One of the most efficient ways to generate sulfate radical is by heterogeneous transition metal activation of peroxymonosulfate (PMS, available commercially as Oxone®). To date, many studies employed cobalt oxide catalysts which can potentially lead to the cobalt pollution due to cobalt leaching during treatment. In order to eliminate the cobalt leaching problem, the main objective of this study is to fabricate other types of metal oxide catalysts to activate PMS for the degradation of recalcitrant organic contaminants.

In the first part of the study, a novel dipicolinic acid–functionalized Fe_2O_3 (DPA–Fe_2O_3) with high surface area was prepared by co–precipitation of a Fe(III)–DPA complex. It was used as a catalyst to activate PMS for bisphenol A (BPA) detoxification. A higher catalytic activity of DPA–Fe_2O_3 over other Fe(III)–based catalysts was observed for BPA oxidation in the presence of Oxone®. The performance of the catalyst was optimized with respect to the initial pH, Oxone® dosage and catalyst loading. The acute toxicity of BPA solution over time was studied using *Vibrio fischeri* bacteria and the results indicated that the evolution of acute toxicity was highly dependent on the initial Oxone® dosage.

In the second part of the study, the catalytic activity of Fe_2O_3 catalyst was successfully improved by incorporating Cu(II) during the co–precipitation synthesis to produce a mixed metal $CuFe_2O_4$–Fe_2O_3 catalyst for BPA oxidation *via* PMS activation. The formation mechanism of $CuFe_2O_4$–Fe_2O_3 is proposed. The performance of $CuFe_2O_4$–Fe_2O_3 as a PMS activator was compared with those of other catalysts and the results indicated that the performance was in the following order: $CuFe_2O_4$–Fe_2O_3 > $CuFe_2O_4$ > $CoFe_2O_4$ > $CuBi_2O_4$ > $CuAl_2O_4$ > DPA–Fe_2O_3 > $MnFe_2O_4$. A kinetic model with

mechanistic consideration of the influence of pH, PMS dosage and catalyst loading is developed to describe the degradation of BPA. The intrinsic rate constant (k_i) was obtained from the kinetic study and the relationship between the pseudo first–order rate constant and k_i was successfully established. The influence of water matrix species (*i.e.* Cl^-, NO_3^-, HCO_3^-, PO_4^{3-} and humic acid) on the BPA degradation rate was also investigated and the results indicated that Cl^- and humic acid exerted noticeable reduction in the BPA degradation rate. The $CuFe_2O_4$–Fe_2O_3 catalyst exhibited excellent stability and could be reused several times without significant deterioration in performance.

The third phase of this study involved the fabrication of an efficient bi–functional $CuBi_2O_4$ catalyst *via* a facile hydrothermal method to activate PMS and persulfate (PS) for benzotriazole (BTZ) removal. Characterization of the $CuBi_2O_4$ catalyst using XRD, FESEM, FTIR, BET and XPS revealed that it has a unique 3–D hierarchical structure with molecular formula of $Cu_{1.2}Bi_{1.6}O_{3.6}$ and 2.4% w/w of CuO. The performance of $CuBi_2O_4$ catalyst was investigated at different initial PMS/PS dosages, catalyst loadings and initial BTZ concentrations. Interestingly, it was found that the inter– and intra–molecular hydrogen bonding play prominent roles in the BTZ removal mechanism in both the PMS and PS systems. Meanwhile, it is relatively easier to activate PMS, leading to a faster BTZ removal rate over the PS system. The intermediate products of BTZ degradation produced from the PMS and PS systems were similar, indicating a similar degradation pathway. The catalyst could still retain its morphology and be reused multiple times.

In the final phase of this study, the $CuBi_2O_4$ catalyst was used to activate PMS for sulfanilamide (SA) removal. A facile method based on the kinetic approach is proposed to calculate the normalized steady–state concentrations of $SO_4^{\bullet-}$ and $^{\bullet}OH$ for the characterization of the intrinsic catalytic activity of heterogeneous catalyst/PMS system.

ACKNOWLEDGEMENT

First and foremost, I would like to express my sincere gratitude to my supervisor Associate Professor Lim Teik Thye for his support in providing insightful guidance and encouragement throughout my PhD study. I would also like to acknowledge my co−supervisor, Associate Professor Dong Zhili, and my mentor, Professor Ng Wun Jern, for their invaluable assistances and advices from time to time.

Secondly, I would like to thank my wife, Wan Ching, and my family members for their support and understanding through this period of hardship.

Thirdly, I would like to take this opportunity to thank the research, office and technical staffs for their kind assistance throughout my PhD study. To name a few, Mr. Jacky Khoo, Ms. Deirdre Lim, Ms. Hera, Mrs. Lim−Tay Chew Wang, Mr. Ong Chee Yung, Dr. Derrick Ang, Dr. Zviad Tsakadze, Mr. Alan Lim Ming Pin, Mr. Tan Han Kiang, Mrs. Maria Chong Ai Shing and Ms. Pearlyn See Shen Yen. I would also like to thank my group members who have worked with me for the past years; thank you and I look forward to work with you again.

Finally, I would like to acknowledge the Interdisciplinary Graduate School (IGS), Nanyang Technological University and Nanyang Environment and Water Research Institute (NEWRI) for providing the PhD research scholarship for my PhD study. I am also grateful to be awarded the DAAD conference scholarship and research fellowship to participate in two conferences and to conduct my research stay in Germany.

LIST OF PUBLICATIONS

Parts of the findings in the following journal papers were presented in this thesis:

1. **W.D. Oh**, S.K. Lua, Z.L. Dong, and T.T. Lim (2014). High surface area DPA−hematite for efficient detoxification of bisphenol A *via* peroxymonosulfate activation. *Journal of Materials Chemistry A*, 38, 15836−15845.
2. **W.D. Oh**, S.K. Lua, Z.L. Dong, and T.T. Lim (2015). Performance of magnetic activated carbon composite as peroxymonosulfate activator and regenerable adsorbent *via* sulfate radical−mediated oxidation processes. *Journal of Hazardous Materials*, 284, 1−9.
3. **W.D. Oh**, S.K. Lua, Z.L. Dong, and T.T. Lim (2015). A novel three−dimensional spherical $CuBi_2O_4$ consisting of nanocolumn arrays with persulfate and peroxymonosulfate activation functionalities for 1H−benzotriazole removal, *Nanoscale*, 7, 8149−8158.
4. **W.D. Oh**, Z.L. Dong, Z.T. Hu and T.T. Lim (2015). A novel quasi−cubic $CuFe_2O_4$–Fe_2O_3 prepared at low temperature for enhanced oxidation of bisphenol A *via* peroxymonosulfate activation. *Journal of Materials Chemistry A*, 3, 22208−22217.
5. **W.D. Oh**, S.K. Lua, Z.L. Dong, and T.T. Lim (2015). Rational design of hierarchically−structured $CuBi_2O_4$ composites by deliberate manipulation of the nucleation and growth kinetics of $CuBi_2O_4$ for environmental applications. *Nanoscale*, **8**, 2016−2054.

6. **W.D. Oh**, Z.L. Dong, and T.T. Lim (2016). Generation of sulfate radical through heterogeneous catalysis for organic contaminants removal: Current development, challenges and prospects. *Applied catalysis B: Environmental*, **194**, 169-201.
7. **W.D. Oh**, Z.L. Dong, and T.T. Lim (2016). Hierarchically−structured Co−$CuBi_2O_4$ and Cu−$CuBi_2O_4$ for sulfanilamide removal *via* peroxymonosulfate activation. *Catalysis today* (In Press).

Co−authorship publications:

1. Z.T. Hu, J.C. Liu, X.L. Yan, **W.D. Oh** and T.T. Lim (2015). Low−temperature synthesis of graphene/$Bi_2Fe_4O_9$ composite for synergistic adsorption−photocatalytic degradation of hydrophobic pollutant under solar irradiation. *Chemical Engineering Journal*, 262, 1022−1032.
2. S.K. Lua, **W.D. Oh**, L.Z. Zhang, L. Yao, T.T. Lim and Z.L. Dong (2015). A molybdovanadophosphate−based surfactant encapsulated heteropolyanion with multi−lamellar nano−structure for catalytic wet air oxidation of organic pollutant under mild conditions. *RSC Advances*, 94743−94751.

TABLE OF CONTENT

LIST OF TABLES

LIST OF FIGURES

LIST OF SYMBOLS AND ABBREVIATIONS

Abbreviation

λ	Wavelength
ρ_s	Specific surface area
k_{app}	Pseudo first−order rate constant
K_{eq}	Equilibrium constant
k_i	Intrinsic reaction rate constant
k_{SD}	Specific rate constant
pH_{zpc}	pH of the point of zero charge
pK_a	Acid dissociation constant
$[^{\bullet}OH]_{ss}$	Steady state concentrations of hydroxyl radical
$[^{\bullet}OH]_{Nss}$	Normalized steady state concentrations of hydroxyl radical
$[SO_4^{\bullet-}]_{ss}$	Steady state concentrations of sulfate radical
$[SO_4^{\bullet-}]_{Nss}$	Normalized steady state concentrations of sulfate radical
AC	Activated carbon
ACF	Activated carbon fiber
BET	Brunauer−Emmett−Teller
BPA	Bisphenol A
BTZ	Benzotriazole
CNT	Carbon nanotube
DOM	Dissolved organic matter
DPA	Dipicolinic acid
ESR	Electron spin resonance
EtOH	Ethanol
FESEM	Field emission scanning electron microscope
FTIR	Fourier transform infrared
GO	Graphene oxide
HPLC	High performance liquid chromatography
MeOH	Methanol
NHE	Normal hydrogen electrode
$^{\bullet}OH$	Hydroxyl radical
OMS	Octahedral molecular sieves

PMS	Peroxymonosulfate
PS	Persulfate
rGO	Reduced graphene oxide
$SO_4^{\bullet-}$	Sulfate radical
SR−AOPs	Sulfate radical−based advanced oxidation processes
SA	Sulfanilamide
SUVA	Specific ultraviolet absorbance
TEM	Transmission electron microscope
TOC	Total organic carbon
UV_{254}	Ultraviolet irradiation at λ = 254 nm
XPS	X−ray photoelectron spectroscope
XRD	X−ray powder diffraction
ZVI	Zero valent iron

CHAPTER 1 INTRODUCTION

1.1. Background

In recent decades, environmental pollution by recalcitrant organics is increasingly becoming a challenging multidisciplinary problem as new chemicals are being introduced continuously into the environment. Water pollution due to recalcitrant organics particularly those classified as emerging contaminants (e.g. pharmaceuticals and their metabolites, endocrine disruptors, disinfection by−products, personal care products and illicit drugs) could lead to serious ecological impacts (Krasner, 2009; Petrie et al., 2015; Sauvé & Desrosiers, 2014). Many recalcitrant organics are toxic, biorefractory and difficult to be removed by the conventional treatment methods (Babuponnusami & Muthukumar, 2014). As such, advanced treatment techniques with chemical oxidation that offer remarkable efficiency for the treatment of recalcitrant organics are highly desired.

Sulfate radical−based advanced oxidation process (SR−AOP) is increasingly gaining attention as effective solution to the removal of recalcitrant organics in water. The SR−AOP utilize highly−reactive sulfate radical ($SO_4^{\bullet-}$) to oxidize organic contaminants to innocuous CO_2 and H_2O. Recent studies have shown that SR−AOP is effective in removing various types of recalcitrant contaminants such as volatile organic compounds (Anipsitakis & Dionysiou, 2003; Huang et al., 2005), endocrine disruptors (Sharma et al., 2015), pharmaceuticals and their metabolites (Nfodzo & Choi, 2011; Zhang et al., 2015), cyanotoxins (Antoniou et al., 2010a; Antoniou et al., 2010b) and perfluorinated compounds (Lee et al., 2013) in water. The SR−AOP is also effective in other applications including disintegration of activated sludge (Ren et al., 2015a), disinfection (Michael-Kordatou et al., 2015) and decontamination of pool water (Anipsitakis et al., 2008).

Most commonly, $SO_4^{\bullet-}$ is generated *via* peroxymonosulfate (PMS) or persulfate (PS) activation. Various activation methods have been proposed which include the use of heat (Ji et al., 2015), chemicals (Fang et al., 2013; Zhou et al., 2015b), base (Furman et al., 2010), ultraviolet (Guan et al., 2011), transition metals (Anipsitakis & Dionysiou, 2004; Anipsitakis et al., 2005b; Rastogi et al., 2009) and ultrasound (Cai et al., 2015). The transition metal activation method is less complex in reactor/system configuration and more economical compared with the energy–based activation methods (e.g. ultrasound, ultraviolet and heat etc.). The transition metal activation of PMS and PS can be achieved in the homogeneous and heterogeneous systems. The heterogeneous system is advantageous over the homogeneous system because (i) the solid heterogeneous catalyst can be easily separated from the treated water for reuse, (ii) secondary treatment to remove dissolved metals from the treated water (as in the homogeneous system) is not required, and (iii) it is more tolerant towards extreme operating conditions (Davis & Davis, 2012). The heterogeneous system is effective over a broader pH range including the prevailing pH for natural water and wastewater (pH 2–9) whereas for the homogeneous system, the dissolved catalyst could precipitate at circumneutral and basic pH which decreases its performance (Chan & Chu, 2009; Zhou et al., 2015a). Compared to PS, PMS is relatively easier to be activated with metal oxide catalysts due to the difference in their molecular structures (i.e. PMS is asymmetrical while PS is symmetrical) and bond dissociation energies. Unlike PS activation reaction which consumes the catalyst, PMS catalysts have a relatively longer lifespan because they can potentially be regenerated (through oxidation–reduction cycle by PMS).

1.2. Knowledge gap and research motivation

For activation of PMS by heterogeneous catalyst, many studies have adopted heterogeneous cobalt oxide catalysts for PMS activation because Co has been identified as the most efficient PMS activator (Anipsitakis & Dionysiou, 2004; Anipsitakis et al., 2005b; Chen et al., 2008; Gerken et al., 2011; Guo et al., 2013). However, Co leaching from heterogeneous Co catalysts during PMS activation (due to dissolution under acidic pH and chemical reaction with PMS) poses a concern as Co is considerably toxic and potentially carcinogenic (Simonsen et al., 2012). Dissolved Co concentration ranging from 0.002 to 0.107 mg L^{-1} has been detected in drinking water (Qiu & Zheng, 2009). To avoid Co leaching, the research direction has been shifted towards the use of other catalysts, namely metal (Mn–, Fe– and Cu–based) and nonmetal (carbon–based) catalysts. The carbon–based catalysts are less active, have lower durability for long term use due to cannibalistic oxidation, and less economical (e.g. CNTs and graphene etc.) compared to metal–based catalysts. Considering that the SR–AOP has been the subject of tremendous research interest due to its potential environmental applications, Mn–, Fe– and Cu–based catalysts are extensively being investigated as PMS activators. The Mn–, Fe– and Cu–based catalysts have the advantages of being less toxic and potentially more stable compared with Co–based catalyst (Saputra et al., 2013a; Wadewitz et al., 2013). However, the applications of Mn–, Fe–, Cu– and nonmetal–based catalysts are usually not as effective as the Co–based catalyst and further study is required to improve their catalytic activity. This can be achieved either by (i) controlling the surface morphology of the catalyst, (ii) introducing surface functionality to improve the electron mobility of the catalyst, and (iii) coupling various transition metals to produce polyfunctional and highly redox active mixed metal oxide catalyst with improved chemical stability.

To date, there are limited studies on the assessment of the toxicity of the degradation

products induced by the $SO_4^{\bullet-}$ oxidation in the heterogeneous catalyst/PMS system. This is mainly because of the difficulty to differentiate the intrinsic toxicity of PMS from that induced by the degradation products in the treated water. The kinetics of pollutant degradation in the heterogeneous catalyst/PMS system can be affected by various factors including the pH, catalyst loading and PMS dosage. However, there are limited studies on the development of a mechanistic kinetic model that can be used to holistically account for the influences of pH, catalyst loading and PMS dosage.

1.3. Objectives and scopes of study

The general objective of this study was to address the knowledge gaps in the current literature which include the (i) development of novel materials for applications as catalysts for organic pollutants removal in water *via* SR−AOPs, (ii) investigation of the acute toxicity of the $SO_4^{\bullet-}$−induced degradation products in the treated water, and (iii) development of a mechanistic kinetic model for heterogeneous catalyst/PMS system incorporating various influencing factors (i.e. pH, catalyst loading and PMS dosage). This study consists of four parts. In the first part of this study, single metal oxide dipicolinic acid encapsulated Fe_2O_3 catalyst (DPA−Fe_2O_3) was fabricated for bisphenol A (BPA) detoxification *via* PMS activation. In the second part of this study, further improvement of the catalyst was achieved by coupling another transition metal with Fe(III) to produce a mixed metal oxide catalyst with enhanced redox activity and potential ferromagnetism for magnetic recovery of the catalyst after use. In the third part of study, the mixed metal oxide catalyst was further modified to possess bi−functional PMS and PS activation functionalities for benzotriazole (BTZ) removal. Finally, the mixed metal oxide catalyst was employed to generate $SO_4^{\bullet-}$ from PMS for sulfanilamide (SA) removal and the steady state concentrations of $SO_4^{\bullet-}$ and $^{\bullet}OH$ during catalytic reaction were estimated. The BPA, BTZ and SA were selected as model pollutants in this study. This is because the pollutants

are difficult to be removed by the conventional treatment methods. They are also increasingly found in water as the result of their ubiquitous applications in many industries. The specific scopes of work in each part of this study are outline below:

1. Fabrication of dipicolinic acid encapsulated Fe_2O_3 (DPA–Fe_2O_3) and evaluation of its performance in BPA detoxification *via* PMS activation.
    a. To optimize the synthesis conditions for preparing high surface area DPA–Fe_2O_3.
    b. To evaluate and optimize the performance of DPA–Fe_2O_3 for BPA detoxification *via* PMS activation.
    c. To investigate the acute toxicity of the $SO_4^{\bullet-}$–induced BPA degradation products in the treated solution.
2. Fabrication of mixed metal oxide catalysts and evaluation of their performance in BPA removal *via* PMS activation.
    a. To fabricate and compare the performance of various mixed metal oxides including $CuFe_2O_4$–Fe_2O_3, $CuAl_2O_4$, $CuBi_2O_4$, $CuFe_2O_4$, $CoFe_2O_4$, and $MnFe_2O_4$ as catalysts BPA removal.
    b. To develop a kinetic model based on the mechanistic consideration of various influencing parameters (pH, catalyst loading, and Oxone® dosage).
    c. To investigate the kinetics of heterogeneous catalyst/PMS system.
3. Fabrication of a novel bi–functional mixed metal $CuBi_2O_4$ catalyst with PMS and PS activation functionalities for BTZ removal.
    a. To optimize the synthesis conditions for preparing bi–functional mixed metal $CuBi_2O_4$ catalyst for BTZ removal *via* catalytic PMS and PS activation.
    b. To evaluate and optimize the performance of mixed metal $CuBi_2O_4$ catalyst for BTZ removal *via* PMS and PS activation.
    c. To investigate the mechanisms of BTZ removal *via* PMS and PS activation.

4. Performance of bi−functional mixed metal $CuBi_2O_4$ catalyst for SA removal *via* PMS activation.
    a. To evaluate and optimize the performance of mixed metal $CuBi_2O_4$ catalyst for SA removal *via* PMS activation.
    b. To develop a kinetic approach to estimate the normalized steady−state concentrations of $SO_4^{\bullet-}$ and $^{\bullet}OH$ in heterogeneous catalyst/PMS system.

1.4. Organization of thesis

This thesis consists of seven chapters. This chapter presents a brief background of study, current knowledge gap and research motivation, objectives, scopes of study and the organization of this thesis.

Chapter 1 provides a brief background, knowledge gap and research motivation, objectives and scopes, and organization of the thesis.

Chapter 2 provides an up−to−date literature review of the fundamentals of SR−AOP covering the chemistry of $SO_4^{\bullet-}$, PMS activation by transition metals and current development in the heterogeneous catalysts with specific emphasis on the Mn−, Fe−, and Cu−based catalysts.

In **Chapter 3**, the low−temperature co−precipitation synthesis of dipicolinic acid encapsulated Fe_2O_3 and its performance as a catalyst for BPA detoxification *via* PMS activation are described. The acute toxicity of $SO_4^{\bullet-}$−induced BPA degradation products in the treated solution is also presented.

Chapter 4 describes the synthesis of mixed metal oxide catalysts including $CuFe_2O_4$−Fe_2O_3, $CuAl_2O_4$, $CuBi_2O_4$, $CuFe_2O_4$, $CoFe_2O_4$ and $MnFe_2O_4$ and their performance as a catalyst for BPA removal *via* PMS activation. A new mechanistic kinetic

model for heterogeneous catalyst/PMS system is also presented.

In **Chapter 5**, the hydrothermal synthesis of mixed metal $CuBi_2O_4$ catalyst is described. The performance of bi−functional mixed metal $CuBi_2O_4$ catalyst for BTZ removal in water *via* PMS and PS activation is presented.

In **Chapter 6**, the performance of mixed metal $CuBi_2O_4$ catalyst for SA removal in water *via* PMS activation is described. A kinetic approach to estimate the normalized steady−state concentrations of $SO_4^{\bullet-}$ and $^{\bullet}OH$ in heterogeneous catalyst/PMS system is also presented.

Finally, in **Chapter 7**, a summary of all the major findings in this thesis and several recommendations for future work are provided.

CHAPTER 2: LITERATURE REVIEW

2.1. The chemistry of sulfate radical

Table 2.1 shows a comparison of the standard reduction potentials of $SO_4^{\bullet-}$ with various oxidants. In general, $SO_4^{\bullet-}$ is a powerful oxidant with a standard redox potential of +2.60 V *vs.* NHE (normal hydrogen electrode), comparable to the standard redox potential of the $^{\bullet}OH$ (+2.80 V *vs.* NHE) but slightly below that of F_2 (+3.03 V *vs.* NHE) (Eberson, 1982; Lim et al., 2011). Compared to $^{\bullet}OH$ ($t_{1/2}$ = <1 μs), the freely–diffusible $SO_4^{\bullet-}$ has a longer lifetime ($t_{1/2}$ = 30–40 μs) allowing excellent mass transfer and contact between $SO_4^{\bullet-}$ with the target pollutant in the heterogeneous catalysis system (Matta et al., 2011; Olmez-Hanci & Arslan-Alaton). The reactivity of $SO_4^{\bullet-}$ is pH independent while that of $^{\bullet}OH$ is pH dependent (removal efficiency of $^{\bullet}OH$–based reaction decreases with increasing pH). Thus, at circumneutral pH (most prevailing in the natural aquatic system), $SO_4^{\bullet-}$ could be more reactive than $^{\bullet}OH$ because of its higher oxidative potential. The reaction between $SO_4^{\bullet-}$ with organic molecules is very fast, typically near diffusion controlled rate with second–order rate constants between 10^5 to 10^9 M^{-1} s^{-1} (Neta et al., 1977; Tsitonaki et al., 2010) while the typical reaction rates for $^{\bullet}OH$ are between 10^6 to 10^{11} M^{-1} s^{-1} (Buxton et al., 1988). The $SO_4^{\bullet-}$–induced degradation could lead to a better mineralization rate than $^{\bullet}OH$ (Sánchez-Polo et al., 2013). Owning to the higher selectivity of $SO_4^{\bullet-}$ compared to $^{\bullet}OH$, $SO_4^{\bullet-}$ can be employed to attack directly at specific functional groups (that may give rise to the ecotoxicity characteristics of the pollutant) *via* electron transfer reaction. On the contrary, higher amount of $^{\bullet}OH$ is required to attack a specific functional group because $^{\bullet}OH$ non–selectively reacts through a series of reactions involving electron transfer, electrophilic/radical addition and hydrogen abstraction (Neta

et al., 1977; Tully et al., 1981). As $SO_4^{\bullet-}$ is electrophilic, it prefers to react with electron–donating groups such as amino (–NH_2), hydroxyl (–OH), alkoxy (–OR), π electrons present on aromatic molecules, and other organic compounds that contain unsaturated bonds. The reaction of $SO_4^{\bullet-}$ with electron–withdrawing groups such as nitro (–NO_2) and carbonyl (C=O) substitutes is generally slower.

Hydroxyl radical can be generated from the pH dependent redox reaction between H_2O/OH^- and $SO_4^{\bullet-}$ as follows (Mahdi Ahmed et al., 2012; Neta et al., 1988; Pagano et al., 2012; Shukla et al., 2010a):

$$SO_4^{\bullet-} + H_2O \rightarrow SO_4^{2-} + {}^{\bullet}OH + H^+,\ k_{SO_4^{\bullet-}+H_2O} < 1.0 \times 10^3\ M^{-1}\ s^{-1} \quad (2.1.1)$$

$$SO_4^{\bullet-} + OH^- \rightarrow SO_4^{2-} + {}^{\bullet}OH,\ k_{SO_4^{\bullet-}+OH^-} = 6.5 \times 10^7\ M^{-1}\ s^{-1} \quad (2.1.2)$$

At pH < 9, $SO_4^{\bullet-}$ is the dominant reactive radical while at pH > 9.0, $^{\bullet}OH$ becomes the dominant reactive radical (Liang & Huang, 2012). The $SO_4^{\bullet-}$ is less influenced by the dissolved organic matter (DOM) compared to $^{\bullet}OH$ (with the second–order rate constant, $k_{SO_4^{\bullet-}+DOM}$ = 6.8 x 10^3 mg C^{-1} s^{-1} and $k_{^{\bullet}OH+DOM}$ = 1.4 x 10^4 mg C^{-1} s^{-1} for the reaction of DOM with $SO_4^{\bullet-}$ and $^{\bullet}OH$, respectively) and thus $SO_4^{\bullet-}$ can selectively attacks the target pollutant in the presence of DOM (Lutze et al., 2015a). However, $SO_4^{\bullet-}$ is more influenced by anionic species (particularly halides) in water than $^{\bullet}OH$ (Yang et al., 2014a). For instance, $SO_4^{\bullet-}$ reacts with common water anions such as Cl^- (Anipsitakis et al., 2006; Lutze et al., 2015b), Br^- (Fang & Shang, 2012; Liu et al., 2015b; Lutze et al., 2014), CO_3^{2-}/HCO_3^- (Dogliotti & Hayon, 1967; Huie & Clifton, 1990; Tsitonaki et al., 2010; Yang et al., 2015b) and HPO_4^- (Yang et al., 2010) to form weaker radicals.

$$SO_4^{\bullet-} + Cl^- \rightarrow Cl^{\bullet} + SO_4^{2-},\ k_{SO_4^{\bullet-}+Cl^-} = 3.0 \times 10^8\ M^{-1}\ s^{-1} \quad (2.1.3)$$

Table 2.1. Comparison of standard reduction potentials of various common oxidants.

Half equation	Standard reduction potential, E^o (V)	Reference
$\mathbf{F_2} + 2\ e^- \rightarrow 2F^-$	2.87	(Haynes, 2013)
$\mathbf{^{\bullet}OH} + e^- \rightarrow OH^-$	2.80	(Lim et al., 2011)
$\mathbf{SO_4^{\bullet-}} + e^- \rightarrow SO_4^{2-}$	2.60–3.10	(Eberson, 1982)
$\mathbf{SO_5^{\bullet-}} + e^- \rightarrow SO_5^{2-}$	1.10	(Das et al., 1999)
$\mathbf{HSO_5^-} + 2H^+ + 2e^- \leftrightarrow HSO_4^- + 2H_2O$	1.82	(Spiro, 1979)
$\mathbf{HSO_5^-} + H^+ + 2e^- \leftrightarrow SO_4^{2-} + H_2O$	1.75	(Spiro, 1979)
$\mathbf{SO_5^{2-}} + H_2O + 2e^- \leftrightarrow SO_4^{2-} + OH^-$	1.22	(Spiro, 1979)
$\mathbf{S_2O_8^{2-}} + 2e^- \leftrightarrow 2SO_4^{2-}$	2.01	(Haynes, 2013)
$\mathbf{S_2O_8^{2-}} + 2H^+ + 2e^- \leftrightarrow 2HSO_4^-$	2.12	(Haynes, 2013)
$\mathbf{H_2O_2} + 2H^+ + 2e^- \leftrightarrow 2H_2O$	1.78	(Haynes, 2013)
$\mathbf{O_3} + 2H^+ + 2e^- \leftrightarrow O_2 + H_2O$	2.08	(Haynes, 2013)
$\mathbf{O_3} + 2\ H_2O + 2e^- \leftrightarrow O_2 + 2OH^-$	1.24	(Haynes, 2013)

$$SO_4^{\bullet-} + Br^- \rightarrow Br^{\bullet} + SO_4^{2-},\ k_{SO_4^{\bullet-}+Br^-} = 3.5 \times 10^9\ M^{-1}\ s^{-1} \quad (2.1.4)$$

$$SO_4^{\bullet-} + HCO_3^- \rightarrow HCO_3^{\bullet} + SO_4^{2-},\ k_{SO_4^{\bullet-}+HCO_3^-} = 2.8–9.1 \times 10^6\ M^{-1}\ s^{-1} \quad (2.1.5)$$

$$SO_4^{\bullet-} + CO_3^{2-} \rightarrow CO_3^{\bullet-} + SO_4^{2-},\ k_{SO_4^{\bullet-}+CO_3^{2-}} = 6.1–410 \times 10^6\ M^{-1}\ s^{-1} \quad (2.1.6)$$

$$SO_4^{\bullet-} + HPO_4^{2-} \rightarrow HPO_4^{\bullet-} + SO_4^{2-},\ k_{SO_4^{\bullet-}+HPO_4^{2-}} = 1.2 \times 10^6\ M^{-1}\ s^{-1} \quad (2.1.7)$$

Under certain conditions, the $SO_4^{\bullet-}$ can oxidize Cl^- and Br^- to produce oxyanions and halogenated disinfection byproducts (Anipsitakis et al., 2006; Liu et al., 2015b; Lutze et al., 2014; Lutze et al., 2015b). Sulfate radical can be scavenged by another $SO_4^{\bullet-}$ or transition metal (e.g. Fe(II) and Co(II)) (Dogliotti & Hayon, 1967; Huie et al., 1991; Kim & Edwards, 1995; Rastogi et al., 2009).

$$SO_4^{\bullet-} + SO_4^{\bullet-} \rightarrow S_2O_8^{2-},\ k_{SO_4^{\bullet-}+SO_4^{\bullet-}} = 3.7 \times 10^8\ M^{-1}\ s^{-1} \quad (2.1.8)$$

$$M^{n+} + SO_4^{\bullet-} \rightarrow M^{(n+1)+} + SO_4^{2-} \quad (2.1.9)$$

The self–scavenging effect (**Eq. 2.1.8**) is not significant provided that the concentration of $SO_4^{\bullet-}$ is low attributed to the rapid consumption of $SO_4^{\bullet-}$ during oxidation reactions (Ghauch et al., 2012).

2.2. Activation of peroxymonosulfate by heterogeneous catalysts

Peroxymonosulfate (HSO_5^-, pKa = 9.4) is commercially available in the form of a triple salt $2KHSO_5 \cdot KHSO_4 \cdot K_2SO_4$ with the trade name Oxone® and Caroat®. It is an acidic oxidant with standard reduction potentials for the aqueous half reactions as follow (Rani et al., 2009; Spiro, 1979; Steele & Appelman, 1982):

$$HSO_5^- + H^+ + 2e^- \leftrightarrow SO_4^{2-} + H_2O,\ E^o = 1.75\ V\ vs.\ NHE \quad (2.2.1)$$

$$SO_5^{2-} + H_2O + 2e^- \leftrightarrow SO_4^{2-} + OH^-,\ E^o = 1.22\ V\ vs.\ NHE \quad (2.2.2)$$

Peroxymonosulfate is widely used as a versatile oxidant for various organic syntheses (Kennedy & Stock, 1960). Although PMS can oxidize organic contaminant, it is kinetically not favorable compared to the radical–based oxidation. The molecular structure of PMS is similar to that of H_2O_2 except that one of the H atoms is replaced with a $-SO_3$ group. The distance of the peroxide bond (–O–O–) in PMS (1.460 Å) is comparable to that of solid state H_2O_2 (1.453 Å) but shorter than that of $S_2O_8^{2-}$ (1.497 Å) (Flanagan et al., 1984). It is estimated that the (–O–O–) bond energy of PMS is between the bond energies of H_2O_2 (213 kJ mol^{-1} (Reints et al., 2000)) and PS (140 kJ mol^{-1} (Kolthoff & Miller, 1951)). The PMS concentration can be quantified by an iodometric method coupled with titration or spectrophotometric technique (Shukla et al., 2010a;

Wacławek et al., 2015; Zou et al., 2014).

Contrary to the $^{\bullet}OH$ which can be generated from water (*via* photocatalysis), PMS is required to be added into the polluted water stream to generate $SO_4^{\bullet-}$. The prerequisite for the generation of $SO_4^{\bullet-}$ from PMS *via* heterogeneous catalysis is to have the PMS to be in close proximity to the redox active surface of the catalyst. At close proximity, various surface PMS–catalyst interactions take place. Generally, PMS is activated to produce both $SO_4^{\bullet-}$ and $^{\bullet}OH$ when its peroxide bond –O–O–) is homolytically cleaved by accepting one electron from the transition metal (M) (**Eq. 2.2.3**) (Anipsitakis & Dionysiou, 2004):

$$M^{n+} + HSO_5^- \rightarrow M^{(n+1)+} + SO_4^{\bullet-} + OH^- \quad (2.2.3)$$

$$M^{n+} + HSO_5^- \rightarrow M^{(n+1)+} + SO_4^{2-} + {}^{\bullet}OH \quad (2.2.4)$$

As the $SO_4^{\bullet-}$ has a relatively short lifetime, the target pollutant must be within the diffusion limit of the $SO_4^{\bullet-}$ for the oxidation reaction to occur effectively. Meanwhile, the oxidized transition metal can be reduced back to its original oxidation state *via* a one–electron reduction process by PMS (**Eq. 2.2.5**) producing peroxymonosulfate radical ($SO_5^{\bullet-}$, +1.1 V *vs.* NHE), which is a relatively weaker transient species but serves to regenerate the catalyst (Das et al., 1999).

$$M^{(n+1)+} + HSO_5^- \rightarrow M^{n+} + SO_5^{\bullet-} + H^+ \quad (2.2.5)$$

$$2HSO_5^- \rightarrow SO_5^{\bullet-} + SO_4^{\bullet-} + H_2O \text{ (net reaction of Eqs. 2.2.3 and 2.2.5)} \quad (2.2.6)$$

$$2HSO_5^- \rightarrow SO_5^{\bullet-} + HSO_4^- + {}^{\bullet}OH \text{ (net reaction of Eqs. 2.2.4 and 2.2.5)} \quad (2.2.7)$$

Peroxymonosulfate radical is more reactive than the molecular oxygen and can also reduce certain transition metals (Duca, 2012). The oxidized transition metal ions can also be regenerated by directly oxidizing organics *via* disproportionation reactions. The working mechanism of the electron transfer reaction is illustrated in **Figure 2.1**. The

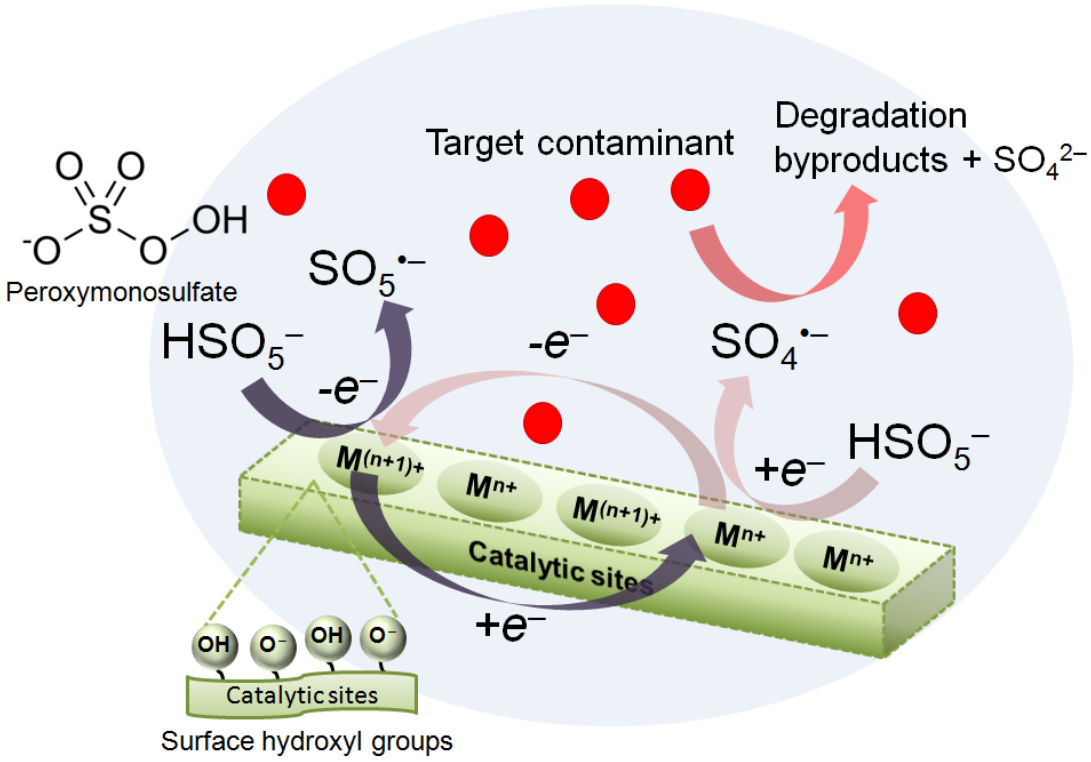

Figure 2.1. The redox reaction involving peroxymonosulfate and transition metal catalyst.

surface hydroxyl group (M–OH) on the catalyst surface plays a functional role in facilitating the activation of PMS (Stoyanova et al., 2014; Yang et al., 2009; Zhang et al., 2010). The presence of surface hydroxyl group, either on the catalyst surface or support, has been reported to enhance PMS activation (Ren et al., 2015b; Zhang et al., 2010).

The standard reduction potential is not the only governing factor involved in predicting the catalytic activity of the metal catalyst. Also, the reactivity and behavior of the heterogeneous catalysts cannot be predicted exclusively based on the ionic size and charge of the transition metal (Anipsitakis & Dionysiou, 2004). For instance, Co–based catalysts are efficient PMS activator and the high standard reduction potential of Co(III)/Co(II) (E^o = +1.92 V *vs.* NHE) enables efficient self–recycling of Co(II) for the catalytic reaction to proceed until all the PMS has been consumed. Similarly, despite having a relatively low standard reduction potential to participate in the redox reaction with PMS, Cu–based catalysts (Cu(II)/Cu(I), E^o = +0.15 V *vs.* NHE) have also been reported to be able to activate PMS.

2.3. Heterogeneous transition metal catalysts

2.3.1. Single metal catalysts

Table 2 summarizes the synthesis methods and performances of various single metal catalysts as PMS activator. In general, the single metal catalysts can be grouped into Co–, Cu–, Fe–, and Mn–based catalysts. Although Ag (Antoniou et al., 2010a) and Ru catalysts (Muhammad et al., 2012c) can activate PMS, they are not extensively investigated as catalysts for PMS activation due to their relatively high cost and potential toxicity.

2.3.1.1. Co–based catalysts

Several reported studies employed cobalt oxides to activate PMS and observed undesirable Co leaching during catalysis especially under acidic condition (Anipsitakis et al., 2005b; Chen et al., 2008; Guo et al., 2013). Up to 0.73 and 0.03 mg L^{-1} of Co were detected in the treated water after catalytic PMS activation reaction at acidic and neutral pHs, respectively (Anipsitakis et al., 2005b). In order to reduce the Co leaching problem, Co_3O_4 has been deposited on various supports including inert 1/2/3–D materials (Andrew Lin et al., 2015; Shi et al., 2012), metal oxides (Yang et al., 2008), industrial wastes (Muhammad et al., 2012a; Muhammad et al., 2012b; Saputra et al., 2012a), magnetic particles (Wang et al., 2014b), molecular sieves (Shukla et al., 2011; Shukla et al., 2010a) and adsorbents (Huang et al., 2015; Shukla et al., 2010b). The supported Co_3O_4 catalysts generally have better catalytic activity than Co_3O_4, improved Co_3O_4 dispersion, reduced Co leaching, better separation/recovery of the catalysts from the treated water, and added functionality (such as antibacterial and photocatalytic). However, this did not eliminate the Co leaching problem.

Table 2.2. Synthesis methods and performances of various single metal oxide catalysts as PMS activator.

Reference	Catalysts	Synthesis method	Target pollutant	Performance
Co−based catalysts				
Anipsitakis et al. (2005b)	Co_3O_4 CoO	Commercial	2,4−dichlorophenol	• Catalytic activity of Co_3O_4>CoO. • >99% of 20 mg L^{-1} 2,4−dichlorophenol removed in 15 min with 0.157 g L^{-1} catalyst (as Co) pH neutral, and 2.67 mM Oxone® (as PMS). • Co leaching <0.07 mg L^{-1} and >0.59 mg L^{-1} at neutral and acidic pH, respectively, for Co_3O_4.
Chen et al. (2008)	Co_3O_4	Precipitation method	Acid orange 7	• >99% of 0.2 mM acid orange 7 removed in 30 min with 0.5 g L^{-1} catalyst, pH neutral, and 2 mM PMS.
Guo et al. (2013)	Co_3O_4	Commercial	Amoxicillin	• >95% of 0.12 mM amoxicillin removed in 60 min with 0.060 g L^{-1} catalyst, pH 6, T = 60°C, and 10 mM Oxone®.
Cu−based catalysts				
Ji et al. (2011)	CuO	CTAB−assisted hydrothermal method	Phenol	• 100% of 50 mg L^{-1} phenol removed in 60 min with 1.5 g L^{-1} catalyst, pH 4, and 1.5 mM Oxone®. • Cu leaching was 0.78 mg L^{-1}.
Ji et al. (2014)	Cu/ZSM5	Wet impregnation method	Rhodamine B	• Catalytic activity of Cu/ZSM5>CuO. • For at least 4 cycles, 95% of 50 mg L^{-1} rhodamine B removed in 1 h with 1 g L^{-1} Cu/ZSM5, pH 7, and 0.6 g L^{-1} PMS. • Cu leaching between 0.684−0.139 mg L^{-1} at pH 3−11.
Fe−based catalysts				
Al-Shamsi et al. (2013)	Co–Fe^0	Reduction of Fe^{3+} with $NaBH_4$ + deposition of Co on the as–prepared Fe^0.	Trichloroethylene	• Catalytic activity of Co–Fe^0>Pd–Fe^0=Mn–Fe=Cd–Fe^0>Ni–Fe^0>Cr–Fe^0>Zn–Fe^0>Cu–Fe^0>Ag–Fe^0. • >95% of trichloroethylene removed in 5 h with trichloroethylene:PMS:catalyst molar ratio of 1:10:10.
Chen et al. (2014)	Fe_3O_4/$Cu_{1.5}Ni_{0.5}Cr$–LDH	Two–step microwave–hydrothermal method	Acid orange 7	• 100% of 25 mg L^{-1} acid orange 7 removed with 100 mg L^{-1} catalyst, and AO7/PMS molar ratio of 1:10. • Both Fe^{2+} and Cu^{+} are the active species generating $SO_4^{\bullet-}$. • Activation energy for AO7 degradation is 34.31 kJ mol^{-1}.
Ghanbari et al. (2014)	Fe^0 and Cu^0	Commercially−purchased	Real textile wastewater	• >99% and >80% of decolourization in 150 min with 3 g L^{-1} Fe^0 and 4 g L^{-1} Cu^0, respectively, at pH 4, and 20 mM PMS. • First−order kinetics.

Gong et al. (2015)	Fe@ACFs	Wet impregnation method	Reactive red M−3BE	• >99% of 50 µM Reactive red M−3BE removed in 15 min with 2.0 g L^{-1} catalyst, pH = 3, T = 50°C, and 0.5 mM PMS. • NaCl > 0.1 M increase the decolourization while NaCl < 0.1 M inhibit the decolourization. • First−order kinetics with activation energy of 32.89 kJ mol^{-1}. • Fe leaching was <0.5 mg L^{-1}.
Ji et al. (2013)	Fe_2O_3	Hydrothermal−calcination method	Rhodamine B	• 100% of 50 mg L^{-1} rhodamine B removed in 1 h with 1.5 g L^{-1} catalyst, pH 6.2, and 1mM PMS. • First−order kinetics with activation energy of 69.225 kJ mol^{-1}. • Fe leaching was <0.14 mg L^{-1}.
Sun et al. (2012b)	nano−Fe^0@CS	hydrothermal−carbonization method	Phenol	• Catalytic activity of nano−Fe^0@CS is better than ZVI particles, iron ions, iron oxides and cobalt oxide. • 100% of 20 mg L^{-1} phenol removed in 10 min with 0.5 g L^{-1} catalyst, T = 30°C, and 2.0 g L^{-1} Oxone®.
Tan et al. (2014)	Fe_3O_4	Commercially−purchased	Acetaminophen	• 75% of 10 mg L^{-1} acetaminophen removed in 120 min with 0.8 g L^{-1} catalyst, pH 4.5, and 0.2 mM PMS. • Pseudo first−order kinetics. • Fe leaching was <4 µg L^{-1}.
Wang et al. (2015d)	Fe^0/Fe_3C@CS	Hydrothermal method followed by self−reduction under N_2 atmosphere	Phenol	• 100% of 20 mg L^{-1} phenol removed in 10 min with .1 g L^{-1} catalyst, pH 7.0, and 2 g L^{-1} Oxone®. • First−order kinetics.
Wei et al. (2015a)	$Fe_{3-x}M_xO_4$ (M = Cr, Mn, Co, Ni)	Precipitation−oxidation method	Acid orange II	• Incorporation of Co, Mn and Ni improved the catalytic activity of Fe_3O_4 in the order of Mn<Ni<Co while Cr substitution showed inert effect. • 81% of 0.1 mmol L^{-1}acid orange II removed in 40 min with 1.0 g L^{-1} $Fe_{2.10}Co_{0.90}O_4$, pH 7, and 0.2 mmol L^{-1} Oxone®. • Pseudo first−order kinetics.
Zhang et al. (2016)	Fe_3O_4/MnO_2 (ball–in–ball hollow spheres)	*in situ* growth process + etching method	Methylene blue	• Catalytic activity of Fe_3O_4/MnO_2 (ball–in–ball hollow spheres)>MnO_2 (hollow spheres)>Fe_3O_4 (hollow spheres)>MnO_2 (hollow spheres)>MnO_2 (solid)>Fe_3O_4 (hollow spheres)>Fe_3O_4 (solid). • 100% of 30 mg L^{-1} methylene blue removed in 30 min with 300 mg L^{-1} catalyst, pH = 7.94, and 20 mM PMS. • Mn and Fe leaching for Fe_3O_4/MnO_2 were 0.22–0.45% and 0.51–0.87%, respectively.
Mn−based catalysts				

Liu et al. (2015a)	Fe_3O_4/MnO_2	Hydrothermal method	4−chlorophenol	• >95% of 50 mg L^{-1} 4−chlorophenol removed in 30 min with 0.2 g L^{-1} catalyst, pH 7.5, T=25°C, and 0.5 g L^{-1} PMS. • First−order kinetics.
Luo et al. (2015)	OMS−2	Reflux method	Acid orange 7	• Catalytic activity of OMS−2>MnO_2. • >95% of 20 mg L^{-1} acid orange 7 removed in 10 min with 0.25 g L^{-1} catalyst, pH 2.65, T=25°C, and 0.25 g L^{-1} PMS. • Mn leaching was <0.10 mg L^{-1}.
Saputra et al. (2012b)	nanowires α−MnO_2	Hydrothermal method	Phenol	• Catalytic activity of nanowires α−MnO_2>nanorod α−MnO_2>spherical α−MnO_2. • 100% of 30 mg L^{-1} phenol removed in 90 min with 0.4 g L^{-1} catalyst, and 2 g L^{-1} Oxone®. • First−order kinetics.
	nanosphere α−MnO_2	Reduction of $KMnO_4$ by maleic acid and calcination (300°C)		
	nanorod α−MnO_2	Reduction of $KMnO_4$ by maleic acid and calcination (500°C)		
Saputra et al. (2013c)	α−, β−, γ−MnO_2	Modified hydrothermal method based on the redox reaction of Mn^{2+} with persulfate	Phenol	• Catalytic activity of α−MnO_2 nanowires>γ−MnO_2>β−MnO_2. • 100% of 25 mg L^{-1} phenol removed in 60 min using 0.4 g L^{-1} of catalyst, and 2.0 g L^{-1} of Oxone®. • First−order kinetics with activation energy of 21.9 kJ mol^{-1}.
Saputra et al. (2013b)	MnO_2	Commercially−obtained	Phenol	• Catalytic activity of Mn_2O_3>MnO>Mn_3O_4>MnO_2. • 100% of 25 mg L^{-1} phenol removed in 60 min with 0.4 g L^{-1} catalyst, and 2 g L^{-1} PMS. • Pseudo first−order kinetics with activation energy of 11.4 kJ mol^{-1}. • Reusability required thermal treatment at 500°C for 1 h.
	Mn_2O_3	Calcination of MnO_2		
	Mn_3O_4	Calcination of MnO_2		
	MnO	Two step hydrothermal and calcination method		
Saputra et al. (2014)	cubic−Mn_2O_3	Two−step hydrothermal and calcination method	Phenol	• Catalytic activity of Mn_2O_3−cubic>Mn_2O_3−octahydra>Mn_2O_3−truncated. • 100% of 25 mg L^{-1} phenol removed in 60 min with 0.4 g L^{-1} catalyst, and 2 g L^{-1} PMS. • First−order kinetics with activation energy of 61.2 kJ mol^{-1}.
	octahydra−Mn_2O_3	Solvothermal method		
	truncated−Mn_2O_3	Solvothermal method		

Saputra et al. (2013a)	Mn_3O_4	Solvothermal method	Phenol	• Catalytic activity of Mn_3O_4~Co_3O_4>Fe_3O_4. • 100% of 25 mg L^{-1} phenol and 68% TOC removed in 60 min with 0.4 g L^{-1} catalyst, and 2 g L^{-1} Oxone®. • Pseudo first−order kinetics with activation energy of 38.5 and 66.2 kJ mol^{-1} for Mn_3O_4 and Co_3O_4, respectively.
	Fe_3O_4	Solvothermal method		
	Co_3O_4	Hydrothermal method		
Tang et al. (2015)	Mn_3O_4	Co−precipitation−calcination method	Acid red G	• 100% of 50 mg L^{-1} acid red G removed in 90 min with 0.5 g L^{-1} catalyst, pH 7, T=25°C, and 1.0 g L^{-1} Oxone®. • Pseudo first−order kinetics with activation energy of 65.33 kJ mol^{-1}.
Wang et al. (2014a)	corolla−like $MnO_2/ZnFe_2O_4$ urchin−shaped $MnO_2/ZnFe_2O_4$	Modified hydrothermal method	Phenol	• Catalytic activity of urchin−shaped $MnO_2/ZnFe_2O_4$>corolla−like $MnO_2/ZnFe_2O_4$>$ZnFe_2O_4$. • 100% of 20 mg L^{-1} phenol removed in 180 min with 0.2 g L^{-1} catalyst, T=25°C, and 2.0 g L^{-1} Oxone®. • First−order kinetics activation energy for urchin−shaped $MnO_2/ZnFe_2O_4$ and corolla−like $MnO_2/ZnFe_2O_4$ were 49.4 and 41.7 kJ mol^{-1}, respectively.
Wang et al. (2014c)	Mn/Fe_3O_4/carbon (N_2)	Hydrothermal method followed by calcination in N_2	Phenol	• Catalytic activity Mn/Fe_3O_4/carbon (N_2)>Mn/Fe_3O_4/carbon (air). • 100% of 20 mg L^{-1} phenol removed in 180 min with 0.2 g L^{-1} catalyst, T=25°C, and 2 g L^{-1} Oxone®. • Pseudo first−order kinetics with activation energy of 59.5 and 63.2 kJ mol^{-1} for Mn/Fe_3O_4/carbon (air) and Mn/Fe_3O_4/carbon (N_2), respectively.
	Mn/Fe_3O_4/carbon (air)	Hydrothermal method followed by calcination in air		
Wang et al. (2015c)	corolla−like □−MnO_2 urchin−shaped □−MnO_2	Modified hydrothermal method with reduction of $KMnO_4$	Phenol	• Catalytic activity of corolla−like □−MnO_2>urchin−shaped □−MnO_2. • 100% of 20 mg L^{-1} phenol removed in 30 min with 0.2 g L^{-1} catalyst, T=25°C, and 2.0 g L^{-1} Oxone®. • First−order kinetics activation energy for corolla−like □−MnO_2 was 25.3 kJ mol^{-1}. • Mn leaching was ~3 mg L^{-1}.
Wei et al. (2015b)	OMS−2/Fe_3O_4	Solvent free method	Acid orange 7	• 97% of 20 mg L^{-1} acid orange 7 removed in 15 min with 0.4 g L^{-1} catalyst, pH 3.75, and 0.4 g L^{-1} PMS. • Mn leaching was <0.05 mg L^{-1}.
Xu et al. (2015a)	MnO_x/HCAS	Hydrothermal method	Acid Red 73	• >98% of 50 mg L^{-1} acid red 73 removed in 30 min with 1 g L^{-1} catalyst, pH 7, T=25°C, and 1.0 g L^{-1} Oxone®. • Cl^- (1−150 mg L^{-1}) improve decolourization while HCO_3^- (>1 mg L^{-1}) inhibit decolourization. • First−order kinetics activation energy of 21.87 kJ mol^{-1}.

Yang et al. (2015a)	Fe_3O_4/GO Mn_3O_4/rGO Fe_3O_4/Mn_3O_4/rGO	co−precipitation method reduction of $Mn(C_2H_3O_2)_2.3H_2O$ and GO with hydrazine reduction of $Mn(C_2H_3O_2)_2.3H_2O$ and Fe_3O_4/GO with hydrazine	Methylene blue	• Catalytic activity of Fe_3O_4/Mn_3O_4/rGO>Mn_3O_4/rGO>Fe_3O_4/GO. • >95% of 50 mg L^{-1} methylene blue removed in 30 min with 0.1 g L^{-1} catalyst, pH 7, T=25°C, and 0.3 g L^{-1} PMS.. • Pseudo second−order kinetics with activation energy of 25.4 kJ mol^{-1}.
Yao et al. (2013)	Mn_3O_4/rGO	Reduction of $Mn(C_2H_3O2)_2.4H_2O$−loaded graphene oxide by hydrazine.	Orange II	• Catalytic activity of Mn_3O_4/rGO>Mn_3O_4>rGO • 100% of 30 mg L^{-1} Orange II removed in 120 min with 0.05 g L^{-1} catalyst, pH 7, and 1.5 g L^{-1} Oxone®. • Pseudo second−order kinetics with activation energy of 49.5 kJ mol^{-1}.
Zhang et al. (2014a)	Mn_3O_4/rGO	Hydrothermal method	Orange II	• Catalytic activity of Mn_3O_4/rGO>Mn_3O_4>rGO • 100% of 30 mg L^{-1} Orange II removed in 90 min with 0.05 g L^{-1} catalyst, pH neutral, and 1.5 g L^{-1} Oxone®. • Mn leaching was 20 µg L^{-1} (0.04%).
Other catalysts				
Muhammad et al. (2012c)	RuO_2/AC RuO_2/ZSM−5	General impregnation method	Phenol	• Catalytic activity of RuO_2/AC>RuO_2/ZSM−5. • 100% of 50 mg L^{-1} phenol removed in 60 min using 0.4 g L^{-1} catalyst and 1 g L^{-1} Oxone®. • First−order kinetics with activation energy of 61.4 and 42.2 kJ mol^{-1} for RuO_2/AC and RuO_2/ZSM−5, respectively.

2.3.1.2. Cu–based catalysts

Comparing the two most stable Cu oxide catalysts (CuO and Cu_2O), the catalytic activity of CuO is ~1.5–2.0 times higher than that of Cu_2O (Feng et al., 2015). However, a considerably high CuO loading (up to 1.5 g L^{-1} of CuO and 1.5 mM of Oxone® for treating 50 mg L^{-1} of phenol) is required for effective performance (Ji et al., 2011). The CuO catalyst is also not as redox stable and efficient compared with the mixed metal oxide catalyst such as $CuFe_2O_4$ (Cu leaching of 46±3 and 1.5±0.1 μg L^{-1} for CuO and $CuFe_2O_4$ after catalytic PMS activation under the same condition) (Zhang et al., 2013b). Further improvement of the CuO catalytic activity can be achieved by incorporating the CuO onto a support with high surface area, high stability and good adsorption affinity for the pollutant such as ZSM5 (Kušić et al., 2006; Liu et al., 2014) to decrease the CuO aggregation and improve its specific surface area for catalytic reaction (Ji et al., 2014). Besides activating PMS, it has also been reported that CuO can activate PS to degrade selected organic pollutants without producing $SO_4^{\bullet-}$ (Zhang et al., 2014b).

2.3.1.3. Fe–based catalysts

Iron–based materials are widely employed for catalysis because they are cost–effective, eco–friendly and efficient materials (Zhao et al., 2010). Common PMS activators based on Fe are zero valent iron (ZVI), Fe_2O_3 and Fe_3O_4. The mechanism of PMS activation by ZVI can be delineated as follows (Ghanbari et al., 2014; Volpe et al., 2013):

$$\equiv Fe^0 + HSO_5^- + 2H^+ \rightarrow \equiv Fe(II) + HSO_4^- + H_2O \ (E^o = +2.26 \text{ V } \textit{vs.} \text{ NHE}) \qquad (2.3.1.3.1)$$

$$\equiv Fe(II) + HSO_5^- \rightarrow \equiv Fe(III) + SO_4^{\bullet-} + OH^- \qquad (2.3.1.3.2)$$

$$\equiv Fe(III) + HSO_5^- \rightarrow \equiv Fe(II) + SO_5^{\bullet-} + H^+ \quad (2.3.1.3.3)$$

Besides $SO_4^{\bullet-}$, $^{\bullet}OH$ can also be selectively produced from the reaction between PMS and ZVI as follows (Wang et al., 2015d):

$$\equiv Fe^0 + HSO_5^- \rightarrow Fe(III) + SO_4^{2-} + {}^{\bullet}OH \quad (2.3.1.3.4)$$

As both $SO_4^{\bullet-}$ and $^{\bullet}OH$ are produced from PMS activation *via* irreversible ZVI oxidation, the catalyst needs to be periodically added into the reaction system. In order to decrease the treatment cost, optimizations of the ZVI loading, PMS dosage and pH are critical. This also reduces the corrosion effect and undesirable reactions of $SO_4^{\bullet-}$ and Fe^0 with either Fe(II) and/or Fe(III) (Ahn et al., 2013; Hussain et al., 2012; Oh et al., 2009; Rastogi et al., 2009; Rodriguez et al., 2014) as follow:

$$\equiv Fe^0 + 2H^+ \rightarrow Fe(II) + H_2 \quad (2.3.1.3.5)$$

$$\equiv Fe^0 + 2SO_4^{\bullet-} \rightarrow Fe(II) + SO_4^{2-} \quad (2.3.1.3.6)$$

$$\equiv Fe(III) + \equiv Fe^0 \rightarrow 2Fe(II) \quad (2.3.1.3.7)$$

$$\equiv Fe(II) + SO_4^{\bullet-} \rightarrow Fe(III) + SO_4^{2-} \quad (2.3.1.3.8)$$

Zero valent iron tends to have a serious particle aggregation and high deposition rate due to their strong interparticle attraction and intrinsic magnetic interaction (Li et al., 2011; Tiraferri et al., 2008). Carbon encapsulation of ZVI can solve these problems while improving the hydrophilicity/hydrophobicity and adsorption affinity of the catalyst for pollutants (Sun et al., 2012b; Wang et al., 2015d). For instance, carbon encapsulation of ZVI with glucose increases the hydrophilicity of the catalysts due to the presence of surface C–OH and –C=O groups (Sun & Li, 2004). It has been reported that the introduction of melamine during the encapsulation of ZVI can induce the formation of Fe_3C with better stability and magnetic property for efficient separation from the treated

water (Wang et al., 2015d). However, the conversion of Fe^0 to Fe_2O_3 during catalytic reaction deactivates the carbon encapsulated ZVI (Wang et al., 2015d). This also implies that Fe_2O_3 is less active than Fe^0 for PMS activation. In another study, the deposition of Co on Fe^0 to form bimetallic Co–Fe^0 is reported to have a relatively better catalytic activity than that of the monometallic catalyst (Al-Shamsi et al., 2013). The bimetallic system can potentially provide new intrinsic catalytic property which leads to a higher reaction stoichiometric efficiency and better PMS utilization efficiency over the monometallic system (Ayoub & Ghauch, 2014).

The Fe_2O_3 particles consisting of mainly Fe(III) species have been employed for rhodamine B removal *via* PMS activation but the catalysis process requires a relatively high Fe_2O_3 loading (specific surface area = 34 m^2 g^{-1}, up to 1.8 g L^{-1} for 50 mg L^{-1} of rhodamine B) for effective application (Ji et al., 2013). The surface Fe^{3+} must be reduced to Fe^{2+} (by electron transfer reaction with PMS) before it is able to generate $SO_4^{\bullet-}$ from PMS. The unfavorable standard reduction potential for Fe^{3+}/Fe^{2+} (–0.77 V *vs.* NHE) compared to that of Co^{3+}/Co^{2+} (+1.92 V *vs.* NHE) suggests that Fe^{3+} cannot be reduced effectively by PMS. Although Fe(III) reduction by PMS can still proceed (assisted by many factors such as improved electron transfer due to the complexation of PMS on the surface Fe(III)), Fe(III) cannot generate $SO_4^{\bullet-}$ directly from PMS without being initially reduced implying that it has a relatively poorer catalytic activity than Fe(II). The slower generation of $SO_4^{\bullet-}$ by Fe(III) enables $SO_4^{\bullet-}$ to be utilized more effectively for pollutant oxidation while minimizing the Fe(II) scavenging effect (**Eq. 2.3.1.3.8**) (Rastogi et al., 2009).

The catalytic activity of Fe(III) can be further enhanced *via* immobilization of the Fe(III) ion on the activated carbon fibers (ACFs) (Gong et al., 2015). The Fe(III) forms considerably strong electrostatic bond with ACFs and <0.5 mg L^{-1} of Fe leached out after

10 cycles of reuse. The hydrophilic groups present on the ACFs is capable of reducing Fe(III) to Fe(II), which can then generate $SO_4^{\bullet-}$ from PMS (Uchida et al., 2000). It has been reported that the addition of a reducing agent such as hydroxylamine during catalytic PMS activation by dissolved Fe(III) can improve the performance of the system by promoting the reduction of Fe(III) to Fe(II) (Zou et al., 2013). Although this may seems unsuitable for the heterogeneous system due to the inherent effect on the stability of the catalyst as hydroxylamine promotes dissolution of Fe(III) from the Fe–based catalyst, it can potentially be employed for controlled dissolution–reduction of Fe(III) for PMS activation.

Another common form of iron oxide, namely magnetic Fe_3O_4, can adsorb water molecule and activate PMS *via* the following mechanism (Tan et al., 2014):

$$\equiv Fe(II) + HSO_5^- \rightarrow \equiv Fe(III) + SO_4^{2-} + {}^{\bullet}OH \quad (2.3.1.3.9)$$

$$\equiv Fe(II) - {}^{-}OH + HSO_5^- \rightarrow \equiv Fe(II) - (HO)OSO_3^- + OH^- \quad (2.3.1.3.10)$$

$$\equiv Fe(II) - (HO)OSO_3^- \rightarrow \equiv Fe(III) - {}^{-}OH + SO_4^{\bullet-} \quad (2.3.1.3.11)$$

The slower Fe(II) regeneration in the Fe_3O_4 after generating $^{\bullet}OH$ and $SO_4^{\bullet-}$ from PMS results in the increase in Fe(III):Fe(II) ratio in Fe_3O_4 (Tan et al., 2014). The catalytic activity of Fe_3O_4 can be enhanced by doping with other transition metals such as Co (achieving >10 times improvement over that of Fe_3O_4), Mn, Ni and Cr with the order of decreasing dopant–induced reactivity as follows: Co>Mn>Ni>Cr>Fe (Wei et al., 2015a). The degree of improvement in catalytic activity after Co doping is directly proportional to the percentage of Co present in the Co–doped Fe_3O_4.

A possible disadvantage of iron–based catalysts such as ZVI and Fe_2O_3 is that they can be deactivated by SO_4^{2-} *via* the replacement of two surface hydroxyl groups with SO_4^{2-} forming a binuclear bridge complex consisting of Fe–O–S(O_2) –O–Fe which deactivates

the Fe sites (Al-Shamsi & Thomson, 2013; Parfitt & Smart, 1977; Parfitt & Smart, 1978), as depicted in the following reactions:

$$\equiv Fe^0 + SO_4^{2-} + 2H_2O \rightarrow \equiv FeSO_4 + 2OH^- + H_2 \quad (2.3.1.3.12)$$

$$2\equiv FeOOH + 2SO_4^{2-} + 2H_2O \rightarrow 2\equiv FeSO_4 + 4OH^- + H_2 + O_2 \quad (2.3.1.3.13)$$

2.3.1.4. Mn–based catalysts

Wang and co–workers (Saputra et al., 2013a; Saputra et al., 2013b; Saputra et al., 2014; Saputra et al., 2013c; Saputra et al., 2012b; Wang et al., 2015b; Wang et al., 2015c; Wang et al., 2014a; Wang et al., 2014c; Yao et al., 2013) investigated the performance of various single–metal Mn oxide catalysts as PMS activators. They include Mn oxides with different crystallographic dimensions (α–, β–, and γ–MnO_2), Mn oxides at different oxidation states and supported Mn oxides. In general, the catalytic activity of Mn oxides depends on many factors, namely (i) the presence of oxygen liability which allows a better oxidative transformation between various Mn oxidation states, (ii) density of exposed reactive facets such as MnO_6 edges with double tunneled structure, (iii) presence of mixed valence Mn, (iv) redox potential of different Mn oxidation states, (v) specific surface area, and (vi) degree of crystallinity (Saputra et al., 2013b; Saputra et al., 2014; Saputra et al., 2013c; Saputra et al., 2012b; Tang et al., 2015; Wang et al., 2015c; Xu et al., 2015a). The degree of crystallinity exerts a greater influence on the catalytic activity of Mn oxide than the specific surface area. It is reported that crystalline MnO_2 (146 m^2 g^{-1}) performed ~8 times better (0.359 min^{-1} *vs.* 0.0457 min^{-1}) than the amorphous MnO_2 (179 m^2 g^{-1}) (Saputra et al., 2012b).

The ability of Mn to form many stable oxides makes it versatile for use in a wide range of applications. The mechanisms of PMS activation by heterogeneous Mn oxides (with

different oxidation states) can be delineated by the following reactions (Saputra et al., 2013b):

$$2MnO_2 + 2HSO_5^- \rightarrow Mn_2O_3 + 2SO_5^{\bullet-} + 2OH^- \quad (2.3.1.4.1)$$

$$2Mn_3O_4 + 2HSO_5^- \rightarrow 3Mn_2O_3 + 2SO_4^{\bullet-} + 2H^+ \quad (2.3.1.4.2)$$

$$Mn_2O_3 + 2HSO_5^- \rightarrow 2MnO_2 + 2SO_4^{\bullet-} + 2H^+ \quad (2.3.1.4.3)$$

$$2MnO + 2HSO_5^- \rightarrow Mn_2O_3 + 2SO_4^{\bullet-} + 2H^+ \quad (2.3.1.4.4)$$

$$3Mn_2O_3 + HSO_5^- \rightarrow 2Mn_3O_4 + SO_5^{\bullet-} + OH^- \quad (2.3.1.4.5)$$

Under the same experimental condition (0.4 g L^{-1} of catalyst loading, 2 g L^{-1} of PMS, 120 min), the catalytic activities of Mn oxides with different oxidation states are in the following order: α–Mn_2O_3 (100%) > MnO (90%) > γ–Mn_3O_4 (65%) > γ–MnO_2 (60%) (Saputra et al., 2013b); evidencing that the Mn(IV) species has the poorest redox activity with PMS. It is interesting to note that Mn_3O_4 has a comparable catalytic activity with Co_3O_4 (Saputra et al., 2013a). However, Mn_3O_4 suffers from poor chemical and thermal stabilities but its stability can be ameliorated by depositing Mn_3O_4 on reduced–graphene oxide (rGO) (Yao et al., 2013; Zhang et al., 2014a). It has also been reported that Mn oxides can act as a support to improve the catalytic activity of various metal oxides such as Co_3O_4 and CuO (Liang et al., 2012; Liu et al., 2015a; Wang et al., 2014a; Yang et al., 2014b).

In several studies, the Mn octahedral molecular sieve (OMS–2) was selected as a catalyst for PMS activation because it has favorable properties such as a large specific surface area, high density of lattice oxygen favorable for catalysis and presence of mixed–valence Mn (II, III and IV) (Ding et al., 2005; Duan et al., 2015a; Luo et al., 2015). As OMS–2 generally contains high density of acidic sites (Tian et al., 1997) and PMS activation

favors basic surface (Zhang et al., 2010), surface modification of OMS−2 is usually required for use as an efficient PMS activator. Ferromagnetism can be introduced to OMS−2 by encapsulating Fe_3O_4 with OMS−2 to produce a core shell structure (Wei et al., 2015b). However, this could lead to the catalytic activity reduction of OMS−2 (Luo et al., 2015; Wei et al., 2015b). The technique of introducing ferromagnetism to the catalyst using Fe_3O_4 has also been adopted to prepare Fe_3O_4/Mn_3O_4/rGO (Yang et al., 2015a) and Fe_3O_4/MnO_2 (Zhang et al., 2016). In this case, improvement in the catalytic activity of the catalyst was observed.

Because Mn has many stable oxidation states, it is relatively difficult to retain the chemical phases of Mn oxides after PMS activation reactions. It has been reported that phenol removal *via* PMS activation catalyzed by α−Mn_2O_3 decreased from 100% (first cycle) to 30% (second cycle) due to the change in chemical phase and deposition of degradation intermediates on the surface of the α−Mn_2O_3 catalyst (Saputra et al., 2013b). A post treatment of the catalyst (e.g. calcination, simple washing, chemical treatment etc. depending on the nature of the catalyst) is usually required to restore its performance (Sun et al., 2013a).

2.3.2. Mixed−metal catalysts

Table 2.3 presents an overview of the performances of various mixed metal oxide catalysts. The mixed metal oxide catalysts have improved stability (reduced leaching), polyfunctionality (e.g. photoactive, magnetically separable etc.), high redox activity and better catalytic activity compared with single metal oxide catalysts. This is due to the improvement in the specific surface area, synergistic redox coupling of different metals, increase in the density of basic sites on the surface of the catalyst, and presence of mixed−valence transition metals (Wu et al., 2014). The mixed−metal catalysts can be

Table 2.3. Synthesis methods and performances of various mixed−metal oxide catalysts as PMS activator.

References	Catalysts	Synthesis method	Target pollutant	Performance
Co−based catalysts				
Andrew Lin et al. (2015)	ZIF−67/GO	Carbonization of Co−based MOF (ZIF−67) and GO	Acid Yellow 17	• Catalytic activity of ZIF−67/GO>ZIF−67>rGO. • >75% of 100 mg L^{-1} acid yellow 17 removed in 120 min with 0.5 g L^{-1} catalyst, pH 3.8, and 90 mg L^{-1} PMS. • First−order kinetics with activation energy of 12 kJ mol^{-1}.
Hu et al. (2015)	$CoFe_2O_4$/SBA−15	Wetness impregnation method	Rhodamine B	• >95% of 5 mg L^{-1} Rhodamine B removed in 120 min with 0.1 g L^{-1} catalyst, and PMS:rhodamine B molar ratio of 20:1. • First−order kinetics. • Co leaching was ~60 µg L^{-1}.
Du et al. (2016)	$CoFe_2O_4$/titanate nanotubes	Hydrothermal method to prepare titanate nanotube follow by impregnation–calcination method	Rhodamine B	• Catalytic activity of $CoFe_2O_4$/titanate nanotubes>$CoFe_2O_4$. • 100% of 100 mg L^{-1} Rhodamine B removed in 60 min with 0.20 g L^{-1} catalyst, T = 20°C, and 4.0 g L^{-1} Oxone®. • Pseudo first−order kinetics with activation energy of 70.56 kJ mol^{-1}. • Co leaching was ~928 µg L^{-1}.
Li et al. (2015)	CoAlMn	Hydrothermal + calcination method	Bisphenol A	• >99% of 10 mg L^{-1} bisphenol A removed in 100 min with 0.02 g L^{-1} catalyst, pH 3.6, T = 25°C, and 0.15 g L^{-1} Oxone®. • First−order kinetics activation energy of 76.83 kJ mol^{-1}. • Co leaching was 0.19 (0.19%) and < 0.01 µg L^{-1} for acidic and neutral pH, respectively. Mn leaching was 0.014 (0.67%) and < 0.005 µg L^{-1} for acidic and neutral pH, respectively.
Li et al. (2016)	$Fe_{0.8}Co_{2.2}O_4$	Heating $Fe_yCo_{1-y}[Co(CN)_6]_{0.67}$ •nH_2O	Bisphenol A	• Catalytic activity of $Fe_{0.8}Co_{2.2}O_4$>Co_3O_4>Fe_3O_4. • >95% of 20 mg L^{-1} bisphenol A removed in 60 min with 0.1 g L^{-1} catalyst, pH 6, T = 298 K, and 0.2 g L^{-1} PMS. • Co leaching was 0.36 mg L^{-1}. • Fe leaching was 0.11 mg L^{-1}.
Qin et al. (2013)	Fe_2O_3/Co_3O_4/$CoFe_2O_4$	Template synthesis	Phenol	• >99% of 50 mg L^{-1} phenol removed in 120 min with 0.2 g L^{-1} catalyst, and 4 g L^{-1} PMS.
Ren et al. (2015b)	XFe_2O_4 (X = Co, Cu, Mn, Zn)	Sol−gel method	di−n−butyl phthalate	• Catalytic activity of $CoFe_2O_4$>$CuFe_2O_4$>$MnFe_2O_4$>$ZnFe_2O_4$. • ~60% and ~80% of 2 µmol L^{-1} di−n−butyl phthalate removed with 0.1 g L^{-1} $CuFe_2O_4$ and $CoFe_2O_4$, respectively, in the presence of 20 µmol L^{-1} PMS and pH 7.0.

Su et al. (2013)	$Co_{0.75}Fe_{2.25}O_4$	Hydrothermal method	Rhodamine B	• >99% of 0.014 mM Rhodamine B removed in 40 min with 0.05 g L^{-1} catalyst, pH 6, and 1 mM Oxone®. • Pseudo first−order kinetics with activation energy of 49.01 kJ mol^{-1}.
Xu et al. (2015b)	$CoFe_2O_4$/graphene	Modified Hummers method + precipitation method	Dimethyl phthalate	• Catalytic activity of $CoFe_2O_4$/graphene>$CoFe_2O_4$>graphene. • >99% of 0.05 mM dimethyl phthalate removed in 10 min with 0.5 g L^{-1} catalyst, pH 4, and 2 mM PMS.
Yang et al. (2009)	Fe_2O_3/Co_3O_4/$CoFe_2O_4$	Thermal oxidation of Fe and Co salts	2,4−dichlorophenol	• Catalytic activity of Fe_2O_3/Co_3O_4/$CoFe_2O_4$>Co_3O_4>Fe_2O_3+Co_3O_4 (Fe:Co = 1:1)>Fe_2O_3. • ~80% of 50 mg L^{-1} 2,4−dichlorophenol removed in 120 min with 0.1 g L^{-1} catalyst, pH 7, and 2,4−dichlorophenol:Oxone® molar ratio of 1:3. • Co leaching was 20−50 µg/L at neutral pH.
Yao et al. (2012)	$CoFe_2O_4$/rGO	Hummers method + precipitation method	Phenol	• Catalytic activity of $CoFe_2O_4$/rGO>$CoFe_2O_4$>rGO. • >99% of 20 mg L^{-1} phenol removed in 40 min with 67 mg L^{-1} catalyst, and 2 g L^{-1} PMS. • Pseudo first−order kinetics with activation energy of 15.8 kJ mol^{-1}.
Yao et al. (2015)	$CoMn_2O_4$	Hydrothermal method	Rhodamine B	• Catalytic activity of $CoMn_2O_4$>Co_2MnO_4>$Co_{0.5}Mn_{2.5}O_4$>Co_3O_4>Co_3O_4+Mn_2O_3>Mn_2O_3. • >95% of 0.03 g dm^{-3} rhodamine B removed in 10 min with 0.02 g dm^{-3} catalyst, pH 6.29, T = 25°C, and 0.2 g dm^{-3} PMS. • Co and Mn leaching were <0.1 mg dm^{-3}.
Cu−based catalysts				
Ding et al. (2013)	$CuFe_2O_4$	Sol−gel combustion method	Tetrabromobisphenol A	• $CuFe_2O_4$ performed better than CuO and Fe_2O_3, respectively. • 99% of 10 mg L^{-1} tetrabromobisphenol A removed in 30 min with 0.2 g L^{-1} catalyst, pH 6.3−7.1, and 0.2 mmol L^{-1} PMS. • Pseudo−first order kinetics. • Cu leaching was ~0.094 mg L^{-1}.
(Feng et al., 2016)	$CuFeO_2$	Hydrothermal method	Sulfadiazine	• Catalytic activity of $CuFeO_2$~$CuFe_2O_4$>Cu_2O~Fe_2O_3. • >80% of 8.0 µM sulfadiazine removed in 12 min with 0.10 g L^{-1} catalyst, pH = 6.8, and 33.0 µM PMS. • Pseudo-first order kinetics. • Cu leaching for $CuFeO_2$ was ~21 µg L^{-1}.
Guan et al. (2013)	$CuFe_2O_4$	Sol−gel method	Atrazine	• >98% of 2 µM atrazine removed in 15 min with 0.1 g L^{-1} catalyst, and 1 mM PMS. • Detrimental effect at HCO_3^- concentration ≥ 4 mM while enhancement at HCO_3^- concentration of 2 mM.

Xu et al. (2016)	$CuFe_2O_4$	Sol–gel method	Bisphenol A	• Detrimental effect of NOM (0–3.2 mg L^{-1} NOM corresponding to 98–23% removal). • Catalytic activity of $CuFe_2O_4$>Fe_2O_3>CuO. • >95% of 50 mg L^{-1} bisphenol A removed in 60 min with 0.40 g L^{-1} catalyst, pH = 6.72, and 0.5 g L^{-1} PMS. • Cu leaching in $CuFe_2O_4$ was 1.27 (0.795%) and 0.7 mg L^{-1}, for first and second cycle, respectively.
Zhang et al. (2013b)	$CuFe_2O_4$	Citrate combustion method	Iopromide	• $CuFe_2O_4$ performed better than $MnFe_2O_4$, Fe_2O_3, CuO and homogeneous Cu^{2+}, respectively. • 80% of 10 µM iopromide removed in 30 min with 100 mg L^{-1} catalyst, pH 6, and 20 µM PMS. • Pseudo first–order kinetics. • Cu leaching in $CuFe_2O_4$ and CuO were 1.5±0.1 and 46±3 µg L^{-1}, respectively.
Other catalysts				
Wang et al. (2016)	$NiFe_2O_4$	Thermal decomposition of mixed inorganic salts	Benzoic acid	• Catalytic activity of $CoFe_2O_4$>$NiFe_2O_4$>$MnFe_2O_4$>NiO>Fe_3O_4>Fe_2O_3. • >80% of 10 µM benzoic acid removed in 60 min with 0.10 g L^{-1} $NiFe_2O_4$, T=25°C, pH = 7.0 and 1.0 mM PMS. • Ni leaching was <0.128 mg L^{-1}.
Yao et al. (2014)	$MnFe_2O_4$	Co–precipitation method	Methyl violet, methyl orange, methylene blue, orange II rhodamine B	• Catalytic activity of $MnFe_2O_4$/rGO>$MnFe_2O_4$. • >90% of 20 mg L^{-1} Orange II removed in 120 min with 0.050 g L^{-1} catalyst, T=25°C, and 0.5 g L^{-1} PMS. • Order of effects on anions (0.1 M) on decolourization of Orange II: $Cl^- > HCO_3^- > CH_3COO^- > NO_3^-$. • Pseudo first–order kinetics with activation energy of 25.7 kJ mol^{-1}. • Mn and Fe leaching for $MnFe_2O_4$ were 0.0043 mM and 0.0013 mM, respectively, while for $MnFe_2O_4$/rGO were 0.0045 mM and 0.0020 mM, respectively.
	$MnFe_2O_4$/rGO	Co–precipitation during reduction of GO		

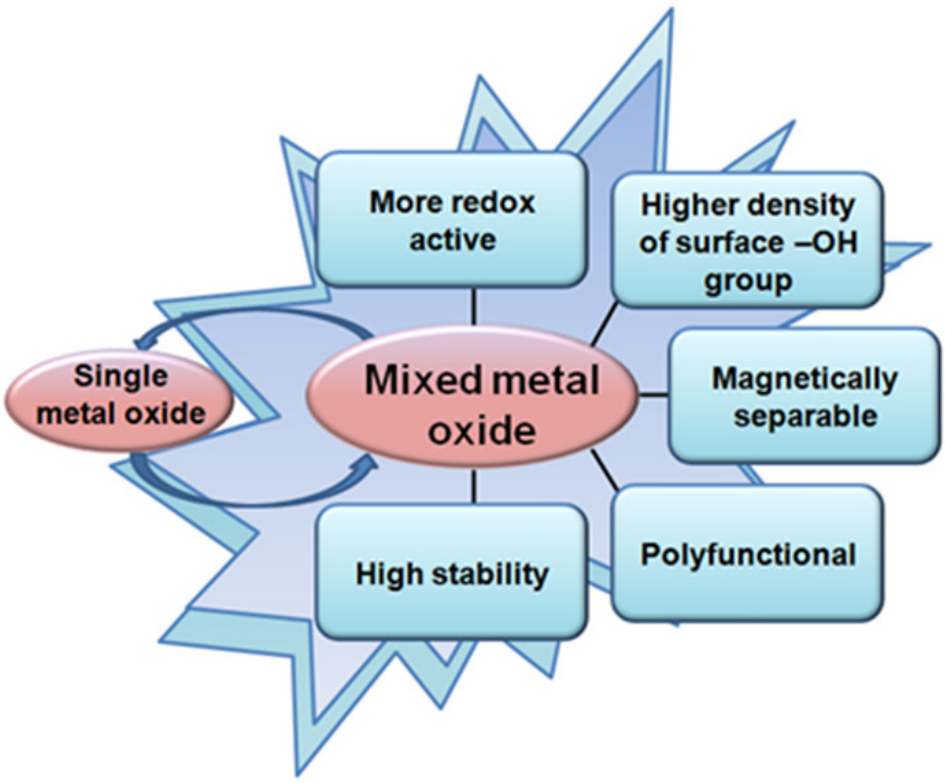

Figure 2.2. Schematic illustration of the advantages of mixed–metal oxide catalysts over the single metal oxide catalysts.

grouped into Co mixed–metal catalysts, Cu mixed–metal catalysts, and other mixed–metal catalysts. A schematic illustration of the advantages of mixed metal catalysts over the single metal catalysts is presented in **Figure 2.2**.

2.3.2.1. Co mixed–metal catalysts

The performance of various Co mixed metal catalysts as PMS activators including $CoFe_2O_4$ (Hu et al., 2015; Qin et al., 2013; Ren et al., 2015b; Stoyanova et al., 2014; Su et al., 2013; Xu et al., 2015b; Yang et al., 2009; Yao et al., 2012), $CoMn_2O_4$ (Yao et al., 2015), CoMnAl (Li et al., 2015), magnetic Co–based metal organic framework (Andrew Lin et al., 2015), and $Fe_{0.8}Co_{2.2}O_4$ (Li et al., 2016) have been investigated by many researchers. Compared with CoO and Co_3O_4, Co mixed metal catalysts exhibit better catalytic activity, improved stability (lower Co leaching), and ferromagnetism (in some catalysts) for the ease of separation of the catalyst from the treated water.

Magnetic $CoFe_2O_4$ is the most widely investigated Co mixed metal catalyst. Magnetic $CoFe_2O_4$ has a better resistance to Co leaching due to its strong Co–Fe interactions (Yang et al., 2009). Magnetic $CoFe_2O_4$ activates PMS *via* the following mechanism:

$$\equiv Co(II) + HSO_5^- \rightarrow \equiv Co(III) + SO_4^{\bullet -} + OH^- \quad (2.3.2.1.1)$$

$$\equiv Co(III) + HSO_5^- \rightarrow \equiv Co(II) + SO_5^{\bullet -} + OH^+ \quad (2.3.2.1.2)$$

$$\equiv Fe(III) + HSO_5^- \rightarrow \equiv Fe(II) + SO_5^{\bullet -} + H^+ \quad (2.3.2.1.3)$$

$$\equiv Fe(II) + HSO_5^- \rightarrow \equiv Fe(III) + SO_4^{\bullet -} + OH^- \quad (2.3.2.1.4)$$

$$\equiv Fe(II) + \equiv Co(III) \rightarrow \equiv Fe(III) + \equiv Co(II) \ (E^o = 1.04 \text{ V } \textit{vs.} \text{ NHE}) \quad (2.3.2.1.5)$$

Although Fe(III) (the predominant Fe species in $CoFe_2O_4$) can activate PMS, it seems unlikely to have a major contribution due to its relatively poor catalytic activity compared with Co(II). This suggests that the thermodynamically–favorable electron transfer from Fe^{2+} (produced mainly from the one electron reduction of Fe^{3+}) to Co^{3+} has a minimum effect on the performance enhancement (**Eq. 2.3.2.1.5**). The promotional effect is more likely to be due to the higher content of the surface hydroxyl groups and high catalytic activity of Co(II) in the mixed metal oxide catalysts (Yang et al., 2009). It has been also reported that the excellent catalytic activities of XFe_2O_4 type catalysts (X= Co, Cu, Mn and Zn) are due to the balance between $X^{n+}/X^{(n+1)+}$, O^{2-}/O_2 and PMS catalysis (Ren et al., 2015b). The catalytic activity of $CoFe_2O_4$ can be improved by ~2–4 times by depositing $CoFe_2O_4$ on a support (i.e. SBA–15, rGO and MgO) for the treatment of various organic pollutants (e.g. plasticizer, acid orange 7, phenol, etc.) *via* PMS activation (Hu et al., 2015; Stoyanova et al., 2014; Xu et al., 2015b; Yao et al., 2012).

The catalytic activities of various spinel–type Co–Mn catalysts prepared at various Co:Mn ratios for dye degradation *via* PMS activation are in the following order:

$CoMn_2O_4$ (99% in 80 min)~Co_2MnO_4 (98% in 80 min)>$Co_{0.5}Mn_{2.5}O_4$ (70% in 80 min)(Yao et al., 2015). This implies that (i) Co^{2+} is the main redox species because increasing Mn does not improve the catalytic activity, and (ii) Co^{3+} has lower catalytic activity than Co^{2+} in the Co–Mn coupling. Because Mn has many stable oxidation states, it is difficult for the mixed–valence Mn species in $CoMn_2O_4$ to be retained at their initial oxidation states after use.

2.3.2.2. Cu mixed–metal catalysts

Several studies (Ding et al., 2013; Feng et al., 2015; Guan et al., 2013; Ren et al., 2015b; Zhang et al., 2013b) reported the performances of spinel $CuFe_2O_4$ and supported $CuFe_2O_4$ catalysts prepared *via* sol–gel and co–precipitation techniques as PMS activators. The schematic illustration of the mechanisms of PMS activation by $CuFe_2O_4$ is presented in **Figure 2.3**. The $CuFe_2O_4$ is catalytically more stable than $CuFeO_2$ delafossite (Viswanathan et al., 2014). The $CuFe_2O_4$ catalyst is ferromagnetic and has two synergistically–coupled redox active transition metals (Fe(III) and Cu(II)) which can activate PMS *via* the following mechanism:

$$\equiv Cu(II) + HSO_5^- \rightarrow \equiv Cu(I) + SO_5^{\bullet-} + H^+ \quad (2.3.2.2.1)$$

$$\equiv Cu(I) + HSO_5^- \rightarrow \equiv Cu(II) + SO_4^{\bullet-} + OH^- \quad (2.3.2.2.2)$$

$$\equiv Cu(I) + \equiv Fe(III) \rightarrow \equiv Cu(II) + \equiv Fe(II) \ (E^o = +0.60 \text{ V } \textit{vs.} \text{ NHE}) \quad (2.3.2.2.3)$$

$$\equiv Fe(III) + HSO_5^- \rightarrow \equiv Fe(II) + SO_5^{\bullet-} + H^+ \quad (2.3.2.2.4)$$

$$\equiv Fe(II) + HSO_5^- \rightarrow \equiv Fe(III) + SO_4^{\bullet-} + OH^- \quad (2.3.2.2.5)$$

The X–ray photoelectron spectroscopy provide evidences of the changes in the Cu valence state from Cu(II) to a mixture of Cu(II)/Cu(I) in $CuFe_2O_4$ before and after

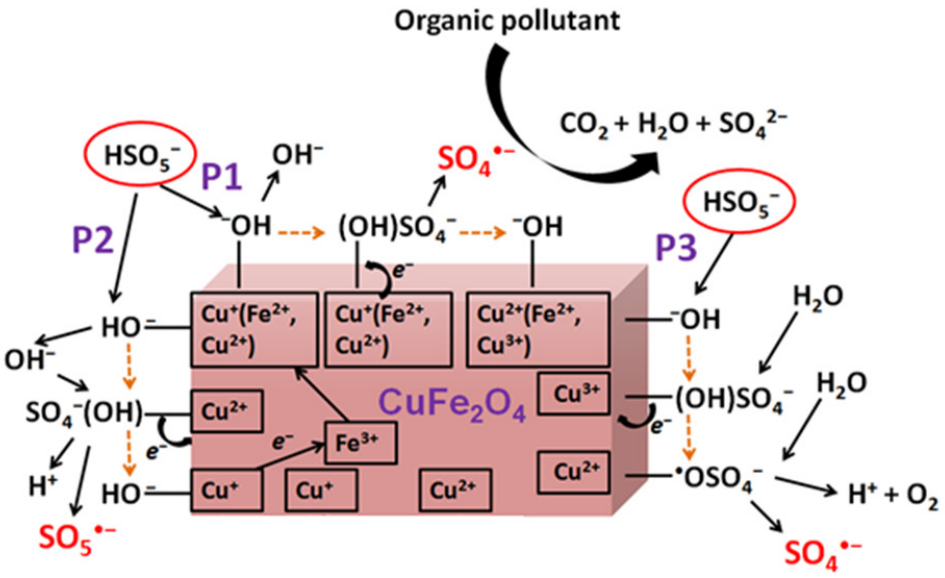

Figure 2.3. Schematic illustration of the mechanisms of PMS activation by magnetic $CuFe_2O_4$ catalyst. **P1-P3** indicates various mechanisms of PMS activation.

reaction (Guan et al., 2013). The synergistic effect could be clearly observed between Cu(II) and Fe(III). Because Cu(I) generated (**Eq. 2.3.2.2.1**) could undergo disproportionation readily (e.g. with molecular oxygen), the electron transfer from Cu(I) to Fe(III) (**Eq. 2.3.2.2.3**) produces Fe(II) which is thermodynamically more stable to disproportionation and hence, increases the $SO_4^{\bullet-}$ generation from PMS (Johnson, 1982).

$$4\equiv Cu(I) + O_2 + 4H^+ \rightarrow 4\equiv Cu(II) + 2H_2O \ (E^o = +1.08 \text{ V } \textit{vs.} \text{ NHE}) \qquad (2.3.2.2.6)$$

$$4\equiv Fe(II) + O_2 + 4H^+ \rightarrow 4\equiv Fe(III) + 2H_2O \ (E^o = +0.46\text{V } \textit{vs.} \text{ NHE}) \qquad (2.3.2.2.7)$$

It is interesting to note that the one–electron transfer from PMS to Cu(II) to form $SO_5^{\bullet-}$ is unfavorable under standard conditions, with Cu(II)/Cu(I) (E^o = +0.17 V *vs.* NHE), $SO_5^{\bullet-}/HSO_5^-$ (E^o = +1.1 V *vs.* NHE) and $SO_5^{\bullet-}/SO_5^{2-}$ (E^o = +0.81 V *vs.* NHE) (Guan et al., 2013). In order for the redox reaction to occur, PMS forms a surface complex on the surface of the catalyst possibly by replacing the surface hydroxyl groups (**Figure 2.3, P1 and P2**). The enhancement of the interfacial electron transfer rate from the formation of PMS–metal oxide complex (Moser et al., 1991) coupled with the relatively low concentration of $SO_5^{\bullet-}$ in the reaction vicinity results in a relatively lower values of the

actual reduction potential of $SO_5^{\bullet-}/HSO_5^-$ and $SO_5^{\bullet-}/SO_5^{2-}$ in the practical aqueous system, thus making it thermodynamically feasible for the reaction (**Eq. 2.3.2.2.1**) to occur (Das et al., 1999; Guan et al., 2013; Neta et al., 1988). Evidences of PMS complex on metal oxide surfaces have been observed *via* IR and Raman spectroscopies (Guan et al., 2013; Ren et al., 2015b).

It is also likely for PMS to be activated by $CuFe_2O_4$ through the Cu(II)–Cu(III)–Cu(II) (Cu(III)/Cu(II), E^o = 2.40 V *vs.* NHE (Haynes, 2013)) redox transition as follows (**Figure 2.3, P1 and P3**) (Feng et al., 2015; Zhang et al., 2013b):

$$\equiv Cu(II)-{}^-OH + HSO_5^- \rightarrow \equiv Cu(II)-(HO)OSO_3^- + OH^- \quad (2.3.2.2.8)$$

$$\equiv Cu(II)-(HO)OSO_3^- \rightarrow \equiv Cu(III)-{}^-OH + SO_4^{\bullet-} \quad (2.3.2.2.9)$$

$$\equiv Cu(III)-{}^-OH + HSO_5^- \rightarrow \equiv Cu(II)-{}^{\bullet}OOSO_3^- + H_2O \quad (2.3.2.2.10)$$

$$2\equiv Cu(II)-{}^{\bullet}OOSO_3^- + 2H_2O \rightarrow 2\equiv Cu(II)-{}^-OH + O_2 + 2\,SO_4^{\bullet-} + 2\,H^+ \quad (2.3.2.2.11)$$

The Cu(III)/Cu(II) has a relatively high standard reduction potential (E^o of Cu(III)/Cu(II) in dissolved and solid phases are +1.57 *vs.* NHE and +2.30 V *vs.* NHE, respectively) (Popova & Aksenova, 2003). The differences in E^o values corresponding to the dissolved and solid Cu(II) phases also explains the relatively lower performance of dissolved Cu(II) ion compared with that of the heterogeneous Cu(II) catalysts.

Compared to the other types of mixed metal oxides, the catalytic activity of $CuFe_2O_4$ is ~23 and ~1.3 times lower than that of $CuCo_2O_4$ (Feng et al., 2015) and $CoFe_2O_4$ (Ren et al., 2015b), respectively. Judging from the mixed metal species (which exists in $CoFe_2O_4$ as Co(II) and $CuCo_2O_4$ as mixed valence Co(II) and Co(III)), the major PMS activation reaction is expected to come from Co(II) species (Bikkarolla & Papakonstantinou, 2015). Clearly, these results imply that Co is an essential transition metal for developing the

mixed metal catalyst for efficient PMS activation.

2.3.2.3. Other mixed–metal catalysts

The performance of other mixed metal catalysts such as $NiFe_2O_4$ (Wang et al., 2016) and $MnFe_2O_4$ (Yao et al., 2014) have also been investigated as catalysts for PMS activation. In a comparative study, $NiFe_2O_4$ (Ni^{2+} as the main active species for redox reaction) has been reported to performed ~1.3 times better than $MnFe_2O_4$ for benzoic acid removal *via* PMS activation (Wang et al., 2016). The magnetic spinel–based $MnFe_2O_4$ generally shows only about 10% improvement in Orange II removal when immobilized on rGO (**Figure 2.4**) (Yao et al., 2014). While these catalysts may have potential for further improvement, at the current state, they are usually not as efficient as $CuFe_2O_4$ and $CoFe_2O_4$ (Ren et al., 2015b; Wang et al., 2016).

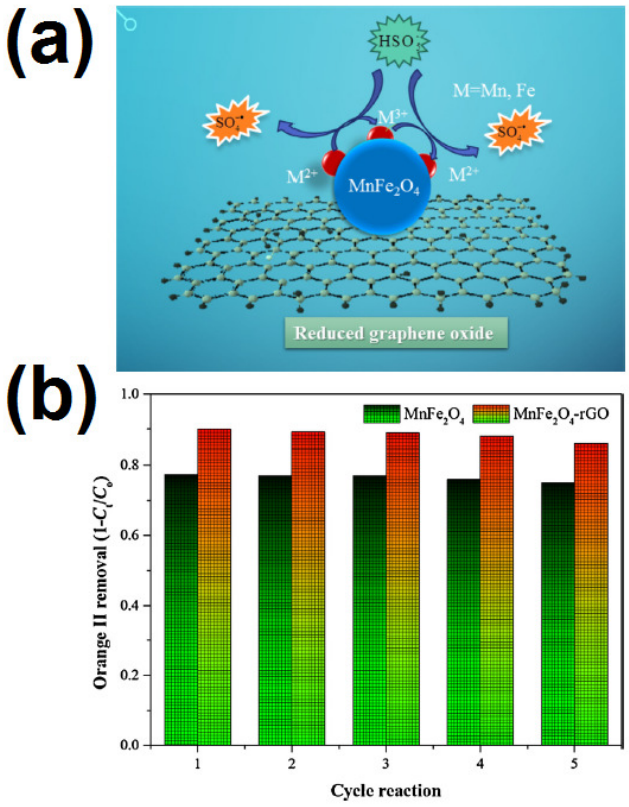

Figure 2.4. (a) The mechanism of PMS activation by $MnFe_2O_4$-rGO, and (b) Comparison of the Orange II removal efficiency using $MnFe_2O_4$ and $MnFe_2O_4$-rGO as the catalysts at the same conditions (Yao et al., 2014).

2.4. Summary of literature review

The $SO_4^{\bullet-}$ has a relatively high standard redox potential of +2.60 V *vs.* NHE. The $SO_4^{\bullet-}$ is also more selective and longer-lived than $^{\bullet}OH$. It is well established that $SO_4^{\bullet-}$ can be generated through catalytic PMS activation for aqueous organic pollutant (pharmaceuticals, phenolic compounds and dyes etc.) degradation. The most investigated PMS activator is Co–based catalyst. However, the undesirable Co leaching during catalytic PMS activation reaction has resulted in the need to explore alternative PMS activators with good stability and high efficiency. As presented in Tables 2.2 and 2.3, various types of metal–based (Mn–, Fe– and Cu–) catalysts comprising of single and mixed have been investigated. While these catalysts are more stable and environmentally-friendly compared with Co–based catalyst, their catalytic activities are generally lower than that of the Co–based catalyst. The following chapters explore the potential of novel catalysts comprising of DPA–Fe_2O_3, $CuFe_2O_4$–Fe_2O_3 and $CuBi_2O_4$ for bisphenol A, benzotriazole and sulfanilamide removal *via* PMS activation.

CHAPTER 3: DIPICOLINIC ACID–FUNCTIONALIZED Fe_2O_3 FOR BISPHENOL A REMOVAL *VIA* PEROXYMONOSULFATE ACTIVATION

3.1. Introduction

Bisphenol A (BPA) has been found ubiquitously in treated effluents and natural water systems due to its widespread usage as a monomer in the production of polycarbonate resins and plastics for various applications (Rochester, 2013; Subagio et al., 2010). BPA is widely known as an anthropogenic endocrine disruptor due to its ability to bind with the estrogen acceptor thus inducing feminization in various aquatic organisms (Metcalfe et al., 2001; Teeguarden & Hanson-Drury, 2013). To date, various treatment methods have been proposed to address the issues of water contamination due to BPA such as adsorption (Tsai et al., 2006), biological treatment (Cajthaml et al., 2009; Nguyen et al., 2013), ozonation (Keykavoos et al., 2013), wet air oxidation (Erjavec et al., 2013), and photocatalytic treatment (Gao et al., 2010). However, these methods suffer from at least one of the disadvantages of high energy requirement, slow process, high cost and generating secondary waste stream.

The SR-AOP based on PMS activation by the heterogeneous transition metal catalyst provides a potential remediation strategy to detoxify BPA in water. As highlighted in **Chapter 1**, the discovery of Co(II) as a prominent PMS activator has resulted in tremendous research interests to produce a myriad of efficient Co–based catalysts as PMS activators (Anipsitakis & Dionysiou, 2004; Anipsitakis et al., 2005b; Ding et al., 2012;

Shi et al., 2012; Shukla et al., 2010a; Zhang et al., 2010). However, due to the toxic nature of Co which could leach excessively during catalytic reaction, it is prohibitive to employ Co–based catalyst for water treatment. As alternatives to Co–based catalysts, various environmentally–friendly catalysts with their main metal framework consisting of either Fe, Mn or Cu have been developed (Ji et al., 2011; Saputra et al., 2013a; Saputra et al., 2013b; Saputra et al., 2012b). Of those, Fe(III)–based catalysts show merits of being eco–friendly, nontoxic and inexpensive materials for catalysis. However, to date, relatively few studies reported on the effective use of Fe(III) catalysts as PMS activators, and they were often considered less effective compared to Co–based catalysts (Ji et al., 2013; Rastogi et al., 2009; Zhang et al., 2013b). The performance of heterogeneous Fe(III) catalysts (such as Fe_2O_3) can be further improved by increasing their surface area and introduction of surface functionality (by incorporating electron–rich species on the surface of Fe(III) catalyst).

In this chapter, a facile co–precipitation synthesis was designed to prepare dipicolinic acid–functionalized Fe_2O_3 (DPA–Fe_2O_3) with high surface area for BPA (**Figure 3.1a**) detoxification *via* PMS activation. The synthesis procedure was carried out at a relatively mild temperature and using environmentally–benign chemicals. Dipicolinic acid or pyridine–2,5–dicarboxylic acid (**Figure 3.1b**) is a nontoxic organic compound and can be found naturally as one of the main components of the bacterial endospore. It is also amphoteric and consists of functional groups with electron–rich nitrogen and oxygen. Previously, it has been reported that DPA is an efficient electron transport mediator that can form complexes with Fe(III) to produce effective catalyst for various biomimetic oxidation processes (Anilkumar et al., 2007; de Faria et al., 2012; Halvorson et al., 1958; Uhrecký et al., 2013). It is believed that the surface Fe–DPA^+ complex could be established from this synthesis approach leading to the improved rate of $SO_4^{\bullet-}$ generation from PMS. For the first time, the acute toxicity of degradation products of BPA at

different initial Oxone® dosages was evaluated in the heterogeneous PMS system. The effects of several operating parameters (pH, DPA–Fe_2O_3 loading and Oxone® dosage) on the performance of the DPA–Fe_2O_3 and its reusability for BPA removal with Oxone® were also evaluated.

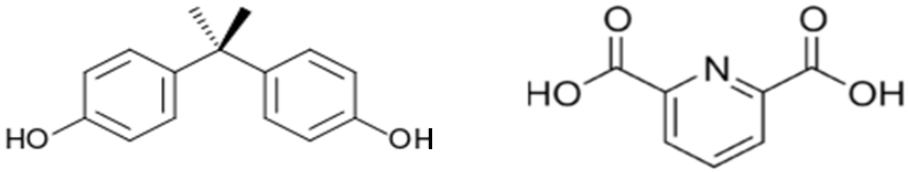

(a) bisphenol A **(b) dipicolinic acid**

Figure 3.1. Chemical structures of (a) bisphenol A and (b) dipicolinic acid.

3.2. Experimental

3.2.1. Chemicals

All the chemicals used in this study were of analytical grade and were used without further purification. The chemicals were iron(III) chloride ($FeCl_3$, Sigma–Aldrich), urea ($CO(NH_2)_2$, Hanawa), dipicolinic acid ($C_7H_5NO_4$, Sigma–Aldrich), BPA ($C_{15}H_{16}O_2$, Sigma–Aldrich), cobalt (II,III) oxide (Co_3O_4, Alfa Aesar), methanol (CH_3OH, Merck), sodium sulfite (Na_2SO_3, Sigma–Aldrich), acetonitrile (C_2H_3N, Merck), potassium iodide (KI, Fisons), potassium peroxymonosulfate in the form of Oxone® ($2KHSO_5 \cdot KHSO_4 \cdot K_2SO_4$, Alfa Aesar), commercial goethite (FeOOH, Sigma–Aldrich), commercial Fe_2O_3 (Alfa Aesar) and sodium hydroxide (NaOH, Alfa Aesar). All the experiments were conducted using the deionized water (18.2 MΩ cm).

3.2.2. Preparation of DPA–Fe_2O_3

The DPA–Fe_2O_3 catalyst was prepared by urea assisted co–precipitation of Fe–DPA^+

complex. In a typical experimental procedure, 3 mmol of $FeCl_3$ and 3 mmol of DPA were dissolved in 80 mL of the deionized water to form a greenish solution consisting of Fe−DPA^+ complex. Then, 30 mmol of urea was added into the above solution and the reaction mixture was gradually heated to 90 ºC under vigorous stirring for 24 h. Under this condition, urea decomposed to ammonia and this leads to the precipitation of Fe−DPA^+ complex to form DPA−Fe_2O_3. The DPA−Fe_2O_3 was separated from the supernatant through centrifugation at 10 000 rpm for 10 min and washed several times with the deionized water. Finally, the DPA−Fe_2O_3 was dried in an oven at 60 ºC for 12 h and stored in a desiccator prior to use. The ratios of Fe(III) to DPA were varied at 1:0, 1:1, 1.5:1 and 2:1 during the preparation process.

3.2.3. Characterization techniques

The X−ray diffraction diffractometer (Bruker D8 Advance XRD) operating on a Cu−Kα X−ray source (λ=1.5418 Å) at 40 kV and 40 mA was used to characterize the crystal structure of DPA−Fe_2O_3. The surface morphology and size of DPA−Fe_2O_3 were examined using a field emission scanning electron microscope (FESEM JEOL 7600F) and transmission electron microscope (TEM JEM−2010F). The Brunauer–Emmett–Teller (BET) specific surface area was determined using the N_2 adsorption−desorption isotherm analysis at 77 K (QuantaChrome Autosorb−1 Analyzer). The Fourier transform infrared spectrometer (Perkin Elmer) was used to characterize the surface functional groups of DPA−Fe_2O_3. The point of zero charge (pH_{zpc}) of DPA−Fe_2O_3 was determined using a Zetasizer (Malvern).

3.2.4. Experimental procedure for BPA degradation

The catalytic oxidation of BPA was evaluated at room temperature (25 ± 1 ºC) in a 500−mL reaction vessel. In a typical experimental procedure, 200 mL of solution

containing 15 mg L^{-1} of BPA was prepared and added into the reaction vessel containing 0.4 g of Oxone®. Then, the pH of the solution was adjusted to pH 7±0.2 using 1 M of NaOH and the reaction was immediately commenced under vigorous stirring with the addition of 0.1 g of DPA–Fe_2O_3 into the solution. No adsorption–desorption equilibrium time was allowed as preliminary studies had showed that less than 5% of BPA was removed *via* adsorption in 24 h. At predetermined time intervals, 1 mL of aliquots from the solution was filtered using a cellulose acetate filter. Then, methanol, which contains α–hydrogen that can react readily with sulfate and hydroxyl radicals, was immediately added into the aliquots to quench the reaction. A control containing only Oxone® and BPA without catalyst was also carried out. The performance of DPA–Fe_2O_3 was compared with different catalysts, namely the synthesized akaganeite and commercial goethite and Fe_2O_3. The effects of initial pH (2.5–9.0), DPA–Fe_2O_3 loading (0.25–1.0 g L^{-1}) and initial Oxone® dosage (0.5–2.0 g L^{-1} corresponding to BPA to Oxone® molar ratio from 1:12.5 to 1:50) were also investigated. All the degradation experiments were conducted in triplicate. For experiments conducted at various initial Oxone® dosages and 0.5 g L^{-1} of DPA–Fe_2O_3, the total organic carbon (TOC), residual PMS concentration and acute toxicity of the treated solution at various reaction times were also determined. Additionally, homogeneous experiments were also carried out following the above–mentioned procedure but using the dissolved Fe–DPA^+, Fe(III) and DPA at 0.2 mmol L^{-1} as the catalysts.

3.2.5. Acute toxicity study

The acute toxicity of BPA and its by–products produced during the catalytic reaction was evaluated by evaluating the effect of the toxicity of sample towards the bioluminescence of standard *Vibrio fischeri* (NRRL number: B11177) using a Microtox Model 500 Analyzer (Azur Environment, Workingham, England). It is well established that in the

presence of toxicity, the rate of respiration and metabolism of *V. fischeri* will be inhibited thus leading to the decrease of its bioluminescence. The *V. fischeri* bacteria was obtained in a freeze–dried form and stored in a freezer at −20 ºC prior to use. To reactivate the bacteria for acute toxicity study, the reconstitution solution containing sterilized NaCl solution was used. Due to the toxic effect of Oxone® to the *V. fischeri*, the sample consisting of treated BPA solution was initially reacted with Na_2SO_3 to convert all the HSO_5^- ions to the innocuous SO_4^{2-}. Then, the sample pH was adjusted to pH 6–7 using 1 M of NaOH and the osmolality adjusted to 2% using 22% NaCl solution. Measurements of the bioluminescence of *V. fischeri* were carried out at 5, 15 and 30–min of incubation times at 15ºC and the percentage inhibition (%) was calculated from the MicrotoxOmni software.

3.2.6. Reusability of DPA–Fe_2O_3

The reusability of DPA–Fe_2O_3 for BPA detoxification was investigated up to three cycles under the following conditions: 2.0 g L^{-1} of Oxone®, 15 mg L^{-1} of initial BPA concentration, 0.5 g L^{-1} of DPA–Fe_2O_3, initial pH of 7.0 over 240 min run–time. After each cycle, the spent DPA–Fe_2O_3 was recovered through centrifugation at 10 000 rpm for 5 min and dried in an oven at 60ºC for 12 h. Then, the spent catalyst was reused under the same condition as stated above. The BPA concentration, TOC and acute toxicity were determined at t = 240 min. Each of the experiments was conducted in triplicate.

3.2.7. Analytical methods

The BPA concentration was quantified using a high performance liquid chromatography (Perkin Elmer) with a UV detector at the wavelength of 220 nm. A reversed phased column (Hypersil GOLD) was used with the mobile phase consisting of 60% acetonitrile to 40% deionized water at the flow rate of 1 mL min^{-1}. The total organic carbon (TOC)

was measured using a TOC analyzer (Shimadzu ASI−V TOC analyzer). For HSO_5^-quantification, 5 mL of the sample was initially mixed with 1 g of KI and vigorously shaken for 30 min to allow the oxidation of I^- by PMS as follows:

$$2I^- + HSO_5^- + 2H^+ \rightarrow HSO_4^- + I_2 + H_2O \quad (3.2.7.1)$$

$$I_2 + I^- \rightarrow I_3^- \quad (3.2.7.2)$$

The concentration of I_3^-, which is directly proportional to PMS, was determined from a calibration curve by using a UV−Vis spectrophotometer at λ_{max} = 352 nm. Several organic acids, namely formic, oxalic and acetic acids were detected using an ion chromatography (Dionex ICS−2100).

3.3. Results and discussions

3.3.1. Characterization of DPA−Fe_2O_3

The schematic illustration of the DPA−Fe_2O_3 synthesis process is presented in **Figure 3.2**. During the synthesis process, it is postulated that the Fe−DPA^+ complex (Formation constant = 227 M) (Bridger et al., 1982) can be slowly dissociated into mobile Fe(III) ion, which subsequently hydrolyze to goethite and then dehydrate to DPA−Fe_2O_3 under basic condition. Based on this synthesis approach, DPA functional groups which contain electron−rich nitrogen and oxygen groups can be introduced as the surface−complex on DPA−Fe_2O_3. Preliminary results showed that DPA can improve the catalytic activity of Fe(III) after complexation as observed by the significantly better performance of the homogeneous Fe−DPA^+/PMS system *vis−à−vis* the Fe(III)/PMS system in BPA removal (**Figure 3.3**). This is because the complexation of DPA with Fe(III) induces chemical shift through (i) the transfer of the unpaired electron spin density from the paramagnetic Fe(III)

into ligand orbitals, (ii) the unpaired electron spin polarization, and/or (iii) the dipolar interactions (Crans Debbie et al., 2003). The chemical shift is dependent on the type of ligand present and can induce significant changes in the redox potential of Fe(II)/Fe(III) leading to different degrees of promotional effects on the catalysis reaction (Pierre & Fontecave, 1999; Rastogi et al., 2009).

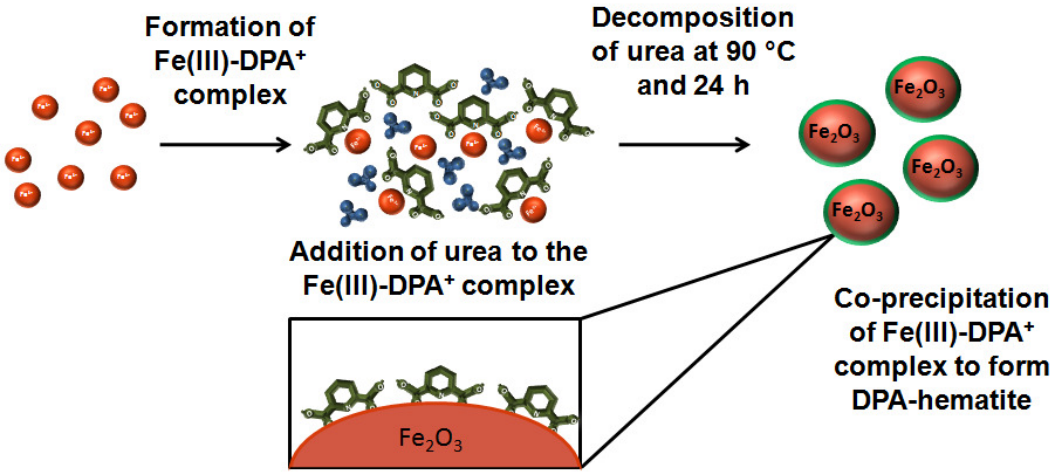

Figure 3.2. Schematic illustration of the synthesis of DPA–Fe_2O_3.

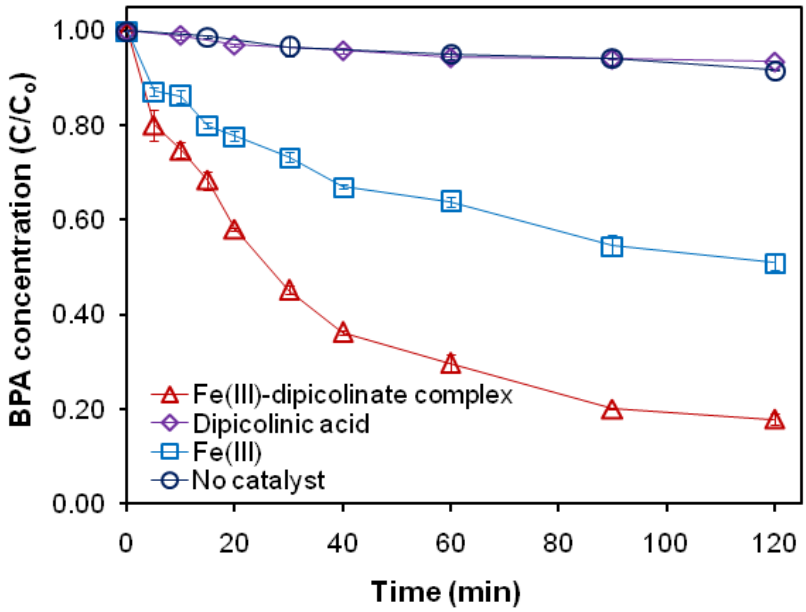

Figure 3.3. Degradation of BPA by Oxone® activated by Fe–DPA$^+$, Fe(III) and DPA. Initial conditions: [BPA] = 15 mg L^{-1}, [Oxone®] = 2 g L^{-1}, pH = 7.0, and [catalyst] = 0.2 mmol L^{-1}.

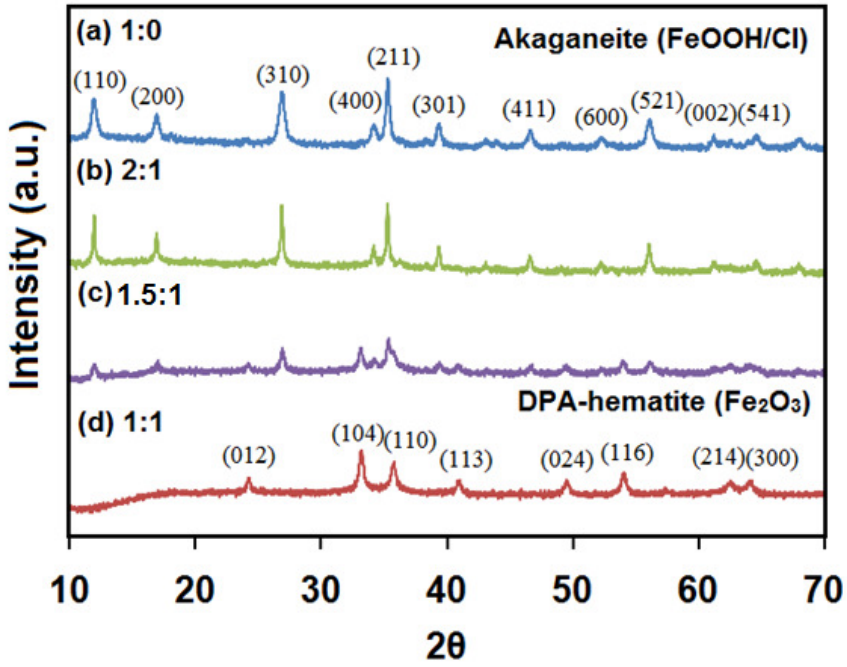

Figure 3.4. X–ray diffraction patterns of the catalysts synthesized at different ratios of Fe to DPA, indicating that pure DPA–Fe_2O_3 can be prepared using DPA:Fe molar ratio of 1:1.

Figure 3.4 shows the XRD patterns of the as–prepared Fe(III) catalysts synthesized with and without DPA. The XRD pattern of the Fe(III) catalyst prepared without DPA (Fe:DPA ratio of 1:0) can be indexed to the akaganeite phase (FeOOH/Cl) with no impurity peak. The presence of Cl in akaganeite is probably due to the use of $FeCl_3$ as the Fe(III) precursor during synthesis. For samples prepared with Fe(III)–to–DPA molar ratio of 1.5:1, peaks at 2θ = 24°, 33°, 37°, 41°, 49° and 54° appeared which can be indexed to DPA–Fe_2O_3. The quantitative Rietveld analysis was conducted. The results show that akaganeite and DPA–Fe_2O_3 phases coexist at 35% and 65%, respectively. However, when the Fe(III)–to–DPA molar ratio was adjusted to 1:1, pure DPA–Fe_2O_3 was obtained and the peaks associated with akaganeite disappear. This clearly indicates that the Fe(III) ion has the tendency to form akaganeite when Cl^- is present under the synthesis condition. The complexation of DPA with Fe(III) hinders the formation of akaganeite by controlling the availability of Fe(III) ions in the solution favoring the formation of DPA–Fe_2O_3. At different DPA:Fe(III) ratios, different Fe–DPA^+:Fe(III) ratios are present and hence,

leading to the formation of different akaganeite:Fe_2O_3 ratios.

The morphologies of akaganeite and DPA–Fe_2O_3 are as shown in FESEM and TEM micrographs (**Figure 3.5**). As presented in **Figure 3.5**, the akaganeite has a nanorod–like structure with an average length of 30–60 nm and BET specific surface area of 120 m^2 g^{-1} while the DPA–Fe_2O_3 consists of aggregated quasi–nanosphere morphology with an average diameter of 10–15 nm and BET specific surface area of 188 m^2 g^{-1}. The relatively larger specific surface area of DPA–Fe_2O_3 compared to that of other reported Fe_2O_3 catalyst (34 m^2 g^{-1}) for PMS activation (Ji et al., 2013) is favorable for the heterogeneous catalysis.

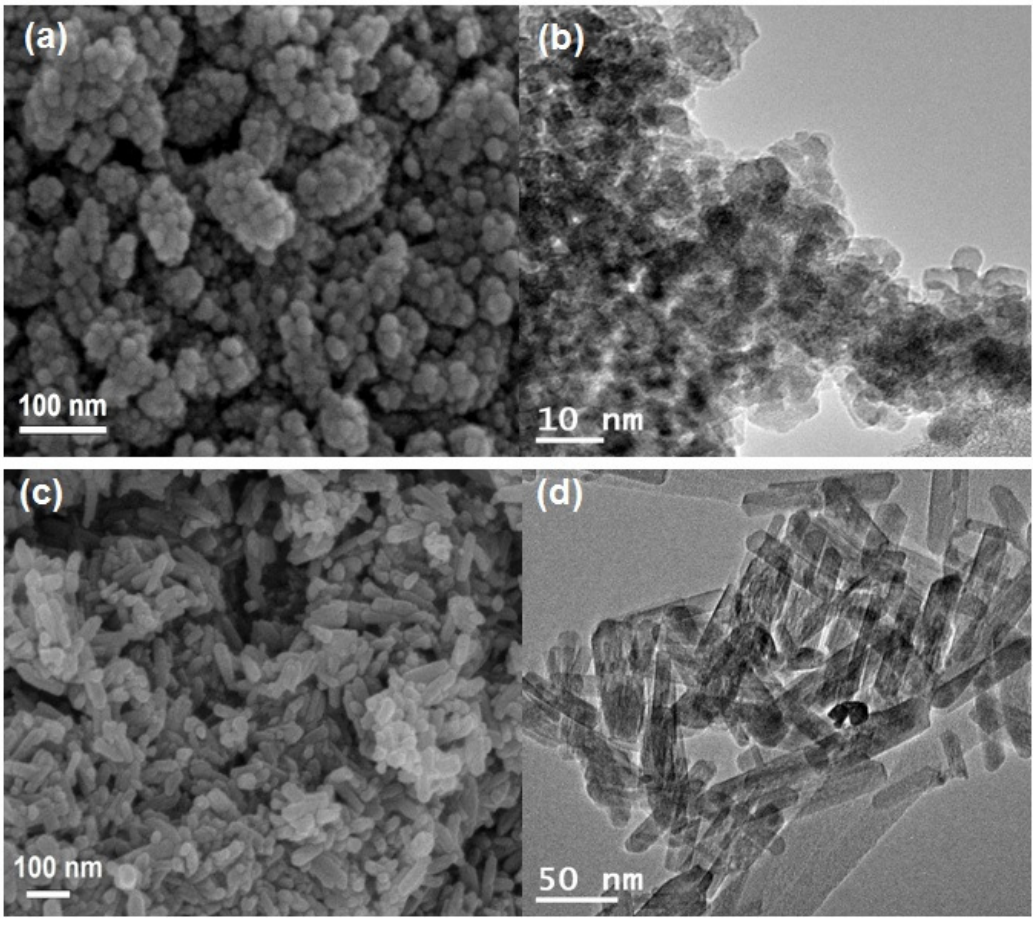

Figure 3.5. FESEM and TEM images of (a and b) akaganeite and (c and d) DPA–Fe_2O_3.

Figure 3.6a shows the FTIR spectrum of a typical akaganeite which is synthesized without DPA in which the characteristic absorbance peaks are at about 1500–1700 cm^{-1} and 600–900 cm^{-1} (García et al., 2008). For the FTIR spectrum of DPA–Fe_2O_3 (**Figure 3.6b**), the peak at about 1700 cm^{-1} can be ascribed to carboxylic C=O stretching while the peaks at 1300–1500 cm^{-1} could probably be attributed to the asymmetric C=O stretching in COO^- group. A broad peak is observed at 600 cm^{-1} which can be indicative of Fe–O bond. These results provide evidences of the presence of DPA functional groups on the surface of DPA–Fe_2O_3.

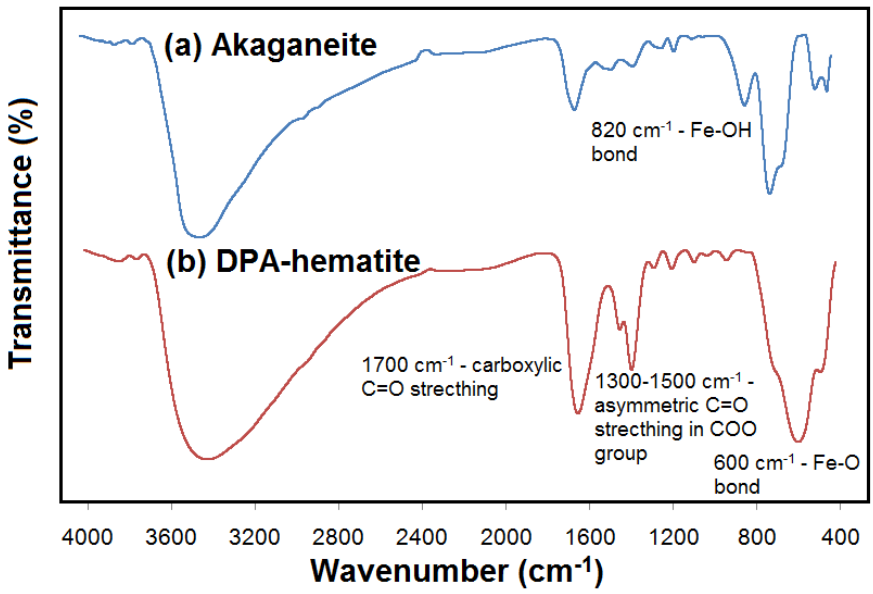

Figure 3.6. FTIR spectra of (a) akaganeite and (b) DPA–Fe_2O_3.

3.3.2. Efficiency and kinetics of BPA degradation

3.3.2.1. Effects of different heterogeneous Fe(III) catalysts and initial pH

Figure 3.7a shows comparison of the time courses of BPA degradation by different heterogeneous Fe(III) catalysts in the presence of 2.0 g L^{-1} of Oxone®. The control experiment containing BPA and Oxone® without catalyst achieved only ~8% reduction in

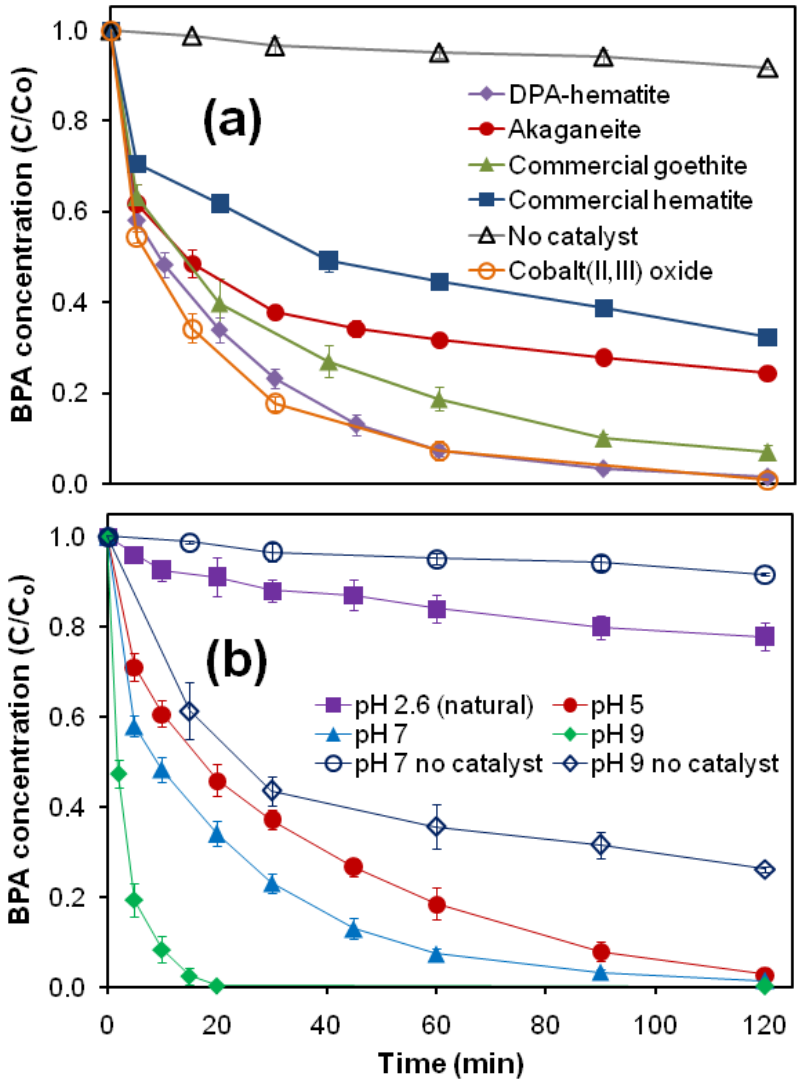

Figure 3.7. Effects of (a) different heterogeneous Fe(III) catalysts and (b) initial pH on BPA degradation. Initial conditions: [BPA] = 15 mg L^{-1}, [Oxone®] = 2.0 g L^{-1} and [catalyst] = 0.5 g L^{-1}.

BPA concentration over 120 min. This signifies that BPA is difficult to be degraded by PMS alone. All the Fe(III)–based catalysts can activate Oxone® to degrade BPA. In general, the surface Fe(III) of the catalyst acts as an electron acceptor and undergoes redox interconversion with Fe(II) in the presence of PMS to generate the freely–diffusible $SO_4^{\bullet-}$ and $SO_5^{\bullet-}$ as follows (Anipsitakis & Dionysiou, 2004):

$$Fe(III) + HSO_5^- \rightarrow SO_5^{\bullet-} + Fe(II) + H^+ \qquad (3.3.2.1.1)$$

$$Fe(II) + HSO_5^- \rightarrow SO_4^{\bullet-} + Fe(III) + OH^- \quad (3.3.2.1.2)$$

$$SO_4^{\bullet-} + BPA \rightarrow \text{degradation products} + SO_4^{2-} \quad (3.3.2.1.3)$$

The initial step involving the generation of the relatively weaker $SO_5^{\bullet-}$ radical by Fe(III) is the rate−determining step which functions to (i) minimize radical quenching effect, (ii) maximize the utilization of the generated radicals, and (iii) generate Fe(II) for $SO_4^{\bullet-}$ production (Rastogi et al., 2009).

The schematic illustration of the BPA detoxification process by DPA−Fe_2O_3 is shown in **Figure 3.8**. The excellent performance of DPA−Fe_2O_3 over all the other Fe(III)−based catalysts is probably attributed to (i) the nano−sized structure of DPA−Fe_2O_3 which provides the highest surface area for reaction, and (ii) the presence of DPA functional groups on the surface of DPA−Fe_2O_3. The surface OH− and DPA−functional groups act as σ−donor ligands and are beneficial in increasing the electron density/mobility and reactivity of Fe(III). The commercial goethite achieved 90% of BPA removal within 120 min but it dissolved substantially during the 120−min reaction. The reaction system with DPA−Fe_2O_3 can be well described by the pseudo first−order kinetic model with the apparent rate constant, k_{app}, of 0.039 min^{-1} (R^2 = 0.950). However, the pseudo first−order kinetic model cannot fit very well into reaction systems with the akaganeite, commercial hematite and commercial goethite. This may be due to the retardation of the BPA degradation towards the end of the reaction time which could be attributed to the deactivation of the catalyst and dissolution of Fe(III) (as observed in the case of commercial goethite). The DPA−Fe_2O_3 was also compared with the commercial Co_3O_4 (k_{app} = 0.041 min^{-1}, R^2 = 0.946). A comparable removal efficiency and rate were obtained for DPA−Fe_2O_3 and Co_3O_4. However, Co leaching from the use of Co_3O_4 as PMS activator is well−reported in the literature with the permissible limit for irrigation water of 0.05 mg L^{-1} (Environmental Bureau of Investigation, Canadian Water Quality Guidelines)

makes it less favorable for use as a catalyst (Anipsitakis et al., 2005b; Bhatnagar et al., 2010; Chen et al., 2008). A possible disadvantage of DPA–Fe_2O_3 is the possibility of oxidation of surface DPA during the catalytic reaction. In view of the eco–friendly nature of DPA–Fe_2O_3 coupled with its high catalytic activity, it was selected for further evaluation.

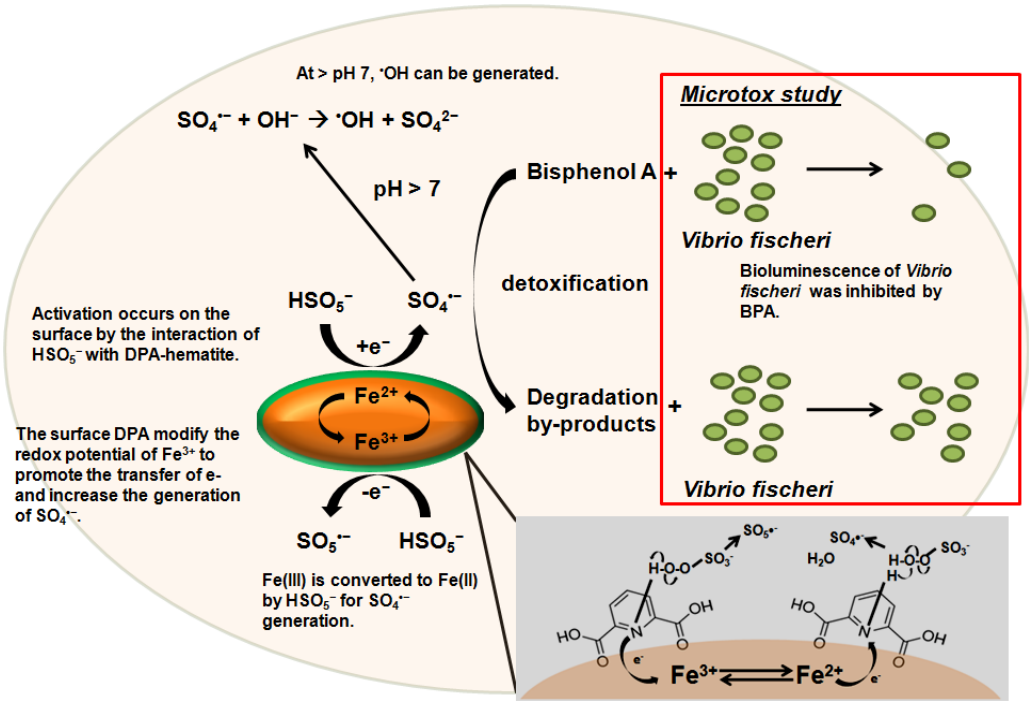

Figure 3.8. The schematic illustration of the BPA detoxification process by DPA–Fe_2O_3.

Figure 3.7b presents the influence of initial pH (pH 2.6 – 9.0) on BPA removal. The BPA removal efficiencies were more than 95% within 120 min for all the initial pHs studied except for pH 2.6 (natural pH) whereby only 22% of BPA was degraded. During the reaction, the pH change over 120–min was insignificant for the initial pH 2.6 and 5.0 while the final pH for initial pH 7.0 and 9.0 were 5.8 and 7.6, respectively. The pH_{zpc} of the DPA–Fe_2O_3 was determined to be pH 9.5. This indicates that the surface charge of the DPA–Fe_2O_3 is dominated by the positively–charged sites for the investigated pH range. This can be attributed to the enhanced surface protonation from the attached DPA ligand. The pKa_1 and pKa_2 of PMS are < 0 and 9.4, respectively, while the pKa for BPA is 9.6–10.2 (Negri et al., 1998; Staples et al., 1998). This appears to imply that the PMS

species is in its negatively−charged state for the range of pH investigated. In this regard, the negatively−charged PMS should be favorably attracted to the catalytic sites of the DPA−Fe_2O_3. However, at acidic pH condition, due to the occurrence of the PMS stabilization effect owning to the attachment of H^+ to the peroxide bond (−O−O−) of PMS, repulsion between PMS and the protonated catalytic sites (e.g. hydroxo and dipicolinate species) occurs (Zhang et al., 2013b). This inhibits the PMS activation reaction resulting in the decrease in BPA degradation particularly at acidic pH. The BPA removal rate increase with increasing pH, especially at pH 9.0 with all the BPA removed within 20 min with the highest k_{app} value of 0.262 min^{-1}. The excellent performance at pH 9.0 can also be ascribed to several factors. First, the abundance SO_5^{2-} ions at pH 9.0 is relatively easier to be activated compared to PMS (Guan et al., 2013). Second, under basic condition, more surface OH−groups are able to increase the electron density of the transition metal and act as σ−donor ligand which lowers the redox activation energy and increase the PMS activation reaction. Third, the electron mediation process generally increases with increasing pH due to the effective linkage of redox partners by bridged−surface ligand and OH^-. Finally, the generation of the highly−reactive $^{\bullet}OH$ at pH 9.0 from the $SO_4^{\bullet-}$ (**Eq. 3.3.2.1.4**) could also accelerate the BPA removal (Mahdi Ahmed et al., 2012).

$$SO_4^{\bullet-} + OH^- \rightarrow {}^{\bullet}OH + SO_4^{2-} \qquad (3.3.2.1.4)$$

3.3.2.2. Effects of DPA−Fe_2O_3 loading and Oxone® dosage

Figures 3.9 and 3.10 present the effects of DPA−Fe_2O_3 loading and Oxone® dosage on BPA degradation, respectively. The BPA removal can be expedited by increasing the DPA−Fe_2O_3 loading and Oxone® dosage. The higher amount of catalytic sites and reactant concentration are the reasons for the increase in reaction rate at various

DPA–Fe_2O_3 loading and Oxone® dosages, respectively. The effects of catalyst loading and Oxone® dosage on reaction rate are more imperative at lower Oxone® dosage and catalyst loading, respectively. Since PMS activation reaction in the heterogeneous system is a surface phenomenon, the main prerequisite for the reaction to occur is the initial formation of a PMS–surface complex which is a diffusion and equilibrium driven processes. Under low catalyst loading and Oxone® dosage, limited PMS–surface contact could be achieved. However, by increasing the Oxone® dosage, the resulting higher probability of PMS–surface contact would generate more $SO_4^{\bullet-}$ for BPA degradation. When catalyst loading is higher, there is abundance effective surface area for the initial formation of PMS–surface complex and the effect of Oxone® dosage becomes less important. Almost complete removal of BPA is observed within 120–min regardless of the Oxone® dosage used in this study when more than 0.5 g L^{-1} of DPA–Fe_2O_3 is employed. To gain further insights into the relationship of catalyst loading and Oxone® dosage and BPA removal rate, the k_{app} coefficient is expanded to include the initial Oxone® dosage (D_o) and reaction surface area per unit volume (ρ_s) as follows:

$$-\frac{d[BPA]}{dt} = k_{app}[BPA] = k_{SD}[D_o]^{1/2}\rho_s[BPA] \qquad (3.3.2.2.1)$$

where k_{SD} ($L^{3/2}$ m^{-2} $g^{-1/2}$ min^{-1}) is the specific rate constant independent of the initial Oxone® dosage and catalyst loading. The assumption that the initial Oxone® concentration is in excess is valid considering the amount of Oxone® consumed for BPA removal is less than 20% and the Oxone®–to–BPA molar ratio is at least 12.5:1. **Eq. 3.3.2.2.1** enables the estimation of k_{app} of the BPA removal rate at various initial Oxone® dosages and catalyst loadings at a given pH. The correlation between k_{app} with ρ_s and D_o can be established through fitting of **Eq. 3.3.2.2.1** to the experimental data (k_{app}) using MATLAB, as shown in **Figure 3.11** whereby the k_{SD} value is 3.2 x 10–4 $L^{3/2}$ m^{-2} $g^{-1/2}$ min^{-1} (R^2 = 0.95) at pH 7.0.

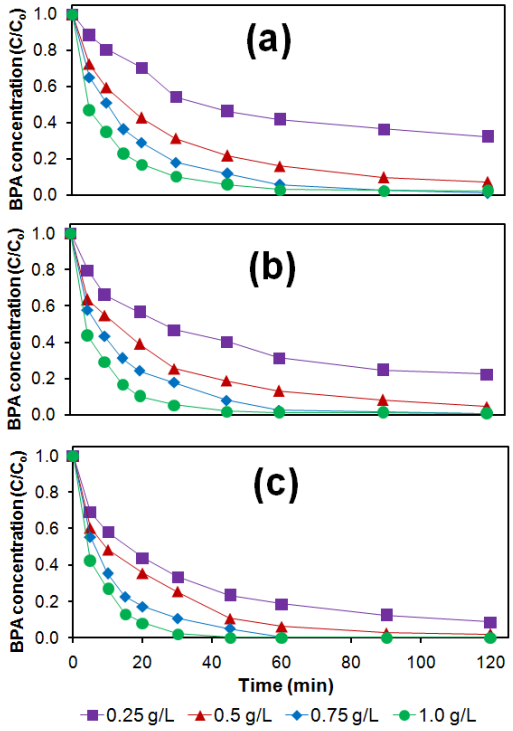

Figure 3.9. Effect of DPA–Fe_2O_3 loading on BPA degradation at Oxone® dosage of (a) 0.5, (b) 1.0 and (c) 2.0 g L^{-1}. Initial conditions: [BPA] = 15 mg L^{-1} and pH = 7.0.

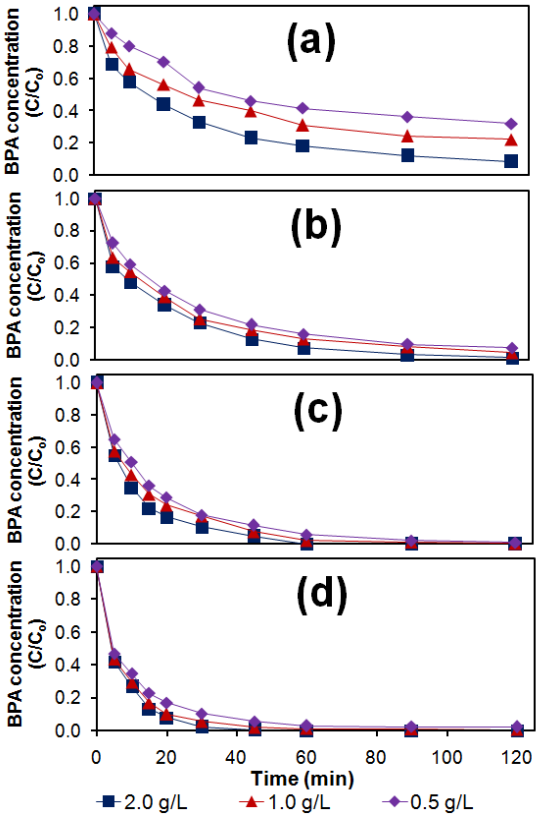

Figure 3.10. Effect of Oxone® dosage on BPA degradation at DPA–Fe_2O_3 loadings of (a) 0.25, (b) 0.50, (c) 0.75 and (d) 1.0 g L^{-1}. Initial conditions: [BPA] = 15 mg L^{-1}, and pH = 7.0.

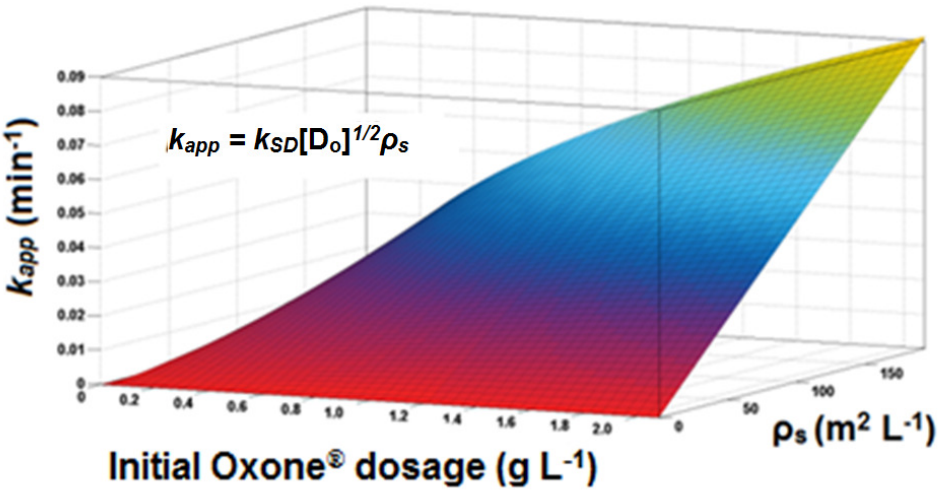

Figure 3.11. Relationship of k_{app}, ρ_s and initial Oxone® dosage at pH 7.0.

3.3.3. Degree of mineralization and peroxymonosulfate consumption

The TOC removal data provides some useful insight into the degree of BPA mineralization while PMS consumption data provides information on the PMS utilization efficiency of the heterogeneous catalyst/PMS system. For complete oxidation of 15 mg L^{-1} of BPA to carbon dioxide and water, the theoretical amount of Oxone® required is 1.45 g L^{-1} which can be calculated from the following chemical equation:

$$C_{15}H_{16}O_2 + 72HSO_5^- \rightarrow 72\ SO_4^{2-} + 44H_2O + 15CO_2 \qquad (3.3.3.1)$$

The degrees of mineralization and PMS consumption were investigated at Oxone® dosages of 0.5, 1.0 and 2.0 g L^{-1} which encompass deficit (BPA to Oxone® molar ratio of 1:12.5 and 1:25) and excess (1:50) Oxone® conditions, all at 0.5 g L^{-1} of DPA–Fe_2O_3 loading. **Figure 3.12** shows a strong influence of the Oxone® dosage on the degree of BPA mineralization (indicated as the TOC removal). Several organic acids, namely oxalic, acetic and formic acids were also detected at twofold concentration when 2.0 g L^{-1} of Oxone® was used compared with 1.0 g L^{-1}. For all cases, despite more than 90% of BPA was removed within 120 min, the degrees of mineralization were determined to be only

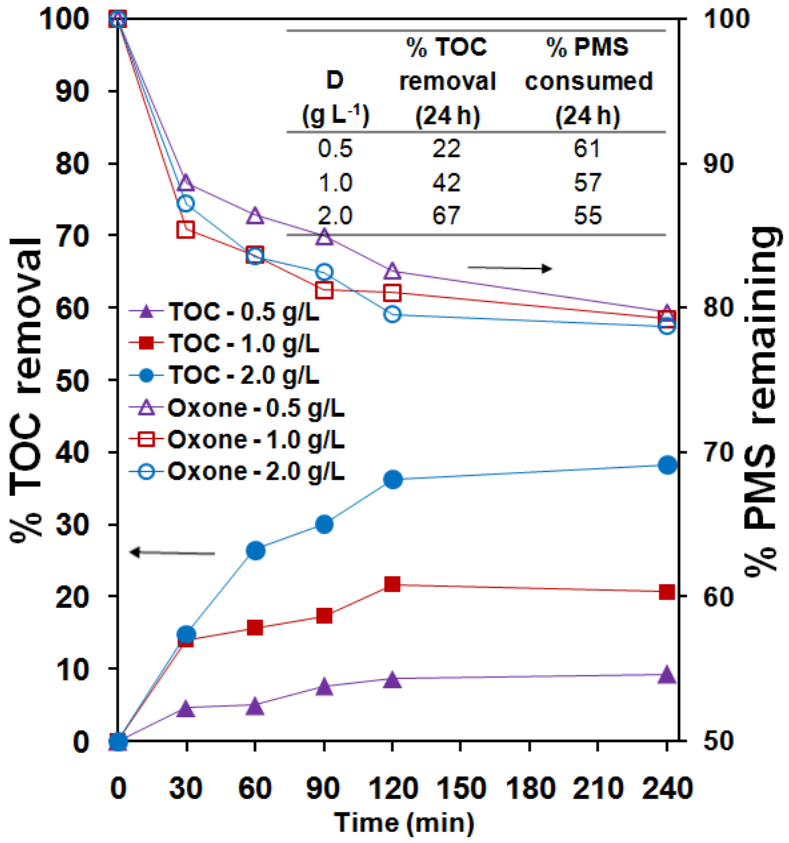

Figure 3.12. Time courses of TOC removal and PMS remaining at various initial Oxone® concentrations. Initial conditions: [BPA] = 15 mg L^{-1}, pH = 7.0, and [catalyst] = 0.50 g L^{-1}.

9±1, 21±4 and 38±2% for Oxone® dosages of 0.5, 1.0 and 2.0 g L^{-1}, respectively, and the corresponding percentages of PMS consumed were only about 20% for all cases. The slower TOC removal and PMS consumption rates after 120 min are probably attributed to (i) the formation of recalcitrant aromatic BPA oxidation products that are resistant to further oxidation (Huang & Huang, 2009), and (ii) the blockage of the catalyst active sites due to the adsorption of the recalcitrant BPA intermediates. Nevertheless, after 24 h of reaction, the TOC removal efficiency increased significantly to 22, 42 and 67% for Oxone® dosages of 0.5, 1.0 and 2.0 g L^{-1}, respectively. This suggests that the temporal deactivation of catalyst surface is reversible. The calculated k_{SD} value for TOC removal using **Eq. 3.3.2.2.1** at a constant DPA–Fe_2O_3 loading and various initial Oxone® dosages is lower (2.6 x 10^{-5} $L^{3/2}$ m^{-2} $g^{-1/2}$ min^{-1}) than the corresponding value for BPA removal attributed to the slower TOC removal.

3.3.4. Acute toxicity study

In view of the production of different recalcitrant BPA intermediates during the catalytic oxidation process which could be more toxic than BPA itself, the transient toxicity of BPA solution need to be evaluated. Hitherto, studies on the evolution of the acute toxicity of pollutants and their intermediates generated from SR-AOP are relatively rare, and most of which dealt with the persulfate system (Liang & Wang, 2013; Olmez-Hanci et al., 2013). The intrinsic toxicity of PMS to microorganisms at elevated concentrations due to the high standard reduction potential of PMS (E^o = 1.82 V) makes it difficult to evaluate the changes in acute toxicity of BPA intermediates over time using microbial bioassay. In this study, a facile protocol was adopted to eliminate the toxicity interference induced by PMS by converting the residual PMS to innocuous sulfate ions through reaction with stoichiometric amount of Na_2SO_3:

$$HSO_5^- + SO_3^{2-} \rightarrow 2\ SO_4^{2-} + H^+ \qquad (3.3.4.1)$$

After treatment of a blank Oxone® solution with Na_2SO_3 and followed by pH restoration to neutral, there was no significant difference (p <0.05) in the acute toxicities based on *V. fischeri* of the blank DI water and Oxone®/ SO_3^{2-} solutions. Similar results were also obtained for the BPA and BPA/PMS/SO_3^{2-} solutions. Furthermore, with the stoichiometric addition of SO_3^{2-}, PMS was not detectable using the iodometric method while a stoichiometric amount of SO_4^{2-} ion was detected in the SO_3^{2-} treated solution. Thus, this validated method that eliminates the PMS interference was employed to investigate the transient toxicity of BPA solution during the course of reaction in the system.

The changes of inhibition of *V. fischeri* bioluminescence (at 5, 15 and 30 min of incubation time) induced by BPA and its degradation intermediates during the oxidation process at different Oxone® dosages are shown in **Figure 3.13**. Although a similar trend

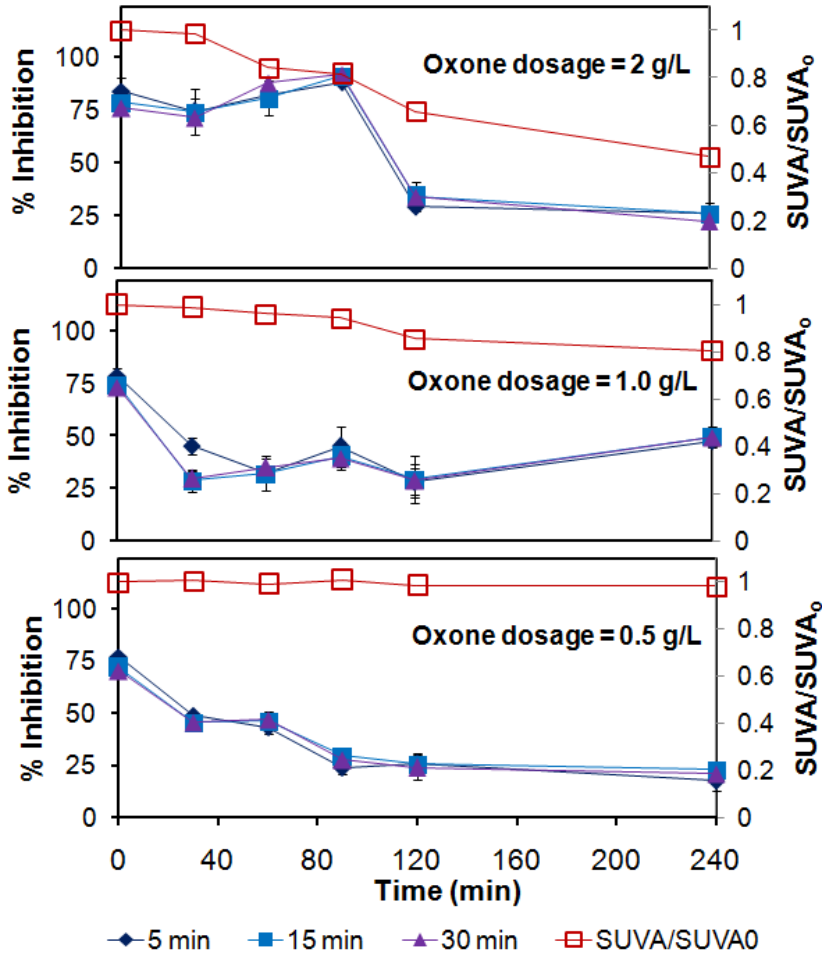

Figure 3.13. Time courses of acute toxicity and SUVA/SUVA$_0$ of BPA solution (± S.D.) during reaction at different initial Oxone® concentrations.

can be observed for 5, 15 and 30 min of incubation time under the same condition, the acute toxicity patterns are greatly influenced by the Oxone® dosage. When 2.0 g L^{-1} of Oxone® (**Figure 3.13a**) was employed, the percentages of inhibition generally increased from 79% at t = 0 min to 90% at t = 90 min. This is probably due to the accumulation of toxic degradation intermediates such as succinic acid, 2,3–dimethyl benzoic acid and 3–hydroxy–4–methyl–benzoic acid which are generally more toxic than BPA itself (Olmez-Hanci et al., 2013; Sánchez-Polo et al., 2013). However, the inhibitory effect was distinctively reduced after 90 min of treatment. This is attributed to the further degradation of the toxic intermediates to nontoxic organic acids as observed by the detection of acetic, formic and oxalic acids in this study using ion chromatography.

The changes in the transient toxicity of BPA solution when 0.5 g L^{-1} and 1.0 g L^{-1} of Oxone® are used can be explained in terms of the BPA intermediates produced during the oxidation process which undergo the dimerization and mineralization pathway as follow (Khataee & Mirzajani, 2010; Lau et al., 2006):

$$Fe(II) + HSO_5^- \rightarrow SO_4^{\bullet -} + Fe(III) + OH^- \quad (3.3.4.2)$$

$$SO_4^{\bullet -} + BPA \rightarrow BPA^{\bullet} + SO_4^{2-} \quad (3.3.4.3)$$

$$BPA^{\bullet} + BPA^{\bullet} \rightarrow BPA_2 \text{ (nontoxic)} \quad (3.3.4.4)$$

$$BPA_2 \rightarrow \text{other aromatic intermediates (toxic)} \quad (3.3.4.5)$$

$$\text{aromatic intermediates} \rightarrow \text{organic acids (nontoxic)} \quad (3.3.4.6)$$

$$\text{organic acids} \rightarrow CO_2 + H_2O \quad (3.3.4.7)$$

During the initial phase of degradation, nontoxic intermediates of higher molecular weight can be formed due to the dimerization reaction of BPA (Olmez-Hanci et al., 2013). Subsequent oxidation of the higher molecular weight intermediates results in the increase in toxicity of BPA solution. This is follow by the further transformation of toxic intermediates to nontoxic organic acids and finally to carbon dioxide and water. Considering that the amount of Oxone® consumed and TOC removal is low when 0.5 and 1.0 g L^{-1} of Oxone® are employed compared to that of 2.0 g L^{-1} of Oxone® but the overall removal of BPA are also more than 95%, it can be implied that for cases with deficit Oxone® dosage (0.5 and 1.0 g L^{-1}), most of the BPA intermediates remain at the BPA_2 stage (**Eq. 3.3.4.4**). The specific UV absorbance (SUVA) or UV_{254}/DOC was determined (**Figure 3.13**) to examine the extent of ring opening reactions. With 2.0 g L^{-1} of Oxone® (**Figure 3.13a**), the decrease in intrinsic toxicity over time and ring opening reactions were observed. This supports the fact that the mineralization is more complete. On the

contrary, the SUVA analysis reveals that ring opening reactions are hardly observed when 0.5 g L^{-1} of Oxone® is used. For the case of 1.0 g L^{-1} of Oxone®, the result suggests a slow conversion of BPA_2 to toxic aromatic intermediates at t = 120 min as indicated by the slow rise in the intrinsic toxicity. Therefore, based on the results, at the deficit Oxone® condition, it could be envisaged that toxic intermediates could potentially accumulate in the treated water and excess Oxone® dosage is needed for achieving a higher detoxification of BPA solution.

3.3.5. Reusability of DPA−Fe_2O_3 for BPA detoxification

Figure 3.14 shows the initial and final percentages of inhibition of the sample to the bioluminescence of *V. fischeri* and TOC removal efficiency for cycles 1, 2 and 3. The DPA−Fe_2O_3 can be reused after simple washing procedure without the need to undergo tedious post−treatment procedure such as the post−calcination treatment. Marginal reduction of TOC removal efficiencies were observed over 3 cycles despite 95% of BPA was removed. This could be due to (i) unavoidable loss of catalyst during the catalyst recovery process which is estimated up to 11% for each cycle, and (ii) deactivation of the catalyst surface due to blockage of the catalyst surface and partial oxidation of DPA during catalytic reaction. Even so, the DPA−Fe_2O_3 can successfully detoxify BPA consistently (**Figure 3.14**) without major change in removal efficiency giving indirect evidence that the DPA can still be retained after several successive cycles. This shows that DPA−Fe_2O_3 is stable for BPA treatment and can be reused for at least 3 cycles.

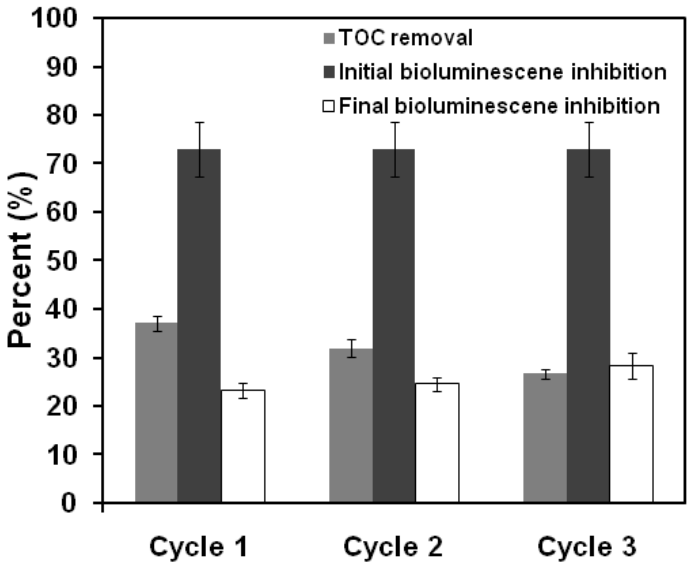

Figure 3.14. Total organic carbon removal efficiency and the corresponding initial and final inhibitions (± S.D.) for 3 cycles.

3.4. Conclusions

DPA–Fe_2O_3 with high surface area was successfully prepared by a facile urea–assisted co–precipitation of Fe–DPA^+ complex to activate PMS for BPA degradation. The DPA–Fe_2O_3 performed remarkably better than other Fe(III)–based catalysts in BPA removal with PMS. The influence of Oxone® dosage is more pronounced at lower DPA–Fe_2O_3 dosage. Similarly, the influence of DPA–Fe_2O_3 loading is more important at lower Oxone® dosage. A simple predictive model was employed to predict the correlation between the rate constant and Oxone® dosages at various catalyst loadings. The change in transient toxicity of BPA solution during the course of reaction was successfully determined for the first time in PMS system at different Oxone® dosages. For detoxification of BPA, excess Oxone® condition needs to be employed to improve the mineralization of BPA. The DPA–Fe_2O_3 is stable and can be used to detoxify BPA *via* PMS activation for at least 3 cycles without any significant loss of its catalytic activity.

CHAPTER 4: MAGNETIC $CuFe_2O_4$–Fe_2O_3 FOR BISPHENOL A REMOVAL *VIA* PEROXYMONOSULFATE ACTIVATION

4.1. Introduction

In **Chapter 3**, DPA–Fe_2O_3 was synthesized at a relatively mild temperature *via* the low temperature co–precipitation synthesis method. The DPA–Fe_2O_3 performed better than other Fe(III)–based catalysts, namely Fe_2O_3, FeOOH and FeOOH/Cl as a catalyst to generate $SO_4^{\bullet-}$ from PMS for BPA detoxification. In order to further improve the catalytic activity of the Fe(III)–based catalyst, an auxiliary metal precursor was deliberately incorporated into the metal oxide framework of the single metal Fe(III) catalyst to fabricate a mixed metal oxide catalyst. As highlighted in **Chapter 2**, mixed metal oxide catalysts have many advantages over the single metal oxide system because mixed metal oxides are generally more redox active, versatile and polyfunctional.

There are many transition metals that could be used to couple with Fe(III) to form a mixed metal oxide catalyst. As presented in **Chapter 2**, although current trend of study suggests that Co is the suitable metal to couple with Fe, this approach suffers from the dissolution of highly–toxic Co ions during treatment (Hardjono et al., 2011; Huang et al., 2014). One appealing transition metal for coupling with Fe(III) is Cu. To date, the Cu–based catalysts which have been reported include $CuFe_2O_4$ (Ding et al., 2013; Zhang et al., 2013b), CuO (Ji et al., 2011) and Cu/ZSM5 (Ji et al., 2014). The coupling of Cu(II) with Fe(III) to form mixed metal oxide has been

reported to significantly improve the performance of the catalyst. However, in most cases, the catalyst preparation method incorporating Fe(III) and Cu(II) involves high–temperature heat treatment, environmentally–harmful solvents and other organic precursors. For pragmatic application, a facile low–energy and eco–friendly synthesis is warranted.

In previous study, most of the heterogeneous catalyst/PMS studies reported the efficiency of the catalyst but provide limited insights to the kinetics of the catalytic reaction. The investigations of the kinetics of pollutant oxidation in SR-AOP dealing with heterogeneous catalyst/PMS system are often based on the pseudo first–order kinetics with the assumption that the oxidant (PMS) added was readily available for reaction (Liu et al., 2015a; Zhang et al., 2013a). Qi et al. (2014) presented a second–order kinetic model to describe the degradation of caffeine by Co–MCM41 catalyst. However, these kinetic models did not take into account the influence of pH, PMS dosage and catalyst loading on pollutant degradation particularly under non–ideal conditions (e.g. non–excess PMS, different pHs, etc.). In this regard, a more robust, holistic kinetic model that takes into account these influencing parameters needs to be employed.

In this chapter, the main objectives were to (i) prepare and characterize a series of mixed metal oxide catalysts encompassing of $CuFe_2O_4$–Fe_2O_3, ferrospinels (YFe_2O_4, Y = Cu, Co and Mn), Cu–based spinels (CuX_2O_4, X = Bi and Al) and DPA–Fe_2O_3, (ii) investigate and compare the performance of the as–prepared catalysts for BPA removal *via* PMS activation, and (iii) develop a kinetic model based on the mechanistic consideration of various influencing parameters (i.e. pH, PMS dosage and catalyst loading) to describe the BPA degradation. In the kinetic modelling study, the intrinsic rate constant, k_i, was calculated explicitly from the

experimentally–derived BPA degradation at various time intervals and it was compared with the pseudo first–order rate constant (k_{app}) to obtain new insights into the use of heterogeneous transition metal catalyst for pollutant removal *via* PMS activation.

4.2. Experimental

4.2.1. Chemicals

All the chemicals used in this study were of analytical grade. The chemicals used were as follow: $Cu(NO_3)_2 \cdot 3H_2O$ (QrëC), $Co(NO_3)_2 \cdot 6H_2O$ (Alfa Aesar), $Mn(NO_3)_2 \cdot 4H_2O$ (Sigma–Aldrich), $Fe(NO_3)_3 \cdot 9H_2O$ (Merck), $Bi(NO_3)_3 \cdot 5H_2O$ (Alfa Aesar), $Al(NO_3)_3 \cdot 9H_2O$ (Sigma–Aldrich), NaOH (Alfa Aesar), HCl (Merck), acetonitrile (Merck), citric acid (Merck), ammonia (Hach), KI (Fisons), PMS (in the form of Oxone®, $2KHSO_5 \cdot KHSO_4 \cdot K_2SO_4$, Alfa Aesar), NaCl (Qrëc™), $NaNO_3$(Sigma–Aldrich), humic acid (HA, Aldrich), $NaHCO_3$ (Sigma–Aldrich), polyethylene glycol (Sigma–Aldrich), sodium acetate (Sigma–Aldrich), BPA (Merck) and methanol (Merck). All the experiments were conducted using deionized (DI) water (18.2 MΩ cm).

4.2.2. Synthesis of catalysts

The $CuFe_2O_4$–Fe_2O_3 catalyst was prepared using a facile co–precipitation method at low temperature. In a typical synthesis procedure, metal precursors consisting of 5 mmol of $Cu(NO_3)_2 \cdot 3H_2O$ and 10 mmol of $Fe(NO_3)_3 \cdot 9H_2O$ were dissolved in 50 mL of DI water and pH of the solution mixture was adjusted to pH 10–11 using 6 M NaOH under rapid magnetic stirring. Then, the resultant solution was heated under vigorous stirring at 95°C for 24 h to promote hydrolysis and the formation of

$CuFe_2O_4$–Fe_2O_3 catalyst. The resultant brownish product was separated from the solution by a simple magnetic separation procedure and freeze–dried for 24 h. Several other catalysts, namely $CuAl_2O_4$, $CuBi_2O_4$, $CuFe_2O_4$, $MnFe_2O_4$, $CoFe_2O_4$ and DPA–Fe_2O_3 were also prepared for performance comparison with $CuFe_2O_4$–Fe_2O_3. The $CuAl_2O_4$ was prepared *via* a sol–gel method (Kwak et al., 2012). The $CuBi_2O_4$ was prepared *via* a low–temperature co–precipitation method. The XFe_2O_4 (X = Mn, Fe and Co) was prepared *via* a solvothermal method (Deng et al., 2007). The details of the synthesis procedures for preparing ferrospinels (YFe_2O_4, Y = Cu, Co and Mn) and Cu–based spinels (CuX_2O_4, X = Bi and Al) are presented in **Appendix 1**.

4.2.3. Characterization techniques

The crystallographic and mineralogical information of the as–prepared catalysts was obtained using a X–ray diffractometer (Bruker AXS D8 Advance) operated at 40 kV and 40 mA with a Cu–Kα (λ = 1.5418 Å) X–ray source. The surface morphology and EDX elemental distribution were studied by obtaining the electron micrographs and elemental mappings using a field emission scanning electron microscopy (FESEM, JEOL JSM–7600F) equipped with a energy dispersive X–ray spectroscope (EDX, Oxford Xmax80 LN_2 Free). The Fourier transform infrared (FTIR) spectra were obtained using a FTIR spectrometer (Perkin Elmer Spectrum GX). The Brunauer–Emmett–Teller (BET) specific surface areas of the catalysts were calculated from the N_2 adsorption–desorption isotherm analysis at 77 K (Quantachrome Autosorb–1 Analyzer).

4.2.4. Performance evaluation

Batch experiment was conducted to investigate the performance of the catalyst for BPA treatment *via* PMS activation. In a typical experimental procedure, a known amount of PMS was introduced into the reaction vessels containing 100 mL of 5 mg L^{-1} of BPA at 25°C. The pH of the solution was immediately adjusted to the desired pH (pH 4.5, 7.0 or 9.5). Then, a known amount of the catalyst was added into the solution to commence the catalytic reaction. At each time intervals, 2–mL aliquot was sampled from the reaction vessel to determine the BPA concentration. The collected aliquot was filtered using a cellulose acetate membrane filter and the catalytic reaction was quenched using methanol. The BPA concentration was determined from the calibration curve which was developed using a HPLC (Perkin Elmer, UV detector) as described in **Section 3.2.7**. The experimental parameters studied were the PMS dosage (0.18, 0.27 and 0.36 g L^{-1}), catalyst loading (0.05, 0.10 and 0.20 g L^{-1}) and initial pH (4.5, 7.0 and 9.5). At the end of the reaction time, the pH change of the solution with initial pH 4.5 was insignificant while for the initial pHs 7.0 and 9.5, the final pHs were 6.1 and 8.1, respectively, due to their unbuffered condition and the formation of acidic BPA intermediates such as organic acid. The PMS–to–pollutant molar ratio used in this study was comparable to other study (Yao et al., 2014). At the end of the reaction time, the total organic carbon and Cu leaching were also determined for selected experimental conditions. For the TOC determination, the samples were filtered and analyzed immediately without quenching with methanol. Investigation of the changes of PMS concentration over time was also conducted.

4.2.5. Analytical methods

The TOC and Cu ion measurements were conducted using a TOC Analyzer (Shimadzu ASI−V) and ICP−OES (PerkinElmer, Elmer Optima 2000DV), respectively. The point of zero charge (pH_{zpc}) of the catalyst was determined using the pH drift method as described by Lopez-Ramon et al. (1999) with slight modification. Briefly, a series of 30 mL of 0.01 mM of NaCl solution was prepared. Then, 0.09 g of the catalyst was added into the solutions and the pH of the solutions was adjusted to different values within pH 3−12 using 1 M NaOH or 0.1 M HCl. After 48 h, the pH of the solutions was measured again and the pH_{zpc} which is the point of which pH(initial) = pH(final) was determined from the intercept of ΔpH vs. pH(initial) plot. The PMS concentration was quantified using the iodometric method with the aid of a UV−Vis spectrophotometer. Briefly, 5 mL of sample was mixed with 1 g of KI and agitated vigorously for 30 min. Then, the sample mixture was analyzed using a UV−Vis spectrophotometer at λ_{max} = 353 nm and the PMS concentration were determined using a pre−developed calibration curve.

4.3. Results and discussions

4.3.1. Synthesis and characteristics of the as−prepared catalysts

The $CuFe_2O_4$–Fe_2O_3 catalyst was successfully prepared by employing an eco−friendly solvent− and surfactant−free co−precipitation method at low temperature. The $CuFe_2O_4$–Fe_2O_3 presents an improvement over the Fe_2O_3 catalyst due to the presence of Cu which can lead to the synergistic Cu and Fe coupling effect. For performance comparison, other catalysts, namely ferrospinels (YFe_2O_4,

Y = Cu, Co and Mn), Cu–based spinels (CuX_2O_4, X = Bi and Al) and DPA–Fe_2O_3, were also prepared using various synthesis methods encompassing solvothermal, sol–gel, hydrothermal and co–precipitation methods. **Figure 4.1** shows the XRD patterns and FTIR spectra of all the as–prepared catalysts. The XRD peaks of the $CuFe_2O_4$–Fe_2O_3 catalyst can be indexed to both $CuFe_2O_4$ spinel and Fe_2O_3 phases. Rietveld refinement analysis shows that the $CuFe_2O_4$–Fe_2O_3 catalyst has a compositional ratio (w/w) of 2 $CuFe_2O_4$ to 3 Fe_2O_3 (83% Fe(III), 17% Cu(II)). Based on the XRD patterns in **Figure 4.1a**, all the solvothermally–prepared ferrospinels are of single phase except for $CuFe_2O_4$ which has 20% w/w of Cu^0 attributed to the use of ethylene glycol which can act as a reducing agent (Li et al., 2014). The XRD pattern of $CuBi_2O_4$ can be indexed to the single phase $CuBi_2O_4$.

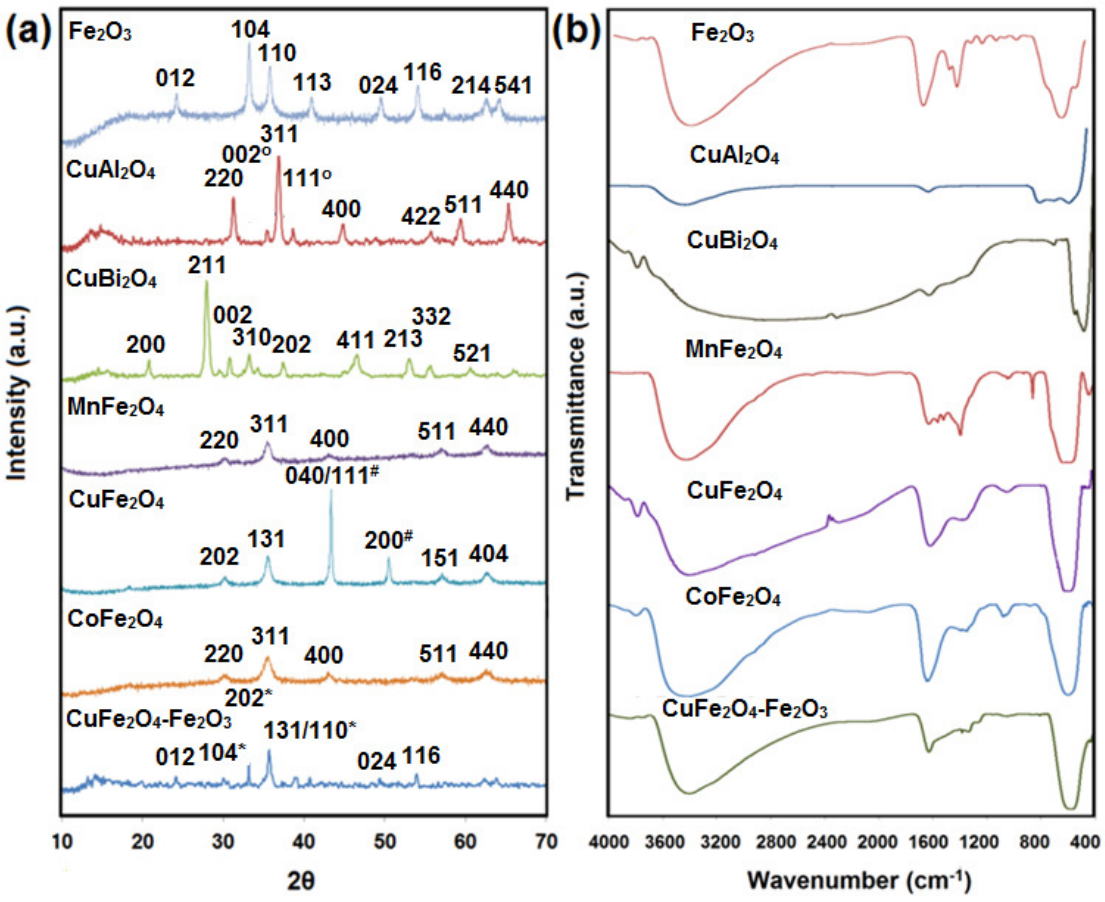

Figure 4.1. (a) XRD patterns, and (b) FTIR spectra of the as–prepared catalysts. * = Fe_2O_3, # = Cu and ° = CuO.

The XRD pattern of $CuAl_2O_4$ shows that additional peaks attributed to a small amount of CuO (~10% w/w by Rietveld refinement analysis) are also present. In all the FTIR spectra (**Figure 4.1b**), the broad band located at ~3400 cm^{-1} is indicative of the presence of surface hydroxyl functional groups. The surface hydroxyl group is partly responsible for enhancing the pollutant oxidation rate (Ren et al., 2015b; Zhang et al., 2010). The distinctive peak at 600 cm^{-1} in all the FTIR spectra is the characteristic Me–O bond.

The FESEM micrograph (**Figure 4.2d**) of $CuFe_2O_4$–Fe_2O_3 catalyst consists of quasi–cubic morphology with mean size of 100–200 nm. The EDX elemental mapping (**Figure 4.2e**) shows that Cu and Fe are homogeneously distributed on the surface at the ratio of 1 Cu to 5.5 Fe which is close to the theoretical ratio of 1 Cu to 5 Fe. This indicates the coexistence of $CuFe_2O_4$ and Fe_2O_3 phases in the cubic nanostructure. The BET result indicates that the $CuFe_2O_4$–Fe_2O_3 catalyst has a specific surface area of 63 $m^2\ g^{-1}$. As the synthesis of spinel $CuFe_2O_4$ was carried out at a relatively lower synthesis temperature than those reported in the literature, the elapsed–aging time was crucial for obtaining the desired morphology and crystallographic phase (Ding et al., 2013; Guan et al., 2013; Zhang et al., 2013b). To obtain insights into the formation of $CuFe_2O_4$–Fe_2O_3, the time–dependent FESEM micrographs and XRD patterns of $CuFe_2O_4$–Fe_2O_3 were obtained (**Figure 4.2**). The catalysts prepared at t = 3 and 5 h have magnetic property but their FESEM micrographs and XRD patterns indicate that they consist of relatively amorphous nanoparticles. The crystallinity of the nanoparticles was further improved by increasing the reaction time and at t = 24 h, the nanoparticles self–assembled to form quasi–cubic structure (**Figure 4.2c**). The increase in synthesis time for the low–temperature synthesis has also been reported to increase

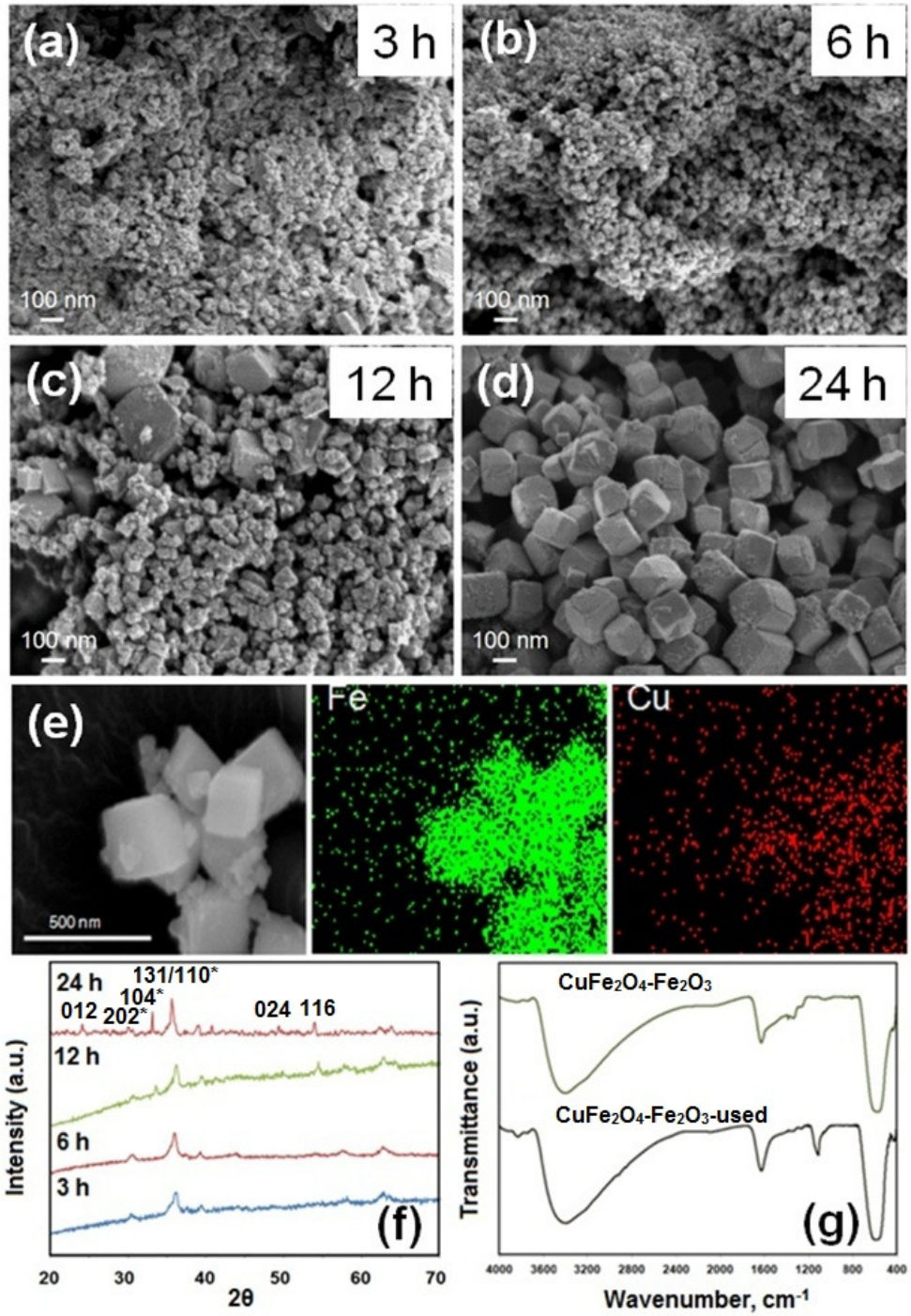

Figure 4.2. (a–d) Time dependent FESEM micrographs, (e) EDX elemental mappings, (f) time–dependent XRD patterns, and (g) pristine and used FTIR spectra of $CuFe_2O_3$–Fe_2O_3 catalyst.

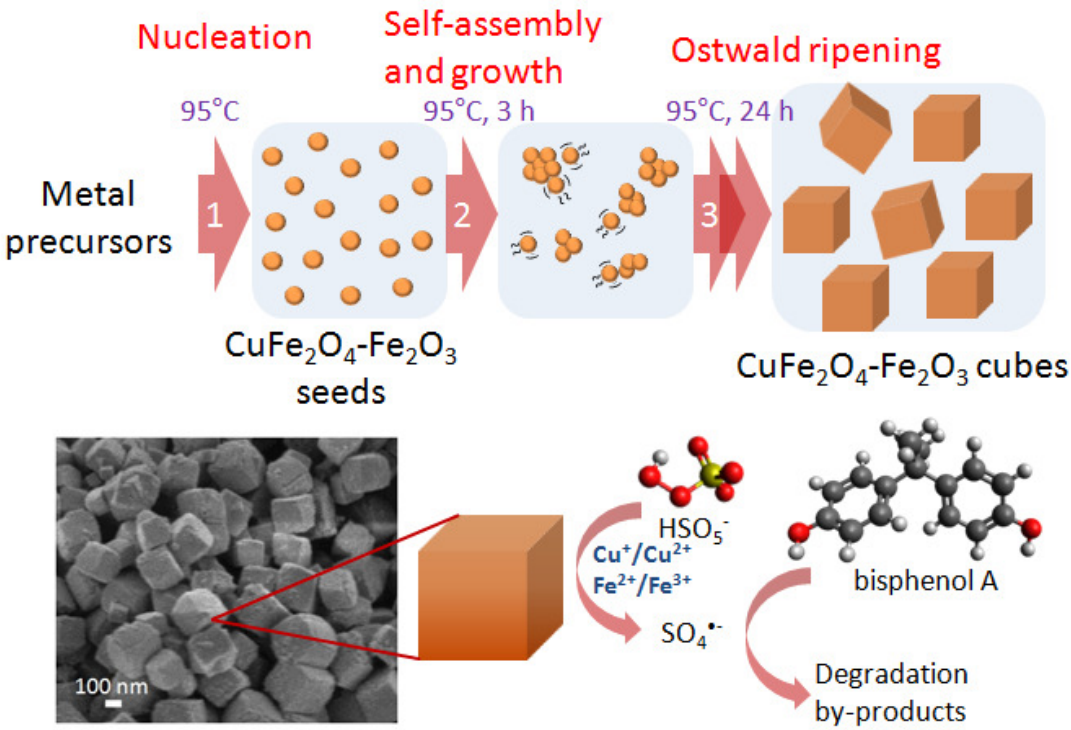

Figure 4.3. Schematic illustration of the low temperature $CuFe_2O_4$–Fe_2O_3 synthesis protocol. Nucleation of the $CuFe_2O_4$–Fe_2O_3 occurs when the metal precursor was subjected to 95°C under basic condition. The $CuFe_2O_4$–Fe_2O_3 nucleus proceeds to grow and self–assemble to form cubic microstructure.

the crystallinity of the material (Hu et al., 2014). The schematic illustration of the proposed $CuFe_2O_4$–Fe_2O_3 formation mechanism is shown in **Figure 4.3**.

All the other catalysts are of quasi–spherical morphology (**Figure A1a–e, Appendix**) except for $CuAl_2O_4$ which consists of irregular microparticles (**Figure A1f, Appendix**). The solvothermal synthesis protocol involving the use of surfactant results in materials with relatively higher specific surface area than the low temperature co–precipitation method due to the significant reduction in agglomeration of the materials prepared with surfactant (Chen et al., 2011). However, this occurs at the expenses of possible environmental pollution due to surfactant leaching during application (if the surfactant is not removed) and higher production cost. As described in **Chapter 3**, the employment of DPA for synthesis control using the low temperature co–precipitation method produced DPA-Fe_2O_3

with high surface area. However, $CuFe_2O_4$–Fe_2O_3 could not be formed in the presence of DPA possibly due to the complexation of Cu with DPA making it less available for co–precipitation.

4.3.2. Performance evaluation

4.3.2.1. Comparison of various catalysts

Figure 4.4 shows the performance comparison of various catalysts, namely $CuFe_2O_4$–Fe_2O_3, DPA–Fe_2O_3, CuX_2O_4 (X = Fe, Bi and Al) and YFe_2O_4 (Y = Cu, Co and Mn) for BPA degradation *via* PMS activation while **Table 4.1** shows the BET specific surface area, TOC removal, first–order rate constant (k_{app}) and Cu leaching for various catalysts. Comparison of the catalysts was made with respect to different synthesis methods (i.e. solvothermal $CuFe_2O_4$ vs. low temperature co–precipitation $CuFe_2O_4$) and different mixed metal oxide systems (i.e. CuX_2O_4

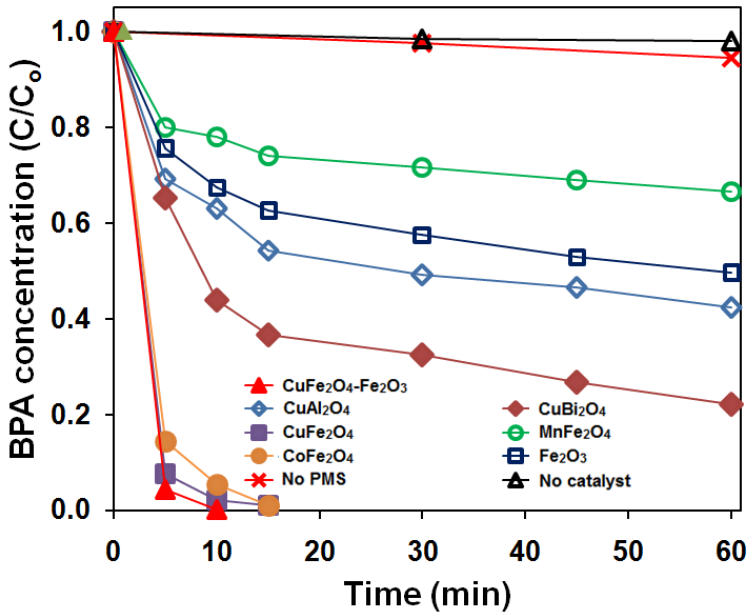

Figure 4.4. BPA degradation curves for different catalysts. Initial conditions: [pH] = 7.0±0.2, [PMS] = 0.36 g L^{-1}, [catalyst] = 0.2 g L^{-1}, and [BPA] = 5 mg L^{-1}.

Table 4.1. Synthesis method, BET specific surface area, TOC removal efficiency, Cu leaching and pseudo first−order rate constant (k_{app}) values for various catalysts.

Catalyst	Synthesis method	Specific surface area (m^2 g^{-1})	TOC removal efficiency at 30 min (%)	Cu leaching (mg L^{-1})	k_{app}
$CuFe_2O_4$–Fe_2O_3	low−temperature co−precipitation	63	24 (52)*	0.9 (<0.1%)	0.62±0.04
$CuFe_2O_4$	solvothermal	101	−23	0.7 (<0.1%)	0.52±0.02
$CuBi_2O_4$	low temperature co−precipitation	9	15	0.6 (<0.1%)	0.08±0.01
$CuAl_2O_4$	sol−gel	39	13	0.2 (<0.1%)	0.07±0.00
$MnFe_2O_4$	solvothermal	151	−12	−	0.04±0.00
$CoFe_2O_4$	solvothermal	139	−32	−	0.38±0.01
Fe_2O_3	low−temperature co−precipitation	188	11	−	0.05±0.00

(*) indicates TOC removal at t = 6 h.

(X = Fe, Bi and Al) and YFe_2O_4 (Y = Cu, Co and Mn)). The metal oxide catalysts contain transition metal (M^{n+}) which can activate PMS to produce $SO_4^{\bullet-}$ for degrading BPA through the following single electron transfer reaction:

$$M^{n+} + HSO_5^- \rightarrow M^{(n+1)+} + SO_4^{\bullet-} + OH^- \quad (4.3.2.1.1)$$

$$M^{(n+1)+} + HSO_5^- \rightarrow M^{+} + SO_5^{\bullet-} + H^+ \quad (4.3.2.1.2)$$

$$SO_4^{\bullet-} + BPA \rightarrow \text{degradation products} \quad (4.3.2.1.3)$$

There was no significant BPA removal (<5% in 30 min) by adsorption and direct PMS oxidation. The performances of $CuFe_2O_4$–Fe_2O_3 catalyst synthesized at 3, 6 and 12 h were almost similar to that of 24 h (**Figure A2a, Appendix**). However, the $CuFe_2O_4$–Fe_2O_3 synthesized at 24 h was selected for further performance evaluation as it was relatively more stable (less amorphous) with homogeneous morphology compared with the others. Several other PMS dosages were also investigated prior to the performance comparison study (**Figure A2b, Appendix**). The results in Table 4.1 shows that the type of metal species present in the catalyst (Cu+Fe>Co+Fe>Cu+Bi>Cu+Al>Fe>Mn+Fe) is more important for PMS

activation than the specific surface area. The activities of the catalysts were in the following order: $CuFe_2O_4$–Fe_2O_3> $CuFe_2O_4$> $CoFe_2O_4$> $CuBi_2O_4$> $CuAl_2O_4$> DPA–Fe_2O_3>$MnFe_2O_4$. The $CuFe_2O_4$–Fe_2O_3 catalyst performed better than all the other catalysts attributed to several factors, namely (i) its eco–friendly preparation method without using any organic precursor/solvent whose residue remaining in the resulting catalyst could reduce its catalytic activity, and (ii) a relatively more efficient synergistic metal coupling (Cu and Fe) in the metal oxide framework compared with other catalysts which has a promotional effect on the PMS activation (Guan et al., 2013; Ren et al., 2015b; Zhang et al., 2013b). The TOC removal efficiency for $CuFe_2O_4$–Fe_2O_3 was 24% but by prolonging the reaction time to 6 h, the TOC removal efficiency increased to 52%. The use of organic precursor/solvent (i.e. surfactant) for synthesis could result in having surface–bound organics which are difficult to remove without using extreme heat treatment. These surface–bound organics could compete for reaction with $SO_4^{\bullet-}$ and prevent the effective utilization of generated radicals for pollutant degradation. This phenomenon explains the lower catalytic performance of the solvothermally–prepared $CuFe_2O_4$ and $CoFe_2O_4$ (k_{app} = 0.52±0.02 and 0.38±0.01, respectively) compared with the $CuFe_2O_4$–Fe_2O_3 catalyst despite having higher surface area for catalysis. In addition, the degradation of the surface–bound organics has the tendency of causing unfavourable TOC leaching. This explains the observed negative TOC removal efficiencies when the $CuFe_2O_4$, $CoFe_2O_4$ and $MnFe_2O_4$ prepared by solvothermal method are employed as the catalyst for BPA treatment.

The redox transition between Cu(II)–Cu(I)–Cu(II) in the presence of PMS yields both $SO_5^{\bullet-}$ and $SO_4^{\bullet-}$. Compared to Cu(II), the Cu(I) species is relatively unstable and can be easily oxidized (e.g. by the dissolved oxygen). The Cu(I) can be

considered as the active species that reacts with PMS to produce $SO_4^{\bullet-}$. Considering the thermodynamic feasibility of the following reaction: Cu(I) + Fe(III) → Cu(II) + Fe(II) (E^o = +0.60 V), the Fe(III) species acts as an intermediate electron acceptor and reduces the amount of Cu(I) scavenged. In this regards, the $CuFe_2O_4$–Fe_2O_3 catalyst has an advantage over $CuFe_2O_4$ by having higher amount of Fe(III) which could decrease Cu(I) scavenging and maximize the production of $SO_4^{\bullet-}$ thus enhancing the BPA degradation rate. The Cu(II) is considered as the active species in $CuFe_2O_4$–Fe_2O_3 catalyst for PMS activation. As such, the Cu leaching for all the Cu catalysts were compared. The Cu leaching during PMS activation of $CuFe_2O_4$–Fe_2O_3 catalyst was comparable with that of the solvothermally–prepared $CuFe_2O_4$ ferrospinel (0.9 mg L^{-1} or 0.05% vs. 0.7 mg L^{-1} or 0.04%, respectively). The Cu leaching were lower than that of the US EPA standard for drinking water (1.3 mg L^{-1}). However, the $CuFe_2O_4$–Fe_2O_3 catalyst prepared with 3 h synthesis time exhibited 15.3 mg L^{-1} of Cu leaching or ~1% of the total catalyst weight loss. This further indicates that a relatively longer preparation time of 24 h is necessary to improve the crystallinity and stability of $CuFe_2O_4$–Fe_2O_3 catalyst for low temperature synthesis of the catalyst.

4.3.2.2. Effects of pH, catalyst loading and PMS dosage

Figures 4.5–4.7 show the influence of several key parameters, namely the pH, PMS dosage and catalyst loading on BPA removal. The pH_{zpc} of $CuFe_2O_4$–Fe_2O_3 was determined to be pH 7.6 (**Figure A2c, Appendix**). Generally, the removal efficiency and rate improve with increasing pH, PMS dosages and catalyst loading. The pseudo–first order kinetics was employed to model the BPA degradation rate. The calculated pseudo first–order rate constants (k_{app}) at different conditions are presented in **Table 4.2**. While the pseudo first–order fittings at pHs 7.0 and 9.5 are

Table 4.2. Kinetic parameters of $CuFe_2O_4$–Fe_2O_3 catalyzed BPA degradation *via* PMS activation at various conditions.

PMS dosage (g L^{-1})	**Catalyst loading (g L^{-1})**	k_{app}	R^2	k_i	k_i ***(calculated)***	k_{PMS}	R^2
pH 4.5							
0.18	0.05	0.031±0.002	0.19	6.07±1.2	-	0.22±0.04	0.996
	0.10	0.046±0.001	0.21	4.85±0.5	-	0.23±0.03	0.991
	0.20	0.13±0.01	0.95	2.15±0.1	-	0.050±0.003	0.999
0.27	0.05	0.043±0.003	0.47	3.85±0.0	-	0.15±0.01	0.998
	0.10	0.062±0.001	0.49	3.27±0.1	-	0.19±0.01	0.985
	0.20	0.17±0.01	0.83	2.13±0.0	-	0.07±0.01	0.999
0.36	0.05	0.067±0.001	0.49	4.59±0.0	-	0.15±0.00	0.997
	0.10	0.083±0.003	0.59	2.71±0.0	-	0.15±0.01	0.995
	0.20	0.23±0.02	0.90	1.98±0.0	-	0.06±0.02	0.996
pH 7.0							
0.18	0.05	0.11±0.01	0.99	4.98±0.4		0.02±0.01	0.996
	0.10	0.16±0.01	0.99	4.68±0.2		0.04±0.01	0.999
	0.20	0.46±0.04	0.98	4.13±0.1		0.004±0.002	0.999
0.27	0.05	0.14±0.01	0.96	4.18±0.1		0.016±0.002	0.999
	0.10	0.24±0.01	0.98	4.03±0.0		0.03±0.01	0.999
	0.20	0.53±0.07	0.91	5.43±0.1		0.11±0.02	0.999
0.36	0.05	0.14±0.01	0.90	4.16±0.2		0.043±0.001	0.999
	0.10	0.28±0.04	0.96	3.98±0.3		0.05±0.01	0.999
	0.20	0.62±0.04	0.99	4.00±0.0		0.002±0.001	0.999
pH 9.0							
0.18	0.05	0.33±0.01	0.97	17.05±0.		0.02±0.01	0.999
	0.10	0.56±0.01	0.88	16.70±0.		0.09±0.01	0.999
	0.20	0.69±0.02	0.91	12.88±1.		0.24±0.03	0.999
0.27	0.05	0.75±0.12	0.98	24.77±0.		0.11±0.07	0.999
	0.10	0.90±0.08	0.97	16.52±1.		0.18±0.13	0.999
	0.20	1.66±0.41	0.99	13.14±2.		0.17±0.08	0.999
0.36	0.05	0.90±0.08	0.93	32.88±1.		0.30±0.08	0.999
	0.10	1.23±0.04	0.98	16.54±1.		0.19±0.05	0.999
	0.20	1.41±0.11	0.99	13.71±1.		0.76±0.01	0.999

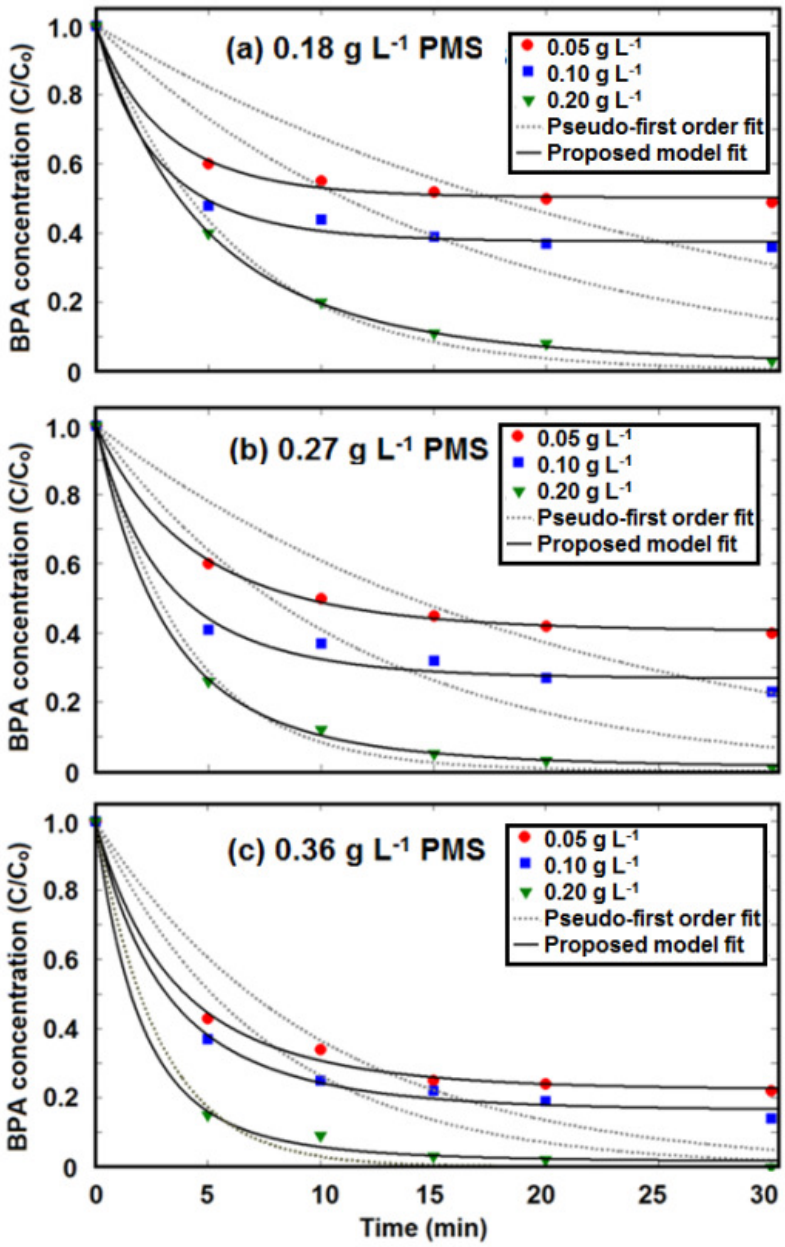

Figure 4.5. Experimental and calculated BPA degradation curves for different PMS dosages at various catalyst loadings. Initial conditions: [pH] = 4.5 and [BPA] = 5 mg L^{-1}.

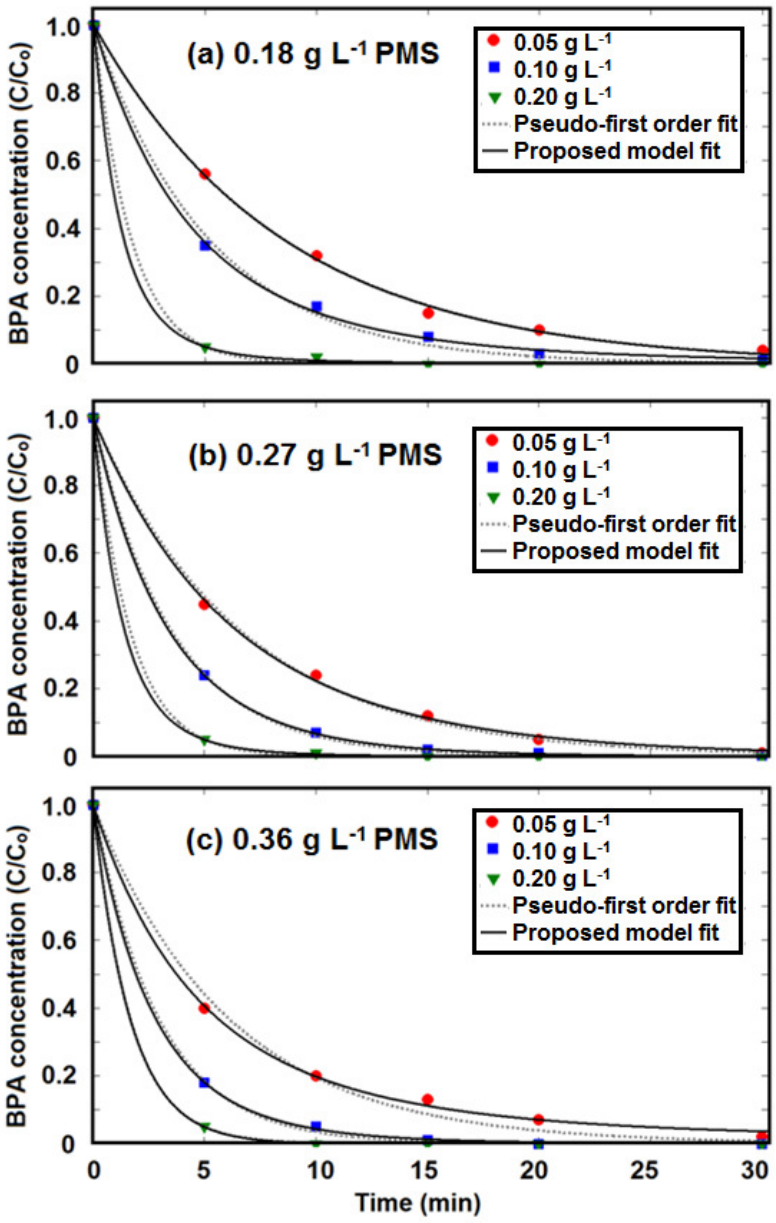

Figure 4.6. Experimental and calculated BPA degradation curves for different PMS dosages at various catalyst loadings. Initial conditions: [pH] = 7.0 and [BPA] = 5 mg L^{-1}.

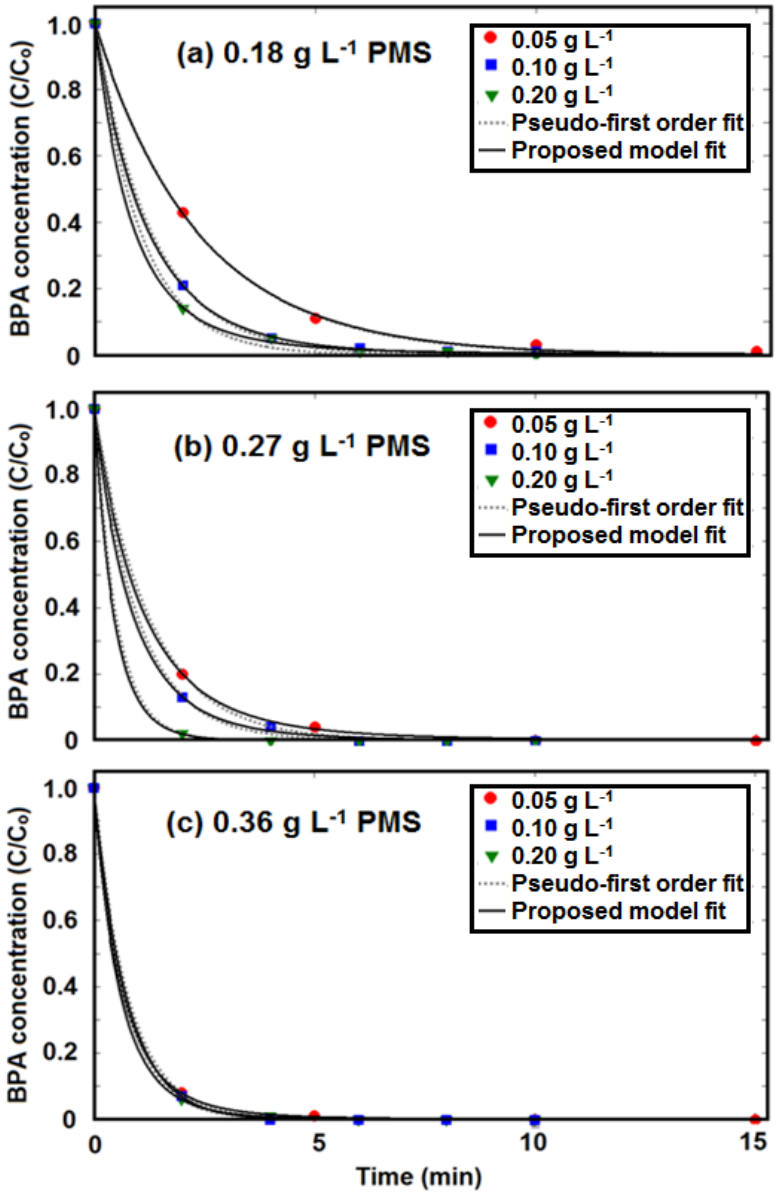

Figure 4.7. Experimental and calculated BPA degradation curves for different PMS dosages at various catalyst loadings. Initial conditions: [pH] = 9.5 and [BPA] = 5 mg L^{-1}.

generally good ($R^2 > 0.9$), the fitting at pH 4.5 is relatively poorer attributed to the oversimplification of the kinetic model which adopts a "black–box" approach. The pseudo first–order kinetics does not take into account the change of catalyst surface charge (**Eq. 4.3.2.2.1**) and possible attachment of the protons to the more electronegative peroxide bond of the PMS molecule (**Eq. 4.3.2.2.2**) at acidic pH which gives rise to the interfacial repulsion leading to the weaker catalytic performance:

$$[Cat - OH] + H^+ \leftrightarrow [Cat - OH_2^+] \quad (4.3.2.2.1)$$

$$SO_2–O–O–H + H^+ \rightarrow SO_2–O–O–H_2^+ \quad (4.3.2.2.2)$$

where [Cat–OH] and [Cat–OH_2^+] are the densities of active and deactivated catalytic sites, respectively. The catalyst surface contains many surface hydroxyl moieties which is important for PMS activation and surface protonation influences the density of surface hydroxyl moiety. The effect is particularly more pronounced at lower catalyst loading and PMS dosage.

To address the limitation of the pseudo first–order kinetics, a kinetic model based on the mechanistic consideration that the catalytic sites could be partially deactivated as a result of surface protonation is proposed in this study. At equilibrium condition, the thermodynamic equilibrium constant (K_{eq}) for **Eq. 4.3.2.2.3** can be expressed as follows:

$$K_{eq} = \frac{[Cat - OH]_o - [Cat - OH]}{[H^+][Cat - OH]} \quad (4.3.2.2.3)$$

where $[Cat–OH]_o$ is the catalyst loading. By incorporating the variables consisting of the catalyst loading and PMS dosage into the kinetic model, the rate of BPA removal can be given as follows:

$$\frac{d[\text{BPA}]}{dt} = -k_i[Cat-OH][\text{BPA}][\text{PMS}] \quad (4.3.2.2.4)$$

where k_i is the intrinsic reaction rate constant. Considering that the change of the [PMS] follows the first–order kinetics (**Figure A3, Appendix**) and by incorporating **Eq. 4.3.2.2.3** into **Eq. 4.3.2.2.4**, the kinetic model can be further simplified as follows:

$$\frac{d[\text{BPA}]}{dt} = -k_i \frac{[Cat-OH]_o}{(K_{eq}[H^+]+1)}[\text{BPA}][PMS]_o e^{-k_{PMS}t} \quad (4.3.2.2.5)$$

where k_{PMS} is the first–order rate constant for PMS consumption. **Eq. (4.3.2.2.5)** can be solved analytically to become **Eq. 4.3.2.2.6** by integrating with respect to t under the following initial conditions: at $t = 0$, [BPA] = $[\text{BPA}]_o$.

$$[\text{BPA}] = [BPA]_o e^{\frac{k_i}{k_{PMS}}\frac{[Cat-OH]_o}{(K_{eq}[H^+]+1)}[BPA]_0\left(e^{-k_{\text{PMS}}t}-1\right)} \quad (4.3.2.2.6)$$

Eq. (4.3.2.2.5) can be compared to the pseudo first-order kinetics. When the PMS is readily available for activation without significant influence by pH (first–order), the general relationship between k_{app} and k_i can be described by the following equation:

$$k_i = \frac{k_{app}\left(K_{eq}[H^+]+1\right)}{[Cat-OH]_o[PMS]_o} \quad (4.3.2.2.7)$$

However, because of the difference in the fitting procedure (with **Eq. 4.3.2.2.6** and pseudo-first order model), **Eq. (4.3.2.2.7)** can only be used to roughly estimate the k_i value from the k_{app} value. **Eq. 4.3.2.2.6** will be explicitly validated by fitting with the experimental–obtained BPA degradation results using Matlab and the kinetic parameters can be calculated by optimization using the nonlinear least square method. Preliminary fittings indicated that all the K_{eq} have the values close to 1.0. The K_{eq} = 1 indicates that neither the [Cat–OH_2^+] nor [Cat–OH] are favoured

species and the equilibrium is dependent on pH (i.e.: when $[H^+]$ is higher at acidic pH, the $[Cat–OH_2^+]/[Cat–OH]$ is higher). Therefore, K_{eq} was used as a constant for the kinetic modelling study.

Table 4.2 also shows the calculated kinetic parameters (from **Eq. 4.3.2.2.6**) consisting of k_i and k_{PMS} with their respective R^2. A relatively good fit can be observed for all cases (R^2>0.99) indicating that the kinetic model is able to account for the effect of different reaction pHs. In general, the trend of k_i value decreases linearly with increasing catalyst loading suggesting that the BPA oxidation reaction per unit catalyst proceeds slower at higher catalyst loading. It should be noted that k_i has been normalized with respect to the catalyst loading and PMS dosage. This was also observed previously for the k_i values calculated from **Eq. 4.3.2.2.7** in other heterogeneous PMS systems employing pseudo–first–order kinetics to model the pollutant degradation rate (Liu et al., 2015a; Tan et al., 2014). This observation could be due to the fact that PMS activation by $CuFe_2O_3–Fe_2O_3$ is a multi–step activation process generating both $SO_4^{\bullet-}$ and $SO_5^{\bullet-}$ for BPA degradation (**Eqs. 4.3.2.2.8–4.3.2.2.11**) (Ren et al., 2015b):

$$Cu(II) + HSO_5^- \rightarrow Cu(I) + SO_5^{\bullet-} + H^+ \quad (4.3.2.2.8)$$

$$Cu(I) + HSO_5^- \rightarrow Cu(II) + SO_4^{\bullet-} + OH^- \quad (4.3.2.2.9)$$

$$Fe(III) + HSO_5^- \rightarrow Fe(II) + SO_5^{\bullet-} + H^+ \quad (4.3.2.2.10)$$

$$Fe(II) + HSO_5^- \rightarrow Fe(III) + SO_4^{\bullet-} + OH^- \quad (4.3.2.2.11)$$

The catalyst consists predominantly of transition metal at higher oxidation state (i.e. Cu(II) and Fe(III)) which favours the generation of $SO_5^{\bullet-}$ as the initial major activation steps (**Eqs. 4.3.2.2.8–4.3.2.2.11**). When a higher catalyst loading is

employed, a higher amount of PMS is instantaneously converted to $SO_5^{\bullet-}$ first for BPA oxidation resulting in less PMS available for producing $SO_4^{\bullet-}$. The $SO_5^{\bullet-}$ is a considerably weaker radical than $SO_4^{\bullet-}$ which lowers the BPA degradation rate. While the redox reaction also produces Fe(II) which is critical for generating $SO_4^{\bullet-}$, excessive Fe(II) generated from $SO_5^{\bullet-}$ production at higher catalyst loading acts as a strong quencher for $SO_4^{\bullet-}$ (Brandt & Van Eldik, 1995; Rastogi et al., 2009):

$$Fe(II) + SO_4^{\bullet-} \rightarrow Fe(III) + SO_4^{2-} \ (k_{SO_4^{\bullet-}+Fe^{2+}} = 3 \times 10^8\ M^{-1}\ s^{-1}) \qquad (4.3.2.2.12)$$

As such, it can be construed that at a lower catalyst loading, the PMS can be utilized more efficiently for BPA degradation. All the k_i values at pH 9.5 are significantly higher than those at pHs 4.5 and 7.0 attributed to the production of $^{\bullet}OH$. At alkaline condition, synergistic BPA degradation by both $SO_4^{\bullet-}$ and $^{\bullet}OH$ occurs. No consistent trend for k_{PMS} can be observed which could be due to the complex interaction of PMS with different generated radicals (e.g.: $SO_4^{\bullet-}$, $^{\bullet}OH$, $SO_5^{\bullet-}$ etc.) (Balakrishnan & Kumar, 2000; Brandt & Van Eldik, 1995; Gimeno et al., 2009). The PMS can also react with both the BPA and its intermediates.

$$HSO_5^- + SO_4^{\bullet-} \rightarrow SO_5^{\bullet-} + SO_4^{2-} + H^+ \qquad (4.3.2.2.13)$$

$$(k_{SO_4^{\bullet-}+HSO_5^-} = 1 \times 10^5\ M^{-1}\ s^{-1})$$

$$HSO_5^- + {}^{\bullet}OH \rightarrow SO_5^{\bullet-} + SO_4^{2-} + H^+ \qquad (4.3.2.2.14)$$

$$(k_{{}^{\bullet}OH+HSO_5^-} = 1 \times 10^7\ M^{-1}\ s^{-1})$$

$$HSO_5^- + SO_5^{\bullet-} + H_2O \rightarrow SO_4^{\bullet-} + SO_4^{2-} + O_2 + H_3O^+ \qquad (4.3.2.2.15)$$

$$HSO_5^- + SO_5^{\bullet-} + H_2O \rightarrow {}^{\bullet}OH + 2SO_4^{2-} + O_2 + 2H^+ \qquad (4.3.2.2.16)$$

4.3.2.3. Effects of water matrix species

Figure 4.8 shows the effects of various water matrix species (Cl^-, NO_3^-, HCO_3^-, PO_4^{3-} and HA) on BPA degradation. The kinetic model (**Eq. 4.3.2.2.6**) was used to describe BPA degradation rate in the presence of different water matrix species. The calculated intrinsic rate constants, k_i (R^2>0.99), in the presence of various water matrix species are presented in **Figure 4.8b**. The concentrations of water matrix species were selected to resemble the typical characteristics of wastewater.

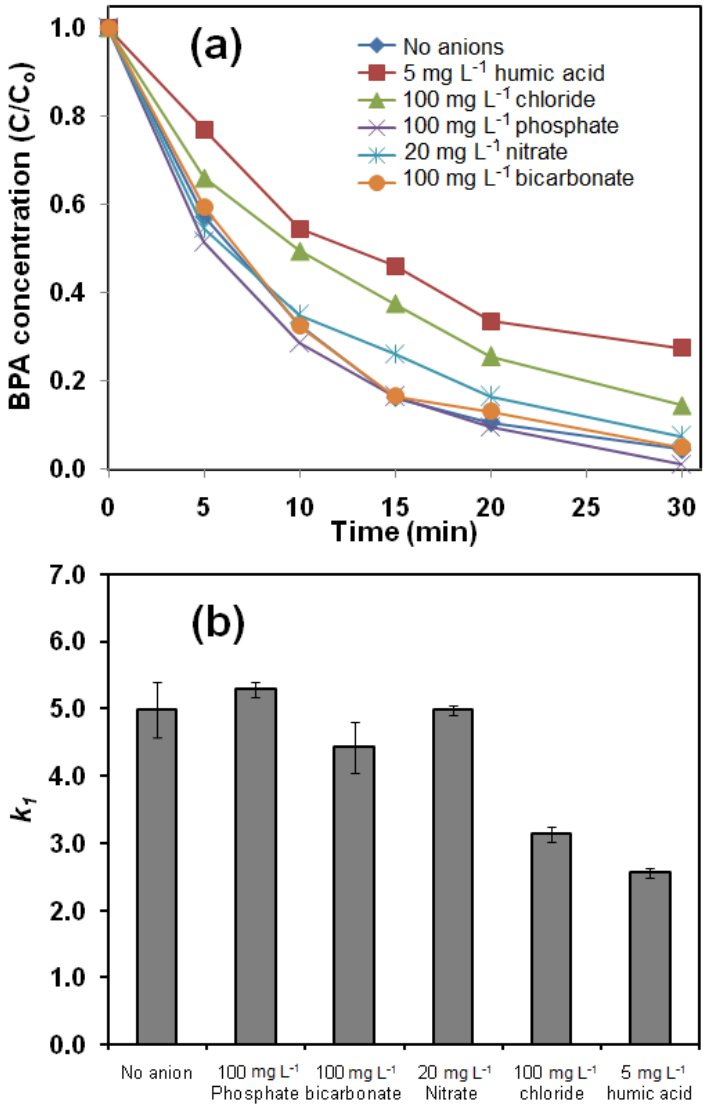

Figure 4.8. (a) Effects of different water matrix species on the BPA degradation and (b) k_i values. Initial conditions: [pH] = 7.0, [PMS] = 0.18 g L^{-1}, [catalyst] = 0.05 g L^{-1}, and [BPA] = 5 mg L^{-1}.

The presence of Cl^- and HA exert significant negative impact while the NO_3^-, HCO_3^- and PO_4^{3-} anions have negligible impact on the BPA degradation. It is known that the Cl^- anion could quench the generated $SO_4^{\bullet-}$ to produce weaker radicals ($Cl^\bullet$ and $Cl_2^{\bullet-}$ as shown in Eqs. 4.3.2.3.1–4.3.2.3.2, respectively) and HClO (Wang et al., 2011b) while HA consumes PMS and competes with BPA for the reactive $SO_4^{\bullet-}$ and PMS (Eqs. 4.3.2.3.3–4.3.2.3.4) thus retarding the BPA degradation reaction. Moreover, HA can also foul the catalyst leading to the deactivation of the catalytic active sites for PMS activation (Chaplin et al., 2006).

$$Cl^- + SO_4^{\bullet-} \rightarrow Cl^\bullet + SO_4^{2-} \left(k_{SO_4^{\bullet-}+Cl^-} = 3 \times 10^8\ M^{-1}\ s^{-1}\right) \quad (4.3.2.3.1)$$

$$Cl^- + Cl^\bullet \rightarrow Cl_2^{\bullet-} \left(k_{Cl^\bullet+Cl^-} = 8 \times 10^9\ M^{-1}\ s^{-1}\right) \quad (4.3.2.3.2)$$

$$\text{Humic acid} + HSO_5^- \rightarrow \text{by–products} + SO_4^{2-} \quad (4.3.2.3.3)$$

$$\text{Humic acid} + SO_4^{\bullet-} \rightarrow \text{by–products} + SO_4^{2-} \quad (4.3.2.3.4)$$

Previous report has indicated that PO_4^{3-} anion at natural pH can induce the formation of $SO_4^{\bullet-}$ from PMS which could have a positive effect on BPA degradation (Lou et al., 2014). However, a higher PO_4^{3-} concentration (up to 9 g L^{-1}) than that used in this study (100 mg L^{-1}) is required to have a significant effect. The HCO_3^- anion is a strong $SO_4^{\bullet-}$ and $^\bullet OH$ quencher (**Eqs. 4.3.2.3.5–4.3.2.3.6**) and previous study has reported that it could induce detrimental effect to the BPA degradation rate (Sharma et al., 2015). However, this phenomenon was not observed in this study due to the use of a lower HCO_3^- concentration in this study.

$$HCO_3^- + SO_4^{\bullet-} \rightarrow SO_4^{2-} + CO_3^{\bullet-} + H^+ \quad (4.3.2.3.5)$$

($k_{SO_4^{\bullet-}+HCO_3^-}$ = 1.6 x 10^6 M^{-1} s^{-1})

$HCO_3^- + {}^{\bullet}OH \rightarrow CO_3^{\bullet-} + H_2O$ ($k_{^{\bullet}OH+HCO_3^-}$ = 8.5 x 10^6 M^{-1} s^{-1}) (4.3.2.3.6)

4.3.3. Catalyst stability and reusability

Figure 4.9 shows the reusability of $CuFe_2O_3$–Fe_2O_3 for BPA removal *via* PMS activation over 3 cycles. After 3 consecutive cycles, the rate of BPA removal decreased slightly. This could be due to the adsorption of BPA degradation intermediates on the catalyst surface, as evidenced by the presence of an additional absorbance band at 1000 cm^{-1} in the FTIR spectra of the used catalyst (**Figure 4.2g**) which could be attributed to C–O stretching of the aromatic ring. After simple washing and drying, the catalyst can be reused with no significant difference in the performance indicating that the low temperature synthesis method could produce a stable, efficient and easily regenerable catalyst for generating $SO_4^{\bullet-}$ from PMS.

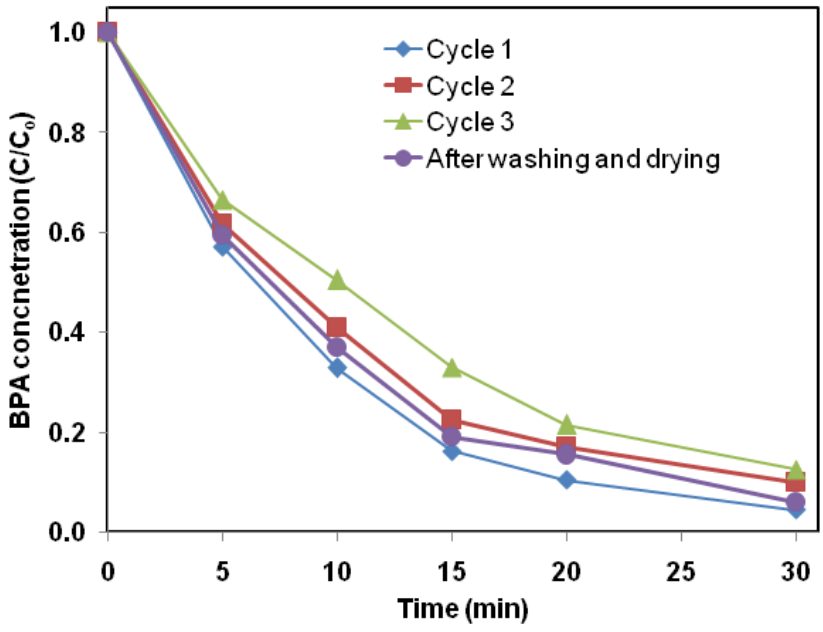

Figure 4.9. Reusability of the $CuFe_2O_3$–Fe_2O_3 catalyst. Initial conditions: pH = 7.0, [PMS] = 0.18 g L^{-1}, [catalyst] = 0.05 g L^{-1}, and [BPA] = 5 mg L^{-1}.

4.4. Conclusions

The $CuFe_2O_3$–Fe_2O_3 catalyst was successfully synthesized *via* an eco–friendly co–precipitation protocol at low temperature to generate $SO_4^{\bullet-}$ from PMS for BPA removal. The mechanism of formation of $CuFe_2O_3$–Fe_2O_3 at low temperature is proposed. The $CuFe_2O_3$–Fe_2O_3 catalyst performed significantly better than other catalysts, namely ferrospinels (YFe_2O_4, Y = Cu, Co and Mn), Cu–based spinels (CuX_2O_4, X = Bi and Al) and DPA–Fe_2O_3. This attributes to the $CuFe_2O_3$–Fe_2O_3 preparation method which uses no organic precursors, and efficient synergistic redox coupling between Cu(II) and Fe(III). A kinetic model was developed based on the mechanistic consideration of the influences of various operating parameters, namely pH, PMS dosage and catalyst loading. The proposed mechanistic kinetic model can fit relatively better than the pseudo–first order kinetics, which does not take into consideration the pH–dependent surface–charge effect. The relationship between the pseudo first–order rate constant (k_{app}) and the intrinsic rate constant (k_i) was established. The presence of Cl^- and HA in the solution could significantly affect the BPA degradation rate.

CHAPTER 5: HIERARCHICALLY–STRUCTURED $CuBi_2O_4$ WITH PEROXYMONOSULFATE AND PERSULFATE ACTIVATION FUNCTIONALITIES FOR BENZOTRIAZOLE REMOVAL

5.1. Introduction

Benzotriazole (BTZ) is a highly soluble (28 g L^{-1} in water) and polar heterocyclic compound with a benzo–fused azole moiety. BTZ is produced in large quantity for applications in the automotive industry (antifreeze agent), aviation industry (de–icing fluid), as corrosion inhibitor, as part of formulation in fluids for brakes and metal–cutting and industrial cooling systems (Matamoros et al., 2010). BTZ is biologically active and has both estrogenic and anti–estrogenic effects on aquatic life (Briguglio et al.; Liang et al., 2014). Due to its ubiquitous use and recalcitrant nature, BTZ has been detected in the surface water (Ni et al., 2008; Voutsa et al., 2006). BTZ is toxic and resistant to biodegradation. The current conventional wastewater treatment plants (e.g.: activated sludge) have difficulty in removing BTZ from water (Vel Leitner & Roshani, 2010). Previously, several studies have been conducted to evaluate BTZ removal efficiency from water using sorption, photoelectro–fenton process, ozone treatment, and photocatalysis (Ruhl et al., 2014; Vel Leitner & Roshani, 2010; Wu et al., 2013; Xu et al., 2013). Although sorption process is effective, the spent sorbent creates a secondary waste problem. Photoelectro–fenton process, ozone treatment and photocatalysis rely on the generation of hydroxyl radicals ($^{\bullet}OH$) for effective BTZ degradation. To date,

reports on the treatment of BTZ *via* generation of reactive radicals by SR–AOPs are lacking. Comparing $^{\bullet}OH$ with $SO_4^{\bullet-}$, $SO_4^{\bullet-}$ is more stable, selective and has a relatively longer lifetime (10^{-3} vs. 30–40 μs) thus allowing better utilization of the generated radicals for BTZ degradation (Sun et al., 2014).

As established in previous chapters, the redox reaction of PMS with transition metal catalyst (e.g.: Co(II), Fe(III), Cu(II) etc.) produces reactive $SO_4^{\bullet-}$ for pollutant degradation (**Eqs. 5.1.1–5.1.2**). Similarly, redox reaction between PS and transition metal (Fe^0, Fe(II)) catalyst also produces $SO_4^{\bullet-}$. However, PS reaction generating $SO_4^{\bullet-}$ is a one way reaction and the catalyst is consumed during the treatment process (**Eq. 5.1.3**).

Transition metal (M) activation of PMS

$$HSO_5^- + M^{n+} \rightarrow M^{(n+1)+} + SO_4^{\bullet-} + OH^- \quad (5.1.1)$$

$$HSO_5^- + M^{(n+1)+} \rightarrow M^{n+} + SO_5^{\bullet-} + H^+ \quad (5.2.2)$$

Transition metal (M) activation of PS

$$S_2O_8^{2-} + M^{n+} \rightarrow M^{(n+1)+} + SO_4^{\bullet-} + SO_4^{2-} \quad (5.3.3)$$

In a recent study, Zhang et al. (2014b) reported that PS can be activated by heterogeneous Cu(II) catalyst to produce reactive species (not radical) which is not as reactive as $SO_4^{\bullet-}$. The heterogeneous Cu(II) catalyst has also been reported as a PMS activator (Ji et al., 2011).

As presented in **Chapter 4**, the mixed metal oxide catalyst has a clear advantage over the single metal oxide catalyst. One of the most distinct advantages of mixed metal oxide catalyst is that it is polyfunctional. An attractive polyfunctional mixed metal oxide catalyst that can potentially be used to activate both PMS and PS is

$CuBi_2O_4$. The $CuBi_2O_4$ mixed metal catalyst have high surface hydroxyl groups that are capable of enhancing the PMS and PS activation reactions. It has also been reported that $CuBi_2O_4$ and its composites can be employed for various applications including photoelectrochemical application (Arai et al., 2007a; Hahn et al., 2012; Wang et al., 2015a), water splitting (Berglund et al., 2013; Nakabayashi et al., 2014; Park et al., 2014; Patil et al., 2014), electrochemical capacitors (Aref et al., 2015), and photocatalysis (Abdelkader et al., 2015; Abdelkader et al., 2012; Arai et al., 2007b; Deng et al., 2013a; Deng et al., 2013b; Elaziouti et al., 2015; Muthukrishnaraj et al., 2015; Nishikawa et al., 2013; Wei et al., 2010; Xie et al., 2013; Zhang et al., 2013c). Since most catalysts used for PMS activation are not efficient when use for PS activation and *vice versa*, this provides an attractive avenue to develop a bi-functional $CuBi_2O_4$ catalyst that can activate both PMS and PS efficiently. Compared to DPA–Fe_2O_3 and $CuFe_2O_4$–Fe_2O_3 which are relatively inert towards PS, $CuBi_2O_4$ can be deliberately designed to activate both PMS and PS.

In the study described in this chapter, a facile hydrothermal synthesis method was employed to prepare $CuBi_2O_4$ catalyst with novel three–dimensional morphology (3D) of spherical nanocolumn arrays. The catalyst was further modified by deliberately increasing the Cu(II) content during synthesis to produce a bi–functional catalyst which can activate both PMS and PS efficiently for BTZ removal. The mechanisms of PMS/PS activation by the bi–functional $CuBi_2O_4$ catalyst are proposed. The effects of several operational parameters, namely initial BTZ concentration, catalyst loading and initial PMS/PS dosage were investigated. Additionally, the influence of chloride ion on BTZ degradation *via* PMS/PS activation was evaluated. The intermediate products of BTZ degradation *via* PMS/PS activation were also studied.

5. 2. Experimental

5.2.1. Chemicals

The chemicals used in this study were of analytical grade without further purification. The chemicals were $Cu(NO_3)_2.3H_2O$ (Qrëc™), $Bi(NO_3)_3.5H_2O$ (Alfa Aesar), HNO_3 (Merck), NaOH (Alfa Aesar), PMS in the form of Oxone® ($2KHSO_5 \cdot KHSO_4 \cdot K_2SO_4$, Alfa Aesar), $K_2S_2O_8$ (Sigma–Aldrich), methanol (Merck), NaCl (Qrëc™), KI (Fisons) and BTZ (Alfa Aesar). The Milli–Q ultrapure water with resistivity of 18.2 MΩ cm was used in all the experiments.

5.2.2. Synthesis

The catalysts were synthesized using a facile one–pot hydrothermal synthesis without using any template or surfactant. In a typical preparation procedure, 2 mmol of $Cu(NO_3)_2.3H_2O$ and 4 mmol $Bi(NO_3)_3.5H_2O$ were fully dissolved in 50 mL of 0.5 M HNO_3 while under stirring. Then, 25 mL of 2 M NaOH was slowly added into the solution while under stirring. The final pH was recorded to be pH 14. After rapid magnetic stirring for 1 h, the solution mixture was sealed in a 125–mL Teflon–lined stainless steel autoclave and heated in an oven at 200°C under autogeneous pressure for 12 h. The resultant brownish–black product was washed with DI water and dried in an oven at 60°C for at least 4 h. The effects of different synthesis conditions were studied by varying the synthesis temperature (140 – 200°C), Cu:Bi mol ratio of 1:2 – 3:2 and NaOH molarity (1–6 M). For comparison, the CuO catalyst was also synthesized using the above–mentioned hydrothermal protocols except without the addition of $Bi(NO_3)_3.5H_2O$.

5.2.3. Characterization techniques

The mineralogy and crystal structures of the as–prepared catalysts were analyzed using a X–ray diffractometer (Bruker D8 Advance XRD) operating on a high intensity Cu–Kα X–ray source at 40 kV and 40 mA. The catalyst samples were scanned from 10–90° at a scan rate of 0.05°/s. The morphological detail of the catalysts was examined using a field emission scanning electron microscope (FESEM, JEOL–7600F). The Brunauer–Emmet–Teller (BET) specific surface area was determined by analyzing the N_2 adsorption–desorption isotherm at 77 K (Quantachrome Autosorb–1 Analyzer). The X–ray photoelectron spectroscopy (XPS) measurement was conducted using a Phoibos 100 spectrometer equipped with a monochromatic Mg X–ray source (SPECS, Germany). The XPS data was calibrated against the adventitious C 1s peak at the binding energy of 284.8 eV. The Fourier transform infrared spectroscopy (FTIR, Perkin Elmer) was employed to investigate the surface functional group of the catalyst.

5.2.4. Performance study

The performances of the as–prepared catalysts were evaluated for the treatment of BTZ in a batch system at ambient temperature. In a typical experimental procedure, 100 mL of solution containing 2.5 mg L^{-1} of BTZ was added into a 250–mL reactive vessel. Then, a known amount of PS/ PMS was dissolved into the solution in the reaction vessel under rapid stirring. The pH was then immediately adjusted to pH 7 using 1 M NaOH. Under rapid stirring, the catalytic BTZ degradation study was initiated (t = 0 min) once 0.5 g L^{-1} of the catalyst was introduced into the reaction vessel. Sampling of the solution was conducted at various time intervals by drawing 1–mL of the aliquot from the reaction vessel and filtering using a

cellulose acetate filter to determine the BTZ concentration. Methanol was used to quench the reaction. The experiment was repeated by using different catalysts (i.e. selected catalysts prepared with different hydrothermal conditions). For PMS system, the experiment was repeated by varying the initial PMS dosage (0.05–0.20 g L^{-1}) and BTZ concentration (2.5–10.0 g L^{-1}). For PS system, the experiment was also repeated by varying the initial PS dosage (0.1–0.8 g L^{-1}) and catalyst dosage (0.5–2.0 g L^{-1}). Control experiments were carried out by repeating the above–mentioned protocols but (i) without catalyst, (ii) without oxidant, and (iii) without catalyst and oxidant. All the experiments were conducted in duplicate.

The total organic carbon (TOC), Cu leaching, degradation products and PMS/PS consumption were determined at the end of the reaction time (t_{PS} = 90 min, t_{PMS} = 10 min) at the following experimental conditions: for PMS, initial pH = 7.0, initial PMS dosage = 0.2 g L^{-1}, initial catalyst dosage = 0.5 g L^{-1}); for PS, initial pH = 7, initial PS dosage = 0.8 g L^{-1}, initial catalyst loading = 2.0 g L^{-1}. The TOC and Cu leaching experiment at the end of the reaction time was conducted without employing methanol as the quencher. For TOC experiment, the analysis was carried out immediately after the end of the reaction. The Cl^- can act as a radical scavenger for $SO_4^{\bullet-}$ with second–order rate constant of 3 x 10^{-8} M^{-1} s^{-1} (Padmaja et al., 1993). Therefore, it is an important water matrix species that could interfere and exert detrimental effect to the BTZ degradation (Anipsitakis et al., 2005a; Lutze et al., 2015b). The effects of Cl^- on BTZ degradation in the PMS and PS systems were investigated by conducting the BTZ oxidation reaction in the presence of Cl^- at various concentrations (0–500 mg L^{-1}). The steady–state [$SO_4^{\bullet-}$] concentration for the PMS system was estimated from the rate of $SO_4^{\bullet-}$ oxidation of benzene by conducting the catalytic experiment with benzene instead of BTZ. The

reusability of the catalyst was also evaluated up to three cycles for both PMS and PS systems to determine the stability of the catalyst.

5.2.5. Analytical methods

The BTZ concentration was determined using a high performance liquid chromatography (HPLC, Perkin Elmer) equipped with a UV detector at λ_{max} = 256 nm. The mobile phase consisted of methanol to ultrapure water ratio of 1:1 at the flow rate of 1 mL min^{-1} while the column used was a reverse phase HPLC column (Hypersil Gold). The TOC measurement was conducted by using a TOC analyzer (Shimadzu TOC analyzer). The PMS/PS concentration was determined by using the spectrophotometric method at λ_{max} = 352 nm. The Cu concentration was determined by using an inductively−coupled plasma−optical emission spectrometer (ICP−OES, Perkin Elmer Optima 2000DV).

The BTZ degradation products were identified using a Shimadzu LC−MS 8030 equipped with electrospray ionization (ESI) source in positive and negative modes. The N_2 gas was used as the nebulizing and drying gas at the flow rates of 3 and 15 L min^{-1}, respectively. The samples were injection *via* a flow injection analysis method and the injection volume was 10 µL at the flow rate of 0.2 mL min^{-1}. The mobile phase used was 1:1 ratio of methanol and ultrapure water, both with 0.1% v/v of formic acid. The heat block and DL temperatures were 400 and 250°C, respectively. The m/z was scanned from 50−400.

5.3. Results and discussions

5.3.1. Synthesis and characterization studies

Single phase tetragonal $CuBi_2O_4$ with space group *P4/ncc* was successfully synthesized by a facile one–pot hydrothermal synthesis route. The mechanism of formation of the $CuBi_2O_4$ during the hydrothermal reaction involves (i) the initial formation of $Cu(OH)_2$ and $Bi(OH)_3$, (ii) hydrolysis reaction, and (iii) lattice fusion of CuO and Bi_2O_3 forming $CuBi_2O_4$ nucleus (iv) anisotropic/isotropic growth of $CuBi_2O_4$ (Abdulkarem et al., 2011). **Figure 5.1** shows the schematic illustration of various synthesis conditions and their corresponding structures while **Figure 5.2** shows the FESEM micrographs of the $CuBi_2O_4$ prepared under various synthesis conditions. The $CuBi_2O_4$ with a near–perfect microspherical morphology can be

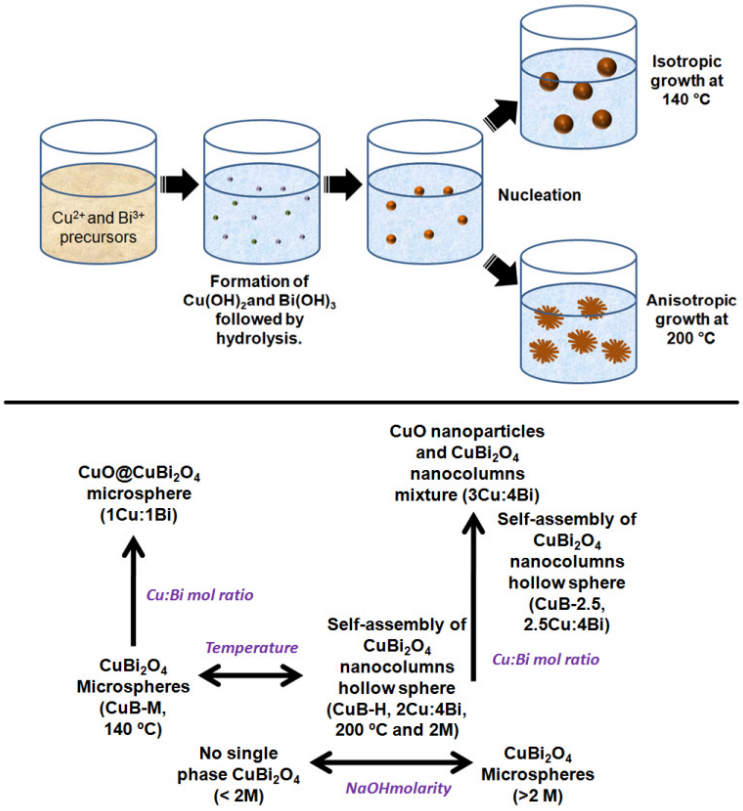

Figure 5.1. Schematic illustration of the synthesis conditions and their resulted morphologies.

easily formed at T = 140°C (CuB–M, diameter = 3–5 μm, **Figure 5.2a**). Control of the size of the microsphere can be achieved by decreasing or increasing the amount of metal precursors (**Figure A4a and d, Appendix**). Similarly, by increasing the Cu:Bi ratio, the average microsphere size can be reduced (**Figure A4d–f, Appendix**) but this resulted in the presence CuO impurity. Higher Cu:Bi ratio favors nucleation of $CuBi_2O_4$ but retards the growth of the nucleus.

By careful control of the reaction temperature and NaOH molarity, the microsphere morphology of the $CuBi_2O_4$ can be tailored to well–defined hierarchical three–dimensional (3–D) self–assembly of $CuBi_2O_4$ nanocolumn arrays (CuB–H, length = 1–1.5 μm, **Figure 5.2b**) with uniform distribution. Unlike the previous studies (Abdulkarem et al., 2011; Neta et al., 1977), which employed polyethylene glycol or introduced ethanol as a co–solvent for morphological control, the synthesis in this study was carried out without the use of any template or surfactant. The $CuBi_2O_4$ nanocolumns spontaneously self–assembled under high autogeneous pressure at 200°C achieving the lowest Gibbs free energy by forming a 3–D spherical nanocolumn arrays connected through non–covalent interactions. An incomplete self–assembly of CuB–H reveals a hollow core with an inner diameter of 1.5 μm (**Figure 5.2c**). The formation of a hollow core is due to the directional alignment of individual nanocolumns in an ordered fashion. The remarkable influence of Na^+ as structure–directing is evidenced when the 3–D structure could not be obtained with NaOH molarity > 2 M. Pure phase of $CuBi_2O_4$ could not be formed with NaOH molarity < 2 M which is attributed to the deficiency of OH^- to form $CuBi_2O_4$ (pH = 14). Xie et al. (2013) also reported the significance of controlling the NaOH molarity to obtain $CuBi_2O_4$ with leaf–like morphology for photocatalysis application.

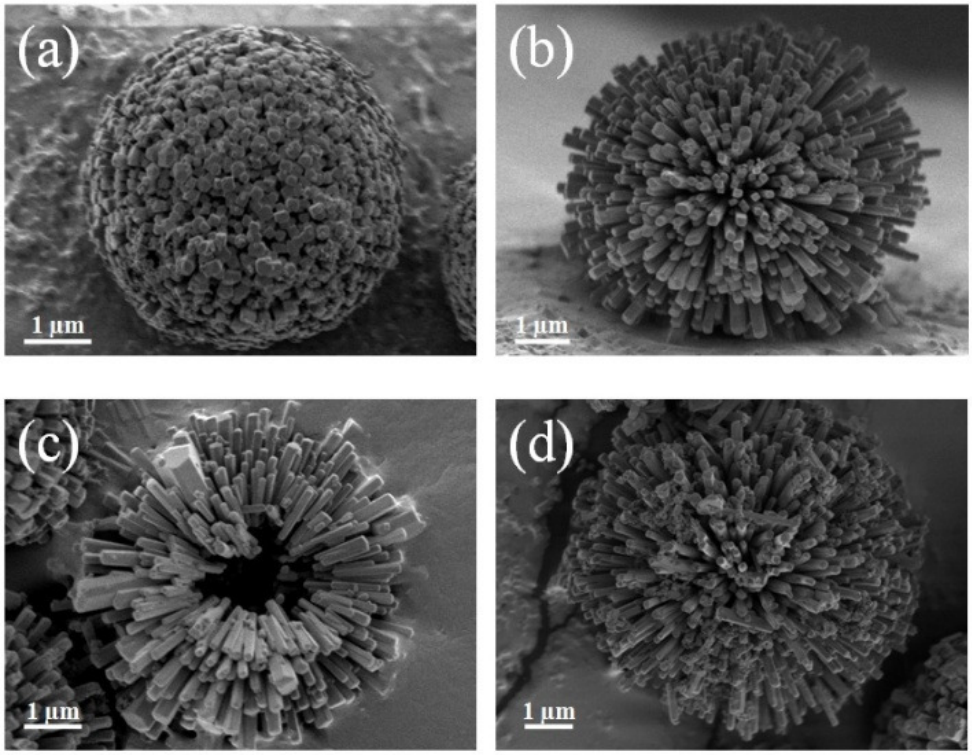

Figure 5.2. FESEM images of (a) CuB−M, (b) CuB−H, (c) incomplete self−assembled CuB−H and (d) CuB−2.5.

The Cu(II) transition metal plays an active role in the activation of PMS and PS (Ji et al., 2011; Liu et al., 2012). Since the main purpose was to develop an efficient catalyst with PMS and PS activation functionalities, the Cu:Bi ratio during synthesis was further elevated from stoichiometry ratio to 2.5:4 (denoted as CuB−2.5) with the intention to enhance the performance of the catalyst. Interestingly, the 3−D morphology of CuB−H could be retained in CuB−2.5. A small amount of sub−micron particles, most likely CuO (size = 20−30 nm), is anchored on the surface of the $CuBi_2O_4$ nanocolumns (**Figure 5.2d**) forming a composite−like structure. Further increment of the Cu:Bi ratio to 3:4 leads to the destruction of the 3−D microstructure resulting in a mixture of $CuBi_2O_4$ nanocolumns and CuO particles (**Figure A4c, Appendix**). This indicates that the optimum Cu:Bi ratio for retaining the morphology is 2.5 to 4.

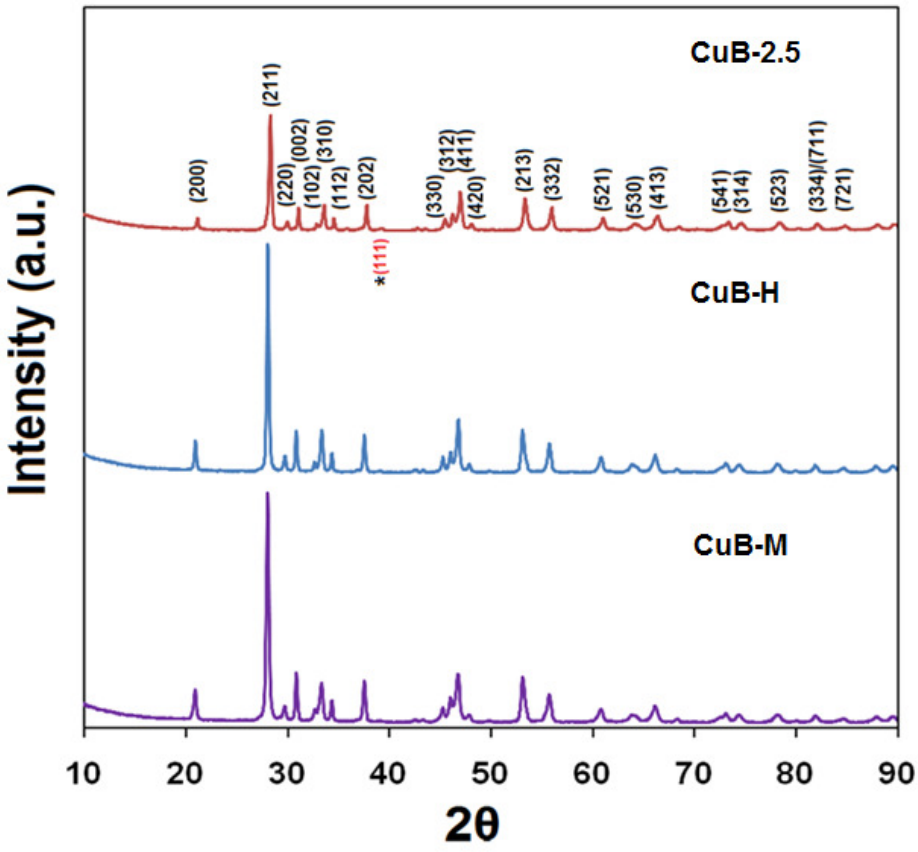

Figure 5.3. XRD patterns of CuB−M, CuB−H and CuB−2.5. The (*) indicates the location of the highest intensity (I/I_o) CuO peak.

Figure 5.3 shows the XRD patterns of the as−prepared CuB−M, CuB−H and CuB−2.5. All the peaks can be indexed to the pure $CuBi_2O_4$ phase (JCPDS file no. 84−1969). The XRD patterns in **Figure 5.3** confirm that the highly−crystalline single−phase $CuBi_2O_4$ was obtained for CuB−M and CuB−H. Due to the use of non−stoichiometric Cu:Bi ratio and the observation of the sub−micron nanoparticles in CuB−2.5, the XRD pattern of CuB−2.5 is expected to have CuO peaks. However, the XRD diffraction peak with the highest intensity belonging to the CuO at $2\theta = 41°$ ($I/I_o = 1$), which can be indexed to (111), is relatively weak. This could be attributed to the relatively low amount of CuO (maximum CuO = ca. 2.4% w/w based on 2.5:4 Cu:Bi ratio).

The diffraction peak intensities of CuB−2.5 are generally lower than those obtained for CuB−M and CuB−H which is due to the difference in X−ray scattering factor

of Cu and Bi. The lower peak intensities could also be an indicative of a doped material. It is postulated that aside from forming $CuO/CuBi_2O_4$ composite, the additional Cu in CuB−2.5 could also be interstitially doped into the crystal lattice to form non−stoichiometric $Cu_{1+x}Bi_{2-2x}O_{4-2x}$. Further analysis was conducted using Rietveld refinement of the XRD patterns. The results indicate that the composition of CuB−2.5 consists of $Cu_{1.2}Bi_{1.6}O_{3.6}$ with 2.4% w/w CuO which further supports the hypothesis. The refinement data for CuB−H and CuB−M shows 100% w/w $CuBi_2O_4$. The CuB−2.5 (18.7 $m^2\ g^{-1}$) exhibits the highest BET specific surface area compared with CuB−H (13.1 $m^2\ g^{-1}$) and CuB−M (4.4 $m^2\ g^{-1}$) allowing higher interacting area for catalysis. Besides improvement in the specific surface area, this strategy increases the overall Cu content from 14% in CuB−H and CuB−M to 20% in CuB−2.5 which is beneficial in enhancing the performance of the catalyst.

Figure 5.4 shows the FTIR and XPS spectra of CuB−2.5. The FTIR absorbance bands at 3300 and 1640 cm^{-1} give evidence of the stretching and bending vibrations, respectively, of absorbed water and also the presence of –OH group on the surface of CuB−2.5 (Faisal et al., 2011). A sharp peak is also observed at 550 cm^{-1} which corresponds to the characteristic peaks of CuO (Bo et al., 2014). The XPS spectra of CuB−2.5 in **Figure 5.4a−c** show that the main peaks for Cu 2p, Bi 4f and O1s are at binding energies 933.2, 159.2 and 530.4 eV, respectively, indicating that the oxidation states are Bi^{3+}, Cu^{2+} and O^{2-} (Berglund et al., 2013). The XPS peaks of Cu from CuO overlap with those from $CuBi_2O_4$. The binding energy of Cu for CuO is 933.7 eV (Klinbumrung et al., 2014) which is very close to 933.2 eV in this study. The oxidation states are in agreement with the theoretical oxidation states of the catalyst.

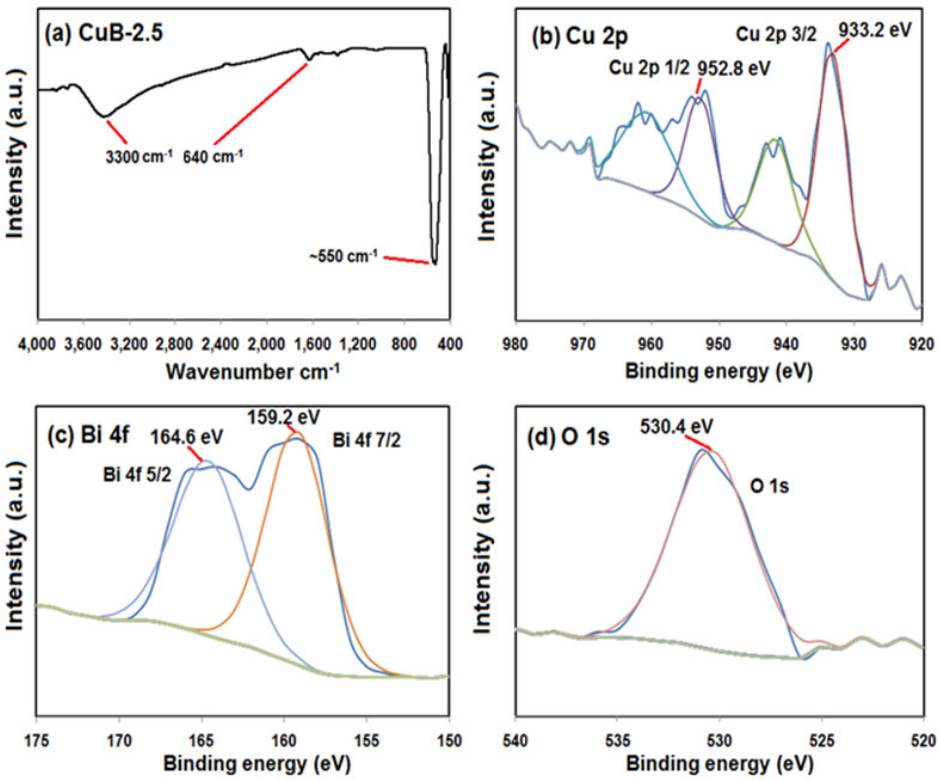

Figure 5.4. (a) FTIR spectrum of CuB−2.5, (b) XPS spectra of Cu 2p, (c) XPS spectra of Bi 4f and (d) XPS spectra of O 1s.

5.3.2. Performance evaluation

5.3.2.1. PMS and PS activation mechanisms

Three different $CuBi_2O_4$ catalysts, namely CuB−M, CuB−H and CuB−2.5, were selected for comparison. The catalysts have diverse potentials and advantages for multifunctional application in water treatment. Besides functioning as PMS and PS activators, this material can be tuned to become an efficient photocatalyst. Furthermore, the $CuBi_2O_4$ catalyst has high density and excellent settling velocity. It can be separated by gravity in less than 5 min without the need of advanced separation technique such as the membrane and magnetic separation technologies.

Preliminary study was conducted to evaluate the effect of pH for BTZ degradation (**Figure A5, Appendix**) and pH 7.0 was selected as an optimum pH due to (i) the

slower reaction rate at acidic pH and (ii) to avoid base activation of PS. The catalytic oxidation of BTZ by PMS and PS systems as shown in **Figure 5.5a and b**, respectively, in the preliminary study indicates that all the as−prepared CuB catalysts have PMS and PS activation functionalities. The catalytic oxidation is the main BTZ removal pathway as contributions due to adsorption and direct PMS/PS oxidation on BTZ removal were minimal. In general, the BTZ removal rate and efficiency in the PMS and PS systems were in the following order: Cu(II) < CuO < CuB−M < CuB−H < CuB−2.5. This is consistent with the TOC removal efficiencies in the PMS and PS systems in **Table 5.1** which indicate that the extent of mineralization is generally the highest when CuB−2.5 is employed as the catalyst. Judging from the relatively lower catalytic activity of CuO (0.20 g L^{-1}), which is at ~20 times the CuO loading found in CuB−2.5 (0.01 g L^{-1}), the main active species is $Cu_{1.2}Bi_{1.6}O_{3.6}$. A relatively lower TOC removal efficiency was observed for PS/CuB−M and PS/CuB−H systems. This suggests that the higher amount of Cu in the CuB−2.5 plays a prominent role in PS activation. Examination of the TOC removal in all the PMS/CuB systems indicated that only 17−18% of TOC was removed within 10 min but by prolonging the reaction time to 90 min, 52−54% of TOC removal efficiency and higher oxidant consumption were achieved. The better performance of CuB−2.5 over CuB−M and CuB−H is attributed to its higher specific surface area and Cu content.

The BTZ degradation rate (**Figure 5.5)** is further investigated using the pseudo first−order kinetics. The results indicate that the BTZ degradation in the PS/CuB−2.5 system (initial pseudo first−order rate constant for PS system, k_{app1} = 0.015±0.001 min^{-1}) is ~13 times slower than that in the PMS/CuB−2.5 system (initial pseudo first−order rate constant for PMS system, k_{app2} = 0.191±0.004 min^{-1}). This is anticipated because the PS activation process involves an outer

Table 5.1. Cu leaching, TOC removal, $[Oxidant]_{final}/[Oxidant]_o$, for the treatment of BTZ by the PMS and PS systems. Initial conditions: [BTZ] = 2.5 mg L^{-1}, [PS] = 0.8 g L^{-1}, [PMS] = 0.2 g L^{-1}, t_{PS} = 90 min and t_{PMS}= 10 min.

Catalyst	**[Catalyst] (g L^{-1})**	**Cycle**	**$[Oxidant]_{final}/[Oxidant]_o$**	**% TOC removal**	**Cu leaching (µg L^{-1} and %)**
PS					
t_{PS} = 90 min					
Cu(II) (aq)	0.002	1	0.97±0.03	9	–
CuO	2.0	1	0.82±0.02	59	6561(0.04%)
CuB–M	2.0	1	0.91±0.02	18	314 (0.01%)
CuB–H	2.0	1	0.91±0.01	21	134 (<0.01%)
CuB–2.5	2.0	1	0.85±0.01	48	505 (0.02%)
	2.0	2	0.91±0.02	42	–
	2.0	3	0.91±0.03	39	–
PMS					
t_{PMS} = 10 min					
Cu(II) (aq)	0.002	1	0.95±0.02	8	–
CuO	0.5	1	0.87±0.03	13	2572 (0.06%)
CuB–M	0.5	1	0.80±0.02	17 (52)*	6 (<0.01%)
CuB_H	0.5	1	0.79±0.03	18 (53)*	B.D.L
CuB–2.5	0.5	1	0.78±0.01	17 (54)*	57 (<0.01%)
		2	0.82±0.01	14 (44)*	–
		3	0.83±0.02	14 (45)*	–

B.D.L. = below detection limit (0.1µg L^{-1}), (*) = % TOC removal at t = 90 min.

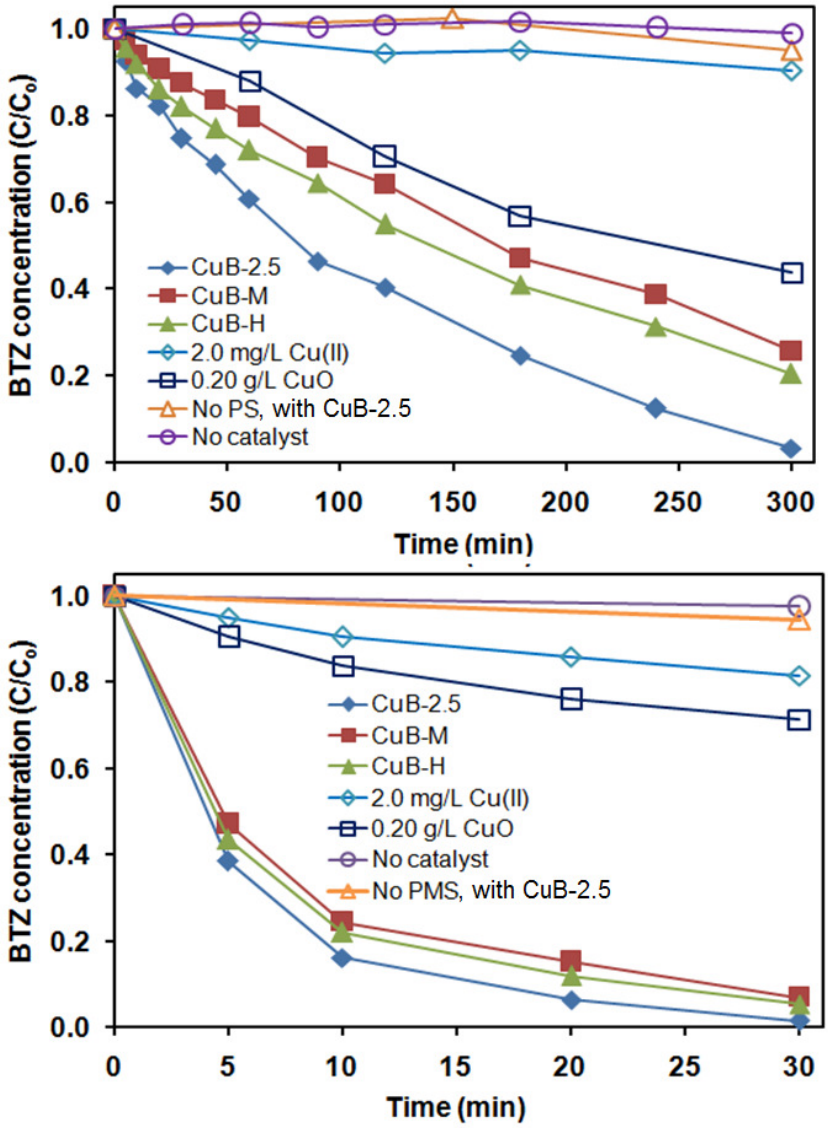

Figure 5.5. BTZ removal *via* (a) 0.1 g L^{-1} of PS and (b) 0.05g L^{-1} of PMS activated by various catalysts. Initial conditions: [catalyst] = 0.5 g L^{-1}, [BTZ] = 2.5 mg L^{-1}, and [pH] = 7.0.

orbital electron transfer reaction which produces reactive oxidizing species to attack the BTZ molecule. Previous report has indicated that the generated reactive radical was not $O_2^{\bullet-}$ or $SO_4^{\bullet-}$ and has a relatively lower reactivity than that of $SO_4^{\bullet-}$ (Zhang et al., 2014b).

It is postulated that the PS molecule can be activated by forming a PS–$CuBi_2O_4$ quasi–complex with specific reactive orientation on the reaction interface. A plausible reactive orientation is presented in **Figure 5.6**. In this orientation, the

reactive peroxide bond of PS is exposed making it more susceptible to oxidation and activation reactions compared with the unactivated PS. Based on the molecular structure of BTZ and PS, the intermolecular hydrogen bonding between BTZ and PS can play a key role in drawing the BTZ molecule to close proximity with the reaction interface. Then, the BTZ molecule could serve as an electron donor for subsequent degradation reaction.

$$S_2O_8^{2-} + Cu(II)Bi_2O_4 \leftrightarrow S_2O_8^{2-} - Cu(II)Bi_2O_4 \quad (5.3.2.1.1)$$

$$S_2O_8^{2-} - Cu(II)Bi_2O_4 + BTZ \rightarrow \text{degradation products} \quad (5.3.2.1.2)$$

On the other hand, the PMS activation process by CuB–2.5 is an inner sphere electron transfer reaction (Zhang et al., 2014b). The PMS molecules have to be in close proximity with the catalyst for redox reaction to occur (**Eqs. 5.3.2.1.3–5.3.2.1.4**) (Anipsitakis & Dionysiou, 2004; Anipsitakis et al., 2005b; Zhang et al., 2013b). This can be easily achieved by the interaction between PMS and surface –OH group on the reaction interface. The presence of Bi(III) could also increase the content of –OH group in view that the pH for the isoelectric point of Bi_2O_3 is 9.4 (Kosmulski, 2009). The role of surface –OH group has been highlighted by previous researchers (Ren et al., 2015b; Zhang et al., 2010). PMS is relatively easier to be activated compared with PS possibly due to the intramolecular hydrogen bonding of the PMS molecule exposing the peroxide (–O–O–) bond for homolytic cleavage reaction (**Figure 5.6**). The molecular structure of BTZ allows it to be drawn closer to the PMS through intermolecular hydrogen bonding which promotes BTZ oxidation within the vicinity of the catalyst. In addition, the surface –OH group can also form hydrogen bond with BTZ molecule and orientates the BTZ molecule to a planar direction favoring the attack of the electrophilic $SO_4^{\bullet-}$.

$$HSO_5^- + Cu(II) \rightarrow Cu(I) + SO_5^{\bullet-} + H^+ \quad (5.3.2.1.3)$$

$$HSO_5^- + Cu(I) \rightarrow SO_4^{\bullet-} + Cu(II) + OH^- \quad (5.3.2.1.4)$$

$$SO_4^{\bullet-} + BTZ \rightarrow \text{degradation products} \quad (5.3.2.1.5)$$

The intermolecular hydrogen bonding plays a significant role in the PMS and PS systems by (i) promoting mass transfer for BTZ degradation in the heterogeneous system, and (ii) maximizing utilization of the generated radicals. The positive role of hydrogen bond for pollutant degradation enhancement is also highlighted in other advanced oxidation systems (Vargas & Núñez, 2009). Due to the remarkable performance of CuB−2.5, it was selected for further evaluation.

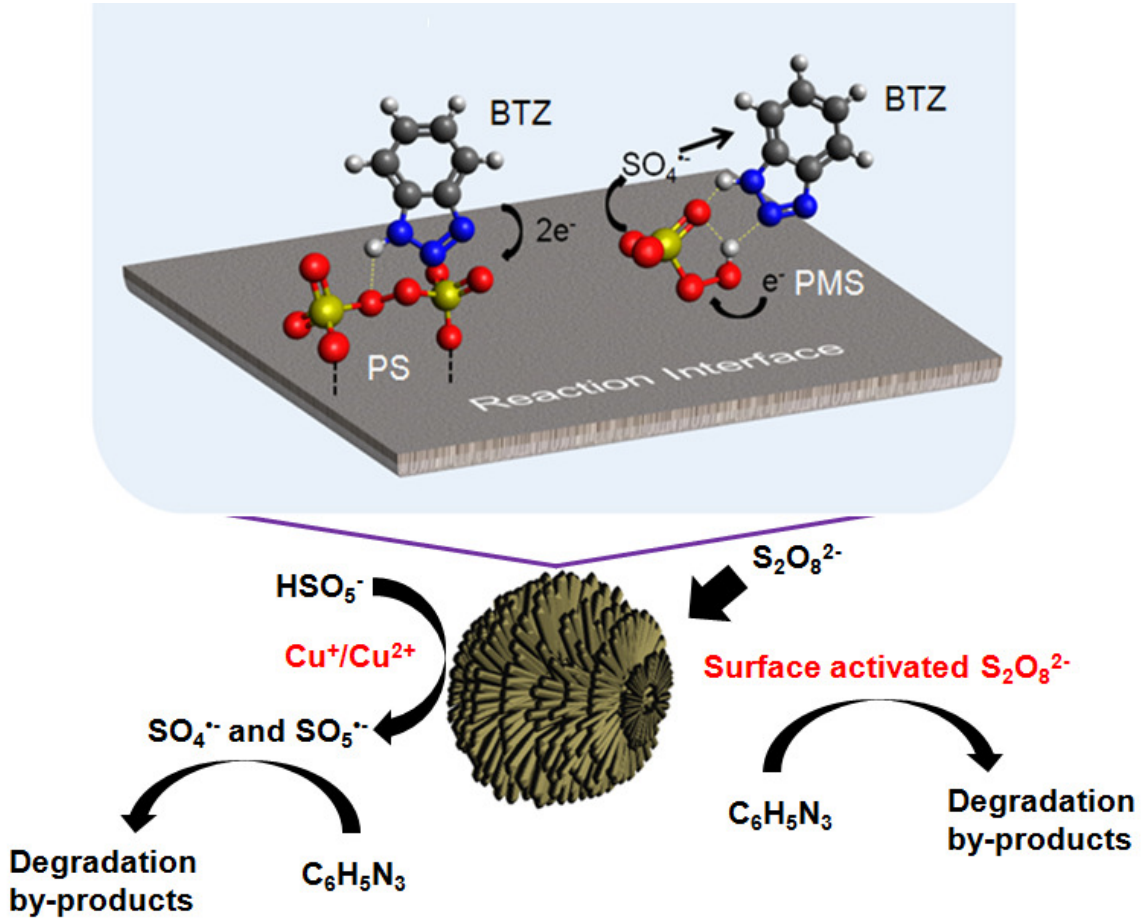

Figure 5.6. Schematic illustration of the mechanisms of PMS and PS activations by CuB−2.5 for BTZ degradation.

5.3.2.2. Parametric optimization study

5.3.2.2.1. PS/CuB−2.5 system

Figure 5.7a−c shows the effects of different PS dosages at various catalyst loadings. The BTZ removal rate, as characterized by the initial pseudo−first order rate constant, k_{app1}, increase linearly with increasing PS dosage and catalyst loading. However, the positive effect of increasing the PS dosage is marginal compared with increasing the catalyst loading. This provides an indirect evidence that the initial formation of the activated PS−Cu(II)Bi_2O_4 quasi−complex is an instantaneous reaction process. At a constant catalyst loading, rapid saturation of the reaction interface occurs immediately when sufficient PS is in contact with the catalyst. Because of the limited availability of active sites for reaction, the presence of excess amount of PS could not significantly enhance the BTZ removal rate. In this regards, the rate limiting step is the contact of BTZ with the established PS−Cu(II)Bi_2O_4 quasi−complex, which requires a specific steric orientation of the reacting functional groups to lead to the electron donation and degradation reactions. Kinetic analysis was further conducted to correlate k_{app1}, catalyst loading and PS dosage at pH 7.0 using the following kinetic expression:

$$-\frac{d[BTZ]}{dt} = k_{SD}[PS]_o^m[Cat]^n[BTZ] \qquad (5.3.2.2.1.1)$$

where k_{SD} is the specific rate constant and $[PS]_o$ and $[Cat]$ are the PS dosage and CuB−2.5 loading, respectively. By 3−D plotting of the experimentally−derived k_{app1} against [Cat] and $[PS]_o$ through a forced origin intercept (**Figure 5.8**) using MATLAB, the estimated values of m and n are 0.25 and 0.5, respectively, while the value of k_{SD} is 0.022 $g^{3/4}$ $L^{-3/4}$ min^{-1} (R^2 = 0.98). This clearly indicates that the

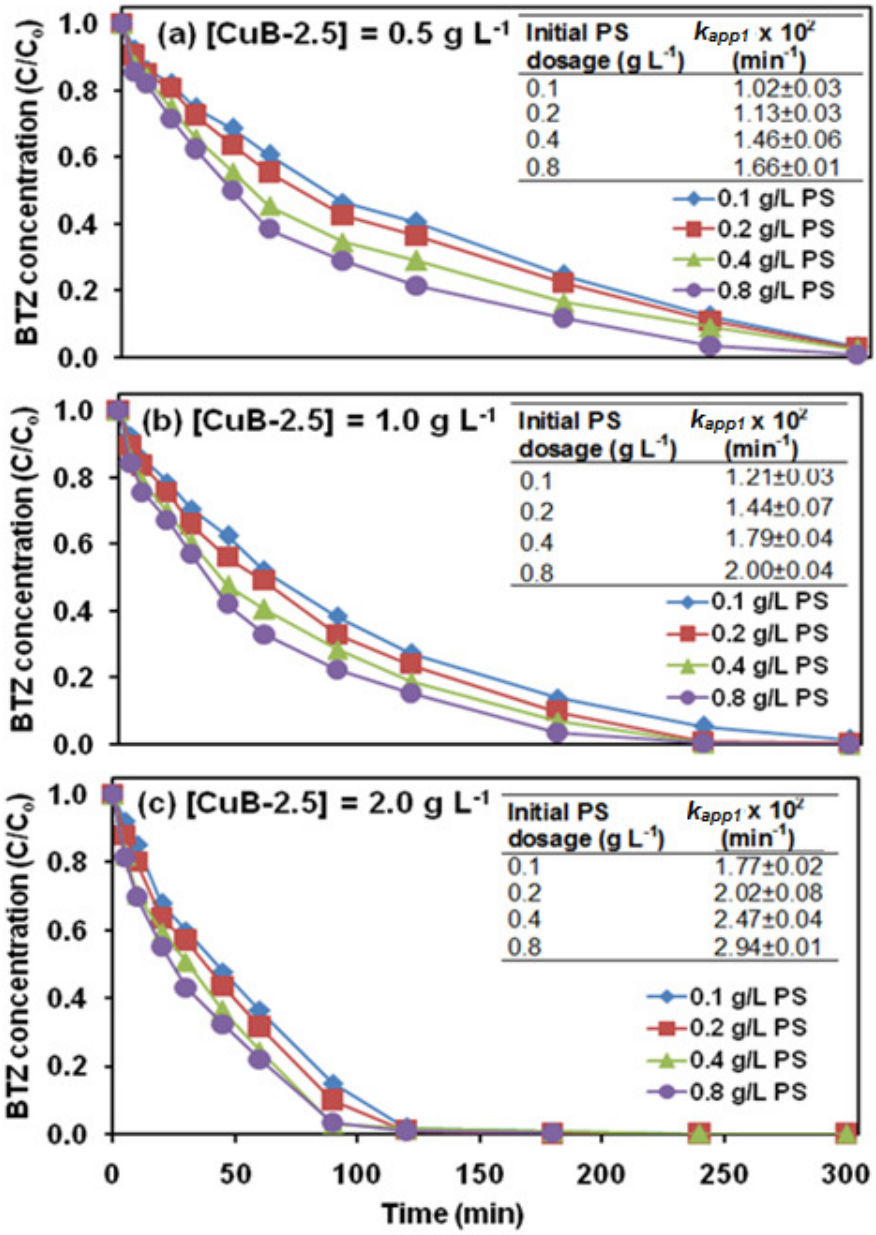

Figure 5.7. BTZ removal at various initial PS dosage and (a) 0.5 g L^{-1}, (b) 1.0 g L^{-1} and (c) 2.0 g L^{-1} of CuB–2.5. Initial conditions: [BTZ] = 2.5 mg L^{-1}, and [pH] = 7.0.

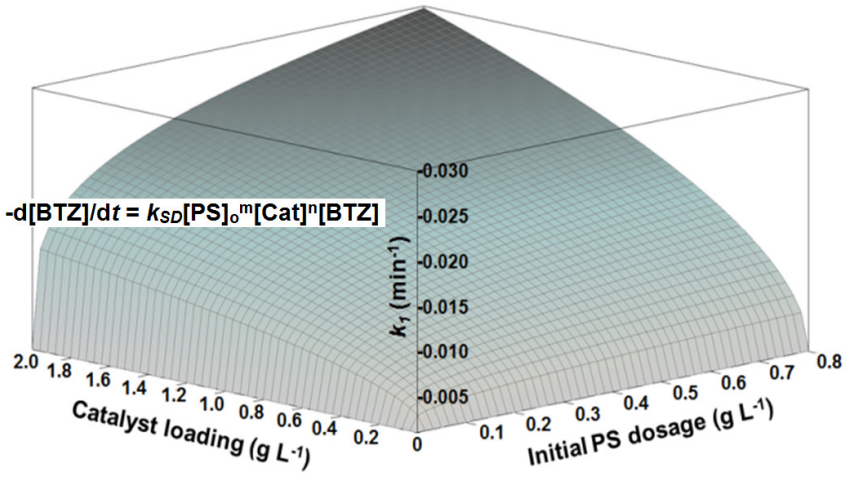

Figure 5.8. Relationship between initial rate constant, initial PS dosage, and catalyst loading at pH 7.

reaction surface area is more influential than the PS dosage on BTZ removal rate by a magnitude of 2.

5.3.2.2.2. PMS/CuB–2.5 system

Figure 5.9a–c shows the effects of different initial BTZ concentrations at different PMS dosages. The trend of k_{app2} shows a linear increase with (i) increasing PMS dosage and (ii) decreasing initial BTZ concentration. At higher BTZ concentrations, the BTZ degradation rate is limited by the specific surface area for reaction to achieve equitable removal efficiency within the same amount of time as those at lower BTZ concentrations. The higher amount of BTZ molecule could also induce steric constraint and block the active sites of the catalyst rendering it unavailable for PMS activation (Ji et al., 2014). Although accumulation of the BTZ degradation products on the catalyst surface could also contributes to the temporal deactivation of the catalyst, it is insignificant as supported by the catalyst reusability study. **Figure 5.9a** also shows the remarkable effect of increasing the catalyst loading (from 0.50 to 2.0 g L^{-1}) which leads to a complete BTZ removal in less than 1 min.

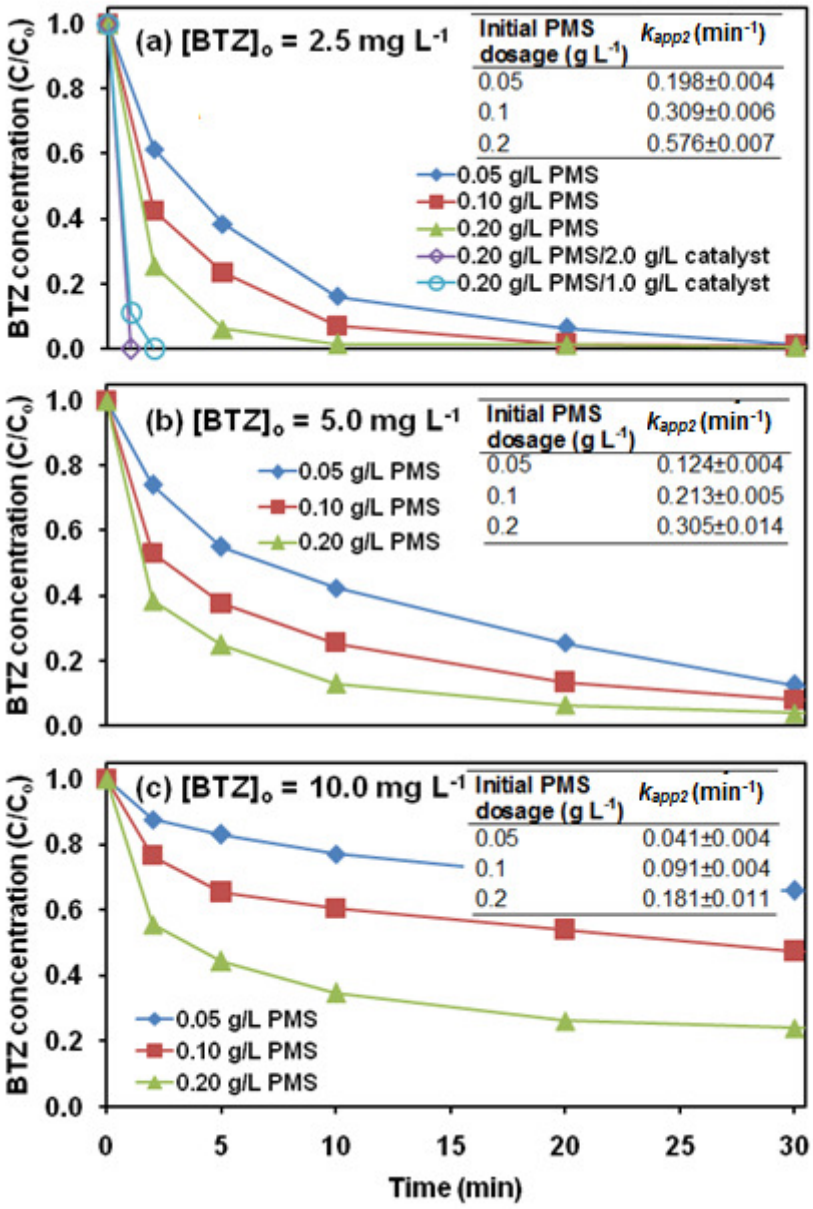

Figure 5.9. BTZ removal at various initial PMS dosages and (a) 2.5 mg L^{-1}, (b) 5.0 mg L^{-1} and (c) 10.0 mg L^{-1} of BTZ. Conditions: [CuB–2.5] = 0.5 g L^{-1} and $[pH]_o$ = 7.0.

5.3.2.3. Comparison of PMS and PS systems for BTZ degradation

5.3.2.3.1. Effects of Cl^-

The Cl^- is an important $SO_4^{\bullet-}$ scavenger and can react with $SO_4^{\bullet-}$ to produce $Cl^{\bullet}$ which will then be converted to a weaker $Cl_2^{\bullet-}$ (E^o = 2.09 V) (Nagarajan & Fessenden, 1985; Neta et al., 1988; Padmaja et al., 1993) as follow:

$$Cl^- + SO_4^{\bullet-} \rightarrow Cl^{\bullet} + SO_4^{2-} \ (k_{SO_4^{\bullet-}+Cl^-} = 3 \times 10^8\ M^{-1}\ s^{-1}) \quad (5.3.2.3.1.1)$$

$$Cl^- + Cl^{\bullet} \rightarrow Cl_2^{\bullet-} \ (k_{Cl^{\bullet}+Cl^-} = 8 \times 10^9\ M^{-1}\ s^{-1}) \quad (5.3.2.3.1.2)$$

Figure 5.10 shows the effects of Cl^- on BTZ degradation at pH 7.0 indicating that Cl^- exerts detrimental effects on the BTZ removal rate and efficiency in both the PMS and PS systems. In the PS system, the observed decrease of k_{app1} and BTZ removal efficiency could be attributed to two major factors, namely (i) the increase in ionic strength which is in agreement with the results reported by Zhang et al. (2014b) and (ii) the scavenging of miniature amount of $SO_4^{\bullet-}$ generated from the inefficient PS activation by Cu. The phenomenon (ii) plays a very minor role considering that PS activation by Cu(II) to generate $SO_4^{\bullet-}$ is highly inefficacious.

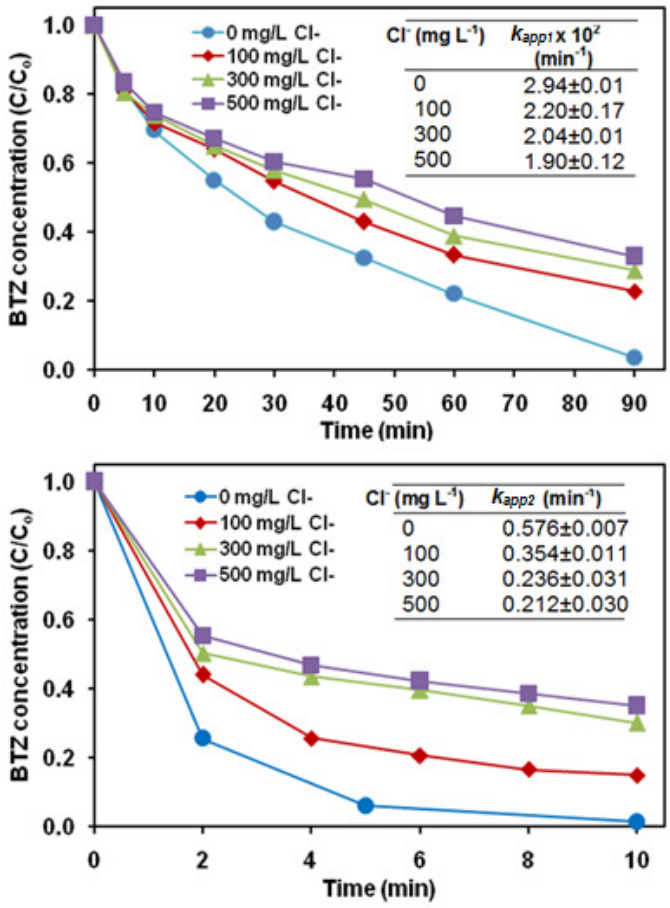

Figure 5.10. Effects of Cl^- on BTZ degradation at pH 7.0 for (a) PS/CuB–2.5 and (b) PMS/CuB2.5 systems.

In the PMS system, the oxidation reaction is mainly mediated by $SO_4^{\bullet-}$ and therefore, the Cl^- ion has an adverse effect on the BTZ degradation as observed by the decrease of the k_{app2} value with increasing Cl^- concentration. The steady–state $[SO_4^{\bullet-}]$ in the PMS reaction system can be estimated from the $SO_4^{\bullet-}$ oxidation of benzene at pH 7.0 as follows:

Benzene + $SO_4^{\bullet-}$ → degradation products + SO_4^{2-},

(5.3.2.3.1.3)

($k_{SO_4^{\bullet-}+benzene}$ = 3 x 10^9 M^{-1} s^{-1})

where k_5 is the second–order rate constant for the $SO_4^{\bullet-}$+benzene reaction (Neta et al., 1977). At pH 7.0, the contribution of $^{\bullet}OH$ in the degradation of BTZ is expected to be minimal due to the low rate of conversion of PMS/$SO_4^{\bullet-}$ to $^{\bullet}OH$ (Neta et al., 1988). The pseudo–first order rate constant value for benzene removal in the PMS system (**Figure A6, Appendix**), k_{app}, is 0.0051±0.0004 s^{-1} and thus, the estimated steady–state $[SO_4^{\bullet-}]$ is 1.7 x 10^{-12} M by calculating $[SO_4^{\bullet-}]$ = $k_{app}/k_{SO_4^{\bullet-}+benzene}$. In this regards, the second–order rate constant for the reaction BTZ+ $SO_4^{\bullet-}$ can be estimated from the k_{app2} value.

$SO_4^{\bullet-}$ + BTZ → degradation products + SO_4^{2-},

(5.3.2.3.1.4)

($k_{SO_4^{\bullet-}+BTZ}$ = 5.6 x 10^9 M^{-1} s^{-1})

This indicates that $SO_4^{\bullet-}$ reacts preferentially with BTZ than with Cl^- at the same condition. However, taking into account the high Cl^- concentration (40 times higher than BTZ), and the $k_{SO_4^{\bullet-}+Cl^-}[Cl^-]$ values at 100, 300 and 500 mg L^{-1} of Cl^- are 7.9x 10^6, 2.4x 10^6, 3.9 x 10^6 s^{-1}, respectively, this indicates that the Cl^- + $SO_4^{\bullet-}$ reaction is more favourable under this condition ($k_{SO_4^{\bullet-}+BTZ}$ [BTZ] = 1.2 x 10^5 s^{-1}). Nevertheless, BTZ degradation could still proceed at these Cl^- concentrations due

to the production of various reactive radicals (i.e. $Cl^{\bullet}$, $Cl_2^{\bullet-}$ and $^{\bullet}OH$) from the side reactions of $Cl^{\bullet}$ which could also attack and degrade BTZ (Fang et al., 2012).

5.3.2.3.2. Cu leaching, reusability and PMS/PS consumption

Table 5.1 shows a comparison of PMS and PS systems in terms of Cu leaching and PMS/PMS_o after BTZ oxidation reaction with various catalysts. The morphology of CuB−2.5 can be retained after redox reaction with PMS and PS (**Figure A7, Appendix**). The PMS/CuO and PS/CuO systems have the highest Cu leaching indicating that CuO is not suitable for PMS and PS activation processes. On the other hand, Cu(II) (*aq*) at 2 mg L^{-1} cannot effectively activate PMS and PS for BTZ degradation. The results commensurate with the relatively high residual PMS/PS in the Cu(II) systems as indicated in **Table 5.1** due to the inefficient PMS/PS consumption. The Cu leaching in the PMS/CuB system is at least 10 times lower than their corresponding PS/CuB system attributed to the (i) shorter treatment time (10 min vs. 90 min), and (ii) lower catalyst loading (0.5 g L^{-1} vs. 2.0 g L^{-1}). Metal dissolution especially after activation reaction is a major issue and has been heavily reported particularly for Co−based activators (Anipsitakis et al., 2005b; Patil et al., 2014).

The estimated cost of PMS required for treating 2.5 mg L^{-1} of BTZ is about 3 times more expensive than that of PS ($0.74 per kg of PS vs. $2.2 per kg of PMS). However, the PMS/CuB−2.5 system has the potential to treat at least 8−9 times higher volume of water than PS/CuB−2.5 system. It is anticipated that the PS system could achieve the same BTZ removal rate as the PMS system by increasing the specific surface area or catalyst loading by 14 times to 523.6 m^2 g^{-1} or 28 g L^{-1}, respectively. However, this is not practical since having increasing the catalyst

loading could also lead to a significantly higher Cu leaching and require an additional post treatment process. In both PMS/CuB−2.5 and PS/CuB−2.5 systems, excellent reusability was observed. This indicates that the catalyst is stable can be consistently reused for multiple cycles with >95% BTZ removal at t = 90 min (**Figure A8, Appendix**).

5.3.2.3.3. Degradation pathways

The major BTZ degradation pathways were investigated for the PMS/CuB−2.5 and PS/CuB−2.5 systems. The mass spectra (**Figure A9, Appendix**) after the BTZ oxidation reaction in the PMS/CuB−2.5 and PS/CuB−2.5 systems show similar profile. This indicates that the BTZ oxidation in the two systems leads to similar main oxidation intermediates (**Figure 5.11**). In this study, two reaction intermediates, namely diazoimine (A, m/z = 106) and benzene (B, m/z = 79) were identified with the positive mode ESI. It is proposed that the initial oxidation of BTZ by PMS and PS could result in the generation of the several different unstable intermediates which subsequently leads to the triazole ring opening *via* bond scission of the N−NH. This is follow by the elimination of NH group yielding diazoimine (A, m/z 106). Similarly, Wu et al. (2013) also observed diazoimine (m/z 105) as their main BTZ oxidation intermediate in their heterogeneous photoelectro−Fenton like process. Due to the instability of the diazoimine molecule, the molecule can be further degraded to benzene (B) (m/z = 79) with the loss of N_2. Then, ring cleavage of the benzene ring occurs producing lower molecular weight acids and subsequently to CO_2 and H_2O. Two peaks with higher m/z (m/z = 181 and 199) were also detected suggesting that dimerization−mineralization reaction could also occur. Dimerization−mineralization pathway is common for $SO_4^{\bullet-}$−mediated oxidation

reaction (Lau et al., 2006). Besides polymerization induced by sulfate radical, BTZ polymerization to form higher molecular weight organics was also previously observed in the solar photocatalysis system (Xu et al., 2013).

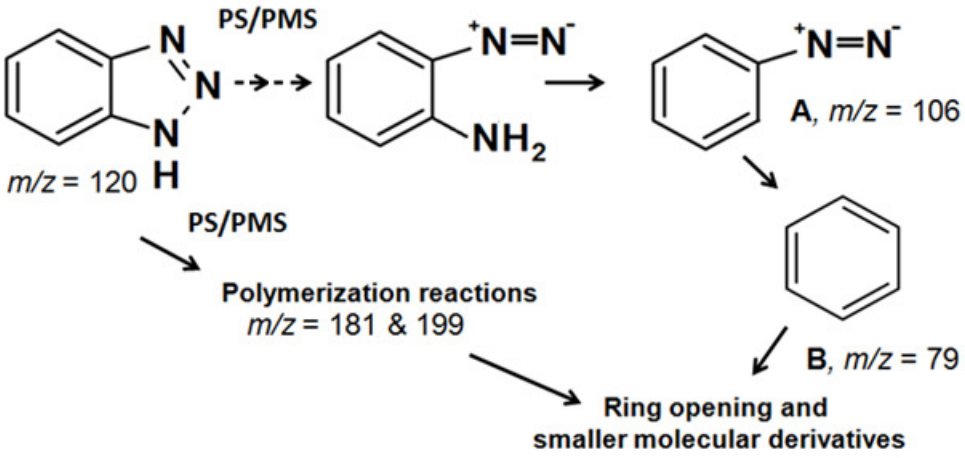

Figure 5.11. Proposed major BTZ degradation pathway in the PS/CuB−2.5 and PMS/CuB−2.5 systems.

5.4. Conclusions

A novel 3−D spherical $CuBi_2O_4$ consisting of nanocolumn arrays with efficient bi−functional PMS and PS activation functionalities was successfully synthesized *via* a facile hydrothermal method. The catalyst (CuB−2.5) has the highest surface area and Cu content compared with other CuB catalyst (CuB−M and CuB−H) and can be employed to treat BTZ *via* PMS and PS activation. The CuB−2.5 catalyst performed remarkably better compared with the homogeneous Cu(II), CuO, CuB−M and CuB−H. The performance of CuB−2.5 was optimized by varying the initial PMS/PS dosage, catalyst loading and initial BTZ concentration. The PMS/CuB−2.5 system was found to be more efficient than the PS/CuB−2.5 system. The inter− and intra−molecular hydrogen bonds play a crucial role in the mechanism of BTZ degradation in both PMS and PS systems. The BTZ degradation pathway in the PMS/CuB−2.5 and PS/CuB−2.5 systems was similar

whereby several identical intermediates were produced. The CuB−2.5 catalyst could retain its morphology even after use and the reusability study indicated that it can be reused for multiple cycles. This study shows that the CuB−2.5 catalyst is a promising catalyst with versatile PMS and PS activation functionalities for BTZ removal.

CHAPTER 6: PERFORMANCE OF HIERARCHICALLY−STRUCTURED $CuBi_2O_4$ FOR SULFANILAMIDE REMOVAL *VIA* PEROXYMONOSULFATE ACTIVATION

6.1. Introduction

Over the decades, environmental pollution due to pharmaceuticals has drawn tremendous attention due to their adverse ecological impact. Water pollution due to pharmaceuticals is increasingly becoming a major problem as the pollution can lead to the emergence of antibiotic resistant pathogenic microorganisms (Ding et al., 2016). One of the most widely−used pharmaceuticals is sulfonamide antibiotics, which is characterized by the presence of the sulfonamide functional group, $R_1–S(=O)_2–N–R_2R_3$ in their molecular structure. The sulfonamide antibiotics are widely used for treating urinary and upper respiratory tract infections (Connor, 1998). Increasingly, sulfonamide drugs have been detected in water (García-Galán et al., 2011). Various treatment methods have been proposed for sulfonamide antibiotics removal in water such as employing adsorption (Yu et al., 2015), photocatalysis (Hu et al., 2007), photo−Fenton (Batista & Nogueira, 2012), Fenton−like (Zhou et al., 2014), and ozonation (Garoma et al., 2010) processes. While these methods are effective, they are generally limited by the possibilities of secondary pollutant generation after treatment, huge capital cost for installation and tedious operating conditions.

One potential solution to address the issue of water pollution due to sulfonamide antibiotics is by employing heterogeneous SR−AOP. In **Chapter 5**, a mixed metal

$CuBi_2O_4$ catalyst (CuB−2.5) was fabricated. It was found that the catalyst was polyfunctional and can activate both PMS and PS. In this chapter, the CuB−2.5 was further employed for the removal of sulfanilamide (SA) in water *via* PMS activation. Furthermore, principal reactive radicals and mechanisms of PMS activation by the CuB−2.5 were also evaluated. A simple kinetic approach based on the kinetics of SA degradation is proposed to estimate the steady state concentrations of $SO_4^{\bullet-}$ and $^{\bullet}OH$ and to characterize the intrinsic catalytic activity of heterogeneous catalyst/PMS system.

6.2. Experimental

6.2.1. Chemicals

The chemicals used in this study were of analytical grade. The chemicals used were $Cu(NO_3)_2 \cdot 3H_2O$ (Qrëc™), $Bi(NO_3)_3 \cdot 5H_2O$ (Alfa Aesar), Oxone® (which is a registered trademark of DuPont and in the form of $2KHSO_5 \cdot KHSO_4 \cdot K_2SO_4$, Alfa Aesar), nitrobenzene (NB, Merck) and sulfanilamide (Sigma−Aldrich). All the experiments were conducted using the deionized (DI) water (18.2 MΩ cm).

6.2.2. Synthesis and characterization techniques

The CuB−2.5 was prepared using a facile hydrothermal synthesis as described in **Section 5.2.2**. The characterization techniques used for studying the characteristics of CuB−2.5 were presented in **Section 5.2.3**.

6.2.2. Performance study

The performance of the catalysts as PMS activator for sulfanilamide removal was

evaluated in a batch system. In a typical experimental procedure, 100 mL of a solution containing 15 μM of SA was prepared in a reaction vessel and calculated amount of Oxone® was added into the solution to obtain 0.12 mM of PMS (~PMS:SA molar ratio of 1:8, ~37 mg L^{-1} of Oxone®). The pH of the solution was adjusted to pH 7.0 using 0.5 M NaOH. Then, exactly 20 mg of CuB−2.5 was added into the solution to initiate the reaction. At various time intervals, 1 mL of the aliquot was drawn out from the reaction vessel, quenched with EtOH and the concentration of SA was quantified from the SA calibration curve using a high performance liquid chromatography (HPLC, Perkin Elmer) equipped with a UV−Vis detector (λ_{max} = 260 nm). The HPLC was operated with a reverse phase column (Hypersil Gold) and the mobile phase consists of 70:30 of water to acetonitrile *v/v* ratio (1 mL min^{-1}). At t = 30 min, the Co concentration of the solution was also quantified using a ICP−OES (PerkinElmer, Elmer Optima 2000DV). To ensure reproducibility, each of the experiment was duplicated. The experiment was repeated at various pH, Oxone® dosages and catalyst loading. To identify the principal reactive radical, similar experiments were conducted but in the presence of either EtOH or NB in the reaction matrix.

6.3. Results and discussions

6.3.1. Synthesis and characterization study

The optimization of the hydrothermal synthesis of CuB−2.5 was described in **Section 5.3.1**. The characteristics of CuB−2.5 were also presented in **Section 5.3.1**.

6.3.2. Performance study

Figure 6.1 shows the empirical relationship between the pseudo first−order rate constants (k_{app}), catalyst loading (L, g L^{-1}) and Oxone® dosage (D, g L^{-1})) while **Table 6.1** shows

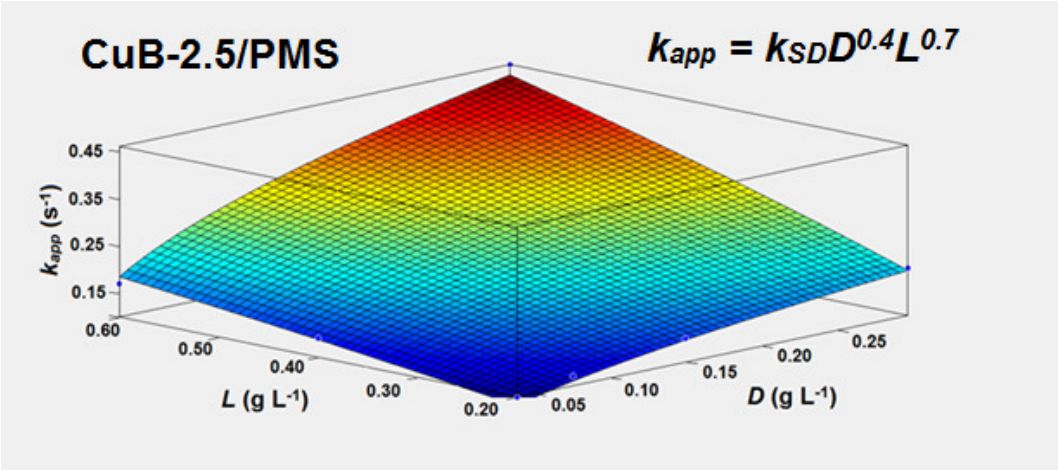

Figure 6.1. Relationship between k_{app}, L and D for SA removal in the CuB−2.5/PMS system.

Table 6.1. The pseudo first−order rate constants of SA degradation *via* PMS activation by CuB-2.5 at various conditions at pH 7.0.

CuB-2.5/condition	***L*** **(g L^{-1})**	***D*** **(g L^{-1})**	k_{app} **(min^{-1})**
CuB-2.5	0.2	0.037	0.10
CuB-2.5	0.4	0.037	0.14
CuB-2.5	0.6	0.037	0.17
CuB-2.5	0.2	0.074	0.12
CuB-2.5	0.2	0.148	0.15
CuB-2.5	0.2	0.295	0.20
CuB-2.5	0.4	0.295	0.29
CuB-2.5	0.6	0.295	0.46
CuB-2.5	0.4	0.300	0.21
CuB-2.5with NB	0.4	0.300	0.17

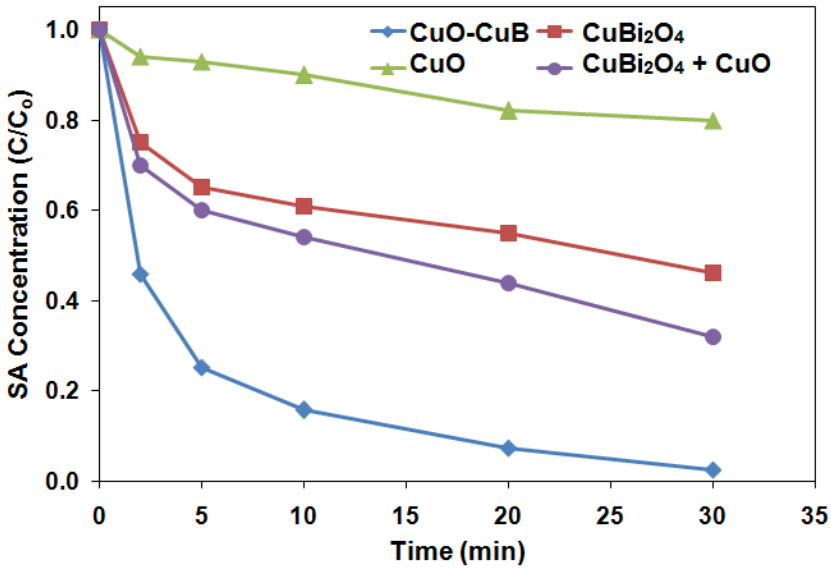

Figure 6.2. The performance of CuB-2.5 (CuO-CuB), $CuBi_2O_4$, CuO and CuO + $CuBi_2O_4$ for SA removal *via* PMS activation. Initial conditions: [SA] = 2.5 mg L^{-1}, pH = 7.0, [CuO-CuB]&[$CuBi_2O_4$] = 0.4 g L^{-1} and CuO = 0.05 g L^{-1}. The performance of mechanically mixed $CuBi_2O_4$ (0.4 g L^{-1}) and CuO (0.05 g L^{-1}, with at least 5 times the loading of CuO-CuB) is lower than that of the CuO-CuB indicating synergistic effect exists between $CuBi_2O_4$ and CuO coupling.

the calculated k_{app} values of SA degradation *via* PMS activation by CuB–2.5 at various conditions. The empirical relationship of k_{app}, L and D for CuB–2.5 can be described by the following equation: $k_{app} = k_{SD}D^{0.4}L^{0.7}$, where the value of k_{SD} (specific rate constant) is 1.1. Increasing the Oxone® dosage and catalyst loading have a positive effect on the SA removal in both systems due to the increment in the number of active sites and reactants available for reaction. The kinetic results suggest that in the CuB–2.5/PMS system, L is the secondary factor influencing SA degradation (compared to D). To prove that the synergistic effect exists, the catalytic activities of pure $CuBi_2O_4$, CuO and $CuBi_2O_4$ + CuO mixture were compared with that of the CuO–CuB for the treatment of SA *via* PMS activation (**Figure 6.2**). The results in **Figure 6.2** indicate that the catalytic activities of $CuBi_2O_4$, CuO and $CuBi_2O_4$–CuO mixture are lower than that of the CuO–CuB further evidencing the synergistic coupling effect.

6.3.3. Determination of principal reactive radicals

The radical scavenging method using selective radical scavenger was employed to identify the principal reactive radicals responsible for SA degradation in the CuB−2.5/PMS system. **Figure 6.3** shows the effect of radical scavenger addition (NB and EtOH) on SA degradation *via* catalytic PMS activation. Based on the reactivities of the radical scavengers with •OH and $SO_4^{\bullet-}$, EtOH ($k_{EtOH+{}^{\bullet}OH}$= 1.9 x 10^9 M^{-1} s^{-1}, $k_{EtOH+SO_4^{\bullet-}}$ < 1.6 x 10^7 M^{-1} s^{-1}) can be used to confirm the presence of both •OH and $SO_4^{\bullet-}$ while NB ($k_{NB+{}^{\bullet}OH}$ = 3.9 x 10^9 M^{-1} s^{-1}, $k_{NB+SO_4^{\bullet-}}$ < 10^6 M^{-1} s^{-1}) can be selected as the •OH selective scavenger to confirm the presence of $SO_4^{\bullet-}$ (Buxton et al., 1988; Neta et al., 1988). Meanwhile, the relative contributions (in %) of •OH and $SO_4^{\bullet-}$ can be calculated based on the difference in the calculated pseudo first−order rate constants between the experiments conducted with and without NB.

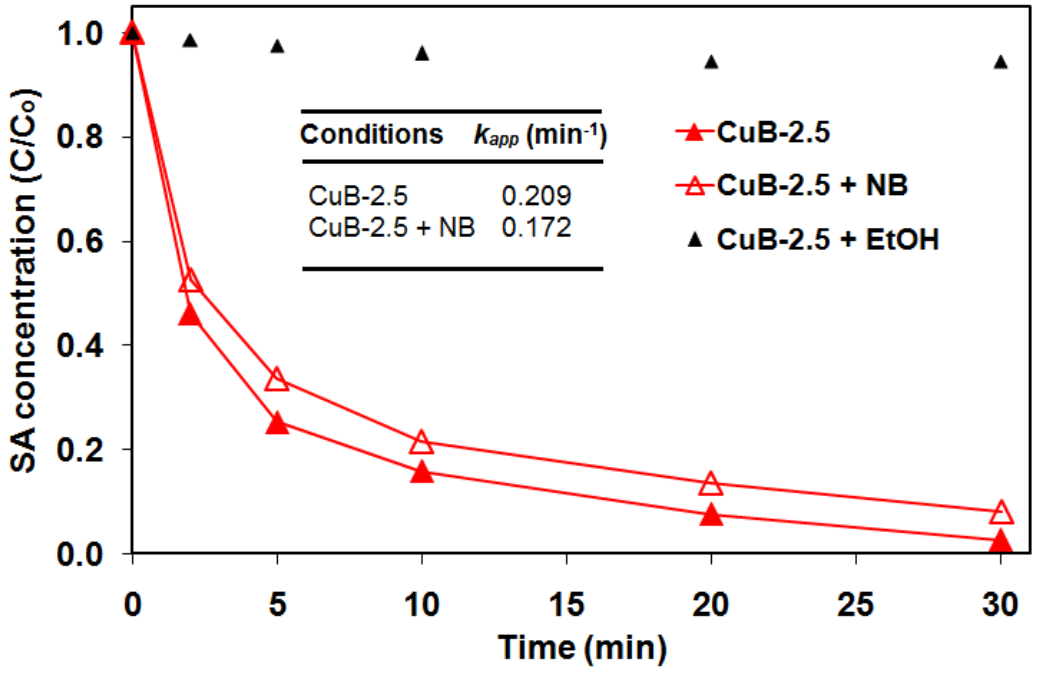

Figure 6.3. Effect of chemical probes addition (NB and EtOH) on the degradation of 2.5 mg L^{-1} SA at pH 7.0. [NB] = 0.15 mM and [EtOH] = 1 mM. Initial: [CuB−2.5] = 0.40 g L^{-1} and [Oxone®] = 0.30 g L^{-1}.

$$SO_4^{\bullet-} \text{ contribution to SA degradation (in \%)} = \frac{k_{app}(with\ NB)}{k_{app}(without\ NB)} \text{ x } 100\% \quad (6.3.3.1)$$

where k_{app} is the pseudo−first order rate constant. The results as presented in **Figure 6.3** indicate that the main radical responsible for SA degradation is $SO_4^{\bullet-}$ with only ~16±1% of $^{\bullet}OH$ contribution in the CuB−2.5/PMS system (or ~19% of that of $SO_4^{\bullet-}$ contribution). The main mechanisms of PMS activation by $CuBi_2O_4$ composites to produce $SO_4^{\bullet-}$ is proposed as follow (Anipsitakis et al., 2005b; Ghanbari et al., 2014):

$$Cu^{2+} + HSO_5^- \rightarrow SO_4^{\bullet-} + OH^- + Cu^{3+} \quad (6.3.3.2)$$

$$Cu^{3+} + HSO_5^- \rightarrow SO_5^{\bullet-} + H^+ + Cu^{2+} \quad (6.3.3.3)$$

$$Cu^{2+} + HSO_5^- \rightarrow SO_5^{\bullet-} + H^+ + Cu^{+} \quad (6.3.3.4)$$

$$Cu^{+} + HSO_5^- \rightarrow SO_4^{\bullet-} + OH^- + Cu^{2+} \quad (6.3.3.5)$$

On the other hand, the main mechanism of PMS activation by $CuBi_2O_4$ composites to produce $^{\bullet}OH$ is proposed as follows (Gilbert & Stell, 1990; Gilbert et al., 1991; Ji et al., 2011):

$$Cu^{+} + HSO_5^- \rightarrow {}^{\bullet}OH + SO_4^{2-} + Cu^{2+} \quad (6.3.3.6)$$

The generation of $^{\bullet}OH$ *via* Eq. (6.3.3.6) has a very minor contribution possibly because the $SO_4^{\bullet-}$ generation from homolytic splitting of –O–O– bond of PMS is thermodynamically more feasible than the $^{\bullet}OH$ generation. The conversion of $SO_4^{\bullet-}$ to $^{\bullet}OH$ is expected to be minimal due to the low reactivity of $SO_4^{\bullet-}$ with water at neutral pH ($k_{H_2O+SO_4^{\bullet-}} < 1.0 \text{ x } 10^3\ M^{-1}\ s^{-1}$) (Neta et al., 1988).

$$SO_4^{\bullet-} + H_2O \rightarrow {}^{\bullet}OH + SO_4^{2-} + H^+ \quad (6.3.3.7)$$

6.3.4. Estimation of steady–state $SO_4^{\bullet-}$ and $^{\bullet}OH$ concentrations

The CuB–2.5/PMS system are further characterized by determining the normalized steady–state concentrations of $SO_4^{\bullet-}$ ($[SO_4^{\bullet-}]_{Nss}$) and $^{\bullet}OH$ ($[^{\bullet}OH]_{Nss}$), using a simple kinetic approach with SA as the molecular probe. The second–order rate constants of the reaction of SA with $SO_4^{\bullet-}$ ($k_{SA+SO_4^{\bullet-}}$) is determined to be 6 x 10^9 M^{-1} s^{-1} *via* the competitive kinetic approach with benzene ($k_{benzene+SO_4^{\bullet-}}$ = 3 x 10^9 M^{-1} s^{-1}) as the chemical probe (Neta et al., 1977). The second–order rate constants of the reaction of SA with $^{\bullet}OH$ ($k_{SA+^{\bullet}OH}$) is 1.6 x 10^9 M^{-1} s^{-1} (Phillips et al., 1973). Based on the rate of change of SA concentration with respect to the steady state concentrations of $SO_4^{\bullet-}$ ($[SO_4^{\bullet-}]_{ss}$) and $^{\bullet}OH$ ($[^{\bullet}OH]_{ss}$), the following kinetic expression can be obtained:

$$-\frac{dC_{SA}}{dt} = k_{NB+SO_4^{\bullet-}}[SO_4^{\bullet-}]_{ss}C_{SA} + k_{SA+^{\bullet}OH}[^{\bullet}OH]_{ss}C_{SA} \quad (6.3.4.1)$$

where C_{SA} is the concentration of SA at time *t*, $k_{NB+SO_4^{\bullet-}}$, and $k_{SA+^{\bullet}OH}$ are the second–order rate constants for the reaction of SA with $^{\bullet}OH$ and $SO_4^{\bullet-}$, respectively. Taking into consideration that $^{\bullet}OH$ contributes to ~19% of the $SO_4^{\bullet-}$ contribution and by employing the pseudo first–order assumption whereby the PMS is in excess, the expression becomes:

$$-\frac{dC_{SA}}{dt} = k_{SA+SO_4^{\bullet-}}[SO_4^{\bullet-}]_{ss}C_{SA} + 0.19k_{SA+SO_4^{\bullet-}}[SO_4^{\bullet-}]_{ss}C_{SA} \quad (6.3.4.2)$$

$$-\frac{dC_{SA}}{dt} = 1.19k_{SA+SO_4^{\bullet-}}[SO_4^{\bullet-}]_{ss}C_{SA} = k_{app}C_{SA} \quad (6.3.4.3)$$

Therefore, the $[SO_4^{\bullet-}]_{ss}$ can be calculated as follows:

$$[SO_4^{\bullet-}]_{ss} = \frac{k_{app}}{1.19k_{SA+SO_4^{\bullet-}}} \quad (6.3.4.4)$$

By normalizing the $[SO_4^{\bullet-}]_{ss}$ with respect to the L and D, the following equation can be obtained:

$$[SO_4^{\bullet-}]_{Nss} = \frac{k_{app}}{1.19LDk_{SA+SO_4^{\bullet-}}} \quad (6.3.4.5)$$

Similarly, the $[^{\bullet}OH]_{Nss}$ can be obtained by comparing Eqs. (6.3.4.1) and (6.3.4.2).

$$k_{SA+^{\bullet}OH}[^{\bullet}OH]_{ss}C_{SA} = 0.19k_{SA+SO_4^{\bullet-}}[SO_4^{\bullet-}]_{ss}C_{SA} \quad (6.3.4.6)$$

$$[^{\bullet}OH]_{ss} = \frac{0.19k_{SA+SO_4^{\bullet-}}[SO_4^{\bullet-}]_{ss}}{k_{SA+^{\bullet}OH}} \quad (6.3.4.7)$$

$$[^{\bullet}OH]_{Nss} = \frac{0.19k_{SA+SO_4^{\bullet-}}[SO_4^{\bullet-}]_{ss}}{LDk_{SA+^{\bullet}OH}} \quad (6.3.4.8)$$

The calculated $[SO_4^{\bullet-}]_{Nss}$ is 4.07 x 10^{-12} M g^{-2} L^2 for the CuB−2.5/PMS system, while its corresponding $[^{\bullet}OH]_{Nss}$ is 2.90 x 10^{-12} M g^{-2} L^2. The characteristic $[SO_4^{\bullet-}]_{Nss}$ and $[^{\bullet}OH]_{Nss}$ can be used to compare the intrinsic catalytic activity of various heterogeneous catalyst/PMS system.

6.4. Conclusions

In conclusion, the CuB−2.5 catalyst was successfully−prepared using a facile hydrothermal method for SA removal *via* PMS activation. The effects of catalyst loading and Oxone® dosage on SA degradation were investigated and their empirical relationship with k_{app} was established. A facile method is proposed to calculate the normalized steady−state concentrations of $SO_4^{\bullet-}$ ($[SO_4^{\bullet-}]_{Nss}$) and $^{\bullet}OH$ ($[^{\bullet}OH]_{Nss}$) for the characterization of the intrinsic catalytic activity of heterogeneous catalyst/PMS system.

CHAPTER 7 CONCLUSIONS AND RECOMMENDATIONS

7.1. Conclusions

In the first part of this study (**Chapter 3**), DPA–Fe_2O_3 was synthesized *via* a low temperature co–precipitation method. The DPA–Fe_2O_3 has an improved catalytic activity for BPA detoxification *via* PMS activation compared to other Fe(III)–based catalysts, namely FeOOH, FeOOH/Cl, and Fe_2O_3. The investigation of the acute toxicity of the treated BPA solution in the heterogeneous catalyst/PMS system shows that excess Oxone® needs to be employed to efficiently detoxify BPA.

In order to further improve the catalytic activity of Fe_2O_3, an auxiliary transition metal precursor (Cu(II)) was incorporated into the Fe_2O_3 during the low–temperature co–precipitation synthesis to form a mixed metal $CuFe_2O_4$–Fe_2O_3 catalyst (**Chapter 4**). The $CuFe_2O_4$–Fe_2O_3 catalyst has high stability, ferromagnetism and excellent catalytic activity for BPA removal *via* PMS activation. A kinetic model based on the mechanistic consideration of the effects of initial pH, PMS dosage and catalyst loading has been successfully developed to describe the heterogeneous catalyst/PMS system.

In the subsequent chapter (**Chapter 5**), a bi–functional mixed metal $CuBi_2O_4$ catalyst was fabricated *via* a hydrothermal synthesis method for BTZ removal. The catalyst showed remarkable performance in activating both PMS and PS for BTZ removal. The mechanism of PMS and PS activation by $CuBi_2O_4$ catalyst and the major BTZ degradation pathways are proposed.

The $CuBi_2O_4$ catalyst was further evaluated in **Chapter 6** by investigating its performance as a catalyst for SA removal *via* PMS activation. A simple kinetic approach based on the SA degradation rate was successfully employed to characterize the intrinsic catalytic

activity of the heterogeneous catalyst/PMS system.

In summary, the as–prepared DPA–Fe_2O_3, $CuFe_2O_4$–Fe_2O_3 and $CuBi_2O_4$ catalysts are highly–efficient for the treatment of various recalcitrant pollutants such as BPA and BTZ in water. The DPA–Fe_2O_3 can detoxify BPA within 2 h under the following experimental conditions: [BPA] = 15 mg L^{-1}, [Oxone®] = 2 g L^{-1}, pH = 7.0, and [catalyst] = 0.50 g L^{-1}. The $CuFe_2O_4$–Fe_2O_3 was effectively used for BPA removal within 30 min under the following experimental conditions: [pH] = 7.0, [PMS] = 0.18 g L^{-1}, [catalyst] = 0.05 g L^{-1}, and [BPA] = 5 mg L^{-1}. The $CuBi_2O_4$ catalyst (CuB–2.5) performed effectively well for the removal of BTZ within 1 h *via* PS ([BTZ] = 2.5 mg L^{-1}, [PS] = 0.1 g L^{-1}, pH = 7.0, and [catalyst] = 0.50 g L^{-1}) and PMS ([BTZ] = 2.5 mg L^{-1}, [PMS] = 0.05 g L^{-1}, pH = 7.0, and [catalyst] = 0.50 g L^{-1}) activations. The CuB–2.5 was also able to remove SA (([SA] = 2.5 mg L^{-1}, [CuB–2.5] = 0.40 g L^{-1} and [Oxone®] = 0.30 g L^{-1}, pH = 7.0) in 30 min. All the catalysts can be reused for at least 3 cycles. These catalysts can be potentially–used as alternatives to Co–based catalysts. In particular, the $CuBi_2O_4$ catalyst has bi–functionalities as PMS and PS activator with good settling velocity for ease of recovery after treatment.

7.2. Recommendations for future works

7.2.1. Detection of reactive species in SR-AOP system

In SR–AOP system involving peroxymonosulfate activation by transition metals, $^{\bullet}OH$ and $SO_4^{\bullet-}$ co–exist and participate in the oxidation reactions. Due to the differences in their reactivities with target pollutants, it is important to identify the principal reactive radical in a SR–AOP system because it has a direct implication on the associated pollutant degradation pathways, intermediates formed, degradation efficiencies and rates. It is also important to quantify the reactive species to characterize and compare the performance of

the SR-AOP system. To the best of our knowledge, there are limited studies on the direct technique for $SO_4^{\bullet-}$ quantification. Future studies on the development of a reliable technique for the detection and quantification of the generated reactive radicals in SR−AOP is warranted.

It is proposed that a possible approach for $SO_4^{\bullet-}$ quantification is by adopting the $^{\bullet}OH$ quantification techniques which may also be appropriate for $SO_4^{\bullet-}$ quantification. For instance, quantitative $^{\bullet}OH$ determination has been conducted by measuring of the concentration of the byproducts formed (which is proportional to the concentration of $^{\bullet}OH$) from the reaction between $^{\bullet}OH$ with chemical probes such as 1,5–diphenylcarbohydrazide (Wang et al., 2011a), benzoic acid (Sarifuddin & Rajakumar, 2012), dimethyl sulfoxide (Tai et al., 2004), *p*–chlorobenzoic acid (Pi et al., 2005; Rosenfeldt et al., 2006; Westerhoff et al., 2009), terephthalate (Page et al., 2010), *p*–nitrosodimethylaniline (Feng et al., 2003), coumarin and its derivatives (Zhang & Nosaka, 2014; Zhang & Nosaka, 2015), and salicylic acid (Jen et al., 1998; Wu et al., 2007) using high performance liquid chromatography, spectrophotometer, photoluminescence spectrometer and fluorescence spectrometer in various aqueous systems. The chemical probe is expected to have the following criteria: (i) it can react with $SO_4^{\bullet-}$ to produce a stable, quantifiable byproduct, (ii) it is stable to oxidation by PMS, and (iii) it does not affect the catalyst activity (e.g. deposit/adsorb onto and deactivate the catalyst, participate in the reaction with the target pollutant etc.). Because of the selectivity of $SO_4^{\bullet-}$, the byproducts formed from $SO_4^{\bullet-}$ oxidation are expected to be more specific and less diverse compared to those produced from the oxidation by $^{\bullet}OH$. However, the reaction needs to be carried out either in the presence of $^{\bullet}OH$ scavengers or under acidic condition whereby the $^{\bullet}OH$ contribution is not prevalent.

7.2.2. Nonmetal carbon–catalyst

Recently, nonmetal carbon–based catalysts such as AC, GO, rGO, CNTs as PMS activator have been employed as PMS activators (Duan et al., 2015b; Duan et al., 2015c; Duan et al., 2016; Duan et al., 2015d; Duan et al., 2015e; Duan et al., 2015f; Indrawirawan et al., 2015a; Indrawirawan et al., 2015b; Peng et al., 2013; Sun et al., 2014; Sun et al., 2012a; Sun et al., 2013b; Wang et al.). They are highly effective in PMS activation and provide a potential solution to the metal leaching problem. However, the nonmetal carbon catalysts suffer from various shortcomings such as (i) the low durability for long term use due to cannibalistic oxidation, and (ii) the high cost of certain carbon–based catalysts (e.g. CNTs and graphene etc.) compared to metal–based catalysts. Several reported studies show that the performance of carbon–based catalysts decreased significantly after first use (e.g. from 100% to 31% removal in 45 min for N–doped rGO (Duan et al., 2015b) and 100% to 20% removal for N, B–codoped rGO (Sun et al., 2013b)). The cannibalistic reaction after a single use also implies that the generated radicals are not fully utilized for pollutant degradation. As such, decreasing the cannibalistic reaction is anticipated to have a positive effect on the overall pollutant removal rate. The future studies on improving the durability of the carbon–based catalysts are recommended.

The mechanisms of PMS activation involving carbon–based catalysts are also not fully understood. Besides radical–based mechanism involving $^{\bullet}OH$ and $SO_4^{\bullet -}$generation, it has been reported that a nonradical pathway emerged along with the formation of both $^{\bullet}OH$ and $SO_4^{\bullet -}$ using N–doped single–walled CNT as the PMS activator (**Figure 7.1**) (Duan et al., 2015f). As indicated in **Figure 7.1**, PMS and phenol are first adsorbed on the electron rich sp^2 sites. This is then follow by the activation of PMS (either by radical or nonradical pathway) and subsequent degradation of phenol on the N–doped single–walled CNT surface. It is thought that the asymmetric PMS structure coupled with its relatively weak

oxidation and adsorption on CNTs may be the contributing factor for the emergence of nonradical pathway (Duan et al., 2015c). The occurrence of radical and nonradical pathways depends on the type of carbon structure (Duan et al., 2016). The sp^2 conjugation and ketonic groups promote the dissociation of PMS to generate $^{\bullet}OH$ and $SO_4^{\bullet-}$ for pollutant degradation. On the other hand, the presence of carbon networks with defective edges promotes nonradical pathway which have the advantages of being more selective in targeting organic contaminants, resistant to pH variation, and less influenced by the presence of water matrix species. In another study, singlet oxygen ($^1O_2$) has been detected as the dominant reactive radical during PMS activation by quinones (Zhou et al., 2015b). Future investigation can be conducted to detect the generated radicals and ascertain the role of different surface functional groups in facilitating the nonradical pathway. This could allow the exploitation of the nonradical pathway which could be a potential solution to the cannibalistic oxidation. This also provides an attractive research opportunity for future studies on engineering heterogeneous carbon–based catalysts *via* chemical functionalization with specific functional groups such as quinones that could activate PMS.

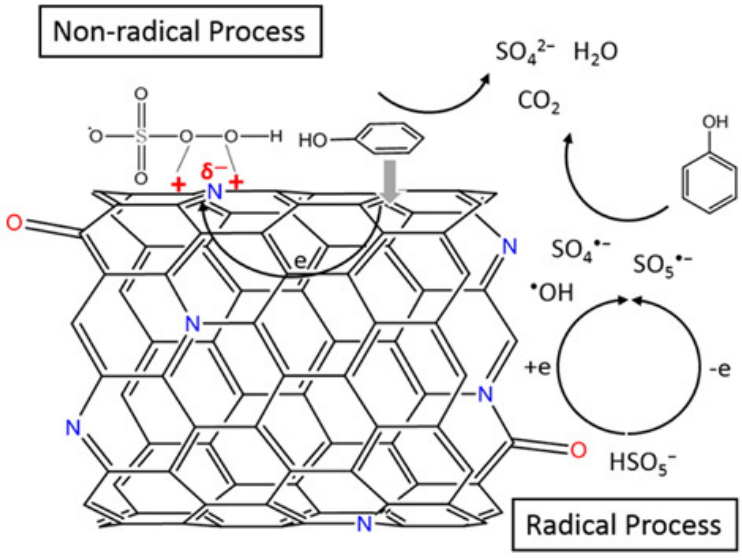

Figure 7.1: The nonradical and radical mechanism of PMS activation by N–doped CNTs (Duan et al., 2015f).

7.2.3. Application of heterogeneous catalyst/PMS system

To date, studies on the PMS activation by heterogeneous catalysts are limited to the bench−scale batch system. For practical application, future studies can be extended to develop practical design for heterogeneous catalyst/PMS reactor systems based on batch or continuous flow (e.g. completely mixed or plug flow) reactor configuration with catalyst recovery. There are three possible strategies to retain and recover the catalyst from the treated water, namely (i) sedimentation, (ii) magnetic separation, and (iii) membrane separation. Gravitational sedimentation of the catalyst is the most cost effective option but it is difficult to implement because, in general, many nanosized catalysts have low settling velocity. However, if the catalyst exhibits weak ferromagnetism, its sedimentation can be enhanced through external magnetic field. For (ii), magnetic catalysts, such as $CuFe_2O_4$ and $CoFe_2O_4$, have been extensively reported as effective PMS activators (**Chapter 2**). These catalysts can be separated from the treated water by incorporating magnetic separator as shown in **Figure 7.2**. When magnetic separation is not feasible, a membrane module can be incorporated in the hybrid membrane−catalytic reactor similar to the membrane reactors proposed by other researchers (Wang et al., 2013; Wang & Lim, 2012). Ceramic membrane is preferred over polymeric membrane because of its better chemical and mechanical stabilities (Hofs et al., 2011).

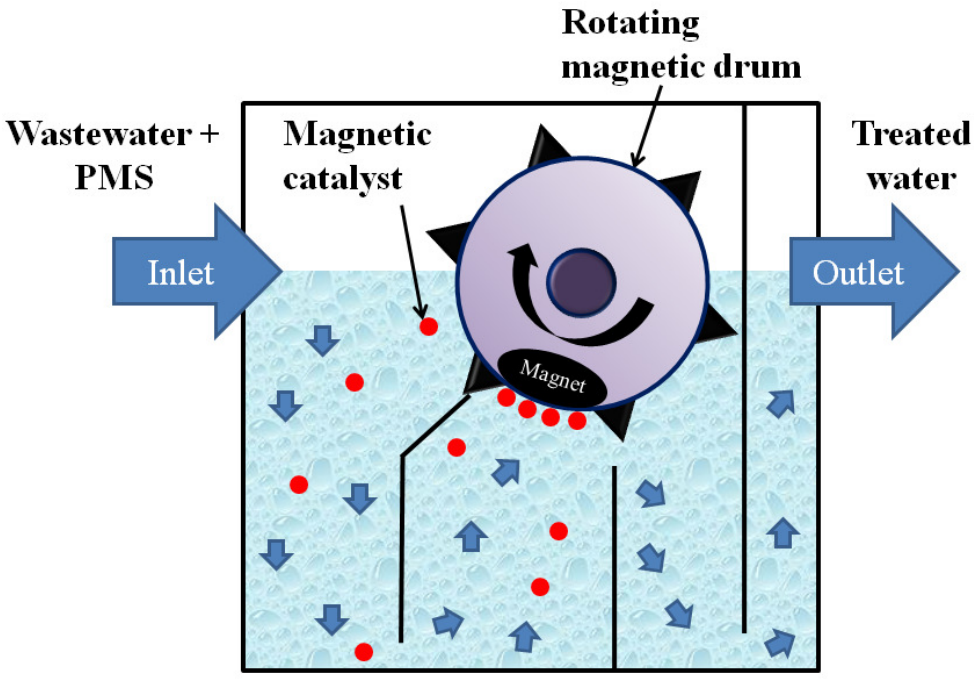

Figure 7.2: The possible reactor configuration for heterogeneous magnetic catalyst/PMS system.

Alternatively, it is proposed that the heterogeneous catalyst can be immobilized on/in the membrane (typically microfiltration or ultrafiltration type ceramic membrane) to produce an intrinsically catalytic membrane with PMS activation and membrane separation dual–functionality for a continuous flow–through operation. The future studies should aim to develop a robust dual functional catalytic ceramic membrane incorporating SR–AOPs. In general, depending on the type of application and quality of the feed water, there are two practical schemes to incorporate catalyst nanoparticles in the ceramic membrane module (**Figure 7.3**), namely (i) thin–film coating on the membrane feed side, and (ii) decorating catalyst nanoparticles on the macroporous matrix of the membrane support through impregnation technique. The advantage of immobilizing the catalyst on the feed side (as top layer) of the ceramic membrane is that it imparts self–cleaning or antifouling property (*via* oxidation of foulant by $SO_4^{\bullet-}$ generated from PMS activation), and thus the membrane will exhibit improved flux. However, the catalyst can be susceptible to deactivation by the foulant when treating the water with high DOM concentration and future investigation can be conducted to address this issue.

Immobilization of the catalyst in the internal pores of the membrane support layer creates microreactor environment whereby the target pollutant and their intermediates are degraded more effectively by $SO_4^{\bullet-}$ due to the longer reaction time and much less interference by DOM (which can be mostly retained by the membrane top layer). Several reported catalytic membranes decorated with metal oxide catalysts that are active to PMS such as MnO_2–Co_3O_4 (Guo et al., 2016), iron oxide (Harman et al., 2010) and Mn oxide (Byun et al., 2011; Corneal et al., 2011) can be considered for future studies on the development of catalytic membranes with PMS activation functionality.

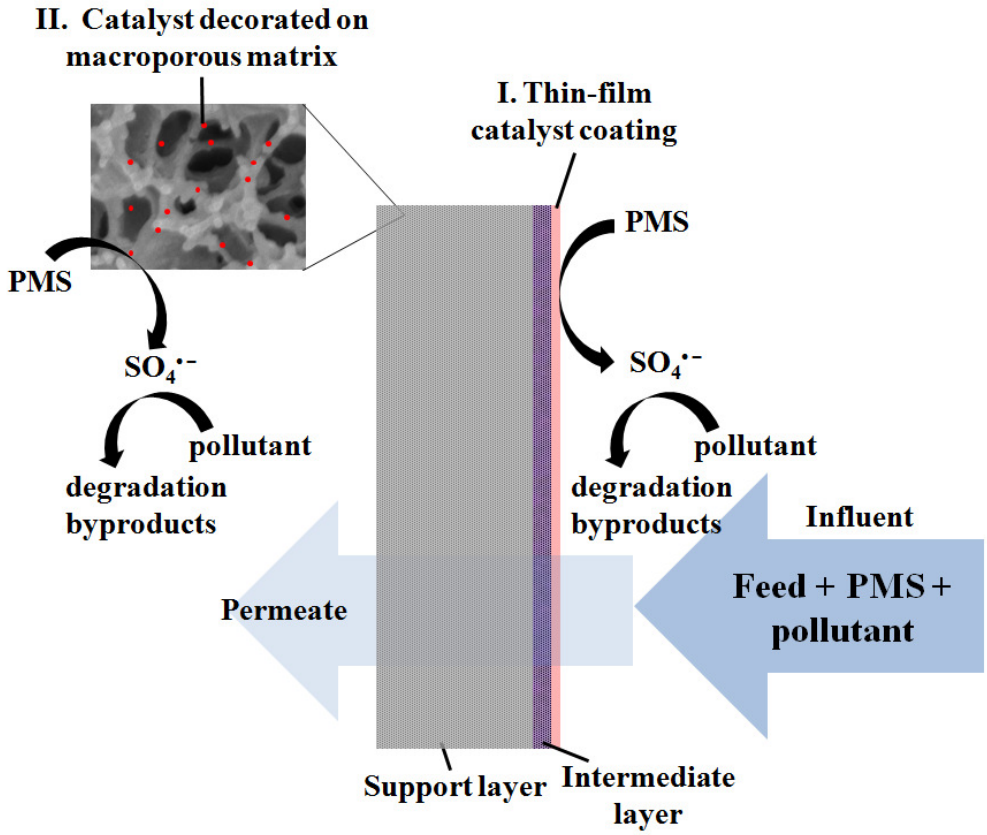

Figure 7.3: The two schemes to incorporate catalyst nanoparticles in the ceramic membrane module.

Appendix

Appendix 1

(a) Solvothermal synthesis methods for XFe_2O_4 (X = Cu, Co and Mn) (Deng et al., 2007).

Metal precursors at the stoichiometric ratio of 1X to 2Fe were dissolved in 80 mL of ethylene glycol. Then, 7.2 g of sodium acetate and 1.0 g of polyethylene glycol was added into the solution. The mixture was stirred vigorously for 6 h using a magnetic stirrer and then sealed in a Teflon−lined stainless steel autoclave (capacity = 125 mL). The autoclave was then placed in an oven for 12 h at 200°C. The resultant product magnetically separated and washed with ethanol and deionized water.

(b) Sol−gel synthesis of $CuAl_2O_4$ (Kwak et al., 2012).

Metal precursors and citric acid (CA) at the stoichiometric ratio of 1Cu:2Al:6CA were mixed and dissolved in 30 mL of deionized water. The pH of the solution mixture was then adjusted to pH 2.5 using ammonia and heated at 80°C for 4 h. The resultant sol was then calcined using a furnace at 800°C for 2 h.

(c) Low−temperature co−precipitation synthesis of $CuBi_2O_4$.

Metal precursors at the stoichiometric ratio of 1Cu:2Bi was dissolved in 50 mL of 0.5 M nitric acid. Then, 25 mL of 5M NaOH was slowly introduced into the solution. The resultant solution was heated at 90°C for 24 h. The product was separated by filtration and washed with deionised water.

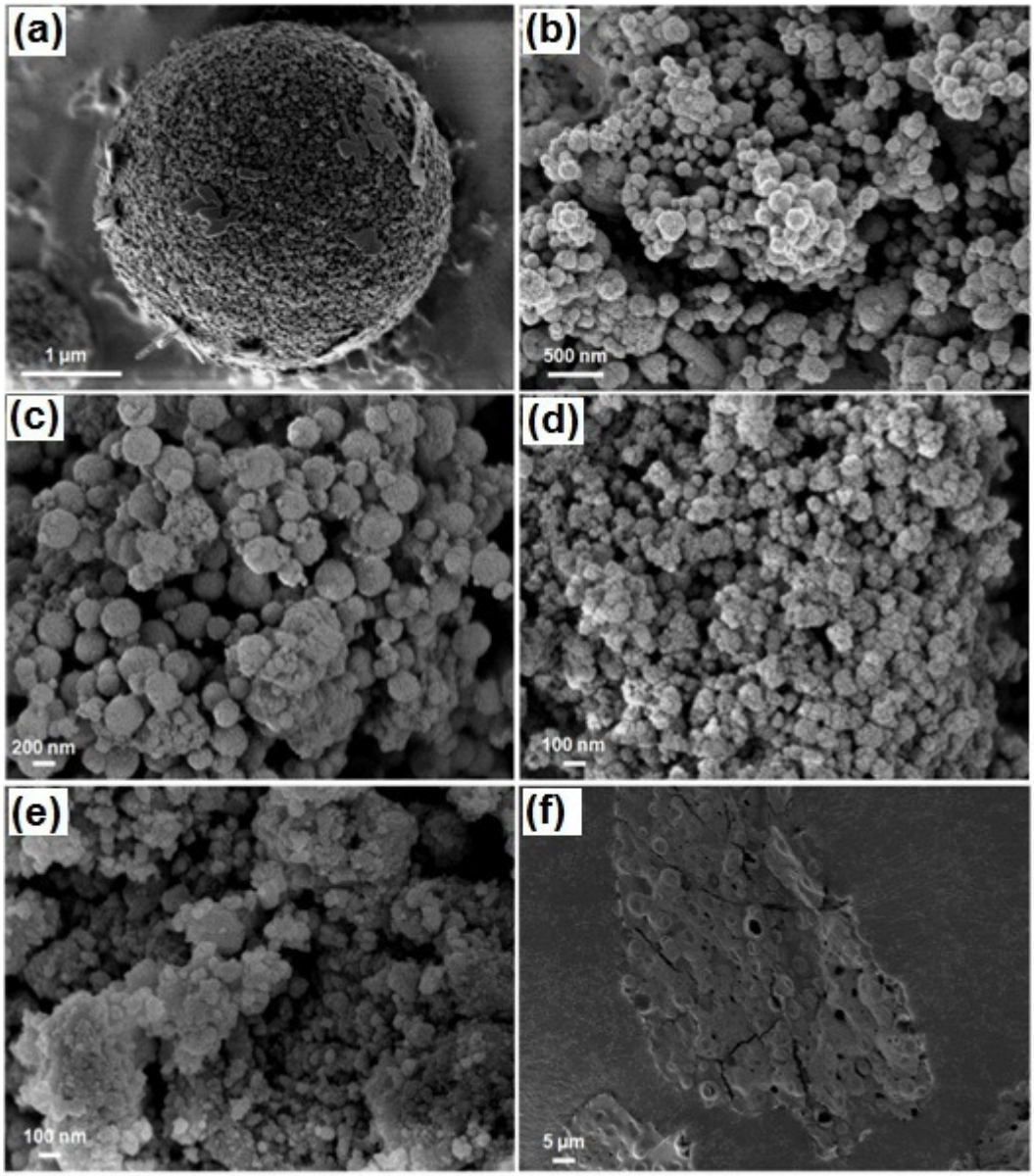

Figure A1. FESEM micrographs of (a) $CuBi_2O_4$, (b) $MnFe_2O_4$, (c) $CuFe_2O_4$, (d) $CoFe_2O_4$, (e) DPA−Fe_2O_3 and (f) $CuAl_2O_4$.

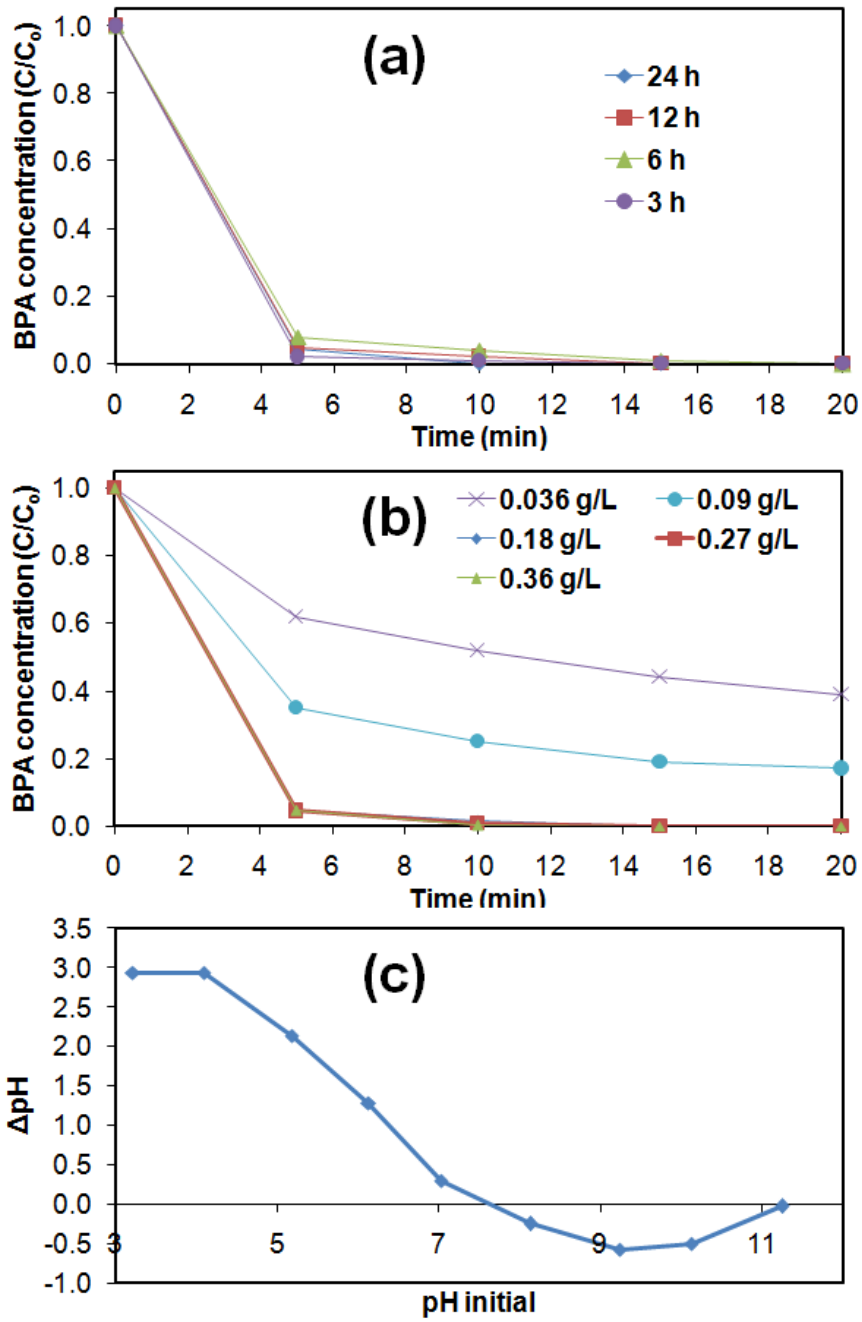

Figure A2. Performance of $CuFe_2O_4$–Fe_2O_3 synthesized at different synthesis time with 0.36 g L^{-1} PMS, (b) Effects of different PMS dosage and (c) pH_{zpc} of $CuFe_2O_4$ fabricated at t = 24 h. Initial conditions: [pH] = 7.0, [catalyst] = 0.20 g L^{-1}, and [BPA] = 5.0 mg L^{-1}.

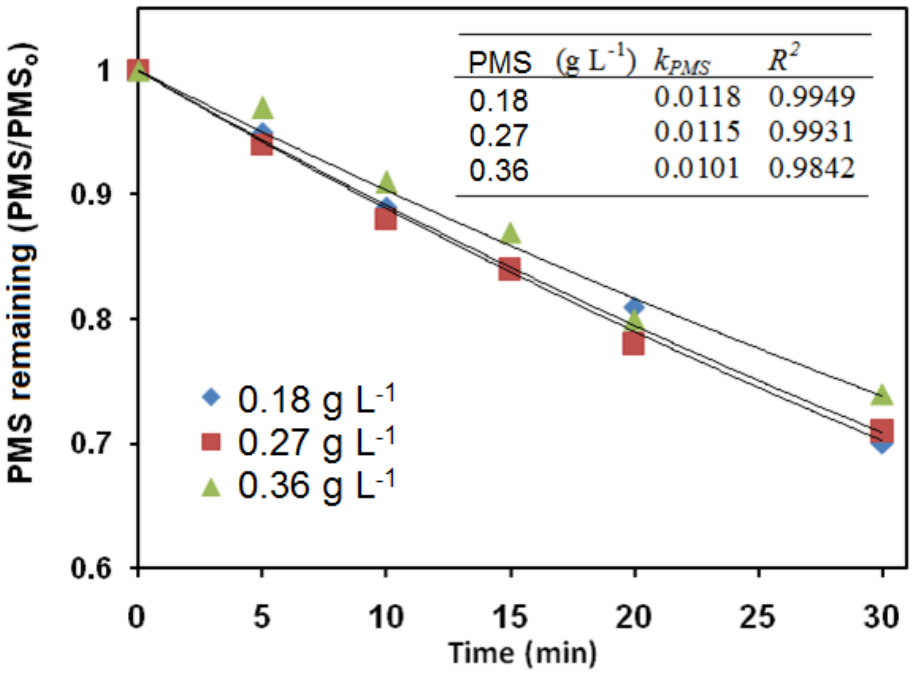

Figure A3. PMS remaining in the solution at various time intervals. Initial conditions: [pH] = 7.0, [catalyst] = 0.05 g L^{-1}, and [BPA] = 5.0 mg L^{-1}.

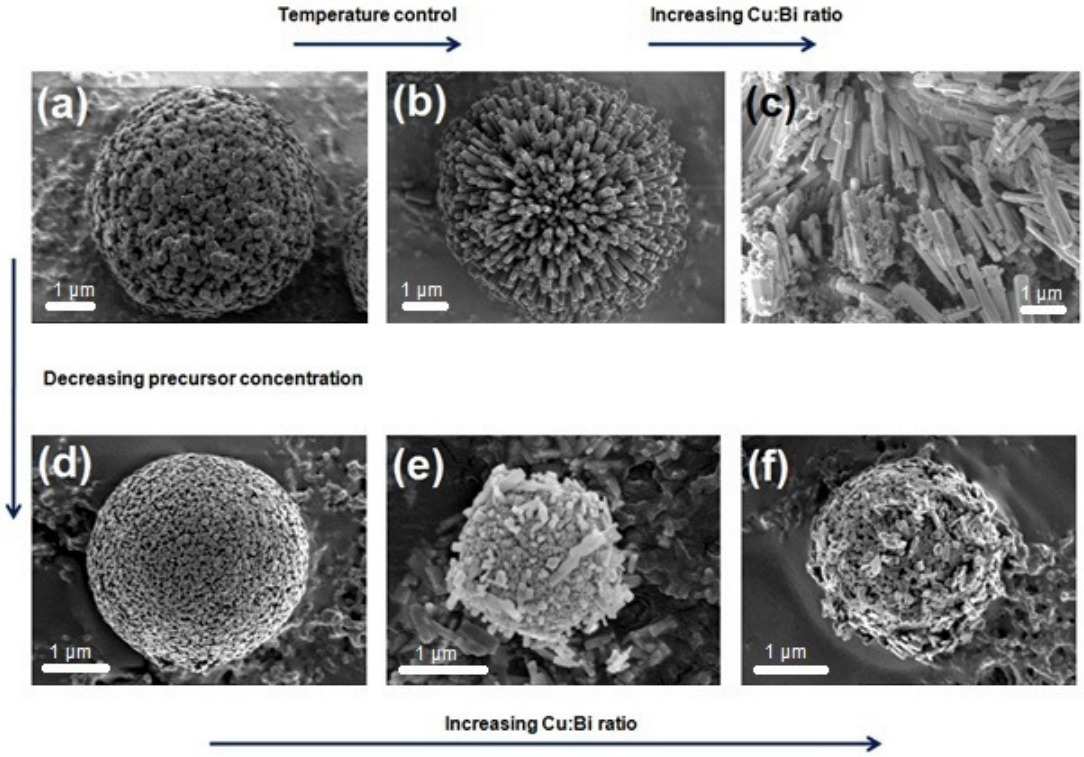

Figure A4. The FESEM images of $CuBi_2O_4$ prepared with different conditions.

Note: **Figure A4** shows the morphology of the $CuBi_2O_4$ prepared with different hydrothermal conditions. From (a), temperature control resulted in a 3−D spherical nanocolumns arrays morphology with hollow core structure (b). Increasing the Cu to Bi concentration above the optimum condition resulted in the destruction of the CuB−H morphology (c). Decreasing the initial precursor concentration resulted in the decrease of microsphere size (d). The microsphere size can also be controlled by increasing the Cu to Bi ratio but resulted in CuO impurity.

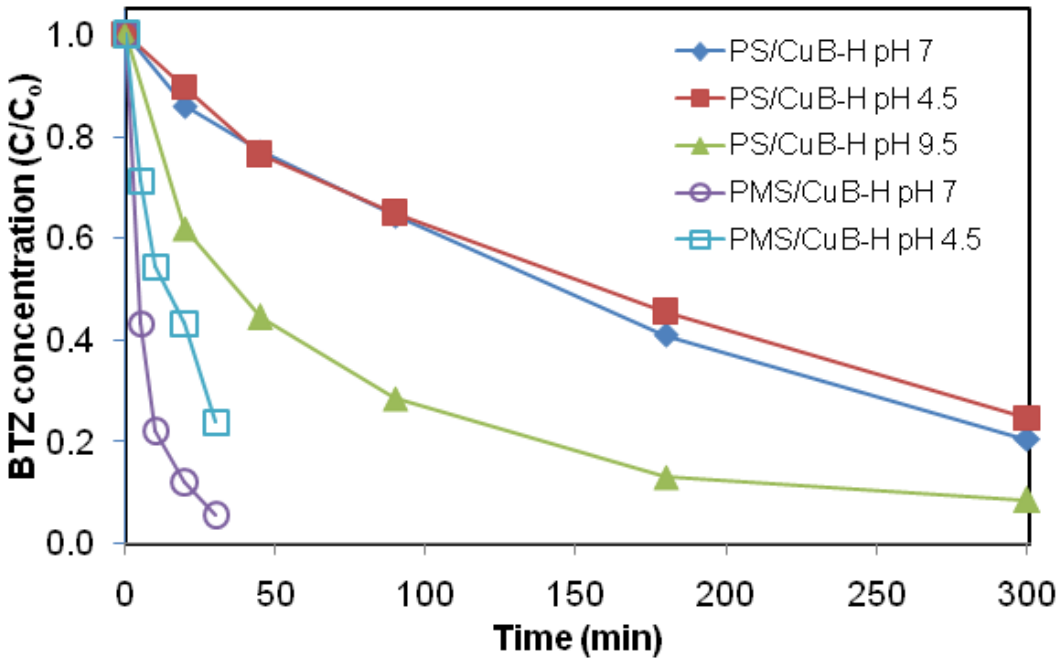

Figure A5. Effects of pH of the degradation of BTZ. Conditions: [CuB−H] = 0.5 g L^{-1}, $[PS]_o$ = 0.1 g L^{-1}, $[PMS]_o$ = 0.05g L^{-1} and $[BTZ]_o$ = 2.5 mg L^{-1}. At pH 9.5 for the PMS/CuB−H system, BTZ was completely removed in less than 5 min.

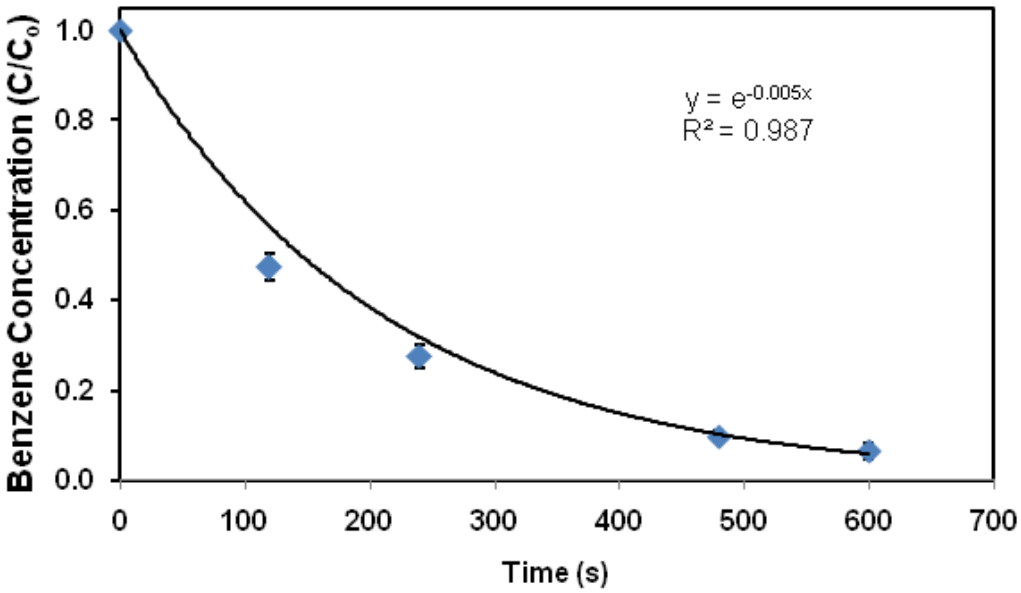

Figure A6. Benzene oxidation by $SO_4^{\bullet-}$. Without catalyst, the benzene removal was < 5%. Initial conditions: [Benzene] = 2.5 mg L^{-1}, [CuB−2.5] = 0.5 g L^{-1}, [PMS] = 0.2 g L^{-1}, [pH] = 7.0.

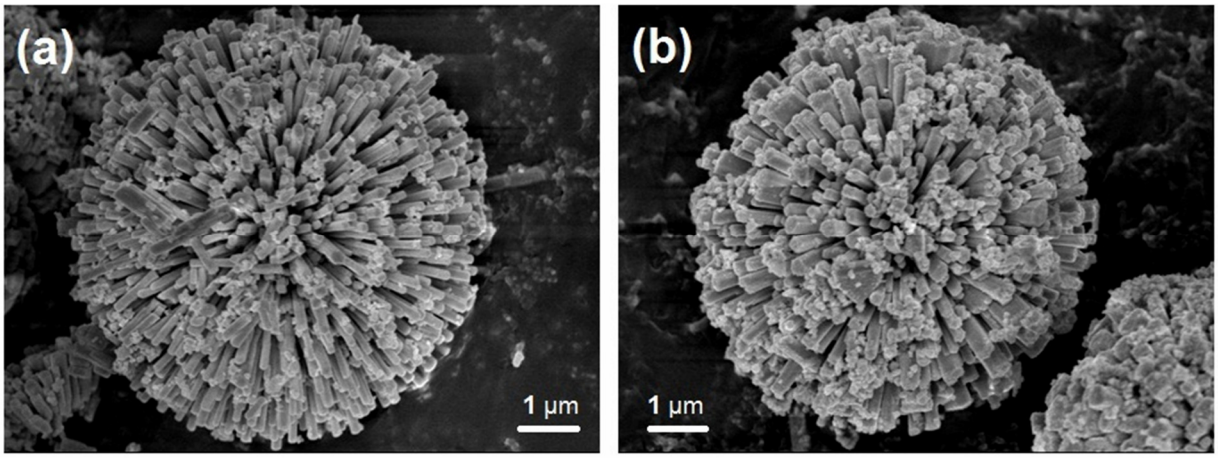

Figure A7: The FESEM images of $CuBi_2O_4$ after catalytic reaction with (a) PS and (b) PMS. Reaction conditions: $[BTZ]_o$ = 2.5 mg L^{-1}, $[PS]_o$ = 0.8 g L^{-1}, $[oxone]_o$ = 0.6 g L^{-1}, t_{PS} = 90 min and t_{PMS} = 10 min.

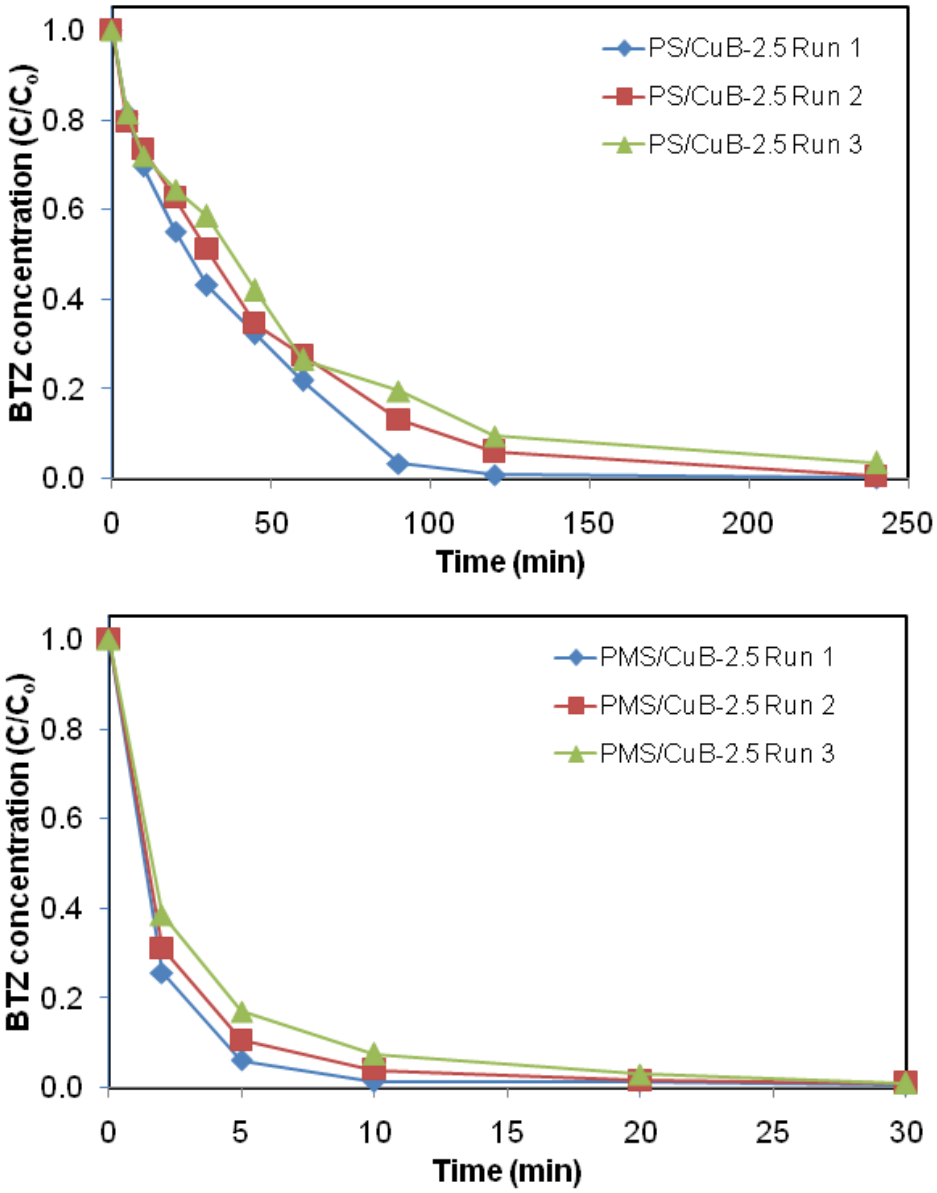

Figure A8. The reusability of CuB−2.5 catalyst for 3 cycles for (a) PS/CuB−2.5 and (b) PMS/CuB−2.5 systems. Conditions: [CuB−2.5] = 0.5 g L^{-1}, $[BTZ]_o$ = 2.5 mg L^{-1}, $[PS]_o$ = 0.8 g L^{-1}, $[PMS]_o$ = 0.2 g L^{-1}.

(a) Initial BTZ solution

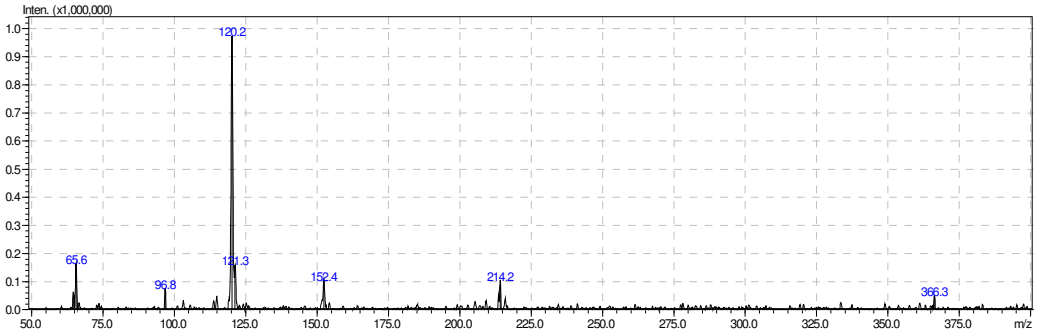

(b) After PS oxidation

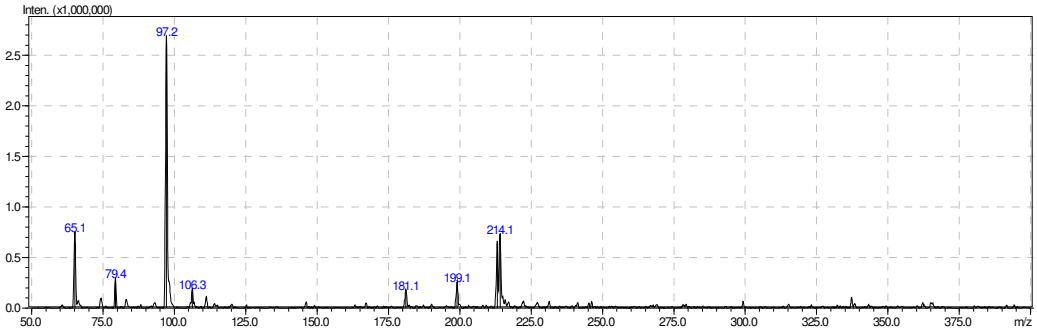

(c) After PMS oxidation

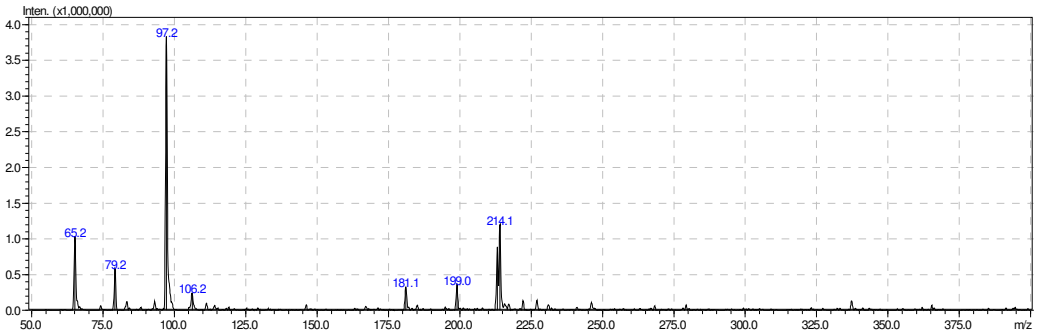

Figure A9. Mass spectrum of initial BTZ solution and BTZ solution after treatment with (b) PS and (c) oxone. Reaction conditions: $[BTZ]_o$ = 2.5 mg L^{-1}, $[CuB{-}2.5]_{PS}$ = 2.0 g L^{-1}, $[CuB{-}2.5]_{PMS}$ = 0.5 g L^{-1}, $[PS]_o$ = 0.8 g L^{-1}, $[PMS]_o$ = 0.2 g L^{-1}, t_{PS} = 90 min and t_{PMS} = 10 min.

References

Abdelkader, E., Nadjia, L., Ahmed, B. 2015. Preparation and characterization of novel CuBi2O4/SnO2 p–n heterojunction with enhanced photocatalytic performance under UVA light irradiation. *Journal of King Saud University - Science*, **27**(1), 76-91.

Abdelkader, E., Nadjia, L., Ahmed, B. 2012. Synthesis, characterization and UV-A light photocatalytic activity of 20 wt%SrO–CuBi2O4 composite. *Applied Surface Science*, **258**(12), 5010-5024.

Abdulkarem, A.M., Li, J., Aref, A.A., Ren, L., Elssfah, E.M., Wang, H., Ge, Y., Yu, Y. 2011. CuBi2O4 single crystal nanorods prepared by hydrothermal method: Growth mechanism and optical properties. *Materials Research Bulletin*, **46**(9), 1443-1450.

Ahn, S., Peterson, T.D., Righter, J., Miles, D.M., Tratnyek, P.G. 2013. Disinfection of Ballast Water with Iron Activated Persulfate. *Environmental Science & Technology*, **47**(20), 11717-11725.

Al-Shamsi, M.A., Thomson, N.R. 2013. Treatment of Organic Compounds by Activated Persulfate Using Nanoscale Zerovalent Iron. *Industrial & Engineering Chemistry Research*, **52**(38), 13564-13571.

Al-Shamsi, M.A., Thomson, N.R., Forsey, S.P. 2013. Iron based bimetallic nanoparticles to activate peroxygens. *Chemical Engineering Journal*, **232**, 555-563.

Andrew Lin, K.-Y., Hsu, F.-K., Lee, W.-D. 2015. Magnetic cobalt-graphene nanocomposite derived from self-assembly of MOFs with graphene oxide as an activator for peroxymonosulfate. *Journal of Materials Chemistry A*, **3**(18), 9480-9490.

Anilkumar, G., Bitterlich, B., Gelalcha, F.G., Tse, M.K., Beller, M. 2007. An efficient biomimetic Fe-catalyzed epoxidation of olefins using hydrogen peroxide. *Chemical Communications*(3), 289-291.

Anipsitakis, G.P., Dionysiou, D.D. 2003. Degradation of Organic Contaminants in Water with Sulfate Radicals Generated by the Conjunction of Peroxymonosulfate with Cobalt. *Environmental Science & Technology*, **37**(20), 4790-4797.

Anipsitakis, G.P., Dionysiou, D.D. 2004. Radical Generation by the Interaction of Transition Metals with Common Oxidants. *Environmental Science & Technology*, **38**(13), 3705-3712.

Anipsitakis, G.P., Dionysiou, D.D., Gonzalez, M.A. 2006. Cobalt-Mediated Activation of Peroxymonosulfate and Sulfate Radical Attack on Phenolic Compounds. Implications of Chloride Ions. *Environmental Science & Technology*, **40**(3), 1000-1007.

Anipsitakis, G.P., Dionysiou, D.D., Gonzalez, M.A. 2005a. Cobalt-Mediated Activation of Peroxymonosulfate and Sulfate Radical Attack on Phenolic Compounds. Implications of Chloride Ions. *Environmental Science & Technology*, **40**(3), 1000-1007.

Anipsitakis, G.P., Stathatos, E., Dionysiou, D.D. 2005b. Heterogeneous Activation of Oxone Using Co3O4. *The Journal of Physical Chemistry B*, **109**(27), 13052-13055.

Anipsitakis, G.P., Tufano, T.P., Dionysiou, D.D. 2008. Chemical and microbial decontamination of pool water using activated potassium peroxymonosulfate. *Water Research*, **42**(12), 2899-2910.

Antoniou, M.G., de la Cruz, A.A., Dionysiou, D.D. 2010a. Degradation of microcystin-LR using sulfate radicals generated through photolysis, thermolysis and e– transfer mechanisms. *Applied Catalysis B: Environmental*, **96**(3–4), 290-298.

Antoniou, M.G., de la Cruz, A.A., Dionysiou, D.D. 2010b. Intermediates and Reaction Pathways from the Degradation of Microcystin-LR with Sulfate Radicals. *Environmental Science & Technology*, **44**(19), 7238-7244.

Arai, T., Konishi, Y., Iwasaki, Y., Sugihara, H., Sayama, K. 2007a. High-Throughput Screening Using Porous Photoelectrode for the Development of Visible-Light-Responsive Semiconductors. *Journal of Combinatorial Chemistry*, **9**(4), 574-581.

Arai, T., Yanagida, M., Konishi, Y., Iwasaki, Y., Sugihara, H., Sayama, K. 2007b. Efficient Complete Oxidation of Acetaldehyde into CO2 over CuBi2O4/WO3 Composite Photocatalyst under Visible and UV Light Irradiation. *The Journal of Physical Chemistry C*, **111**(21), 7574-7577.

Aref, A.A., Muneerah, A.A., Sun, D.M., Wang, H., Qing, C., Tang, Y.W. 2015. Preparation and electrochemical capacitance of MnO2 thin films doped by CuBi2O4. *Materials Science in Semiconductor Processing*, **29**(0), 262-271.

Ayoub, G., Ghauch, A. 2014. Assessment of bimetallic and trimetallic iron-based systems for persulfate activation: Application to sulfamethoxazole degradation. *Chemical Engineering Journal*, **256**, 280-292.

Babuponnusami, A., Muthukumar, K. 2014. A review on Fenton and improvements to the Fenton process for wastewater treatment. *Journal of Environmental Chemical Engineering*, **2**(1), 557-572.

Balakrishnan, T., Kumar, S.D. 2000. The kinetics and mechanism of induced thermal decomposition of peroxomonosulphate by phase transfer catalysts. *Journal of Chemical Sciences*, **112**(4), 497-505.

Batista, A.P.S., Nogueira, R.F.P. 2012. Parameters affecting sulfonamide photo-Fenton degradation – Iron complexation and substituent group. *Journal of Photochemistry and Photobiology A: Chemistry*, **232**, 8-13.

Berglund, S.P., Lee, H.C., Nunez, P.D., Bard, A.J., Mullins, C.B. 2013. Screening of transition and post-transition metals to incorporate into copper oxide and copper bismuth oxide for photoelectrochemical hydrogen evolution. *Physical Chemistry Chemical Physics*, **15**(13), 4554-4565.

Bhatnagar, A., Minocha, A.K., Sillanpää, M. 2010. Adsorptive removal of cobalt from aqueous solution by utilizing lemon peel as biosorbent. *Biochemical Engineering Journal*, **48**(2), 181-186.

Bikkarolla, S.K., Papakonstantinou, P. 2015. CuCo2O4 nanoparticles on nitrogenated graphene as highly efficient oxygen evolution catalyst. *Journal of Power Sources*, **281**, 243-251.

Bo, Y., Huang, B., Zhang, Y., Wang, J., Lau, W.M., Zheng, Z. 2014. Controlled growth of biomorphic CuO via an one-step thermal decomposition on biotemplates. *Powder Technology*, **264**(0), 396-400.

Brandt, C., Van Eldik, R. 1995. Transition metal-catalyzed oxidation of sulfur(IV) oxides. Atmospheric-relevant processes and mechanisms. *Chemical Reviews*, **95**(1), 119-190.

Bridger, K., Patel, R.C., Matijević, E. 1982. Thermodynamics and kinetics of complexation of iron(III) ion by picolinic and dipicolinic acids. *Polyhedron*, **1**(3), 269-275.

Briguglio, I., Piras, S., Corona, P., Gavini, E., Nieddu, M., Boatto, G., Carta, A. Benzotriazole: An overview on its versatile biological behavior. *European Journal of Medicinal Chemistry*(0).

Buxton, G.V., Greenstock, C.L., Helman, W.P., Ross, A.B. 1988. Critical review of rate constants for reactions of hydrated electrons, hydrogen atoms and hydroxyl

radicals (· OH/· O– in aqueous solution. *Journal of physical and chemical reference data*, **17**(2), 513-886.
Byun, S., Davies, S.H., Alpatova, A.L., Corneal, L.M., Baumann, M.J., Tarabara, V.V., Masten, S.J. 2011. Mn oxide coated catalytic membranes for a hybrid ozonation–membrane filtration: Comparison of Ti, Fe and Mn oxide coated membranes for water quality. *Water Research*, **45**(1), 163-170.
Cai, C., Zhang, H., Zhong, X., Hou, L. 2015. Ultrasound enhanced heterogeneous activation of peroxymonosulfate by a bimetallic Fe–Co/SBA-15 catalyst for the degradation of Orange II in water. *Journal of Hazardous Materials*, **283**, 70-79.
Cajthaml, T., Křesinová, Z., Svobodová, K., Möder, M. 2009. Biodegradation of endocrine-disrupting compounds and suppression of estrogenic activity by ligninolytic fungi. *Chemosphere*, **75**(6), 745-750.
Chan, K.H., Chu, W. 2009. Degradation of atrazine by cobalt-mediated activation of peroxymonosulfate: Different cobalt counteranions in homogenous process and cobalt oxide catalysts in photolytic heterogeneous process. *Water Research*, **43**(9), 2513-2521.
Chaplin, B.P., Roundy, E., Guy, K.A., Shapley, J.R., Werth, C.J. 2006. Effects of Natural Water Ions and Humic Acid on Catalytic Nitrate Reduction Kinetics Using an Alumina Supported Pd−Cu Catalyst. *Environmental Science & Technology*, **40**(9), 3075-3081.
Chen, D., Ma, X., Zhou, J., Chen, X., Qian, G. 2014. Sulfate radical-induced degradation of Acid Orange 7 by a new magnetic composite catalyzed peroxymonosulfate oxidation process. *Journal of Hazardous Materials*, **279**, 476-484.
Chen, X., Cai, W., Fu, C., Chen, H., Zhang, Q. 2011. Synthesis and morphology of Ba(Zr0.20Ti0.80)O3 powders obtained by sol–gel method. *Journal of Sol-Gel Science and Technology*, **57**(2), 149-156.
Chen, X., Chen, J., Qiao, X., Wang, D., Cai, X. 2008. Performance of nano-Co3O4/peroxymonosulfate system: Kinetics and mechanism study using Acid Orange 7 as a model compound. *Applied Catalysis B: Environmental*, **80**(1–2), 116-121.
Connor, E.E. 1998. Sulfonamide antibiotics. *Primary Care Update for OB/GYNS*, **5**(1), 32-35.
Corneal, L.M., Baumann, M.J., Masten, S.J., Davies, S.H.R., Tarabara, V.V., Byun, S. 2011. Mn oxide coated catalytic membranes for hybrid ozonation-membrane filtration: Membrane microstructural characterization. *Journal of Membrane Science*, **369**(1–2), 182-187.
Crans Debbie, C., Yang, L., Gaidamauskas, E., Khan, R., Jin, W., Simonis, U. 2003. Applications of Paramagnetic NMR Spectroscopy for Monitoring Transition Metal Complex Stoichiometry and Speciation. in: *Paramagnetic Resonance of Metallobiomolecules*, Vol. 858, American Chemical Society, pp. 304-326.
Das, T.N., Huie, R.E., Neta, P. 1999. Reduction Potentials of SO3•-, SO5•-, and S4O6•3-Radicals in Aqueous Solution. *The Journal of Physical Chemistry A*, **103**(18), 3581-3588.
Davis, M.E., Davis, R.J. 2012. *Fundamentals of chemical reaction engineering*. Courier Corporation.
de Faria, E.H., Ricci, G.P., Marçal, L., Nassar, E.J., Vicente, M.A., Trujillano, R., Gil, A., Korili, S.A., Ciuffi, K.J., Calefi, P.S. 2012. Green and selective oxidation reactions catalyzed by kaolinite covalently grafted with Fe(III) pyridine-carboxylate complexes. *Catalysis Today*, **187**(1), 135-149.
Deng, H., Chen, H., Li, H. 2007. Synthesis of crystal MFe2O4 (M = Mg, Cu, Ni) microspheres. *Materials Chemistry and Physics*, **101**(2–3), 509-513.

Deng, Y., Chen, Y., Chen, B., Ma, J. 2013a. ChemInform Abstract: Preparation, Characterization and Photocatalytic Activity of CuBi2O4/NaTaO3 Coupled Photocatalysts. *ChemInform*, **44**(25), no-no.

Deng, Y., Chen, Y., Chen, B., Ma, J. 2013b. Preparation, characterization and photocatalytic activity of CuBi2O4/NaTaO3 coupled photocatalysts. *Journal of Alloys and Compounds*, **559**(0), 116-122.

Ding, H., Wu, Y., Zou, B., Lou, Q., Zhang, W., Zhong, J., Lu, L., Dai, G. 2016. Simultaneous removal and degradation characteristics of sulfonamide, tetracycline, and quinolone antibiotics by laccase-mediated oxidation coupled with soil adsorption. *Journal of Hazardous Materials*, **307**, 350-358.

Ding, Y.-s., Shen, X.-f., Sithambaram, S., Gomez, S., Kumar, R., Crisostomo, V.M.B., Suib, S.L., Aindow, M. 2005. Synthesis and Catalytic Activity of Cryptomelane-Type Manganese Dioxide Nanomaterials Produced by a Novel Solvent-Free Method. *Chemistry of Materials*, **17**(21), 5382-5389.

Ding, Y., Zhu, L., Huang, A., Zhao, X., Zhang, X., Tang, H. 2012. A heterogeneous Co3O4-Bi2O3 composite catalyst for oxidative degradation of organic pollutants in the presence of peroxymonosulfate. *Catalysis Science & Technology*, **2**(9), 1977-1984.

Ding, Y., Zhu, L., Wang, N., Tang, H. 2013. Sulfate radicals induced degradation of tetrabromobisphenol A with nanoscaled magnetic CuFe2O4 as a heterogeneous catalyst of peroxymonosulfate. *Applied Catalysis B: Environmental*, **129**(0), 153-162.

Dogliotti, L., Hayon, E. 1967. Flash photolysis of per[oxydi]sulfate ions in aqueous solutions. The sulfate and ozonide radical anions. *The Journal of Physical Chemistry*, **71**(8), 2511-2516.

Du, Y., Ma, W., Liu, P., Zou, B., Ma, J. 2016. Magnetic CoFe2O4 nanoparticles supported on titanate nanotubes (CoFe2O4/TNTs) as a novel heterogeneous catalyst for peroxymonosulfate activation and degradation of organic pollutants. *Journal of Hazardous Materials*, **308**, 58-66.

Duan, L., Sun, B., Wei, M., Luo, S., Pan, F., Xu, A., Li, X. 2015a. Catalytic degradation of Acid Orange 7 by manganese oxide octahedral molecular sieves with peroxymonosulfate under visible light irradiation. *Journal of Hazardous Materials*, **285**, 356-365.

Duan, X., Ao, Z., Sun, H., Indrawirawan, S., Wang, Y., Kang, J., Liang, F., Zhu, Z.H., Wang, S. 2015b. Nitrogen-Doped Graphene for Generation and Evolution of Reactive Radicals by Metal-Free Catalysis. *ACS Applied Materials & Interfaces*, **7**(7), 4169-4178.

Duan, X., Ao, Z., Sun, H., Zhou, L., Wang, G., Wang, S. 2015c. Insights into N-doping in single-walled carbon nanotubes for enhanced activation of superoxides: a mechanistic study. *Chemical Communications*, **51**(83), 15249-15252.

Duan, X., Ao, Z., Zhou, L., Sun, H., Wang, G., Wang, S. 2016. Occurrence of radical and nonradical pathways from carbocatalysts for aqueous and nonaqueous catalytic oxidation. *Applied Catalysis B: Environmental*, **188**, 98-105.

Duan, X., Indrawirawan, S., Sun, H., Wang, S. 2015d. Effects of nitrogen-, boron-, and phosphorus-doping or codoping on metal-free graphene catalysis. *Catalysis Today*, **249**, 184-191.

Duan, X., O'Donnell, K., Sun, H., Wang, Y., Wang, S. 2015e. Sulfur and Nitrogen Co-Doped Graphene for Metal-Free Catalytic Oxidation Reactions. *Small*, **11**(25), 3036-3044.

Duan, X., Sun, H., Wang, Y., Kang, J., Wang, S. 2015f. N-Doping-Induced Nonradical Reaction on Single-Walled Carbon Nanotubes for Catalytic Phenol Oxidation. *ACS Catalysis*, **5**(2), 553-559.

Duca, G. 2012. *Homogeneous catalysis with metal complexes: fundamentals and applications*. Springer Science & Business Media.
Eberson, L. 1982. Electron-Transfer Reactions in Organic Chemistry. in: *Advances in Physical Organic Chemistry*, (Eds.) V. Gold, D. Bethell, Vol. Volume 18, Academic Press, pp. 79-185.
Elaziouti, A., Laouedj, N., Bekka, A., Vannier, R.-N. 2015. Preparation and characterization of p–n heterojunction CuBi2O4/CeO2 and its photocatalytic activities under UVA light irradiation. *Journal of King Saud University - Science*, **27**(2), 120-135.
Erjavec, B., Kaplan, R., Djinović, P., Pintar, A. 2013. Catalytic wet air oxidation of bisphenol A model solution in a trickle-bed reactor over titanate nanotube-based catalysts. *Applied Catalysis B: Environmental*, **132–133**(0), 342-352.
Faisal, M., Khan, S.B., Rahman, M.M., Jamal, A., Umar, A. 2011. Ethanol chemi-sensor: Evaluation of structural, optical and sensing properties of CuO nanosheets. *Materials Letters*, **65**(9), 1400-1403.
Fang, G.-D., Dionysiou, D.D., Wang, Y., Al-Abed, S.R., Zhou, D.-M. 2012. Sulfate radical-based degradation of polychlorinated biphenyls: Effects of chloride ion and reaction kinetics. *Journal of Hazardous Materials*, **227–228**(0), 394-401.
Fang, G., Gao, J., Dionysiou, D.D., Liu, C., Zhou, D. 2013. Activation of Persulfate by Quinones: Free Radical Reactions and Implication for the Degradation of PCBs. *Environmental Science & Technology*, **47**(9), 4605-4611.
Fang, J.-Y., Shang, C. 2012. Bromate Formation from Bromide Oxidation by the UV/Persulfate Process. *Environmental Science & Technology*, **46**(16), 8976-8983.
Feng, C., Sugiura, N., Shimada, S., Maekawa, T. 2003. Development of a high performance electrochemical wastewater treatment system. *Journal of Hazardous Materials*, **103**(1–2), 65-78.
Feng, Y., Liu, J., Wu, D., Zhou, Z., Deng, Y., Zhang, T., Shih, K. 2015. Efficient degradation of sulfamethazine with CuCo2O4 spinel nanocatalysts for peroxymonosulfate activation. *Chemical Engineering Journal*, **280**, 514-524.
Feng, Y., Wu, D., Deng, Y., Zhang, T., Shih, K. 2016. Sulfate Radical-mediated Degradation of Sulfadiazine by CuFeO2 Rhombohedral Crystal-catalyzed Peroxymonosulfate: Synergistic Effects and Mechanisms. *Environmental Science & Technology*.
Flanagan, J., Griffith, W.P., Skapski, A.C. 1984. The active principle of Caro's acid, HSO5-: X-ray crystal structure of KHSO5[middle dot]H2O. *Journal of the Chemical Society, Chemical Communications*(23), 1574-1575.
Furman, O.S., Teel, A.L., Watts, R.J. 2010. Mechanism of Base Activation of Persulfate. *Environmental Science & Technology*, **44**(16), 6423-6428.
Gao, B., Lim, T.M., Subagio, D.P., Lim, T.-T. 2010. Zr-doped TiO2 for enhanced photocatalytic degradation of bisphenol A. *Applied Catalysis A: General*, **375**(1), 107-115.
García-Galán, M.J., Díaz-Cruz, M.S., Barceló, D. 2011. Occurrence of sulfonamide residues along the Ebro river basin: Removal in wastewater treatment plants and environmental impact assessment. *Environment International*, **37**(2), 462-473.
García, K.E., Barrero, C.A., Morales, A.L., Greneche, J.M. 2008. Characterization of akaganeite synthesized in presence of Al3+, Cr3+, and Cu2+ ions and urea. *Materials Chemistry and Physics*, **112**(1), 120-126.
Garoma, T., Umamaheshwar, S.K., Mumper, A. 2010. Removal of sulfadiazine, sulfamethizole, sulfamethoxazole, and sulfathiazole from aqueous solution by ozonation. *Chemosphere*, **79**(8), 814-820.
Gerken, J.B., McAlpin, J.G., Chen, J.Y.C., Rigsby, M.L., Casey, W.H., Britt, R.D., Stahl, S.S. 2011. Electrochemical Water Oxidation with Cobalt-Based Electrocatalysts

from pH 0–14: The Thermodynamic Basis for Catalyst Structure, Stability, and Activity. *Journal of the American Chemical Society*, **133**(36), 14431-14442.
Ghanbari, F., Moradi, M., Manshouri, M. 2014. Textile wastewater decolorization by zero valent iron activated peroxymonosulfate: Compared with zero valent copper. *Journal of Environmental Chemical Engineering*, **2**(3), 1846-1851.
Ghauch, A., Tuqan, A.M., Kibbi, N. 2012. Ibuprofen removal by heated persulfate in aqueous solution: A kinetics study. *Chemical Engineering Journal*, **197**, 483-492.
Gilbert, B.C., Stell, J.K. 1990. Mechanisms of peroxide decomposition: an electron paramagnetic resonance study of the reaction of the peroxomonosulphate anion (HOOSO) with CuI. A marked contrast in behaviour with that of TiIII and FeII. *Journal of the Chemical Society, Faraday Transactions*, **86**(19), 3261-3266.
Gilbert, B.C., Stell, J.K., Whitwood, A.C., Halliwell, C., Sanderson, W.R. 1991. Mechanisms of peroxide decomposition. An EPR investigation of the reactions between some transition metal ions (Ti, Fe, Cu) and monoperoxyphthalic acid and its anion. *Journal of the Chemical Society, Perkin Transactions 2*(5), 629-634.
Gimeno, O., Rivas, J., Carbajo, M., Borralho, T. 2009. Catalytic Decomposition of Potassium Monopersulfate. The Kinetics. *WORLD*, **57**, 223-226.
Gong, F., Wang, L., Li, D., Zhou, F., Yao, Y., Lu, W., Huang, S., Chen, W. 2015. An effective heterogeneous iron-based catalyst to activate peroxymonosulfate for organic contaminants removal. *Chemical Engineering Journal*, **267**, 102-110.
Guan, Y.-H., Ma, J., Li, X.-C., Fang, J.-Y., Chen, L.-W. 2011. Influence of pH on the Formation of Sulfate and Hydroxyl Radicals in the UV/Peroxymonosulfate System. *Environmental Science & Technology*, **45**(21), 9308-9314.
Guan, Y.-H., Ma, J., Ren, Y.-M., Liu, Y.-L., Xiao, J.-Y., Lin, L.-q., Zhang, C. 2013. Efficient degradation of atrazine by magnetic porous copper ferrite catalyzed peroxymonosulfate oxidation via the formation of hydroxyl and sulfate radicals. *Water Research*, **47**(14), 5431-5438.
Guo, W., Su, S., Yi, C., Ma, Z. 2013. Degradation of antibiotics amoxicillin by Co3O4-catalyzed peroxymonosulfate system. *Environmental Progress & Sustainable Energy*, **32**(2), 193-197.
Guo, Y., Xu, B., Qi, F. 2016. A novel ceramic membrane coated with MnO2–Co3O4 nanoparticles catalytic ozonation for benzophenone-3 degradation in aqueous solution: Fabrication, characterization and performance. *Chemical Engineering Journal*, **287**, 381-389.
Hahn, N.T., Holmberg, V.C., Korgel, B.A., Mullins, C.B. 2012. Electrochemical Synthesis and Characterization of p-CuBi2O4 Thin Film Photocathodes. *The Journal of Physical Chemistry C*, **116**(10), 6459-6466.
Halvorson, H., Doi, R., Church, B. 1958. Dormancy of Bacterial Endospores: Regulation of Electron Transport by Dipicolinic Acid. *Proceedings of the National Academy of Sciences of the United States of America*, **44**(12), 1171-1180.
Hardjono, Y., Sun, H., Tian, H., Buckley, C.E., Wang, S. 2011. Synthesis of Co oxide doped carbon aerogel catalyst and catalytic performance in heterogeneous oxidation of phenol in water. *Chemical Engineering Journal*, **174**(1), 376-382.
Harman, B.I., Koseoglu, H., Yigit, N.O., Beyhan, M., Kitis, M. 2010. The use of iron oxide-coated ceramic membranes in removing natural organic matter and phenol from waters. *Desalination*, **261**(1–2), 27-33.
Haynes, W.M. 2013. *CRC Handbook of Chemistry and Physics, 94th Edition*. CRC Press.
Hofs, B., Ogier, J., Vries, D., Beerendonk, E.F., Cornelissen, E.R. 2011. Comparison of ceramic and polymeric membrane permeability and fouling using surface water. *Separation and Purification Technology*, **79**(3), 365-374.

Hu, L., Flanders, P.M., Miller, P.L., Strathmann, T.J. 2007. Oxidation of sulfamethoxazole and related antimicrobial agents by TiO2 photocatalysis. *Water Research*, **41**(12), 2612-2626.

Hu, L., Yang, F., Zou, L., Yuan, H., Hu, X. 2015. CoFe/SBA-15 catalyst coupled with peroxymonosulfate for heterogeneous catalytic degradation of rhodamine B in water. *Chinese Journal of Catalysis*, **36**(10), 1785-1797.

Hu, Z.-T., Chen, B., Lim, T.-T. 2014. Single-crystalline Bi2Fe4O9 synthesized by low-temperature co-precipitation: performance as photo- and Fenton catalysts. *RSC Advances*, **4**(53), 27820-27829.

Huang, K.-C., Zhao, Z., Hoag, G.E., Dahmani, A., Block, P.A. 2005. Degradation of volatile organic compounds with thermally activated persulfate oxidation. *Chemosphere*, **61**(4), 551-560.

Huang, Y.-F., Huang, Y.-H. 2009. Behavioral evidence of the dominant radicals and intermediates involved in Bisphenol A degradation using an efficient Co2+/PMS oxidation process. *Journal of Hazardous Materials*, **167**(1–3), 418-426.

Huang, Z., Bao, H., Yao, Y., Lu, J., Lu, W., Chen, W. 2015. Key role of activated carbon fibers in enhanced decomposition of pollutants using heterogeneous cobalt/peroxymonosulfate system. *Journal of Chemical Technology and Biotechnology*.

Huang, Z., Bao, H., Yao, Y., Lu, W., Chen, W. 2014. Novel green activation processes and mechanism of peroxymonosulfate based on supported cobalt phthalocyanine catalyst. *Applied Catalysis B: Environmental*, **154–155**(0), 36-43.

Huie, R.E., Clifton, C.L. 1990. Temperature dependence of the rate constants for reactions of the sulfate radical, SO4-, with anions. *The Journal of Physical Chemistry*, **94**(23), 8561-8567.

Huie, R.E., Clifton, C.L., Neta, P. 1991. Electron transfer reaction rates and equilibria of the carbonate and sulfate radical anions. *International Journal of Radiation Applications and Instrumentation. Part C. Radiation Physics and Chemistry*, **38**(5), 477-481.

Hussain, I., Zhang, Y., Huang, S., Du, X. 2012. Degradation of p-chloroaniline by persulfate activated with zero-valent iron. *Chemical Engineering Journal*, **203**, 269-276.

Indrawirawan, S., Sun, H., Duan, X., Wang, S. 2015a. Low temperature combustion synthesis of nitrogen-doped graphene for metal-free catalytic oxidation. *Journal of Materials Chemistry A*, **3**(7), 3432-3440.

Indrawirawan, S., Sun, H., Duan, X., Wang, S. 2015b. Nanocarbons in different structural dimensions (0–3D) for phenol adsorption and metal-free catalytic oxidation. *Applied Catalysis B: Environmental*, **179**, 352-362.

Jen, J.-F., Leu, M.-F., Yang, T.C. 1998. Determination of hydroxyl radicals in an advanced oxidation process with salicylic acid trapping and liquid chromatography. *Journal of Chromatography A*, **796**(2), 283-288.

Ji, F., Li, C., Deng, L. 2011. Performance of CuO/Oxone system: Heterogeneous catalytic oxidation of phenol at ambient conditions. *Chemical Engineering Journal*, **178**(0), 239-243.

Ji, F., Li, C., Liu, Y., Liu, P. 2014. Heterogeneous activation of peroxymonosulfate by Cu/ZSM5 for decolorization of Rhodamine B. *Separation and Purification Technology*, **135**(0), 1-6.

Ji, F., Li, C., Wei, X., Yu, J. 2013. Efficient performance of porous Fe2O3 in heterogeneous activation of peroxymonosulfate for decolorization of Rhodamine B. *Chemical Engineering Journal*, **231**(0), 434-440.

Ji, Y., Dong, C., Kong, D., Lu, J., Zhou, Q. 2015. Heat-activated persulfate oxidation of atrazine: Implications for remediation of groundwater contaminated by herbicides. *Chemical Engineering Journal*, **263**, 45-54.

Johnson, D.A. 1982. *Some Thermodynamic Aspects of Inorganic Chemistry*. Cambridge University Press.

Kennedy, R.J., Stock, A.M. 1960. The Oxidation of Organic Substances by Potassium Peroxymonosulfate. *The Journal of Organic Chemistry*, **25**(11), 1901-1906.

Keykavoos, R., Mankidy, R., Ma, H., Jones, P., Soltan, J. 2013. Mineralization of bisphenol A by catalytic ozonation over alumina. *Separation and Purification Technology*, **107**(0), 310-317.

Khataee, A.R., Mirzajani, O. 2010. UV/peroxydisulfate oxidation of C. I. Basic Blue 3: Modeling of key factors by artificial neural network. *Desalination*, **251**(1–3), 64-69.

Kim, J., Edwards, J.O. 1995. A study of cobalt catalysis and copper modification in the coupled decompositions of hydrogen peroxide and peroxomonosulfate ion. *Inorganica Chimica Acta*, **235**(1–2), 9-13.

Klinbumrung, A., Thongtem, T., Thongtem, S. 2014. Characterization and gas sensing properties of CuO synthesized by DC directly applying voltage. *Applied Surface Science*, **313**(0), 640-646.

Kolthoff, I.M., Miller, I.K. 1951. The Chemistry of Persulfate. I. The Kinetics and Mechanism of the Decomposition of the Persulfate Ion in Aqueous Medium1. *Journal of the American Chemical Society*, **73**(7), 3055-3059.

Kosmulski, M. 2009. Compilation of PZC and IEP of sparingly soluble metal oxides and hydroxides from literature. *Advances in Colloid and Interface Science*, **152**(1–2), 14-25.

Krasner, S.W. 2009. The formation and control of emerging disinfection by-products of health concern. *Philosophical Transactions of the Royal Society of London A: Mathematical, Physical and Engineering Sciences*, **367**(1904), 4077-4095.

Kušić, H., Koprivanac, N., Selanec, I. 2006. Fe-exchanged zeolite as the effective heterogeneous Fenton-type catalyst for the organic pollutant minimization: UV irradiation assistance. *Chemosphere*, **65**(1), 65-73.

Kwak, B.K., Park, D.S., Yun, Y.S., Yi, J. 2012. Preparation and characterization of nanocrystalline CuAl2O4 spinel catalysts by sol–gel method for the hydrogenolysis of glycerol. *Catalysis Communications*, **24**(0), 90-95.

Lau, T.K., Chu, W., Graham, N.J.D. 2006. The Aqueous Degradation of Butylated Hydroxyanisole by UV/S2O82-: Study of Reaction Mechanisms via Dimerization and Mineralization. *Environmental Science & Technology*, **41**(2), 613-619.

Lee, Y.-C., Lo, S.-L., Kuo, J., Huang, C.-P. 2013. Promoted degradation of perfluorooctanic acid by persulfate when adding activated carbon. *Journal of Hazardous Materials*, **261**, 463-469.

Li, J., Zhu, J., Liu, X. 2014. Ultrafine silver nanoparticles obtained from ethylene glycol at room temperature: catalyzed by tungstate ions. *Dalton Transactions*, **43**(1), 132-137.

Li, W., Wu, P.-x., Zhu, Y., Huang, Z.-j., Lu, Y.-h., Li, Y.-w., Dang, Z., Zhu, N.-w. 2015. Catalytic degradation of bisphenol A by CoMnAl mixed metal oxides catalyzed peroxymonosulfate: Performance and mechanism. *Chemical Engineering Journal*, **279**, 93-102.

Li, X., Wang, Z., Zhang, B., Rykov, A.I., Ahmed, M.A., Wang, J. 2016. FexCo3−xO4 nanocages derived from nanoscale metal–organic frameworks for removal of bisphenol A by activation of peroxymonosulfate. *Applied Catalysis B: Environmental*, **181**, 788-799.

Li, Y., Zhang, Y., Li, J., Zheng, X. 2011. Enhanced removal of pentachlorophenol by a novel composite: Nanoscale zero valent iron immobilized on organobentonite. *Environmental Pollution*, **159**(12), 3744-3749.

Liang, C.-J., Huang, S.-C. 2012. Kinetic model for sulfate/hydroxyl radical oxidation of methylene blue in a thermally-activated persulfate system at various pH and temperatures. *change*, **2**, 2.

Liang, C., Wang, C.-W. 2013. Assessing acute toxicity potential of persulfate ISCO treated water. *Chemosphere*, **93**(11), 2711-2716.

Liang, H., Sun, H., Patel, A., Shukla, P., Zhu, Z.H., Wang, S. 2012. Excellent performance of mesoporous Co3O4/MnO2 nanoparticles in heterogeneous activation of peroxymonosulfate for phenol degradation in aqueous solutions. *Applied Catalysis B: Environmental*, **127**(0), 330-335.

Liang, X., Wang, M., Chen, X., Zha, J., Chen, H., Zhu, L., Wang, Z. 2014. Endocrine disrupting effects of benzotriazole in rare minnow (Gobiocypris rarus) in a sex-dependent manner. *Chemosphere*, **112**(0), 154-162.

Lim, T.-T., Yap, P.-S., Srinivasan, M., Fane, A.G. 2011. TiO2/AC Composites for Synergistic Adsorption-Photocatalysis Processes: Present Challenges and Further Developments for Water Treatment and Reclamation. *Critical Reviews in Environmental Science and Technology*, **41**(13), 1173-1230.

Liu, C.S., Shih, K., Sun, C.X., Wang, F. 2012. Oxidative degradation of propachlor by ferrous and copper ion activated persulfate. *Science of The Total Environment*, **416**(0), 507-512.

Liu, J., Jiang, G., Liu, Y., Di, J., Wang, Y., Zhao, Z., Sun, Q., Xu, C., Gao, J., Duan, A., Liu, J., Wei, Y., Zhao, Y., Jiang, L. 2014. Hierarchical Macro-meso-microporous ZSM-5 Zeolite Hollow Fibers With Highly Efficient Catalytic Cracking Capability. *Scientific Reports*, **4**, 7276.

Liu, J., Zhao, Z., Shao, P., Cui, F. 2015a. Activation of peroxymonosulfate with magnetic Fe3O4–MnO2 core–shell nanocomposites for 4-chlorophenol degradation. *Chemical Engineering Journal*, **262**, 854-861.

Liu, K., Lu, J., Ji, Y. 2015b. Formation of brominated disinfection by-products and bromate in cobalt catalyzed peroxymonosulfate oxidation of phenol. *Water Research*, **84**, 1-7.

Lopez-Ramon, M.V., Stoeckli, F., Moreno-Castilla, C., Carrasco-Marin, F. 1999. On the characterization of acidic and basic surface sites on carbons by various techniques. *Carbon*, **37**(8), 1215-1221.

Lou, X., Wu, L., Guo, Y., Chen, C., Wang, Z., Xiao, D., Fang, C., Liu, J., Zhao, J., Lu, S. 2014. Peroxymonosulfate activation by phosphate anion for organics degradation in water. *Chemosphere*, **117**(0), 582-585.

Luo, S., Duan, L., Sun, B., Wei, M., Li, X., Xu, A. 2015. Manganese oxide octahedral molecular sieve (OMS-2) as an effective catalyst for degradation of organic dyes in aqueous solutions in the presence of peroxymonosulfate. *Applied Catalysis B: Environmental*, **164**, 92-99.

Lutze, H.V., Bakkour, R., Kerlin, N., von Sonntag, C., Schmidt, T.C. 2014. Formation of bromate in sulfate radical based oxidation: Mechanistic aspects and suppression by dissolved organic matter. *Water Research*, **53**, 370-377.

Lutze, H.V., Bircher, S., Rapp, I., Kerlin, N., Bakkour, R., Geisler, M., von Sonntag, C., Schmidt, T.C. 2015a. Degradation of Chlorotriazine Pesticides by Sulfate Radicals and the Influence of Organic Matter. *Environmental Science & Technology*, **49**(3), 1673-1680.

Lutze, H.V., Kerlin, N., Schmidt, T.C. 2015b. Sulfate radical-based water treatment in presence of chloride: Formation of chlorate, inter-conversion of sulfate radicals into hydroxyl radicals and influence of bicarbonate. *Water Research*, **72**, 349-360.

Mahdi Ahmed, M., Barbati, S., Doumenq, P., Chiron, S. 2012. Sulfate radical anion oxidation of diclofenac and sulfamethoxazole for water decontamination. *Chemical Engineering Journal*, **197**(0), 440-447.

Matamoros, V., Jover, E., Bayona, J.M. 2010. Occurrence and fate of benzothiazoles and benzotriazoles in constructed wetlands. in: *Water Science and Technology*, Vol. 61, pp. 191-198.

Matta, R., Tlili, S., Chiron, S., Barbati, S. 2011. Removal of carbamazepine from urban wastewater by sulfate radical oxidation. *Environmental Chemistry Letters*, **9**(3), 347-353.

Metcalfe, C.D., Metcalfe, T.L., Kiparissis, Y., Koenig, B.G., Khan, C., Hughes, R.J., Croley, T.R., March, R.E., Potter, T. 2001. Estrogenic potency of chemicals detected in sewage treatment plant effluents as determined by in vivo assays with Japanese medaka (Oryzias latipes). *Environmental Toxicology and Chemistry*, **20**(2), 297-308.

Michael-Kordatou, I., Iacovou, M., Frontistis, Z., Hapeshi, E., Dionysiou, D.D., Fatta-Kassinos, D. 2015. Erythromycin oxidation and ERY-resistant Escherichia coli inactivation in urban wastewater by sulfate radical-based oxidation process under UV-C irradiation. *Water Research*, **85**, 346-358.

Moser, J., Punchihewa, S., Infelta, P.P., Graetzel, M. 1991. Surface complexation of colloidal semiconductors strongly enhances interfacial electron-transfer rates. *Langmuir*, **7**(12), 3012-3018.

Muhammad, S., Saputra, E., Sun, H., Ang, H.-M., Tadé, M.O., Wang, S. 2012a. Heterogeneous Catalytic Oxidation of Aqueous Phenol on Red Mud-Supported Cobalt Catalysts. *Industrial & Engineering Chemistry Research*, **51**(47), 15351-15359.

Muhammad, S., Saputra, E., Sun, H., Izidoro, J.d.C., Fungaro, D.A., Ang, H.M., Tade, M.O., Wang, S. 2012b. Coal fly ash supported Co3O4 catalysts for phenol degradation using peroxymonosulfate. *RSC Advances*, **2**(13), 5645-5650.

Muhammad, S., Shukla, P.R., Tadé, M.O., Wang, S. 2012c. Heterogeneous activation of peroxymonosulphate by supported ruthenium catalysts for phenol degradation in water. *Journal of Hazardous Materials*, **215–216**(0), 183-190.

Muthukrishnaraj, A., Vadivel, S., Joni, I.M., Balasubramanian, N. 2015. Development of reduced graphene oxide/CuBi2O4 hybrid for enhanced photocatalytic behavior under visible light irradiation. *Ceramics International*, **41**(5, Part A), 6164-6168.

Nagarajan, V., Fessenden, R.W. 1985. Flash photolysis of transient radicals. 1. X2- with X = Cl, Br, I, and SCN. *The Journal of Physical Chemistry*, **89**(11), 2330-2335.

Nakabayashi, Y., Nishikawa, M., Nosaka, Y. 2014. Fabrication of CuBi2O4 photocathode through novel anodic electrodeposition for solar hydrogen production. *Electrochimica Acta*, **125**(0), 191-198.

Negri, A.R., Jimenez, G., Hill, R.T., Francis, R.C. 1998. Caroate delignification. Part 4: the generation and role of hydroxyl radicals. *Tappi journal*, **81**(5), 241-246.

Neta, P., Huie, R.E., Ross, A.B. 1988. Rate Constants for Reactions of Inorganic Radicals in Aqueous Solution. *Journal of Physical and Chemical Reference Data*, **17**(3), 1027-1284.

Neta, P., Madhavan, V., Zemel, H., Fessenden, R.W. 1977. Rate constants and mechanism of reaction of sulfate radical anion with aromatic compounds. *Journal of the American Chemical Society*, **99**(1), 163-164.

Nfodzo, P., Choi, H. 2011. Sulfate radicals destroy pharmaceuticals and personal care products. *Environmental Engineering Science*, **28**(8), 605-609.

Nguyen, L.N., Hai, F.I., Yang, S., Kang, J., Leusch, F.D.L., Roddick, F., Price, W.E., Nghiem, L.D. 2013. Removal of trace organic contaminants by an MBR

comprising a mixed culture of bacteria and white-rot fungi. *Bioresource Technology*, **148**(0), 234-241.
Ni, H.-G., Lu, F.-H., Luo, X.-L., Tian, H.-Y., Zeng, E.Y. 2008. Occurrence, Phase Distribution, and Mass Loadings of Benzothiazoles in Riverine Runoff of the Pearl River Delta, China. *Environmental Science & Technology*, **42**(6), 1892-1897.
Nishikawa, M., Hiura, S., Mitani, Y., Nosaka, Y. 2013. Enhanced photocatalytic activity of BiVO4 by co-grafting of metal ions and combining with CuBi2O4. *Journal of Photochemistry and Photobiology A: Chemistry*, **262**(0), 52-56.
Oh, S.-Y., Kim, H.-W., Park, J.-M., Park, H.-S., Yoon, C. 2009. Oxidation of polyvinyl alcohol by persulfate activated with heat, Fe2+, and zero-valent iron. *Journal of Hazardous Materials*, **168**(1), 346-351.
Olmez-Hanci, T., Arslan-Alaton, I. Comparison of sulfate and hydroxyl radical based advanced oxidation of phenol. *Chemical Engineering Journal*(0).
Olmez-Hanci, T., Arslan-Alaton, I., Genc, B. 2013. Bisphenol A treatment by the hot persulfate process: Oxidation products and acute toxicity. *Journal of Hazardous Materials*, **263, Part 2**, 283-290.
Padmaja, S., Neta, P., Huie, R.E. 1993. Rate constants for some reactions of inorganic radicals with inorganic ions. Temperature and solvent dependence. *International Journal of Chemical Kinetics*, **25**(6), 445-455.
Pagano, M., Volpe, A., Mascolo, G., Lopez, A., Locaputo, V., Ciannarella, R. 2012. Peroxymonosulfate–Co(II) oxidation system for the removal of the non-ionic surfactant Brij 35 from aqueous solution. *Chemosphere*, **86**(4), 329-334.
Page, S.E., Arnold, W.A., McNeill, K. 2010. Terephthalate as a probe for photochemically generated hydroxyl radical. *Journal of Environmental Monitoring*, **12**(9), 1658-1665.
Parfitt, R.L., Smart, R.S.C. 1977. Infrared spectra from binuclear bridging complexes of sulphate adsorbed on goethite ([small alpha]-FeOOH). *Journal of the Chemical Society, Faraday Transactions 1: Physical Chemistry in Condensed Phases*, **73**(0), 796-802.
Parfitt, R.L., Smart, R.S.C. 1978. The Mechanism of Sulfate Adsorption on Iron Oxides. *Soil Science Society of America Journal*, **42**(1), 48-50.
Park, H.S., Lee, C.-Y., Reisner, E. 2014. Photoelectrochemical reduction of aqueous protons with a CuO|CuBi2O4 heterojunction under visible light irradiation. *Physical Chemistry Chemical Physics*, **16**(41), 22462-22465.
Patil, R., Kelkar, S., Naphade, R., Ogale, S. 2014. Low temperature grown CuBi2O4 with flower morphology and its composite with CuO nanosheets for photoelectrochemical water splitting. *Journal of Materials Chemistry A*, **2**(10), 3661-3668.
Peng, W., Liu, S., Sun, H., Yao, Y., Zhi, L., Wang, S. 2013. Synthesis of porous reduced graphene oxide as metal-free carbon for adsorption and catalytic oxidation of organics in water. *Journal of Materials Chemistry A*, **1**(19), 5854-5859.
Petrie, B., Barden, R., Kasprzyk-Hordern, B. 2015. A review on emerging contaminants in wastewaters and the environment: Current knowledge, understudied areas and recommendations for future monitoring. *Water Research*, **72**, 3-27.
Phillips, G.O., Power, D.M., Sewart, M.C.G. 1973. Effects of γ-Irradiation on Sulphonamides. *Radiation Research*, **53**(2), 204-215.
Pi, Y., Schumacher, J., Jekel, M. 2005. The Use of para-Chlorobenzoic Acid (pCBA) as an Ozone/Hydroxyl Radical Probe Compound. *Ozone: Science & Engineering*, **27**(6), 431-436.
Pierre, J.L., Fontecave, M. 1999. Iron and activated oxygen species in biology: The basic chemistry. *Biometals*, **12**(3), 195-199.

Popova, T.V., Aksenova, N.V. 2003. Complexes of Copper in Unstable Oxidation States. *Russian Journal of Coordination Chemistry*, **29**(11), 743-765.

Qi, F., Chu, W., Xu, B. 2014. Modeling the heterogeneous peroxymonosulfate/Co-MCM41 process for the degradation of caffeine and the study of influence of cobalt sources. *Chemical Engineering Journal*, **235**(0), 10-18.

Qin, F.X., Jia, S.Y., Liu, Y., Han, X., Ren, H.T., Zhang, W.W., Hou, J.W., Wu, S.H. 2013. Metal-organic framework as a template for synthesis of magnetic CoFe2O4 nanocomposites for phenol degradation. *Materials Letters*.

Qiu, W., Zheng, Y. 2009. Removal of lead, copper, nickel, cobalt, and zinc from water by a cancrinite-type zeolite synthesized from fly ash. *Chemical Engineering Journal*, **145**(3), 483-488.

Rani, S.K., Easwaramoorthy, D., Bilal, I.M., Palanichamy, M. 2009. Studies on Mn(II)-catalyzed oxidation of α-amino acids by peroxomonosulphate in alkaline medium-deamination and decarboxylation: A kinetic approach. *Applied Catalysis A: General*, **369**(1–2), 1-7.

Rastogi, A., Al-Abed, S.R., Dionysiou, D.D. 2009. Sulfate radical-based ferrous–peroxymonosulfate oxidative system for PCBs degradation in aqueous and sediment systems. *Applied Catalysis B: Environmental*, **85**(3–4), 171-179.

Reints, W., Pratt, D.A., Korth, H.-G., Mulder, P. 2000. O−O Bond Dissociation Enthalpy in Di(trifluoromethyl) Peroxide (CF3OOCF3) as Determined by Very Low Pressure Pyrolysis. Density Functional Theory Computations on O−O and O−H Bonds in (Fluorinated) Derivatives. *The Journal of Physical Chemistry A*, **104**(46), 10713-10720.

Ren, W., Zhou, Z., Zhu, Y., Jiang, L.-M., Wei, H., Niu, T., Fu, P., Qiu, Z. 2015a. Effect of sulfate radical oxidation on disintegration of waste activated sludge. *International Biodeterioration & Biodegradation*, **104**, 384-390.

Ren, Y., Lin, L., Ma, J., Yang, J., Feng, J., Fan, Z. 2015b. Sulfate radicals induced from peroxymonosulfate by magnetic ferrospinel MFe2O4 (M = Co, Cu, Mn, and Zn) as heterogeneous catalysts in the water. *Applied Catalysis B: Environmental*, **165**, 572-578.

Rochester, J.R. 2013. Bisphenol A and human health: A review of the literature. *Reproductive Toxicology*, **42**(0), 132-155.

Rodriguez, S., Vasquez, L., Costa, D., Romero, A., Santos, A. 2014. Oxidation of Orange G by persulfate activated by Fe(II), Fe(III) and zero valent iron (ZVI). *Chemosphere*, **101**, 86-92.

Rosenfeldt, E.J., Linden, K.G., Canonica, S., von Gunten, U. 2006. Comparison of the efficiency of OH radical formation during ozonation and the advanced oxidation processes O3/H2O2 and UV/H2O2. *Water Research*, **40**(20), 3695-3704.

Ruhl, A.S., Zietzschmann, F., Hilbrandt, I., Meinel, F., Altmann, J., Sperlich, A., Jekel, M. 2014. Targeted testing of activated carbons for advanced wastewater treatment. *Chemical Engineering Journal*, **257**(0), 184-190.

Sánchez-Polo, M., Abdel daiem, M.M., Ocampo-Pérez, R., Rivera-Utrilla, J., Mota, A.J. 2013. Comparative study of the photodegradation of bisphenol A by HO, SO4− and CO3−/HCO3 radicals in aqueous phase. *Science of The Total Environment*, **463–464**(0), 423-431.

Saputra, E., Muhammad, S., Sun, H., Ang, H.-M., Tadé, M.O., Wang, S. 2013a. A comparative study of spinel structured Mn3O4, Co3O4 and Fe3O4 nanoparticles in catalytic oxidation of phenolic contaminants in aqueous solutions. *Journal of Colloid and Interface Science*, **407**(0), 467-473.

Saputra, E., Muhammad, S., Sun, H., Ang, H.-M., Tadé, M.O., Wang, S. 2013b. Manganese oxides at different oxidation states for heterogeneous activation of

peroxymonosulfate for phenol degradation in aqueous solutions. *Applied Catalysis B: Environmental*, **142–143**(0), 729-735.

Saputra, E., Muhammad, S., Sun, H., Ang, H.-M., Tadé, M.O., Wang, S. 2014. Shape-controlled activation of peroxymonosulfate by single crystal α-Mn2O3 for catalytic phenol degradation in aqueous solution. *Applied Catalysis B: Environmental*, **154–155**, 246-251.

Saputra, E., Muhammad, S., Sun, H., Ang, H.M., Tade, M.O., Wang, S. 2013c. Different Crystallographic One-dimensional MnO2 Nanomaterials and Their Superior Performance in Catalytic Phenol Degradation. *Environmental Science & Technology*.

Saputra, E., Muhammad, S., Sun, H., Ang, H.M., Tadé, M.O., Wang, S. 2012a. Red mud and fly ash supported Co catalysts for phenol oxidation. *Catalysis Today*, **190**(1), 68-72.

Saputra, E., Muhammad, S., Sun, H., Patel, A., Shukla, P., Zhu, Z.H., Wang, S. 2012b. α-MnO2 activation of peroxymonosulfate for catalytic phenol degradation in aqueous solutions. *Catalysis Communications*, **26**(0), 144-148.

Sarifuddin, G., Rajakumar, A. 2012. Semi-Quantitative Determination of Hydroxyl Radicals by Benzoic Acid Hydroxylation: An Analytical Methodology for Photo-Fenton Systems. *Current Analytical Chemistry*, **8**(1), 143-149.

Sauvé, S., Desrosiers, M. 2014. A review of what is an emerging contaminant. *Chem. Cent. J*, **8**, 15.

Sharma, J., Mishra, I.M., Dionysiou, D.D., Kumar, V. 2015. Oxidative removal of Bisphenol A by UV-C/peroxymonosulfate (PMS): Kinetics, influence of co-existing chemicals and degradation pathway. *Chemical Engineering Journal*, **276**, 193-204.

Shi, P., Su, R., Zhu, S., Zhu, M., Li, D., Xu, S. 2012. Supported cobalt oxide on graphene oxide: Highly efficient catalysts for the removal of Orange II from water. *Journal of Hazardous Materials*, **229–230**(0), 331-339.

Shukla, P., Sun, H., Wang, S., Ang, H.M., Tadé, M.O. 2011. Co-SBA-15 for heterogeneous oxidation of phenol with sulfate radical for wastewater treatment. *Catalysis Today*, **175**(1), 380-385.

Shukla, P., Wang, S., Singh, K., Ang, H.M., Tadé, M.O. 2010a. Cobalt exchanged zeolites for heterogeneous catalytic oxidation of phenol in the presence of peroxymonosulphate. *Applied Catalysis B: Environmental*, **99**(1–2), 163-169.

Shukla, P.R., Wang, S., Sun, H., Ang, H.M., Tadé, M. 2010b. Activated carbon supported cobalt catalysts for advanced oxidation of organic contaminants in aqueous solution. *Applied Catalysis B: Environmental*, **100**(3–4), 529-534.

Simonsen, L.O., Harbak, H., Bennekou, P. 2012. Cobalt metabolism and toxicology—A brief update. *Science of The Total Environment*, **432**, 210-215.

Spiro, M. 1979. The standard potential of the peroxosulphate/sulphate couple. *Electrochimica Acta*, **24**(3), 313-314.

Staples, C.A., Dome, P.B., Klecka, G.M., Oblock, S.T., Harris, L.R. 1998. A review of the environmental fate, effects, and exposures of bisphenol A. *Chemosphere*, **36**(10), 2149-2173.

Steele, W.V., Appelman, E.H. 1982. The standard enthalpy of formation of peroxymonosulfate (HSO5−) and the standard electrode potential of the peroxymonosulfate-bisulfate couple. *The Journal of Chemical Thermodynamics*, **14**(4), 337-344.

Stoyanova, M., Slavova, I., Christoskova, S., Ivanova, V. 2014. Catalytic performance of supported nanosized cobalt and iron–cobalt mixed oxides on MgO in oxidative degradation of Acid Orange 7 azo dye with peroxymonosulfate. *Applied Catalysis A: General*, **476**, 121-132.

Su, S., Guo, W., Leng, Y., Yi, C., Ma, Z. 2013. Heterogeneous activation of Oxone by CoxFe3−xO4 nanocatalysts for degradation of rhodamine B. *Journal of Hazardous Materials*, **244–245**(0), 736-742.

Subagio, D.P., Srinivasan, M., Lim, M., Lim, T.-T. 2010. Photocatalytic degradation of bisphenol-A by nitrogen-doped TiO2 hollow sphere in a vis-LED photoreactor. *Applied Catalysis B: Environmental*, **95**(3–4), 414-422.

Sun, H., Kwan, C., Suvorova, A., Ang, H.M., Tadé, M.O., Wang, S. 2014. Catalytic oxidation of organic pollutants on pristine and surface nitrogen-modified carbon nanotubes with sulfate radicals. *Applied Catalysis B: Environmental*, **154–155**, 134-141.

Sun, H., Liang, H., Zhou, G., Wang, S. 2013a. Supported cobalt catalysts by one-pot aqueous combustion synthesis for catalytic phenol degradation. *Journal of Colloid and Interface Science*, **394**(0), 394-400.

Sun, H., Liu, S., Zhou, G., Ang, H.M., Tadé, M.O., Wang, S. 2012a. Reduced Graphene Oxide for Catalytic Oxidation of Aqueous Organic Pollutants. *ACS Applied Materials & Interfaces*, **4**(10), 5466-5471.

Sun, H., Wang, Y., Liu, S., Ge, L., Wang, L., Zhu, Z., Wang, S. 2013b. Facile synthesis of nitrogen doped reduced graphene oxide as a superior metal-free catalyst for oxidation. *Chemical Communications*, **49**(85), 9914-9916.

Sun, H., Zhou, G., Liu, S., Ang, H.M., Tadé, M.O., Wang, S. 2012b. Nano-Fe0 Encapsulated in Microcarbon Spheres: Synthesis, Characterization, and Environmental Applications. *ACS Applied Materials & Interfaces*, **4**(11), 6235-6241.

Sun, X., Li, Y. 2004. Ga2O3 and GaN Semiconductor Hollow Spheres. *Angewandte Chemie International Edition*, **43**(29), 3827-3831.

Tai, C., Peng, J.F., Liu, J.F., Jiang, G.B., Zou, H. 2004. Determination of hydroxyl radicals in advanced oxidation processes with dimethyl sulfoxide trapping and liquid chromatography. *Analytica Chimica Acta*, **527**(1), 73-80.

Tan, C., Gao, N., Deng, Y., Deng, J., Zhou, S., Li, J., Xin, X. 2014. Radical induced degradation of acetaminophen with Fe3O4 magnetic nanoparticles as heterogeneous activator of peroxymonosulfate. *Journal of Hazardous Materials*, **276**(0), 452-460.

Tang, D., Zhang, G., Guo, S. 2015. Efficient activation of peroxymonosulfate by manganese oxide for the degradation of azo dye at ambient condition. *Journal of Colloid and Interface Science*, **454**, 44-51.

Teeguarden, J.G., Hanson-Drury, S. 2013. A systematic review of Bisphenol A “low dose” studies in the context of human exposure: A case for establishing standards for reporting “low-dose” effects of chemicals. *Food and Chemical Toxicology*, **62**(0), 935-948.

Tian, Z.-R., Tong, W., Wang, J.-Y., Duan, N.-G., Krishnan, V.V., Suib, S.L. 1997. Manganese Oxide Mesoporous Structures: Mixed-Valent Semiconducting Catalysts. *Science*, **276**(5314), 926-930.

Tiraferri, A., Chen, K.L., Sethi, R., Elimelech, M. 2008. Reduced aggregation and sedimentation of zero-valent iron nanoparticles in the presence of guar gum. *Journal of Colloid and Interface Science*, **324**(1–2), 71-79.

Tsai, W.-T., Lai, C.-W., Su, T.-Y. 2006. Adsorption of bisphenol-A from aqueous solution onto minerals and carbon adsorbents. *Journal of Hazardous Materials*, **134**(1–3), 169-175.

Tsitonaki, A., Petri, B., Crimi, M., MosbÆK, H., Siegrist, R.L., Bjerg, P.L. 2010. In Situ Chemical Oxidation of Contaminated Soil and Groundwater Using Persulfate: A Review. *Critical Reviews in Environmental Science and Technology*, **40**(1), 55-91.

Tully, F.P., Ravishankara, A.R., Thompson, R.L., Nicovich, J.M., Shah, R.C., Kreutter, N.M., Wine, P.H. 1981. Kinetics of the reactions of hydroxyl radical with benzene and toluene. *The Journal of Physical Chemistry*, **85**(15), 2262-2269.

Uchida, M., Shinohara, O., Ito, S., Kawasaki, N., Nakamura, T., Tanada, S. 2000. Reduction of Iron(III) Ion by Activated Carbon Fiber. *Journal of Colloid and Interface Science*, **224**(2), 347-350.

Uhrecký, R., Padělková, Z., Moncol, J., Koman, M., Dlháň, L.u., Titiš, J., Boča, R. 2013. Synthesis, crystal structure, spectra and magnetic properties of new manganese(III) and iron(III) dipicolinate complexes. *Polyhedron*, **56**(0), 9-17.

Vargas, R., Núñez, O. 2009. Hydrogen bond interactions at the TiO2 surface: Their contribution to the pH dependent photo-catalytic degradation of p-nitrophenol. *Journal of Molecular Catalysis A: Chemical*, **300**(1–2), 65-71.

Vel Leitner, N.K., Roshani, B. 2010. Kinetic of benzotriazole oxidation by ozone and hydroxyl radical. *Water Research*, **44**(6), 2058-2066.

Viswanathan, B., Subramanian, V., Lee, J.S. 2014. *Materials and Processes for Solar Fuel Production*. Springer New York.

Volpe, A., Pagano, M., Mascolo, G., Lopez, A., Ciannarella, R., Locaputo, V. 2013. Simultaneous Cr(VI) reduction and non-ionic surfactant oxidation by peroxymonosulphate and iron powder. *Chemosphere*, **91**(9), 1250-1256.

Voutsa, D., Hartmann, P., Schaffner, C., Giger, W. 2006. Benzotriazoles, Alkylphenols and Bisphenol A in Municipal Wastewaters and in the Glatt River, Switzerland. *Environmental Science and Pollution Research*, **13**(5), 333-341.

Wacławek, S., Grübel, K., Černík, M. 2015. Simple spectrophotometric determination of monopersulfate. *Spectrochimica Acta Part A: Molecular and Biomolecular Spectroscopy*, **149**, 928-933.

Wadewitz, D., Gruner, W., Herklotz, M., Klose, M., Giebeler, L., Voß, A., Thomas, J., Gemming, T., Eckert, J., Ehrenberg, H. 2013. Investigation of Copper-Cobalt-Oxides as Model Systems for Composite Interactions in Conversion-Type Electrodes for Lithium-Ion Batteries. *Journal of The Electrochemical Society*, **160**(8), A1333-A1339.

Wang, C., Kang, J., Sun, H., Ang, H.M., Tadé, M.O., Wang, S. One-pot synthesis of N-doped graphene for metal-free advanced oxidation processes. *Carbon*.

Wang, J., Guo, Y., Liu, B., Jin, X., Liu, L., Xu, R., Kong, Y., Wang, B. 2011a. Detection and analysis of reactive oxygen species (ROS) generated by nano-sized TiO2 powder under ultrasonic irradiation and application in sonocatalytic degradation of organic dyes. *Ultrasonics Sonochemistry*, **18**(1), 177-183.

Wang, M., Zai, J., Wei, X., Chen, W., Liang, N., Xu, M., Qi, R., Qian, X. 2015a. N-type hedgehog-like CuBi2O4 hierarchical microspheres: room temperature synthesis and their photoelectrochemical properties. *CrystEngComm*, **17**(21), 4019-4025.

Wang, P., Fane, A.G., Lim, T.-T. 2013. Evaluation of a submerged membrane vis-LED photoreactor (sMPR) for carbamazepine degradation and TiO2 separation. *Chemical Engineering Journal*, **215–216**, 240-251.

Wang, P., Lim, T.-T. 2012. Membrane vis-LED photoreactor for simultaneous penicillin G degradation and TiO2 separation. *Water Research*, **46**(6), 1825-1837.

Wang, P., Yang, S., Shan, L., Niu, R., Shao, X. 2011b. Involvements of chloride ion in decolorization of Acid Orange 7 by activated peroxydisulfate or peroxymonosulfate oxidation. *Journal of Environmental Sciences*, **23**(11), 1799-1807.

Wang, Y., Indrawirawan, S., Duan, X., Sun, H., Ang, H.M., Tadé, M.O., Wang, S. 2015b. New insights into heterogeneous generation and evolution processes of sulfate radicals for phenol degradation over one-dimensional α-MnO2 nanostructures. *Chemical Engineering Journal*, **266**, 12-20.

Wang, Y., Sun, H., Ang, H.M., Tadé, M.O., Wang, S. 2015c. 3D-hierarchically structured MnO2 for catalytic oxidation of phenol solutions by activation of peroxymonosulfate: Structure dependence and mechanism. *Applied Catalysis B: Environmental*, **164**, 159-167.

Wang, Y., Sun, H., Ang, H.M., Tadé, M.O., Wang, S. 2014a. Facile Synthesis of Hierarchically Structured Magnetic MnO2/ZnFe2O4 Hybrid Materials and Their Performance in Heterogeneous Activation of Peroxymonosulfate. *ACS Applied Materials & Interfaces*, **6**(22), 19914-19923.

Wang, Y., Sun, H., Ang, H.M., Tadé, M.O., Wang, S. 2014b. Magnetic Fe3O4/carbon sphere/cobalt composites for catalytic oxidation of phenol solutions with sulfate radicals. *Chemical Engineering Journal*, **245**, 1-9.

Wang, Y., Sun, H., Ang, H.M., Tadé, M.O., Wang, S. 2014c. Synthesis of magnetic core/shell carbon nanosphere supported manganese catalysts for oxidation of organics in water by peroxymonosulfate. *Journal of Colloid and Interface Science*, **433**, 68-75.

Wang, Y., Sun, H., Duan, X., Ang, H.M., Tadé, M.O., Wang, S. 2015d. A new magnetic nano zero-valent iron encapsulated in carbon spheres for oxidative degradation of phenol. *Applied Catalysis B: Environmental*, **172–173**, 73-81.

Wang, Z., Du, Y., Liu, Y., Zou, B., Xiao, J., Ma, J. 2016. Degradation of organic pollutants by NiFe2O4/peroxymonosulfate: efficiency, influential factors and catalytic mechanism. *RSC Advances*, **6**(13), 11040-11048.

Wei, G., Liang, X., He, Z., Liao, Y., Xie, Z., Liu, P., Ji, S., He, H., Li, D., Zhang, J. 2015a. Heterogeneous activation of Oxone by substituted magnetites Fe3−xMxO4 (Cr, Mn, Co, Ni) for degradation of Acid Orange II at neutral pH. *Journal of Molecular Catalysis A: Chemical*, **398**, 86-94.

Wei, L., Shifu, C., Sujuan, Z., Wei, Z., Huaye, Z., Xiaoling, Y. 2010. Preparation and characterization of p–n heterojunction photocatalyst p-CuBi2O4/n-TiO2 with high photocatalytic activity under visible and UV light irradiation. *Journal of Nanoparticle Research*, **12**(4), 1355-1366.

Wei, M., Ruan, Y., Luo, S., Li, X., Xu, A., Zhang, P. 2015b. The facile synthesis of a magnetic OMS-2 catalyst for decomposition of organic dyes in aqueous solution with peroxymonosulfate. *New Journal of Chemistry*.

Westerhoff, P., Moon, H., Minakata, D., Crittenden, J. 2009. Oxidation of organics in retentates from reverse osmosis wastewater reuse facilities. *Water Research*, **43**(16), 3992-3998.

Wu, D., Liu, M., Dong, D., Zhou, X. 2007. Effects of some factors during electrochemical degradation of phenol by hydroxyl radicals. *Microchemical Journal*, **85**(2), 250-256.

Wu, J., Pu, W., Yang, C., Zhang, M., Zhang, J. 2013. Removal of benzotriazole by heterogeneous photoelectro-Fenton like process using ZnFe2O4 nanoparticles as catalyst. *Journal of Environmental Sciences*, **25**(4), 801-807.

Wu, W., Huang, Z.-H., Lim, T.-T. 2014. Recent development of mixed metal oxide anodes for electrochemical oxidation of organic pollutants in water. *Applied Catalysis A: General*, **480**, 58-78.

Xie, Y., Zhang, Y., Yang, G., Liu, C., Wang, J. 2013. Hydrothermal synthesis of CuBi2O4 nanosheets and their photocatalytic behavior under visible light irradiation. *Materials Letters*, **107**(0), 291-294.

Xu, J., Li, L., Guo, C., Zhang, Y., Wang, S. 2013. Removal of benzotriazole from solution by BiOBr photocatalysis under simulated solar irradiation. *Chemical Engineering Journal*, **221**(0), 230-237.

Xu, L., Liu, W., Li, X., Rashid, S., Shen, C., Wen, Y. 2015a. Fabrication of MnOx heterogeneous catalysts from wet sludge for degradation of azo dyes by activated peroxymonosulfate. *RSC Advances*, **5**(16), 12248-12256.

Xu, L.J., Chu, W., Gan, L. 2015b. Environmental application of graphene-based CoFe2O4 as an activator of peroxymonosulfate for the degradation of a plasticizer. *Chemical Engineering Journal*, **263**, 435-443.

Xu, Y., Ai, J., Zhang, H. 2016. The mechanism of degradation of bisphenol A using the magnetically separable CuFe2O4/peroxymonosulfate heterogeneous oxidation process. *Journal of Hazardous Materials*, **309**, 87-96.

Yang, B., Tian, Z., Wang, B., Sun, Z., Zhang, L., Guo, Y., Li, H., Yan, S. 2015a. Facile synthesis of Fe3O4/hierarchical-Mn3O4/graphene oxide as a synergistic catalyst for activation of peroxymonosulfate for degradation of organic pollutants. *RSC Advances*, **5**(27), 20674-20683.

Yang, Q., Choi, H., Al-Abed, S.R., Dionysiou, D.D. 2009. Iron–cobalt mixed oxide nanocatalysts: Heterogeneous peroxymonosulfate activation, cobalt leaching, and ferromagnetic properties for environmental applications. *Applied Catalysis B: Environmental*, **88**(3–4), 462-469.

Yang, Q., Choi, H., Chen, Y., Dionysiou, D.D. 2008. Heterogeneous activation of peroxymonosulfate by supported cobalt catalysts for the degradation of 2,4-dichlorophenol in water: The effect of support, cobalt precursor, and UV radiation. *Applied Catalysis B: Environmental*, **77**(3–4), 300-307.

Yang, S., Wang, P., Yang, X., Shan, L., Zhang, W., Shao, X., Niu, R. 2010. Degradation efficiencies of azo dye Acid Orange 7 by the interaction of heat, UV and anions with common oxidants: Persulfate, peroxymonosulfate and hydrogen peroxide. *Journal of Hazardous Materials*, **179**(1–3), 552-558.

Yang, Y., Jiang, J., Lu, X., Ma, J., Liu, Y. 2015b. Production of Sulfate Radical and Hydroxyl Radical by Reaction of Ozone with Peroxymonosulfate: A Novel Advanced Oxidation Process. *Environmental Science & Technology*, **49**(12), 7330-7339.

Yang, Y., Pignatello, J.J., Ma, J., Mitch, W.A. 2014a. Comparison of Halide Impacts on the Efficiency of Contaminant Degradation by Sulfate and Hydroxyl Radical-Based Advanced Oxidation Processes (AOPs). *Environmental Science & Technology*, **48**(4), 2344-2351.

Yang, Z., Yang, Y., Zhu, X., Chen, G., Zhang, W. 2014b. An Outward Coating Route to CuO/MnO2 Nanorod Array Films and Their Efficient Catalytic Oxidation of Acid Fuchsin Dye. *Industrial & Engineering Chemistry Research*, **53**(23), 9608-9615.

Yao, Y., Cai, Y., Lu, F., Wei, F., Wang, X., Wang, S. 2014. Magnetic recoverable MnFe2O4 and MnFe2O4-graphene hybrid as heterogeneous catalysts of peroxymonosulfate activation for efficient degradation of aqueous organic pollutants. *Journal of Hazardous Materials*, **270**(0), 61-70.

Yao, Y., Cai, Y., Wu, G., Wei, F., Li, X., Chen, H., Wang, S. 2015. Sulfate radicals induced from peroxymonosulfate by cobalt manganese oxides (CoxMn3−xO4) for Fenton-Like reaction in water. *Journal of Hazardous Materials*, **296**, 128-137.

Yao, Y., Xu, C., Yu, S., Zhang, D., Wang, S. 2013. Facile Synthesis of Mn3O4–Reduced Graphene Oxide Hybrids for Catalytic Decomposition of Aqueous Organics. *Industrial & Engineering Chemistry Research*, **52**(10), 3637-3645.

Yao, Y., Yang, Z., Zhang, D., Peng, W., Sun, H., Wang, S. 2012. Magnetic CoFe2O4–Graphene Hybrids: Facile Synthesis, Characterization, and Catalytic Properties. *Industrial & Engineering Chemistry Research*, **51**(17), 6044-6051.

Yu, X., Zhang, L., Liang, M., Sun, W. 2015. pH-dependent sulfonamides adsorption by carbon nanotubes with different surface oxygen contents. *Chemical Engineering Journal*, **279**, 363-371.

Zhang, J., Nosaka, Y. 2014. Mechanism of the OH radical generation in photocatalysis with TiO 2 of different crystalline types. *Journal of Physical Chemistry C*, **118**(20), 10824-10832.

Zhang, J., Nosaka, Y. 2015. Photocatalytic oxidation mechanism of methanol and the other reactants in irradiated TiO2 aqueous suspension investigated by OH radical detection. *Applied Catalysis B: Environmental*, **166–167**, 32-36.

Zhang, J., Shao, X., Shi, C., Yang, S. 2013a. Decolorization of Acid Orange 7 with peroxymonosulfate oxidation catalyzed by granular activated carbon. *Chemical Engineering Journal*, **232**(0), 259-265.

Zhang, L., Zhao, L., Lian, J. 2014a. Nanostructured Mn3O4-reduced graphene oxide hybrid and its applications for efficient catalytic decomposition of Orange II and high lithium storage capacity. *RSC Advances*, **4**(79), 41838-41847.

Zhang, R., Sun, P., Boyer, T.H., Zhao, L., Huang, C.-H. 2015. Degradation of Pharmaceuticals and Metabolite in Synthetic Human Urine by UV, UV/H2O2, and UV/PDS. *Environmental Science & Technology*, **49**(5), 3056-3066.

Zhang, S., Fan, Q., Gao, H., Huang, Y., Liu, X., Li, J., Xu, X., Wang, X. 2016. Formation of Fe3O4@MnO2 ball-in-ball hollow spheres as a high performance catalyst with enhanced catalytic performances. *Journal of Materials Chemistry A*.

Zhang, T., Chen, Y., Wang, Y., Le Roux, J., Yang, Y., Croué, J.-P. 2014b. Efficient Peroxydisulfate Activation Process Not Relying on Sulfate Radical Generation for Water Pollutant Degradation. *Environmental Science & Technology*, **48**(10), 5868-5875.

Zhang, T., Zhu, H., Croué, J.-P. 2013b. Production of Sulfate Radical from Peroxymonosulfate Induced by a Magnetically Separable CuFe2O4 Spinel in Water: Efficiency, Stability, and Mechanism. *Environmental Science & Technology*, **47**(6), 2784-2791.

Zhang, W., Tay, H.L., Lim, S.S., Wang, Y., Zhong, Z., Xu, R. 2010. Supported cobalt oxide on MgO: Highly efficient catalysts for degradation of organic dyes in dilute solutions. *Applied Catalysis B: Environmental*, **95**(1–2), 93-99.

Zhang, Y., Xie, Y., Li, J., Yang, G., Bai, T., Wang, J. 2013c. Effects of synthetic conditions on the morphology and catalytic properties of hierarchical CuBi2O4 nanoflowers grown by low-temperature solution process. *Journal of Alloys and Compounds*, **580**(0), 172-175.

Zhao, J., Zhang, Y., Quan, X., Chen, S. 2010. Enhanced oxidation of 4-chlorophenol using sulfate radicals generated from zero-valent iron and peroxydisulfate at ambient temperature. *Separation and Purification Technology*, **71**(3), 302-307.

Zhou, D., Zhang, H., Chen, L. 2015a. Sulfur-replaced Fenton systems: can sulfate radical substitute hydroxyl radical for advanced oxidation technologies? *Journal of Chemical Technology & Biotechnology*, **90**(5), 775-779.

Zhou, T., Wu, X., Mao, J., Zhang, Y., Lim, T.-T. 2014. Rapid degradation of sulfonamides in a novel heterogeneous sonophotochemical magnetite-catalyzed Fenton-like (US/UV/Fe3O4/oxalate) system. *Applied Catalysis B: Environmental*, **160–161**, 325-334.

Zhou, Y., Jiang, J., Gao, Y., Ma, J., Pang, S.-Y., Li, J., Lu, X.-T., Yuan, L.-P. 2015b. Activation of Peroxymonosulfate by Benzoquinone: A Novel Nonradical Oxidation Process *Environmental Science & Technology*, **49**(21), 12941-12950.

Zou, J., Ma, J., Chen, L., Li, X., Guan, Y., Xie, P., Pan, C. 2013. Rapid Acceleration of Ferrous Iron/Peroxymonosulfate Oxidation of Organic Pollutants by Promoting Fe(III)/Fe(II) Cycle with Hydroxylamine. *Environmental Science & Technology*, **47**(20), 11685-11691.

Zou, J., Ma, J., Zhang, X., Xie, P. 2014. Rapid spectrophotometric determination of peroxymonosulfate in water with cobalt-mediated oxidation decolorization of methyl orange. *Chemical Engineering Journal*, **253**, 34-39.